Kian Eichholz, B.Eng

DEVELOPMENT OF MECHANOBIOMIMETIC STRATEGIES TO DRIVE STEM CELL BEHAVIOUR FOR BONE REGENERATION

Trinity College Dublin, January 2019

A thesis submitted to the University of Dublin in partial fulfilment of
the requirements for the degree of

Doctor of Philosophy

Supervisor: Prof. David Hoey
Internal Examiner: Prof. Daniel Kelly
External Examiner: Prof. Paul Dalton

Declaration

I declare that this thesis has not been submitted as an exercise for a degree at this or any other university and it is entirely my own work.

I agree to deposit this thesis in the University's open access institutional repository or allow the library to do so on my behalf, subject to Irish Copyright Legislation and Trinity College Library conditions of use and acknowledgement.

_____

Kian Eichholz

Summary

There are a host of cases where clinical intervention must be taken to treat diseased or damaged bone, including severe fractures, defects, tumours requiring tissue removal, and debilitating diseases such as osteoporosis. However, there are no current treatments which adequately achieve this goal, with current autografting approaches having severe limitations in terms of quantity of tissue available and additional surgical sites which damage healthy tissue and increase infection risk. There is thus a need to develop new strategies for bone regeneration. Understanding the mechanisms behind bone regeneration, and in particular, the key role of the mesenchymal stem cell (MSC) in this process, would provide invaluable information for the development of strategies to effectively regenerate bone in a physiologically appropriate manner.

The overall aim of this thesis was to investigate the biophysical cues within the stem cell niche in bone which drive the recruitment and osteogenesis of MSCs, with the aim of developing strategies to recapitulate this behaviour and guide bone repair. The two primary means by which MSC behaviour is mediated were investigated in this thesis: indirect biophysical cues from osteocytes (stream 1 – chapter 3), and direct biophysical cues from the underlying fibrous tissue (stream 2 – chapter 4-6), which were subsequently combined to create a mechano-biomimetic scaffold for bone regeneration (chapter 7).

In this thesis, the indirect biophysical cues from osteocyte signalling to MSCs were first investigated (chapter 3), where osteocytes were shown to release distinct mechanically activated osteocyte-derived extracellular vesicles (MAEVs) which contained unique cargo compared to extracellular vesicles (EVs) from statically cultured cells. These MAEVs significantly enhanced MSC recruitment and osteogenesis, with trends being almost identical to MSCs treated with conditioned medium from mechanically stimulated osteocytes. This confirmed that EVs are a key component in osteocyte-MSC

mechanosignaling, and reveals their potential alone for use as mechanotherapeutics to guide regeneration.

Next, the role of direct biophysical cues in mediating MSC behaviour was investigated. To facilitate this, a melt electrowriting (MEW) printer was designed and built (chapter 4) to facilitate the fabrication of defined fibrous microenvironments upon which to study MSC behaviour. Various architectures with 10 μm fibre diameter were fabricated, where it was demonstrated that a 90° architecture enhanced MSC spreading and Yes-associated protein (YAP) nuclear expression, a marker for osteogenesis (chapter 5). Long term culture of MSCs further revealed enhanced osteogenic differentiation in this scaffold architecture.

The role of mineral modifications in driving MSC osteogenesis was further investigated (chapter 6). A biomimetic nano-needle hydroxyapatite (nnHA) coating was developed, characterised and compared to other mineral modification methods, including a commonly used coating method which yields a micro-plate hydroxyapatite (pHA) morphology, and a composite polycaprolactone-hydroxyapatite material to fabricate fibres with incorporated mineral. The nnHA coating significantly enhanced MSC mineralisation compared to all other groups and was also shown to facilitate a more controlled release of BMP2, demonstrating its potential for use in applications requiring controlled drug release.

Finally, stream 1 and 2 were combined, with MAEVs being used for the functionalisation of nnHA scaffolds (chapter 7). The addition of MAEVS further significantly enhanced mineralisation almost 2-fold, in addition to a total 24-fold compared to the 90° scaffold developed in chapter 4 and a total of 52-fold compared to random fibrous scaffolds. This biomimetic scaffold which incorporates both direct and indirect biophysical cues inspired by the native stem cell niche in bone thus holds great potential as a more physiologically relevant and effective strategy to guide bone regeneration.

Acknowledgements

Undertaking this project over the past number of years has been a tough, but rewarding journey. I have been extremely lucky to have enormous support from mentors, family and friends, and have been lucky enough to meet a lot of new people along the way which have also become lifelong friends. Without all of this support, none of this work would have been possible.

First and foremost, I would like to express my greatest thanks to Prof. David Hoey, and state that I genuinely could not have asked for a better supervisor. Dave has been a truly exceptional mentor, and I couldn't have done this work to anywhere near this standard without his help. Most importantly, his endless friendly support has made this project a joy to do. I have learned a lot from Dave over these past few years and will always be grateful to him for giving me this opportunity.

I was extremely lucky to work with a lot of great people throughout this PhD who have become great friends. To my original lab family; Jilly, Marie, Elena and Michele, who taught me from the level of not knowing what a pipette was, and Mathieu (Team Actimel), Ian, Angelica, Dan, Cairnan, Nian, Ivor and Conor, all of whom have helped me countless times throughout this project. I would also like to thank Kieran, Olwyn, Pedro, Paola, Pierluca, Fiona, Stan, Dinorath and Peter for their help and wisdom with various aspects of this project. Thanks also to Jess, Grá, Ian, Simon, Andy, Dave and Ross, my housemates Jenny, Julia and Stefan, and everyone else outside of my research group including those in my office in Parsons and everyone in TCBE, who have also helped along the way and made this journey much more fun than I thought possible.

To some of my great and long-time friends, Killian, Kieron, Daniel, Darragh, Luke, Johnny, Billy, JP and Patrick. There's been many times where things have gotten in the

way and we haven't seen each other for long periods of time, but when we do it's as if nothing has changed at all. So thank you all for always being there throughout the years.

I would like to express my deepest thanks to my family; my parents Libby and Jörg, and my sisters Orlagh and Ciara. I'm sure I haven't said this as much as I should, but I can't thank you all enough for the continuous and endless support you have given me throughout my life, without which I would not be where I am today. I would also like to say a huge thank you to mam in particular, for all your help and time spent reading over this thesis. I am also very lucky to have a close and hugely supportive extended family. I would like to say a special thanks to my grandmother Betty and late grandfather James, who believed my mind for engineering came from him. To my extended family in Ireland and all over the world for your great support over the years; my Opa Jochen, late Oma Marlies, my aunts and uncles Mary, Gerry, Nicky, Seamie, Martin, Michael, Rita, Teresa, Tommy and Silke, and all of my close cousins of which there are too many to name here.

Last but not least, I'd like to say a huge thank you to Sayuri, who has always given me tremendous support and has constantly been there for me throughout all the good times and the bad. I can't imagine how difficult this would have been without you, and feel extremely lucky to always have you by my side.

Thank you all.

Table of Contents

Publications

Eichholz, K.F. and Hoey, D.A. Mediating human stem cell behaviour via defined fibrous architectures by melt electrospinning writing. Acta Biomater, 2018. 75: p. 140-151.

Eichholz, K.F. and Hoey, D.A. Design and build of a melt electrowriting apparatus. (In preparation)

Eichholz, K.F., Woods, I., Johnson, G.J., Shen, N., Corrigan, M., Labour, M.N., Wynne, K., Lowry, M.C., O'Driscoll, L., Hoey, D.A. Osteocytes regulate human bone marrow mesenchymal stem cell behaviour via mechanically activated osteocyte-derived extracellular vesicles (MAEVs). (In preparation)

Eichholz, K.F. and Hoey, D.A. Melt electrospun written scaffolds with tailored fibrous and mineral architectures to enhance protein delivery and human MSC osteogenesis for bone regeneration. (In preparation)

Eichholz, K.F., Federici, A., Mahon, O.R., Hoey, D.A. Mechanically activated osteocyte-derived extracellular vesicle functionalised melt electrowritten materials for bone regeneration: A mechanobiomimetic scaffold (In preparation)

Book chapters

Eichholz, K.F. and Hoey, D.A. The Role of the Primary Cilium in Cellular Mechanotransduction, in Mechanobiology, C.F. Rawlinson, Editor. 2017, John Wiley & Sons, Inc: Hoboken, New Jersey.

Conference abstracts

Eichholz, K.F. and Hoey, D.A. Mimicking Cellular and ECM Mechanobiological Cues to Drive MSC Osteogenesis and Bone Regeneration. 25th Annual Conference of the section of Bioengineering of the Royal Academy of Medicine in Ireland, Limerick, 2019.

Eichholz, K.F. and Hoey, D.A. Mediating Human Stem Cell Behaviour Via Defined Fibrous Architectures By Melt Electrospinning Writing. In: Proc. of the European Orthopaedic Research Society, Galway, Ireland, 2018.

Eichholz, K.F., Woods, I., Shen, N., Johnson, G.J., Corrigan, M., Labour, M.N., Wynne, K., Lowry, M.C., O'Driscoll, L., Hoey, D.A. Quantitative analysis of the osteocyte secretome following oscillatory fluid shear stimulation. In: Proc. of the European Orthopaedic Research Society, Galway, Ireland, 2018.

Eichholz, K.F. and Hoey, D.A. Melt electrospun written constructs for skeletal tissue regeneration: The effect of fibre architecture on YAP signalling and hMSC differentiation. World Congress of Biomechanics, Dublin, Ireland, 2018.

Eichholz, K.F., Johnson, G.J., Corrigan, M., Labour, M.N., Wynne, K., Hoey, D.A. Quantitative analysis of the osteocyte secretome following oscillatory fluid shear stimulation. In: Proc. of the Orthopaedic Research Society, New Orleans, USA, 2018.

Eichholz, K.F. and Hoey, D.A. Melt electrospun written constructs for skeletal tissue regeneration: The effect of fibre architecture. In: Proc. of the Orthopaedic Research Society, New Orleans, USA, 2018.

Eichholz, K.F. and Hoey, D.A. Melt Electrospun Written Constructs For Skeletal Tissue Regeneration: The Effect Of Fibre Architecture. 24th Annual Conference of the section of Bioengineering of the Royal Academy of Medicine in Ireland, Dublin, 2018.

Eichholz, K.F. and Hoey, D.A. Melt Electrospun Written Scaffolds As *In vitro* Platforms For Cell Culture: The Effect Of Scaffold Pore Architecture. TERMIS EU Meeting, Davos, Switzerland, 2017.

Eichholz, K.F. and Hoey, D.A. Melt Electrospun Written Scaffolds As *In vitro* Platforms For Cell Culture: The Effect Of Scaffold Pore Architecture. 23rd Annual Conference of the section of Bioengineering of the Royal Academy of Medicine in Ireland, Belfast, 2017.

Eichholz, K.F. Design and Manufacture of an Innovative Biofabrication Method for 3D Tissue Engineering Constructs. 19th Sir Bernard Crossland Symposium, Belfast, 2016.

Eichholz, K.F., Mac Guinness, A.D., Hoey, D.A. Design and Fabrication of Tissue Engineering Scaffolds using Melt Electrospinning Writing. In: Proc. of the Orthopaedic Research Society, Florida, US, 2016.

Eichholz, K.F. and Hoey, D.A. Design And Fabrication Of Tissue Engineering Scaffolds Using Melt Electrospinning Writing. 22nd Annual Conference of the section of Bioengineering of the Royal Academy of Medicine in Ireland, Galway, 2016.

Eichholz, K.F. and Hoey, D.A. Design of a 3-axis Direct Writing Apparatus for Controlled Deposition of Melt Electrospun Fibres. 21st Annual Conference of the section of Bioengineering of the Royal Academy of Medicine in Ireland, Dublin, 2015.

Nomenclature

This is a list of commonly used abbreviations used in this thesis. Any other abbreviations will be explained in the text when used.

ALP	Alkaline phosphatase
ANOVA	Analysis of variance
BMP2	Bone morphogenic protein 2
BSA	Bovine serum albumin
C	Control
CAD	Computer aided design
CaP	Calcium phosphate
COX2	Cyclooxygenase 2
DMEM	Dulbecco's modified eagle medium
DNA	Deoxyribonucleic Acid
ECM	Extracellular matrix
EDX	Energy-dispersive x-ray spectroscopy
EV	Extracellular vesicle
FBS	Fetal bovine serum
FDM	Fused deposition modelling
HA	Hydroxyapatite
hMSC	Human mesenchymal stem cell
iHA	Incorporated hydroxyapatite
MAEV	Mechanically activated osteocyte-derived extracellular vesicles
MEW	Melt electrowriting / melt electrospinning writing
miRNA	Micro RNA (ribonucleic acid)
MLO-Y4	Osteocyte cell line from murine long bone osteocyte Y4
MSC	Mesenchymal stem cell
NaOH	Sodium hydroxide
nHA	Nano-hydroxyapatite
NM	Normal medium
nnHA	Nano-needle hydroxyapatite
OCN	Osteocalcin
OM	Osteogenic medium
OPN	Osteopontin
OSX	Osterix

PBS	Phosphate buffered saline
PCL	Polycaprolactone
pHA	Plate hydroxyapatite
PID	Proportional-integral-derivative
RUNX2	Runt-related transcription factor 2
S10	10° scaffold architecture
S45	45° scaffold architecture
S90	90° scaffold architecture
SBF	Simulated body fluid
SEM	Scanning electron microscope
TEM	Transmission electron microscope
SD	Standard deviation
SR	Random scaffold architecture
TCP	Tricalcium phosphate
TE	Tissue engineering
TTCP	Tetracalcium phosphate
XRD	X-ray diffraction
YAP	Yes-associated protein

Chapter 1

Introduction

1.1 The need for new strategies to regenerate tissue

There is an ever-increasing need for solutions to heal and replace damaged and diseased tissue. This can be appreciated by the millions of grafting procedures performed every year worldwide, including 2,000,000 bone graft procedures (Campana *et al.*, 2014), 800,000 coronary artery bypass grafts (Grand View Research, 2017) and 300,000 anterior cruciate ligament constructions (Giedraitis, Arnoczky, & Bedi, 2014), in addition to the 11,000,000 people requiring medical attention for severe burns each year (World Health Organisation, 2017). The vast majority of these procedures utilise autografts, which have two substantial drawbacks due to the necessity of a second surgical donor site as well as the limited amount of tissue which may be harvested. Allografts are also commonly used, however, this approach is also limited in terms of the amount of tissue which may be taken, as well as issues associated with biocompatibility and the increased potential for triggering an immune response. Synthetic engineered scaffolds for tissue regeneration are thus an attractive solution and have the potential to overcome the above issues to provide a reliable and effective source of tissue for regenerative applications *in vivo*. Moreover, use of these scaffolds to engineer tissues *in vitro* has considerable potential for the development of tissue models or organoids. These may aid in the further understanding of native tissue behaviour, in addition to their use as powerful biological platforms for the study of development and disease, and the safe and ethical development of pharmaceutical therapies.

1.2 Mechanobiological cues driving tissue regeneration

Throughout the body, cells are intimately intertwined with their surrounding environment. Both intrinsic and extrinsic forces play a fundamental role in defining this environment, which in turn guides cell behaviour in response to the constantly changing external cues. The mechanobiology of a cell's surrounding micro-environment is thus crucial in mediating its behaviour and ensuring tissue specific physiological homeostasis. Two key contributors to mediating this behaviour are the biophysical architecture/mechanical properties of the surrounding matrix in which the cells reside, and the biochemical factors released by resident/adjacent cells in response to adaptations in the mechanical environment. In bone, the close relationship between these cues and stem cell behaviour is of particular interest, due to the crucial role of stem cells in ensuring the continued regeneration and repair of this tissue. Indirect biochemical cues released from osteocytes recruit stem cells from the surrounding periosteum and endosteum, and further drive osteogenic differentiation in conjunction with direct biophysical cues upon binding of the stem cell to the underlying matrix.

Changes in specific tissue mechanical environments can have both local and systemic effects through the release of mechanically-mediated biochemical cues from resident cells that act via an autocrine or paracrine manner to influence neighbouring cells within the tissue, as well as to much greater distances to different tissues and organs throughout the body. This indirect biophysical regulation of cell behaviour is of particular importance in bone, which comprises a range of cell types working in unison to continuously maintain the tissue in response to the complex loading regimes to which it is subjected throughout everyday activity. It is known that cells within the matrix of bone, in particular the osteocyte which is by far the most abundant cell in bone, can detect forces via a combination of means including direct mechanical strain and interstitial fluid flow

induced shear forces (van Oers, Wang, & Bacabac, 2015; Weinbaum, Cowin, & Zeng, 1994). In response. the osteocyte subsequently sends signals to other bone residing cells to infer a response and help the tissue adapt to the changing mechanical environment (Dallas, Prideaux, & Bonewald, 2013). Mechanically stimulated osteocytes have been shown to promote osteoblast proliferation and recruitment (Brady, O'Brien, & Hoey, 2015) and inhibit osteoclast formation (Tan *et al.*, 2007; You *et al.*, 2008) via a paracrine mechanism. Importantly, osteocytes are also known to enhance the recruitment and osteogenic differentiation of stem cells (Brady *et al.*, 2015; Hoey, Kelly, & Jacobs, 2011) via the release of various factors (P. M. Govey *et al.*, 2014; Moester, Papapoulos, Löwik, & van Bezooijen, 2010), which is of great importance for the continued regeneration of bone. The specific means by which these factors mediate cell behaviour, along with the complete identification of the factors themselves, is yet to be fully understood however. The importance of these signalling cues in mediating tissue appropriate behaviour can truly be appreciated in cases of disease. For example, sclerostin expression is mediated by the osteocyte, with mechanical loading resulting in the inhibition of osteocyte expressed sclerostin and increased bone formation (A. G. Robling *et al.*, 2008). This has been exploited in a treatment for osteoporosis, where antibody treatment to inhibit sclerostin expression enhances bone formation *in vivo* (Xiaodong Li *et al.*, 2009), and has been shown in clinical trials to increase bone mineral density and reduce fracture risk (McClung, 2017).

The extracellular matrix (ECM) imposes a direct, biophysical constraint on the degree to which cells can interact with and spread within their surrounding matrix. In bone, this matrix is comprised of a composite structure composed primarily of collagen fibres and mineral crystals, with collagen fibres at the endosteum and periosteum aligning in a load dependent manner in response to extrinsic forces (Foolen *et al.*, 2008; McMahon, Boyde, & Bromage, 1995). Cell density, shape and degree of spreading are fundamentally defined by the underlying matrix in bone, which provides the blueprints to guide appropriate cellular

behaviour in addition to driving stem cell commitment towards the osteogenic lineage to ensure constant regeneration (Dupont *et al.*, 2011; McBeath, Pirone, Nelson, Bhadriraju, & Chen, 2004). A secondary variable of great importance which is defined by the matrix architecture is matrix stiffness, which is 25–40 kPa at the collagen precursor to bone laid down by osteoblasts, with this being the optimal range upon which MSCs undergo differentiation (Engler, Sen, Sweeney, & Discher, 2006). It is known that cells can sense this stiffness and exert cytoskeletal tension in response, which in turn can trigger a cascade of responses from initial alterations in cell shape through to controlling the cell's final fate and lineage commitment (Engler *et al.*, 2006; Wells, 2008). This has been demonstrated in a range of cell types within bone, including stem cells, osteoblasts and endothelial cells, in addition to other cells throughout the body including neurons, myoblasts, fibroblasts, which may behave in vastly different ways and differentiate towards different lineages in response to altered matrix architecture and stiffness (Y. Yang, Wang, Gu, & Leong, 2017). As with biochemical cues, the importance of tissue specific architecture in maintaining physiologically appropriate behaviour can truly be appreciated by considering cases of disease, and how this can influence the architectural and mechanical properties of native tissue. For example, inappropriately aligned fibres surrounding stroma can facilitate tumour cell migration and metastasis (Hogrebe, Reinhardt, & Gooch, 2017b), while osteoarthritis is associated with altered fibrous architecture in the superficial zone of cartilage resulting in the amplification of tissue strain causing further cell damage and death (Saarakkala *et al.*, 2010).

Appropriate signalling cues are thus fundamental for maintaining physiologically relevant behaviour and guiding appropriate tissue growth and regeneration, with these being present in bone in the form of indirect, mechanically mediated biochemical cues and direct, matrix mediated biophysical cues. It is thus of utmost importance to consider and understand the physical and biochemical cues present in the native environment of bone

and how these influence stem cell behaviour. This knowledge can then be used to design safe, effective and powerful bioengineering strategies for biologically inspired bone tissue regeneration.

1.3 MEW as a means to control the tissue microenvironment

Although cellular derived biochemical cues can be isolated from conditioned media, the ability to fabricate platforms that mimic the precise architecture and scale of the ECM of tissues is a considerable. MEW is a recently developed 3D printing technique which has the capability of fabricating fibres on the micron to sub-micron scale and precisely controlling their deposition in three dimensions (Brown, Dalton, & Hutmacher, 2011; Hochleitner *et al.*, 2015). The unique combination of ECM like fibre production and 3D printing control yields an extremely powerful biofabrication technology with the potential to create complex microenvironments which guide cell behaviour in a specific and desired way. Fibres may be precisely stacked on top of one another to fabricate large volume constructs with precise microarchitectures (F.M. Wunner, Wille, *et al.*, 2018), collected on rotating mandrels to form micro-fibrous tubular structures (McColl, Groll, Jungst, & Dalton, 2018) and used to fabricate scaffolds with intricate non-linear fibre architectures to define complex mechanical environments (Miguel Castilho, Mil, *et al.*, 2018; Hochleitner, Chen, *et al.*, 2018). The great potential of this technology can be seen in the rapid acceleration of MEW based constructs which have been developed for biomedical engineering applications since the technology was first described in 2011 (Brown *et al.*, 2011). Constructs have been developed for applications ranging from tissue engineering strategies for a host of tissue types including bone (Baldwin *et al.*, 2017), cartilage (Visser *et al.*, 2015), skin (Farrugia BL, 2013) and cardiac tissue (Miguel Castilho, Mil, *et al.*, 2018), to models for the study of prostate (Holzapfel *et al.*, 2014), breast (Thibaudeau *et al.*, 2014) and bone (Wagner *et al.*, 2016) tumours, to constructs to be used as platforms for

delivering cancer immunotherapy treatments (Delalat *et al.*, 2017). Many of these constructs have used MEW scaffolds as the foundation upon which to define the microarchitecture perceived by the cells, before the further addition of components such as growth factors, drugs, hydrogels and minerals to further define the cell microenvironment.

This technology thus has the potential to yield powerful and effective strategies in combination with specific growth factors and signalling molecules to precisely mediate cell behaviour for specific biomedical engineering applications. Despite this potential, there are only a few studies which have investigated the role of the defined fibrous architectures, achievable via MEW, on cell behaviour (F. Tourlomousis, Boettcher, Ding, & Chang, 2017; Filippos Tourlomousis & Chang, 2017). Further understanding of the mechanisms by which complex fibrous microarchitectures mediate cell behaviour will undoubtedly progress the already immense potential of this technology in the field of bioengineering. This, in combination with further functionalisation with specific growth factors and signalling molecules which are present in the native tissue environment, will allow for the fabrication of powerful, highly specific microenvironments to intricately guide the desired cell behaviour for a given biomedical engineering or tissue engineering application.

1.4 Objectives of thesis

Bone is characterised by a complex microenvironment consisting of a range of cell types signalling to one another in a constantly changing highly dynamic environment. Stem cells are a fundamental component of this system, responsible for bone development and playing key roles in bone growth, regeneration and healing via constant replenishment of the native cell population. Stem cell behaviour is driven by both direct and indirect biophysical cues in bone, with these cues providing the blueprints for guided stem cell recruitment and differentiation. The objective of this thesis is to study the complex microenvironment of bone and elucidate the appropriate direct and indirect biophysical

cues to drive osteogenic stem cell behaviour. This knowledge will be used to engineer safe, effective biomimetic strategies to regenerate bone. The ultimate goal is to design a next generation bone tissue regeneration strategy via the fabrication of an optimised microarchitecture as a foundation upon which to define specific mineral and biological components to elicit an enhanced osteogenesis response from a native stem cell population. This will be achieved via five specific objectives in two main streams, A and B, as shown below. A schematic of this thesis project outline is also shown in Figure 0-1.

A. Investigate the role of the osteocyte in mediating stem cell behaviour, facilitating the identification of biological factors for scaffold functionalisation:
    1. Study the role of the osteocyte in mechanically mediated signalling to human mesenchymal stem cells (hMSCs). A proteomic analysis will be conducted on the secretome of the osteocyte under static and dynamic conditions to form a map of potential mechanically regulated therapeutic targets to mediate stem cell behaviour. The key role of EVs in these processes will also be investigated.

B. Fabricate an optimised MEW microarchitecture to mediate stem cell behaviour:
    2. Design and build a MEW apparatus. The effect of system parameters on deposition characteristics will be investigated, and the system tuned for precise fibre deposition. This apparatus will be used to fabricate scaffolds with precise microenvironments for tissue engineering applications.
    3. Investigate the role of fibrous architecture in mediating human stem cell behaviour. Various scaffold architectures will be fabricated via MEW after which the mechanisms by which stem cells are influenced by the scaffolds will be investigated in terms of cell morphology, cell behaviour, proliferation and osteogenic differentiation. An optimal design for further development in this thesis will finally be identified.

4. Develop methods by which to modify MEW scaffolds with a mineral component to enhance osteogenic differentiation for bone regeneration. The previously identified optimal architecture will be utilised as a foundation for this work. Scaffolds with incorporated calcium phosphates will also be fabricated by forming a composite material for MEW. The protein loading characteristics of these modified constructs will also be investigated, to assess drug loading capacity and release profiles for further therapeutic applications.

Finally, these two streams will be combined to achieve the ultimate goal of this thesis:

5. Develop a biomimetic fibrous scaffold with controlled nanotopography functionalised with MAEVs to harness the regenerative potential of mechanobiological cues and significantly enhance bone repair

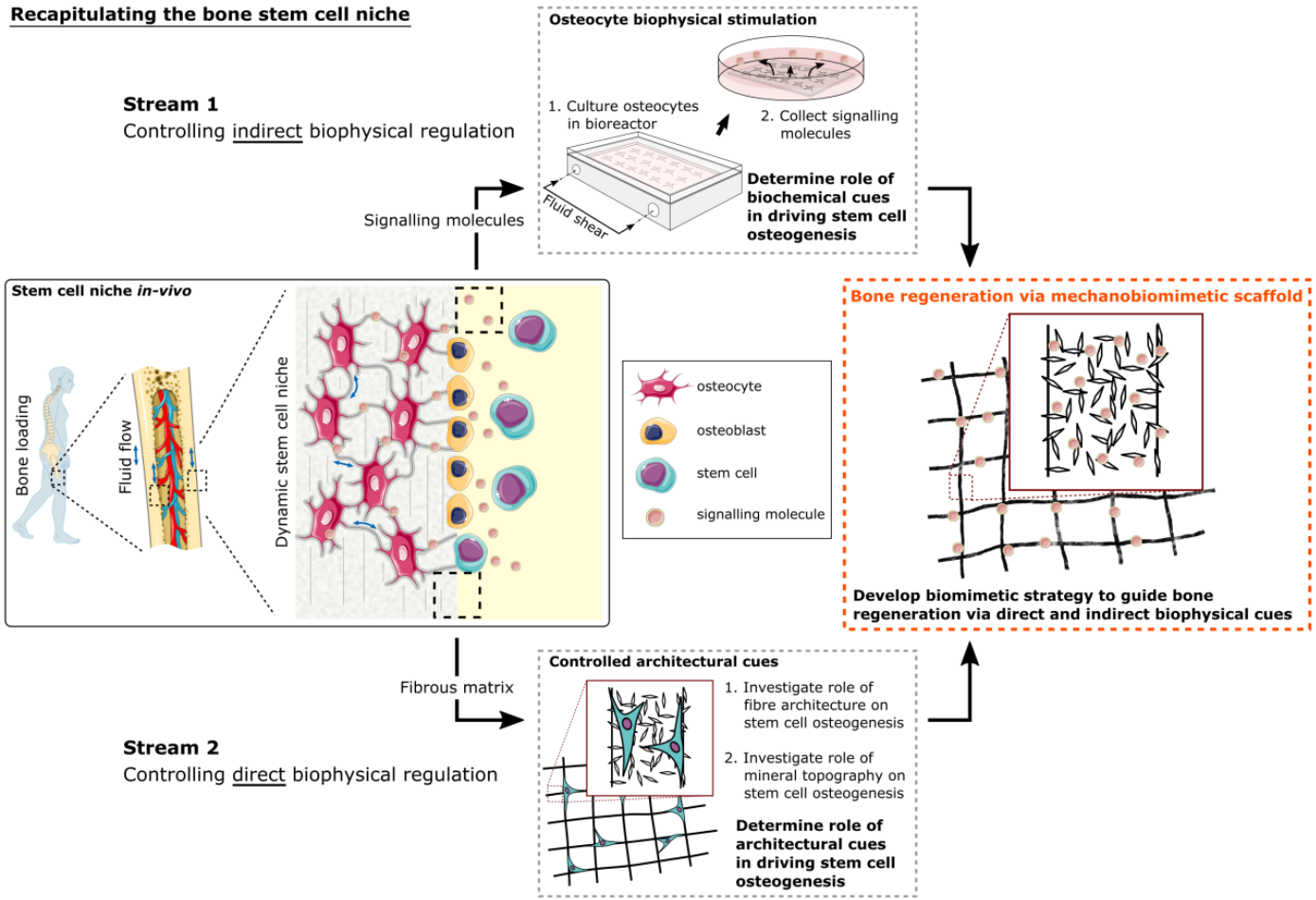

Figure 0-1 Schematic illustrating outline of thesis. Two project streams will be followed with the aim of recapitulating the bone stem cell niche, with the final goal of developing a mechano-biomimetic scaffold for bone regeneration.

Chapter 2

Literature review

2.1 Introduction

Direct and indirect biophysical cues jointly orchestrate cell behaviour throughout the body. This is particularly seen to be the case within bone, where these cues define the dynamic stem cell niche, which is a fundamental for the continuous, controlled regeneration of bone tissue (P. M. Govey, Loiselle, & Donahue, 2013). An understanding of the mechanisms by which the stem cell niche within bone behaves will provide powerful, biomimetic tools for the developments of therapeutics to regenerate diseased and damaged bone. To achieve this, a thorough understanding of the mechanobiology of bone tissue is key. This literature review will thus begin with an introduction to bone biology, before going into greater detail on the crosstalk between the different cells involved in bone regeneration, with a focus on signalling between stem cells and the osteocyte. Furthermore, the role of the surrounding matrix and associated mechanical forces in mediating osteocyte mechanosignalling will also be discussed. Next, the role of tissue architecture and mineral topography will be discussed, with a focus on how stem cells interact with their surrounding matrix in bone, and the implications for this in driving appropriate cell behaviour. How tissue architecture may be altered with disease and the implications of this for further local and systemic disease development will also be discussed, with this providing key insights into the importance of physiologically appropriate cellular behaviour. Taken together, this information will provide key insight for the development of tissue regeneration strategies which can be closely integrated with the biology and mechanics of native healthy tissue.

Previous approaches by which tissue regeneration strategies have been developed will then be discussed, with a focus on two technologies in particular: electrospinning and 3D printing. These two technologies will be discussed due to the sub-micron scale fibrous architectures which can be achieved and the great level of control which can be gained over architecture respectively. These encompass key capabilities which together give substantial control over the architectures which may be fabricated for regenerative medicine applications. A relatively new technology, MEW, does just this, and combines these technologies to form a powerful fabrication strategy with enormous potential. This biofabrication strategy will be introduced and discussed in terms of the underlying technology, fabrication capabilities, and current applications in regenerative medicine. Finally, advanced approaches which have developed this technology for applications in bone regeneration in particular will be discussed, including the development of composite materials, multi-phasic scaffolds, and incorporation of biochemical cues for enhanced therapeutic benefit.

2.2 Bone Anatomy

2.2.1 Cell types

There are several types of cells within bone which collectively regulate the formation, growth and repair of the tissue. One such family of cells is derived from mesenchymal cells (MSCs), which are precursor cells found within the marrow and periosteum. These MSCs are critical components of bone development and are the main source of bone marrow stromal cells, which in turn differentiate into osteoblasts and subsequently into osteocytes (Manolagas, 2000). The osteoclast is another cell resident in bone and is derived from a separate lineage of monocyte/macrophage cells originating from hematopoietic stem cells. These cells and their basic functions will be introduced below,

with a more in-depth discussion of signalling and crosstalk between these cell types being conducted in section 2.3.

Mesenchymal stem cells (MSCs) are precursor cells which play key roles in bone development, differentiating into osteoblasts which lay down bone matrix, and which in turn differentiate into osteocytes. This class of cells have been isolated from bone marrow and expanded in culture and have demonstrated a capacity to differentiate *in vitro*, leading to them being given the name MSCs. These cells are now known to arise from pericytes and adventitial progenitors, collectively known as perivascular stem cells (PSCs), with evidence also suggesting a possible non-blood vessel source in cranial sutures (Murray & Péault, 2015). There is still much debate over what exactly constitutes an MSC, and if these cells may truly be considered stem cells for regenerative purposes. The name was originally coined by Caplan (A. I. Caplan, 1991) due to his and other researchers' findings that this cell could give rise to osteoblasts, chondrocytes, adipocytes and fibroblasts among others (Charbord, 2010). Recently, a more specific cell which can differentiate into bone, cartilage and stroma alone has been identified and characterised, with this being termed a skeletal stem cell (SSC) (Chan *et al.*, 2018). While isolated MSCs or SSCs can self-renew and differentiate *in vitro*, there is a lack of evidence for long term skeletal regeneration or engraftment of these cells to bone or bone marrow *in vivo* and whether they behave as bona fide stem cells is still in question (Murray & Péault, 2015). Nonetheless, their importance in bone biology and key roles in signalling with other cells is well appreciated, leading to an alternative name of medicinal signalling cells being proposed (Arnold I. Caplan, 2017). For the remainder of this thesis, the term MSC will be used to denote "mesenchymal stem cell", with this remaining the most accepted and commonly used term in the literature to date.

Osteoblasts are cuboidal cells which are located on the surface of bone in a single layer. Their primary function is the synthesis of bone matrix which occurs by first depositing an organic matrix of collagen, other non-collagenous proteins such as

osteocalcin (OCN) and osteopontin (OPN), and proteoglycans (Florencio-Silva, Sasso, Sasso-Cerri, Simões, & Cerri, 2015). Subsequently, matrix vesicles are released, which due to their negative charge, immobilize calcium ions. ALP is also released by osteoblasts, resulting in the degradation of phosphate-containing compounds and release of phosphate ions inside the matrix vesicles. The calcium and phosphate ions within the vesicles then nucleate to form hydroxyapatite (HA) crystals, which after growth, eventually leads to their rupture and spreading of mineral crystals to the surrounding matrix. A quiescent variation of this cell is present on bone surfaces where bone remodelling does not occur, with these being given the name bone lining cells.

Osteocytes are the most abundant cell type in bone, comprising 95% of all bone cells with an average density of 20,000 - 80,000 cells/mm^3 bone tissue and a life span of up to several decades (Franz-Odendaal, Hall, & Witten, 2005). They originate from osteoblasts, which become terminally differentiated as osteocytes after becoming embedded in secreted matrix. They play key roles in coordinating the behaviour of other cell types in bone and throughout the body via communication by secreted factors (Bonewald, 2011). Osteocytes extend numerous dendritic processes which connect adjacent osteocytes forming a sensory network throughout bone tissue termed the lacuna-canalicular (LC) network. This network provides the platform through which osteocytes can sense changes in the external mechanical environment such as fluid flow induced shear stress, and signal to other cells within bone to adapt the tissue to these changes. The osteocyte can be considered an orchestrator of bone biology and remodelling and is thus of great relevance for tissue function. The osteocyte and its specific roles in signalling and tissue regulation will be discussed in greater detail in section 2.3.

In contrast to the above cell types, osteoclasts are derived from the hematopoietic stem cell lineage. They are large, multinucleated cells, formed via osteoclastogenesis which is mediated via RANKL (Florencio-Silva *et al.*, 2015). When this factor binds to RANK

receptors in osteoclast precursors, osteoclasts are formed. Conversely, osteoblasts release osteoprotegerin (OPG) which acts as a decoy receptor also binding to RANKL, inhibiting osteoclastogenesis. It is through this process that osteoclast numbers are controlled and the fine balance between bone resorption and deposition is maintained (Boyle, Simonet, & Lacey, 2003).

2.2.2 Development and healing

Understanding the mechanisms by which bone naturally develops and heals is useful for the development of regenerative strategies, which may exploit the natural behaviour of cells in order to form a strategy to heal bone. Bone development may occur via two methods; intramembranous ossification and endochondral ossification. Intramembranous ossification, which creates cortical and cancellous bone, is responsible for creating most of the cranial bones, flat bones of the face and the clavicles (K. A. Young *et al.*, 2013). It is initiated when MSCs proliferate and form compact nodules, before developing into capillaries as well as osteogenic cells (Gilbert, 2000) (Figure 2-1). Osteoblasts become separated from the region of calcification via a secreted osteoid matrix which calcifies due to mineral deposition, with some cells also becoming trapped in this matrix and differentiating into osteocytes. Trabeculae begin to form around this ossification region, with mesenchymal cells on the outer regions forming the periosteum. Blood vessels form within the region forming red bone marrow, with remodelling also taking place via osteoclasts.

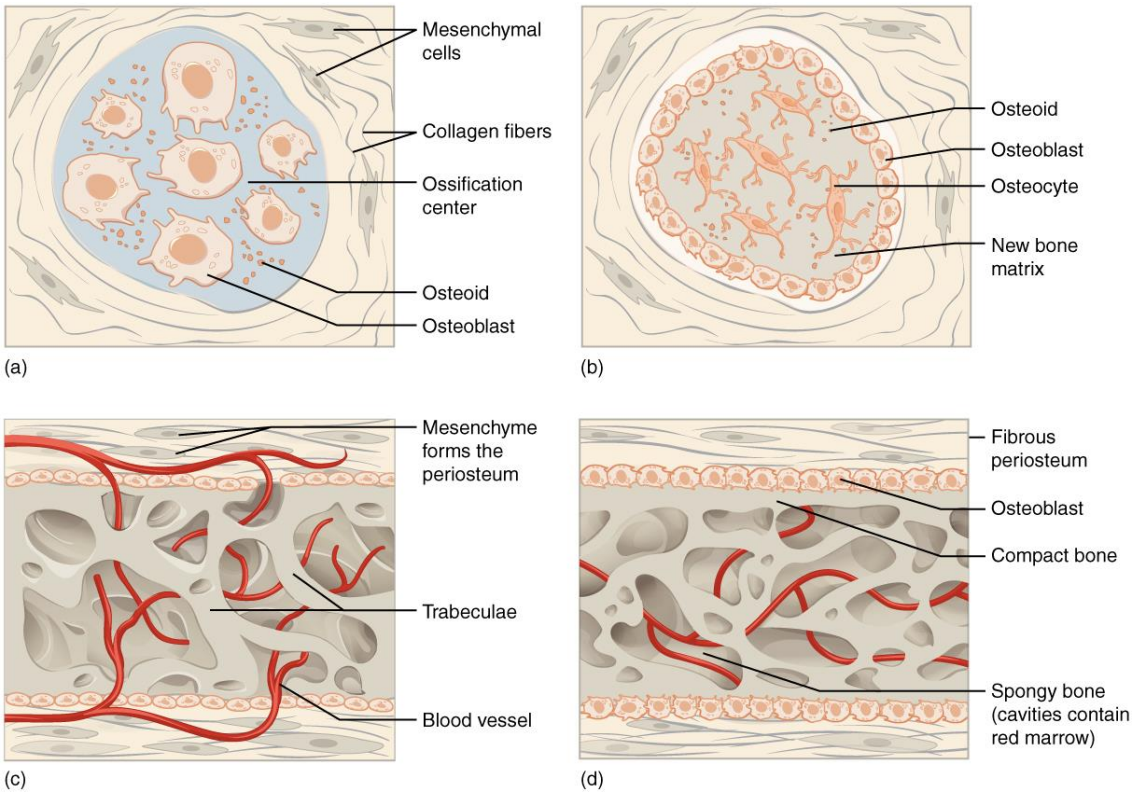

Figure 2-1 The stages of intramembranous ossification. Clusters of mesenchymal cells form in the embryonic skeleton (A), which begin to differentiate into osteogenic cells and secrete matrix which becomes mineralised (B). Trabeculae radiate from this ossification region, with mesenchymal cells lining the periphery and blood vessels branching through them (C). The periosteum is formed and red bone marrow forms from blood vessels, with remodelling continuing via osteoclasts (D). (K. A. Young *et al.*, 2013)

Endochondral ossification is the process but which long bones are formed within the body, in addition to the bones at the base of the skull. Cartilage tissue first forms from an aggregation of mesenchymal cells which differentiate into chondrocytes, with this forming the template for subsequent ossification and bone formation. Chondrocytes in the centre begin to increase in size, and more matrix is produced and becomes calcified, eventually limiting nutrient transfer resulting in cell death (K. A. Young *et al.*, 2013). The cartilage matrix then begins to break down, with blood vessels invading the resulting voids and expanding them to form a cavity. Blood vessels also supply osteogenic cells, which form a periosteal collar consisting of cortical bone around the diaphysis at the centre of the developing bone. A primary ossification centre forms within the diaphysis, resulting in cortical bone formation radiating towards the epiphyses at the ends of the bone.

Simultaneously, chondrocytes continue proliferating and forming cartilage, increasing the length of the developing bone before cartilage is replaced by bone. Secondary ossification centres form postnatally in the epiphyses, resulting in cartilage becoming replaced with cancellous bone in these regions with the exception of the surface, at which articular cartilage forms. An epiphyseal plate, also called the growth plate, allows further proliferation of cartilage and subsequent replacement with bone to continue in this region until bones have fully formed in length. Bone modelling also occurs during bone growth, with this resulting in an increase in bone diameter. Resorption of endosteal bone at the outer surface of the medullary cavity occurs via osteoclasts, along with deposition of bone beneath the periosteum via osteoblasts.

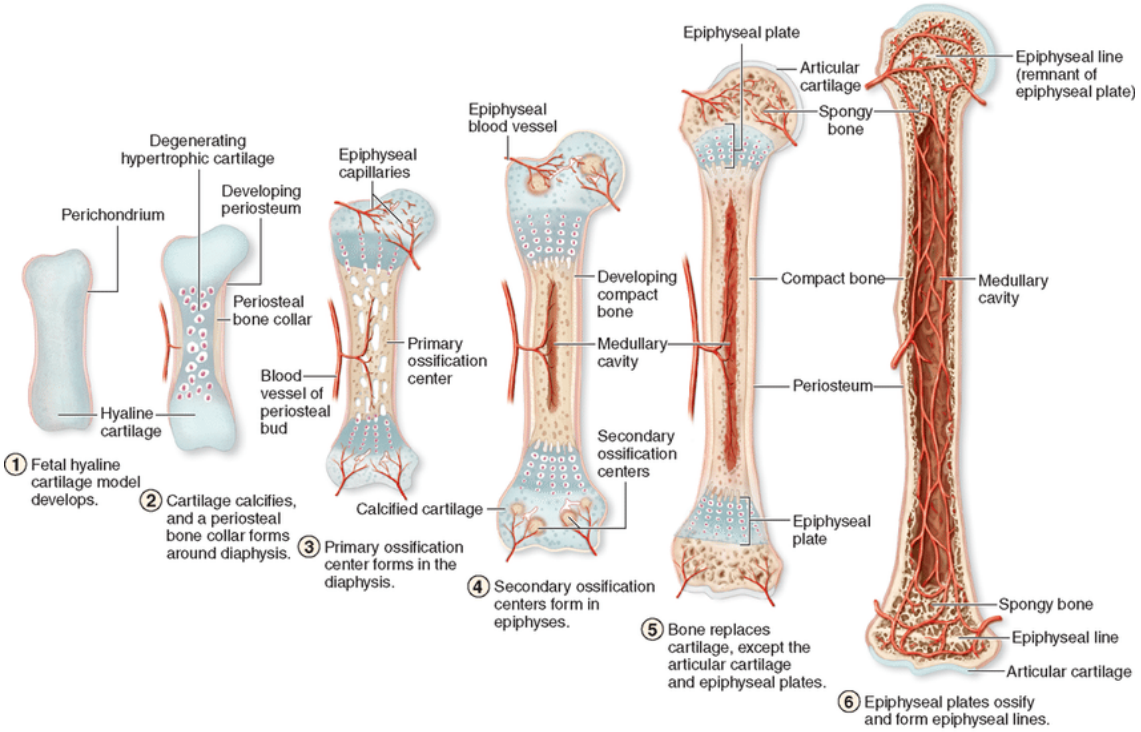

Figure 2-2 The stages of endochondral ossification. A cartilage template first develops via an aggregation of mesenchymal cells which differentiate into chondrocytes (1). Cells in the centre become hypertrophic, with nutrient transfer becoming limited after further matrix deposition, resulting in cell death and infiltration of voids by blood vessels (2). Blood vessels supply osteogenic cells, which form a primary ossification centre (3), which expands towards the epiphyses replacing the cartilage template with bone. Secondary ossification centres form after birth (4), and bone increases in length via chondrocyte proliferation at the epiphyseal (growth) plate, while osteoblasts simultaneously develop cortical bone. This continues until the bone has

reached its final length and structure with complete fusion of the epiphyseal plates (6). (Mescher & Junqueira, 2013)

Bones are continuously remodelled in adulthood, with old tissue and damaged bone being resorbed by osteoclasts, before deposition of new bone matrix by osteoblasts allowing defects and microfractures to be replaced by new tissue. The collaboration of osteoclasts and osteoblasts in this process is called a basic multicellular unit (BMU). In cortical bone, a cylindrical canal approximately 2 mm long and 175 μm wide penetrates the bone at a speed of approximately 20-40 μm/day (Hadjidakis & Androulakis, 2006). Approximately 10 osteoclasts form a tunnel in the dominant direction of loading, with thousands of osteoblasts subsequently filling the tunnel and forming new tissue. The process is similar in cancellous bone, with osteoclasts travelling along the surface of trabeculae and forming trenches which are then refilled with osteoblasts. In the event of serious trauma such as fracture, bone has the capability to regenerate itself. In less serious cases, this may occur via primary (contact) healing. If there is stable contact at the fracture point and a gap of under 0.01 mm, healing may occur similar to bone remodelling, with osteoclasts crossing the fracture point and osteoblasts remodelling the region as outlined above (Marsell & Einhorn, 2011). However secondary (indirect) healing occurs much more commonly. A hematoma first forms, providing a large range of growth factors and cells, while inflammatory factors promote angiogenesis. MSCs are recruited from bone marrow, surrounding tissues and systemically from the circulatory system. Endochondral ossification occurs within the hematoma, with cartilaginous tissue providing stability until bone formation and remodelling occurs. Intramembranous ossification also occurs directly adjacent to the fracture ends, which when bridged, increases rigidity and allows a degree of weight bearing (Marsell & Einhorn, 2011). Tissue is disorganised at first, with remodelling occurring via the osteoblast/osteoclast BMUs to restore the loading optimised structure of the tissue.

2.2.3 Hierarchical structure and composition

Bone is a hierarchical structure with two types on the macro scale: cortical (compact) and cancellous (spongy). Both of these types of bone are found throughout the body. Due to its greater strength, cortical bone found in regions which experience high levels of loading or which require greater protection such as in the diaphysis of long bones and in the skull. Cortical bone consists of osteons, which consist of sheets of circumferentially arranged tissue called lamellae. These contain networks of blood vessels and nerves through their centre as well as vessels which run perpendicularly to adjacent osteons, with this network providing the tissue and cells with a means for nutrient and waste transfer (Figure 2-3A). Osteocytes are regularly distributed through the tissue inside lacunae. The highly compact nature of this osteon derived architecture allows the tissue to withstand the great forces present during movement and loading. Cancellous bone is found at the ends of long bones, in addition to other bones including the ribs, vertebrae, pelvic bones and skull. The basic sub-unit of cancellous bone is the trabecula, which contain lamellae and osteocytes as in cortical bone, however with a more irregular architecture and distribution (Figure 2-3B). As stated by Wolff's law, healthy bone will adapt in response to loading (Frost, 1994). While this may occur in both cortical and cancellous bone, the greater capacity for trabeculae to arrange themselves in response to the load experienced in cancellous bone owes this tissue well to regions which experience complex loading patterns, for example in the femoral neck of the hip.

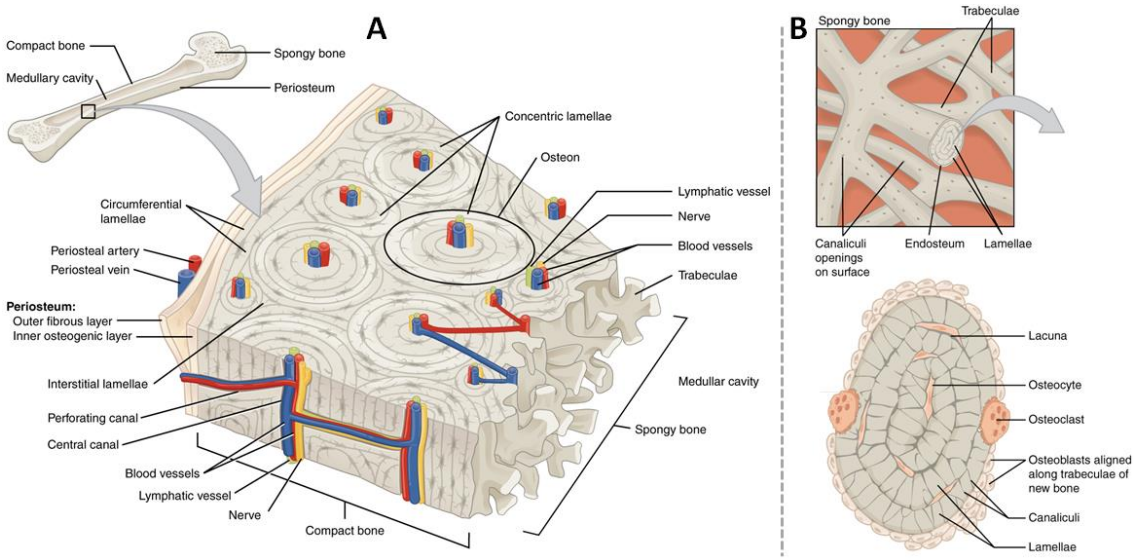

Figure 2-3 Structure of cortical (compact) bone (A), and cancellous (spongy) bone (B). Adapted from (K. A. Young *et al.*, 2013)

Further down the hierarchical structure of bone on the micro-scale, the organic component of the tissue is composed of collagen fibres of diameter 1 – 10 μm, which are arranged parallel to trabeculae in cancellous bone and in sheets of 90° offset between subsequent layers to form osteons in cortical bone (Figure 2-4) (Kane & Ma, 2013). Collagen provides the largest contribution towards the organic component of bone at 90%, with this comprising of primarily collagen type I. Collagen is a structural protein which provides the toughness for bone, as well as influencing bone cell proliferation, differentiation and apoptosis (M. F. Young, 2003). Collagen fibres are composed of fibrillar aggregations approximately 500 nm in diameter which in turn are composed of collagen molecules approximately 2 nm in diameter and 200 nm long. There are many other proteins which comprise the organic component of bone, including fibronectin, osteocalcin, osteopontin, alkaline phosphatase (ALP) and bone morphogenic proteins (BMPs), along with growth factors including insulin like growth factors (IGFs), transforming growth factors (TGFs), fibroblast growth factors (FGFs) and platelet derived growth factors (PDGFs) (Florencio-Silva *et al.*, 2015). All of these components play various roles within bone. BMPs play a key role in bone formation in addition to regeneration in fracture healing (Solheim, 1998). IGFs are known to be involved in the recruitment and

proliferation of MSCs, while TGFs, FGFs, and PDGFs are all involved in maintaining normal cell physiology while also demonstrating roles in promoting tissue repair (Solheim, 1998).

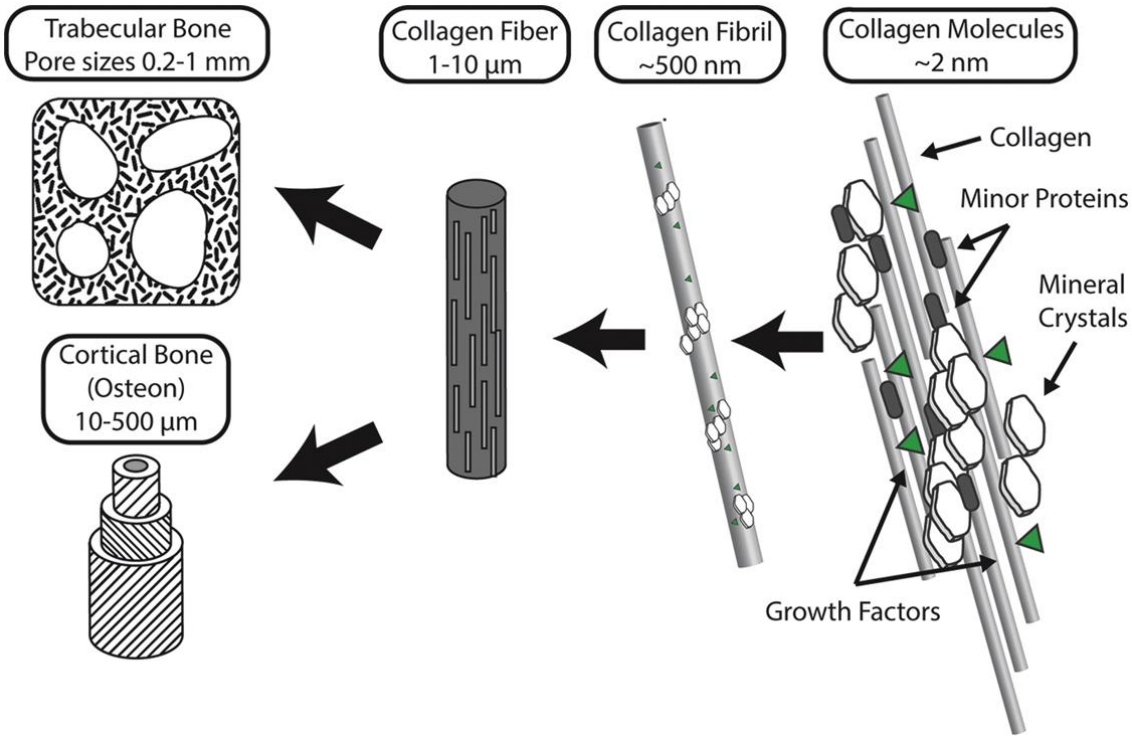

Figure 2-4 Hierarchical structure of bone (Kane & Ma, 2013)

A large proportion of bone is composed of inorganic mineral, which in turn has a hierarchical structure closely integrated with the collagen component, with proteins and growth factors dispersed throughout this composite structure. Bone mineral comprises approximately 60-70% of the tissue by weight (Boskey, 2013), with this providing the majority of the stiffness and hardness of the tissue. The basic mineral unit of bone consists of nano-scale needles with approximate dimensions of base 5 nm and length 50 – 100 nm (Reznikov, Bilton, Lari, Stevens, & Kröger, 2018). These needles form platelets composed of partly merging crystals of the same base and diameter, with width 20 – 30 nm, which in turn form stacks and aggregates with irregular 3D structures of size 200 – 300 nm. Water is known to play a role in this crystal organisation, and contributes to the inorganic structure via mediating the orientation of mineral crystals (Y. Wang *et al.*, 2013). Crystals are neither

exclusively intrafibrillar nor extrafibrillar but form a continuous crossfibrillar organisation which spans throughout and between collagen fibrils. This mineral organisation not only facilitates the high strength and stiffness of bone, but also provides a nano-scale structure to stabilise proteins and maintain their conformational structure (Yu *et al.*, 2017). Remarkably, proteins within the mineral matrix of bone can be preserved for centuries (Yu *et al.*, 2017), with the inverse relationship between protein stability and mineral feature size attesting to the great stability provided by the nano-structural features of bone.

In terms of mineral composition, bone is often approximated to stoichiometric hydroxyapatite (HA). This is a member of the apatite family, referring to a group of phosphate minerals with general formula $Ca_5(PO_4)_3(F,OH,Cl)$, with F-, OH- and Cl- present in the most common forms being fluorapatite, hydroxyapatite and chlorapatite respectively, with geological apatite, the most abundant phosphate mineral in the crust of the Earth containing various proportions of these ions (Wopenka & Pasteris, 2005). However, biological bone apatite has several characteristics which differ significantly from HA, such as the presence of varying amounts of chemical substitutions, the significantly smaller percentage of hydroxyl groups (Loong *et al.*, 2000), and the more disordered and protonated environment at the surface of crystals in biological minerals (Rey, Combes, Drouet, & Glimcher, 2009). Determining the precise chemical composition of bone brings many challenges, in part due to its complexity, presence of ions which are difficult to accurately measure to define their composition, and presence of a hydrated surface layer composed of bone and synthetic crystals containing a great variety of ions. Thus, several researchers have used synthetic calcium apatites, derived from natural geological apatites for example, to help gain a greater understanding of biological apatites. Remarkably, apatite is able to incorporate 50% of the elements of the periodic table, with substitutions that are known to occur in bone and tooth mineral including F, Cl, Na^+, K^+, Fe^{2+}, Zn^{2+}, Sr^{2+}, Mg^{2+}, carbonate (CO_3^{2-}) and citrate (Wopenka & Pasteris, 2005). Of particular relevance is the

substitution of PO_4^{3} anions in the general hydroxyapatite formula with HPO_4^{2-} and CO_3^{2-}, which have also been detected in large amounts in bone mineral samples (Rey *et al.*, 2009). Studies on synthetic apatites have also shown that there is a presence of non-apatite based mineral ions, as well as loosely bound ions on a hydrated surface layer as well as other ions and proteins in solution surrounding the mineral nanocrystals (Figure 2-5). In summary, while bone mineral may largely be approximated as stoichiometric hydroxyapatite, it is more accurately loosely defined as comprising a nano-plate/needle apatite base structure surrounded by a hydrated layer, disordered calcium phosphate (CaP) and loosely bound non-apatitic components.

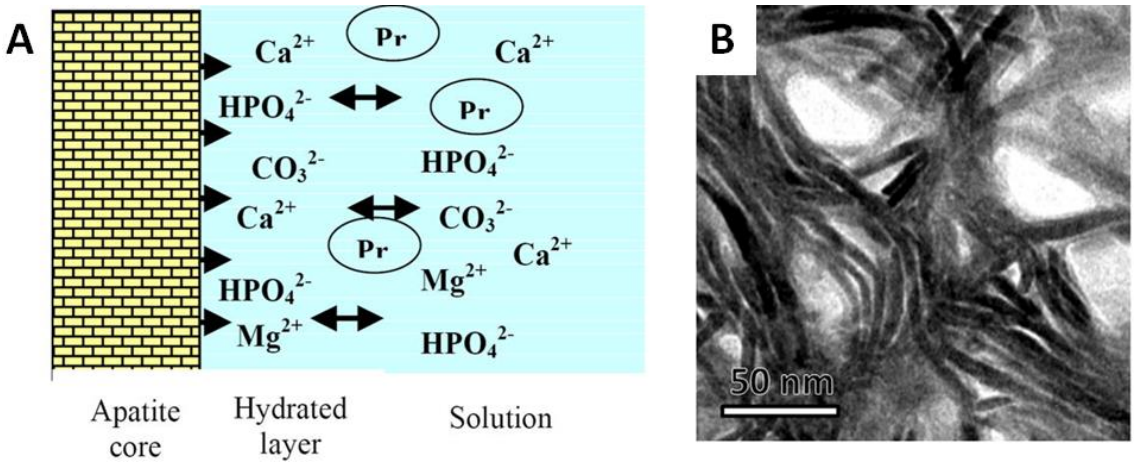

Figure 2-5 Schematic of the structure of bone mineral. The nanocrystal core is composed of non-stoichiometric apatite. A hydrated surface layer contains loosely bound ions, with other ions and proteins (Pr) present in the surrounding fluid. (Rey *et al.,* 2009). Transmission electron microscope image illustrating the needle morphology of the basic mineral unit of bone (Reznikov *et al.,* 2018).

In conclusion, bone is a hierarchical tissue comprised primarily of micron scale collagen fibres and nano scale apatite crystals, with its structure being maintained by the native cell population including osteocytes, osteoblasts, osteoclasts and MSCs. Understanding this structure, and the role of the cells within, is critical for the development of strategies for tissue regeneration, and may additionally facilitate the development of bio-inspired scaffold designs to achieve this.

2.3 Bone mechanobiology

2.3.1 Introduction

It is well known that the structure of bone adapts in response to changes in its mechanical environment (Kontulainen, Sievänen, Kannus, Pasanen, & Vuori, 2003). These adaptive changes are regulated by the resident cells within bone, which sense mechanical forces and transduce this information to generate signals and infer a response. An important component in this system is signalling from the osteocyte to osteoblasts and osteoclasts and their precursors, which mediate bone remodelling. Osteocytes, which are the most abundant cells in bone, sense mechanical forces and send signals to osteoclasts to target microcracks and osteoblasts to lay down new bone matrix (Alexander G. Robling & Turner, 2009). Osteocytes also play a key role in mechanosignalling to MSCs to enhance recruitment and osteogenesis (Birmingham *et al.*, 2012). This process is fundamental for the replenishment of the cell population in bone, ensuring continuous bone regeneration. In addition, MSCs have been demonstrated to exhibit excellent therapeutic potential following *in vivo* transplantation (Parekkadan & Milwid, 2010). Understanding the specific mechanisms behind osteocyte mechanosignalling to MSCs thus has great potential to uncover novel mechano-therapeutics to guide MSC behaviour, with this being discussed in greater detail in the following sections.

2.3.2 Role of the osteocyte in mechanoadaptation

Osteocytes are the primary sensing and metabolism controlling cells within bone tissue, and are key to directing the processes of bone formation and resorption via the release of various signalling molecules which act upon osteoblasts and osteoclasts or their progenitors (Dallas *et al.*, 2013). The two overarching processes of interest in this regard are the means by which osteocytes infer information from their surrounding environment, and the mechanisms by which they communicate the changing stimulus in response. There

are several mechanisms by which it has been theorized that osteocytes detect the forces they are subjected to during bone loading, including sensing of direct mechanical strain, piezoelectric effects, electric ions generated by loading induced fluid flow, and fluid flow itself between osteocyte cell processes and canaliculi (van Oers *et al.*, 2015). Fluid flow *in vivo* is one of the primary mechanisms thought to be responsible for the stimulation of osteocytes in the presence of macro scale loading, with flow induced fluid shear across the membrane of osteocyte processes believed trigger downstream mechanosignalling (Weinbaum *et al.*, 1994). More recently it has been proposed that fluid flow through the lacunar-canalicular network induces strains in actin filament bundles more than an order of magnitude greater than strains on the tissue level (Han, Cowin, Schaffler, & Weinbaum, 2004). Another mechanism which may contribute to osteocyte mechanosensing is the primary cilium, an immobile solitary antennae like organelle which is present in osteocytes (Malone *et al.*, 2007) and may translate information to the cell via bending and transmission of strain to the cell in the presence of fluid flow. Regardless of the precise mechanism or combinations thereof, fluid flow has been shown to be a key stimulus of osteocytes with this being demonstrated via both fluid structure interaction (FSI) modelling (Verbruggen, Vaughan, & McNamara, 2014) and *in vitro* experimentation.

A range of studies have illustrated the role of the osteocyte in mediating behaviour in other cells, primarily via the collection of conditioned medium from osteocytes following loading via parallel plate flow bioreactors. The majority of these *in vitro* osteocyte studies use an osteocyte-like cell called MLO-Y4, which is commonly used due to its versatility as a cell line, similarity to primary osteocytes, and ability to respond to mechanical stimulation (Kato, Windle, Koop, Mundy, & Bonewald, 1997). While other cell lines have been developed which more closely resemble primary osteocytes, including IDG-SW3 (Woo, Rosser, Dusevich, Kalajzic, & Bonewald, 2011) and Ocy454 (Spatz *et al.*, 2015), MLO-Y4 cells are still the most commonly used due to their well-established culture methods, ease of

use and well characterised behaviour. Co-culture studies has shown that fluid flow stimulation of osteocytes significantly reduces osteoblastic proliferation, and enhance differentiation as demonstrated by elevated ALP activity (Vezeridis, Semeins, Chen, & Klein-Nulend, 2006). Similar studies have validated these early findings while also demonstrating a role for gap junctions in this process (Taylor *et al.*, 2007). In contrast, another study has demonstrated that mechanically stimulated osteocytes promote osteoblast proliferation as well as recruitment (Brady *et al.*, 2015). Flow conditioned medium from osteocytes is also known to inhibit osteoclast formation, as demonstrated using multinucleated osteoclast progenitors isolated from bone marrow (Tan *et al.*, 2007) and co-cultures of RAW264.7 macrophage cells with osteocytes and ST2 stromal cells (You *et al.*, 2008). A role for the osteocyte in mediating stem cell behaviour following mechanical stimulation has also been shown, with enhanced migration, proliferation and osteogenic differentiation of MSCs following treatment with fluid shear stimulated osteocyte conditioned medium (Brady *et al.*, 2015; Hoey *et al.*, 2011). Remarkably, the osteocyte has also been shown to be involved in a large host of systemic functions, including regulating lymphoid organs and fat metabolism, increasing muscle myogenesis, influencing heart and liver function and suppressing growth of breast cancer and bone metastasis (Bonewald, 2017).

2.3.3 Osteocyte mechanosignalling

The means by which the osteocyte communicates these biophysical stimuli to bone forming and resorbing effector cells is of great interest, with a host of studies investigating the possible factors released by osteocytes in response to mechanical stimulation. Nitric oxide (NO) (Klein-Nulend, Semeins, Ajubi, Nijweide, & Burger, 1995), prostaglandin E_2 (Cheng *et al.*, 2001; Cherian *et al.*, 2005), ATP (Genetos, Kephart, Zhang, Yellowley, & Donahue, 2007), RANKL (Nakashima *et al.*, 2011), OPG and macrophage colony-stimulating factor (M-CSF) (Zhao *et al.*, 2002) have all be shown to be mechanosignalling

factors released by osteocytes in response to fluid shear, with these mediating a range of functions both within bone and systemically. One factor which has gained significant interest is sclerostin (SOST), which is a protein that is continually released resulting in the inhibition of Wnt-mediated bone formation (Moester *et al.*, 2010). Expression of SOST is inhibited following mechanical loading (A. G. Robling *et al.*, 2008; Shu *et al.*, 2017), with this releasing the inhibition of Wnt signalling and stimulating bone formation. Anti-sclerostin therapies which are currently being investigated are in stage 3 clinical trials (Lewiecki, 2014).

To gain a greater understanding of the role of osteocyte signalling in response to loading, several studies have performed transcriptome analyses via microarrays and proteomic analyses via mass spectrometry. These methods provide the advantage of facilitating the identification of a large datasets of gene/protein targets and their relative expression in response to loading. They also allow further detailed functional and pathway analyses to greater understand enrichments and interactions of defined groups of targets, thus significantly expanding our knowledge of osteocyte mechanobiology. One such study by Chen *et al.* investigated the transcriptome of the osteocyte following cyclic compressive force stimulation for several periods from 10 min to 6 h, with the greatest differential expression of targets (both upregulation and downregulation) compared to statically cultured cells occurring following 6 h stimulation (W. Chen *et al.*, 2010). One cluster of genes with significantly upregulated expression following stimulation was highlighted in particular, containing a large number of chemokines and cytokines and which were associated with the significantly enriched "cytokine-cytokine receptor interaction pathway". Interestingly, many of these genes were associated with bone resorptive signalling, indicating that the osteocyte may trigger resorption via osteoclasts and thus initiate bone remodelling in response to cyclic compressive forces.

A later study aimed to combine transcriptomic and proteomic analyses of the osteocyte to further reveal mechanosensitive signalling pathways (P. M. Govey *et al.*, 2014). Cells were cultured in parallel plate flow chambers with a flow regime of 1 Pa and 1 Hz and were either lysed immediately or further cultured for 2, 8 or 24 h post stimulation. This revealed a range of transcripts and proteins which were differentially expressed with flow stimulation, as well as identifying a time course effect, where the greatest differential expression of transcripts and protein levels occurred at 2 hr and 8 hr post flow respectively. Many of the identified transcripts agreed with the previous work by Chen *et al.,* while 24 proteins out of 558 were differentially expressed with fluid flow and several of these including NDK, calcyclin and GRK-6 being identified as possibly playing key roles in mechanotransduction. This study also identified for the first time a combined transcriptome/proteome signalling network which identified key signalling nodes which would not have been revealed by either method alone. The complex microenvironment of bone was later investigated in two further studies from this research group, which re-analysed the samples via RNA sequencing to more accurately quantify differential gene expression and further analyse network interactions to demonstrate fluid flow induced changes in genes which corresponded to downregulated osteoclast differentiation (Peter M. Govey, Kawasawa, & Donahue, 2015; F. Meng, Murray, Kurgan, & Donahue, 2018).

The mechanobiology of the osteocyte has also been investigated via a more biologically accurate *in vivo* loading model (Wasserman *et al.*, 2013). In this study, the C5 vertebra of mice were either loaded in a single treatment, loaded three times weekly over a four-week period, or unloaded in control mice. Medullary tissue was then isolated and digested to remove all cells except osteocytes with trabecular bone. RNA was isolated from pulverised trabeculae and analysed via microarray analyses. Continuous loading was found to result in the most differentially expressed genes, with a total of 1339 compared to 339 in mouse loaded in a single treatment only. Two of the most enriched biological processes in

differentially expressed genes were “cellular movement” and “cell-to-cell signalling and interaction”, again highlighting the role of the loaded osteocyte in mediating cell behaviour and recruitment. The authors also highlighted the differentially expressed genes which code for extracellular proteins, identifying a total of 55 with continuous loading. While several have of these had previously implicated with osteoblast and osteoclast behaviour, many had not, again highlighting the value of large scale proteomic and genomic studies to further our understanding of cell behaviour. Of note are the identification of several thrombospondins, which promote osteoblast mineralisation and Wnt5a, which is a Wnt signalling pathway agonist, a pathway which plays key roles in bone formation and regulation. Upregulation of Dmp1 upregulation with loading is also of interest, which plays a role in maintaining phosphate homeostasis in bone (Y. Lu, Yuan, *et al.*, 2011).

In summary, the osteocyte plays a primary role in sensing external forces and sending signals to other bone residing cells to respond and adapt to the dynamic mechanical environment. Osteocyte mechanosignalling to MSCs is of particular importance due to the latter’s role in constantly replenishing the cell population in bone. Understanding and exploiting how osteocytes achieve this has great potential to reveal novel therapeutics for bone regeneration.

2.4 Role of EVs in cell signalling

2.4.1 Introduction

Much of the work investigating means of cell signalling has previously focused on factors such as cytokines, chemokines and hormones. Recently however, another means by which cells communicate via EVs has gained significant interest, with EVs being demonstrated to be fundamental to an extensive range of signalling functions throughout the body (van Niel, D'Angelo, & Raposo, 2018). EVs are structures with a lipid bilayer membrane which can further be categorised as exosomes or microvesicles (MVs)

depending on their origin. Exosomes are formed when multivesicular endosomes (MVEs) fuse with the plasma membrane and release intraluminal vesicles (ILVs) from the cell, while MVs are formed in a separate process via budding of the plasma membrane (Figure 2-6A-B). EVs have been shown to carry a wide range of cargo depending on conditions and cell type, including proteins, nucleic acids and lipids, with their composition directly influencing their fate and function thus highlighting their capacity for specific cell targeting and communication. This is achieved through a multitude of methods including surface binding of EVs to initiate signalling, fusion of EVs to the membrane for release of vesicle contents, and complete internalisation of EVs by the cell (Figure 2-6C).

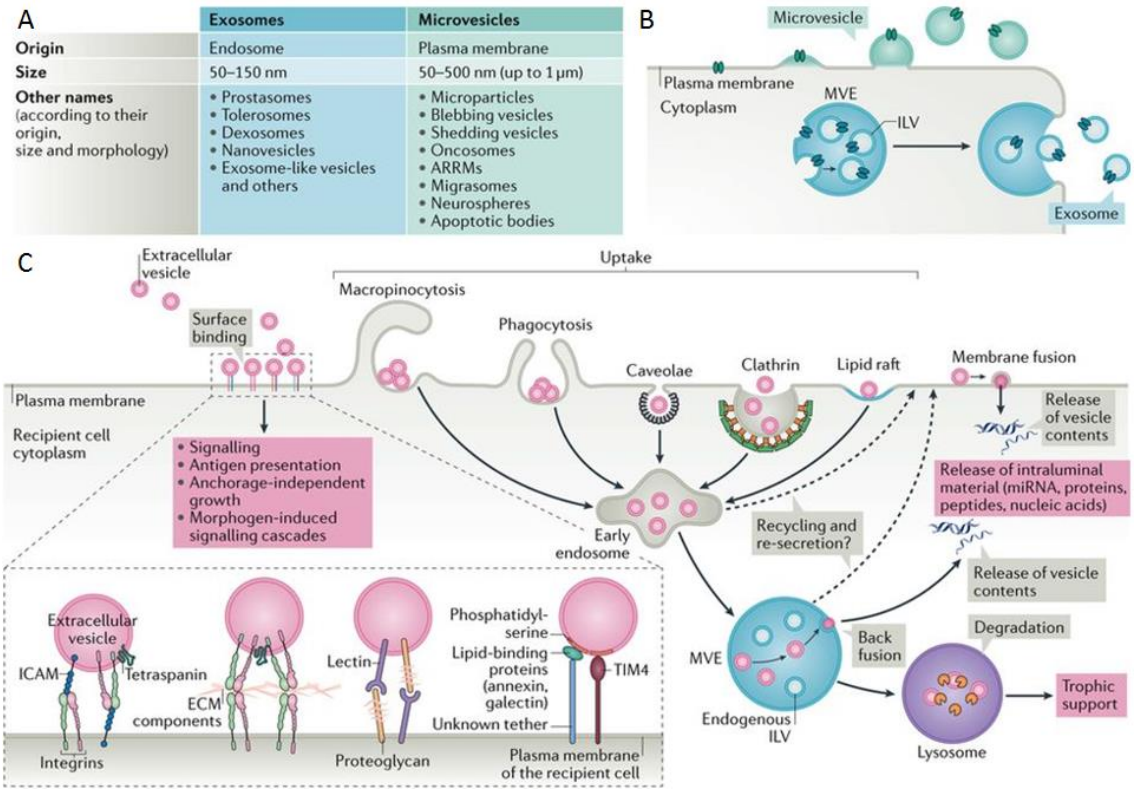

Figure 2-6 Summary of extracellular vesicle (EV) formation and signalling. EVs may be categorised as exosomes or microvesicles (MVs) (A). Exosomes are formed by the release of release of intraluminal vesicles contained within multivesicular endosomes, while microvesicles are formed via budding of the plasma membrane (B). These EVs can carry signals to a recipient cell, where they can initiate a response via surface binding, release of vesicle contents, or complete internalisation and further processing of EV contents (C). Adapted from (van Niel *et al.*, 2018).

2.4.2 EVs in bone

There are a range of studies highlighting the importance of EVs in bone in particular; with these primarily investigating osteoblast released EVs and their role in signalling with other cell types. Osteoblast EVs have been well characterised via proteomic analyses (J. Morhayim *et al.*, 2015; Thouverey *et al.*, 2011), with these studies providing novel insights into in contents of osteoblast EVs and their likely release mechanism from apical microvilli. One study investigated the use of RANKL by osteoblast EVs as a signalling mechanism to communicate with osteoclast precursors (L. Deng *et al.*, 2015), where they were found to transfer RANKL to osteoclast precursor cells thus stimulating osteoclast formation. It was also found that these EVs interact with cells in a highly specific manner indicating targeted signalling, where they would bind to RANK-expressing-NIH3T3 fibroblasts, however in NIH3T3 fibroblasts they were transferred to the cytosol for possible degradation within lysosomes or dismissed via transcytosis. One interesting study investigated the role of osteoblast EVs in signalling and differentiation of MSCs (Davies *et al.*, 2017a). In this study, the osteogenic differentiation of MSCs cultured with osteoblast EVs was investigated and compared to treatment of MSCs with BMP2. ALP levels were found to be comparable in cells treated with EVs and BMP2, however even more remarkably, calcium deposition was significantly enhanced with EV treatment compared to BMP2. The authors then carried out a proteomic analysis on the EVs to further investigate the mechanisms behind these results, where a great number of proteins involved in calcium binding, osteogenesis and collagen modification were identified. One group of proteins of particular interest which was identified were annexins, due to their interaction with phospholipids to form Ca^{2+} complexes, which act as centres for crystallisation and nucleation, thus initiating localised mineralisation at EVs.

Recently, work on EVs released by osteocytes has also emerged, with one such study investigating miRNA expression in EVs isolated from the plasma of osteocyte

ablated mice and wild-type mice, where altered miRNA levels suggest a role for osteocytes in systemic EV signalling (Mari Sato, Suzuki, Kawano, & Tamura, 2017). Another study investigated the influence of unidirectional fluid flow stimulation on osteocyte EV release (Morrell *et al.*, 2018). Mechanical stimulation was not found to influence EV size, however, an upregulation in particle concentration was demonstrated. This increased EV production with flow was blunted when cells were treated with neomycin, an inhibitor of Ca^{2+} signalling, indicating the role of this mechanosensitive signalling pathway in EV release. This was further demonstrated *in vivo*, where Lysosomal-associated membrane protein 1 (LAMP1), a secretory vesicle marker, was upregulated in loaded mice tibia and attenuated in neomycin treated mice. More broadly, another study investigated the role of exercise in regulating systemic EV release (Whitham *et al.*, 2018), with over 300 proteins upregulated, suggesting an EV based means by which osteocytes may communicate systemically to other cells following mechanical stimulation.

Due to the involvement and specificity of EVs in cell signalling, several researchers are beginning to investigate the use of EVs for therapeutic purposes. EVs have been isolated from human dental pulp stem cells (DPSCs), and can be up taken by hMSCs and undifferentiated primary DPSCs, resulting in significantly enhanced differentiation as seen by enhanced BMP2 gene expression (C.-C. Huang, Narayanan, Alapati, & Ravindran, 2016). In this study, EVs were also added to collagen membranes in human root tooth slices and implanted subcutaneously in mice, where they were seen to promote vascularisation and dental pulp-like tissue regeneration. In another study, osteoclast EV interaction with osteoblasts was investigated, with EVs being enriched with a specific miRNA (miR-214), which are taken up by osteoblasts, inhibiting their activity (Weijia Sun *et al.*, 2016). This miRNA was found to be elevated in an osteoporotic mouse model as well as osteoporotic patients further revealing its likely role in the regulation of osteoblast behaviour and as a potential EV based target for osteoporosis therapies. The researchers further demonstrated

this by inhibiting EV release via systemic treatment with Rab27a siRNA, which was shown to promote osteoblast activity. Work is also ongoing into the loading of EVs with drugs for specific therapeutic delivery. In one such paper, two different anti-osteoclast drugs, dasatinib and the clinically approved zoledronate for osteoporosis treatment, were internalised within osteoblast EVs (Cappariello *et al.*, 2017). Acute osteoclast over activation was initiated in mice, after which they were treated with free drugs, as well as drugs loaded within EVs. Drugs loaded within EVs were shown to be just as effective as free drugs in inhibiting osteoclast activity and inducing apoptosis, both *in vitro* and *in vivo*. EVs, either unmodified or loaded with drugs, are thus highly attractive biological tools for the development of effective cell-free therapeutics with targeted delivery.

Due to the regenerative and therapeutic potential of EVs, their use for the functionalisation of tissue engineering scaffolds has recently been investigated. In a paper by Xie *et al.*, EVs were isolated from MSCs and used to functionalise decalcified bone matrix scaffolds, which were subsequently implanted subcutaneously in mice to assess their angiogenic and regenerative potential (H. Xie *et al.*, 2017b). After 1 and 2 months, bone volume did not change with EV treatment, however, scaffolds functionalised with both EVs and cells displayed significantly enhanced bone formation, demonstrating their synergistic effect in bone tissue regeneration. Remarkably, blood vessel formation with EV functionalised scaffolds was not only significantly greater than control scaffolds, but also just as effective as cell seeded scaffolds, while scaffolds with a combination of EVs and cells resulted in even greater vessel formation. Another study modified 3D printed scaffolds with EVs and implanted them in rat calvarial defects to investigate their capacity for bone repair (Diomede *et al.*, 2018). Polyethyleneimine, a polymer which promotes endosomal content release, was modified with EVs and used to coat 3D printed poly(lactide) (PLA) scaffolds. These scaffolds were shown to be pro-angiogenic, allowing the development of an extensive vascular network as seen in the previous work by Xie *et al.*, while also

enhancing bone formation to a greater degree than scaffolds implanted with MSCs. While there is little other work at present demonstrating the use of EVs for TE scaffold modification, these studies report highly promising results which indicate that EVs may be used to enhance regeneration while avoiding the issues of cell sourcing and biocompatibility seen with MSC seeded scaffolds.

In summary, EVs play key roles in cell signalling in bone and throughout the body. The combination of their structurally robust composition and highly specific nature make them ideal for the development of both local and systemic strategies for bone regeneration.

2.5 Direct biophysical regulation of MSCs

2.5.1 Introduction

The architecture within which cells reside imposes constraints on the degree to which they can bind, spread and proliferate, with this in turn having profound implications on their behaviour. This has been demonstrated in a large host of cell types, including MSCs, osteoblasts, myoblasts, fibroblasts, neurons and endothelial cells, among many others, where matrix stiffness, architecture or topography can have significant influences on how cells behave in terms of transcriptional regulation, gene expression and protein synthesis, in turn leading to altered proliferation, recruitment, differentiation or cell death (Y. Yang *et al.*, 2017). One of the mechanisms by which many cells are capable of inferring information from their surrounding matrix is via the sensing of matrix stiffness. Typically, cells on stiff substrates are more spread and form more contact points, termed "focal adhesions", with the matrix. Cells can sense the resistance of their matrix and exert tension on these focal adhesions via their cytoskeleton, resulting in a more spread cell shape with a more organised cytoskeleton (Wells, 2008) (Figure 2-7A). In contrast to this, cells on softer substrates are typically more rounded and form less focal adhesions. Cells also have a

tendency to migrate towards stiffer substrates, with this phenomenon being termed durotaxis (Figure 2-7B).

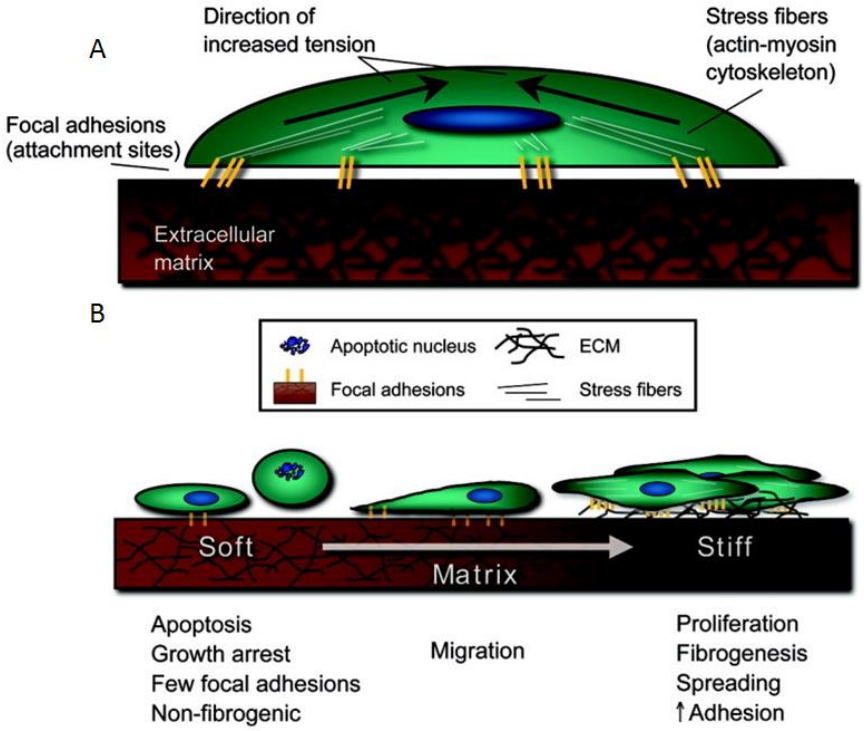

Figure 2-7 Influence of substrate stiffness on cell behaviour. Schematic of cell on a stiff matrix (A). Focal adhesions sense stiffness by pulling on their surrounding matrix, with stiffer substrates resulting in greater tension being exerted by the cell (A). Typical cell behaviour in response to changing matrix stiffness (B). Cells are typically round with minimal focal adhesions on soft substrates, and have a tendency to migrate towards regions with greater stiffness, where they become more spread and proliferative. Adapted from (Wells, 2008)

The physical architecture of the matrix also plays a key role in maintaining physiologically appropriate tissue specific behaviour (Frantz, Stewart, & Weaver, 2010; Rozario & DeSimone, 2010). This is seen in the vastly differing microarchitectures within the body despite similar collagen-based ECM makeup, such as the highly aligned nature of tendon tissue along the axis of loading and the circumferential distribution of fibres in the tunica media of arteries and veins. Bone tissue alone contains a range of different architectures, with fibre and tissue organisation occurring in a load dependent manner (Foolen *et al.*, 2008). The geometry of the fibrous architecture provides a structure for cells to pull against and align along, thus having a significant influence on defining cell shape while also mediating migration and proliferation (Hogrebe *et al.*, 2017b). One way in which

researchers have studied this is via culturing cells on micro patterned substrates with different spacings between pillars to investigate cell shape and actin cytoskeleton organisation (Lehnert *et al.*, 2004). On homogenous surfaces, cells are typically spread, with actin filaments distributed throughout the periphery of the cell, with similar morphologies being maintained with pillar spacings of up to 2 μm (Figure 2-8). Beyond this, cell shape becomes more defined by the substrate geometry, where cells form more defined stress fibres and branch across pillars. Also of interest is the curving of stress fibres towards the centre of the cell, as opposed to forming straight lines between pillars.

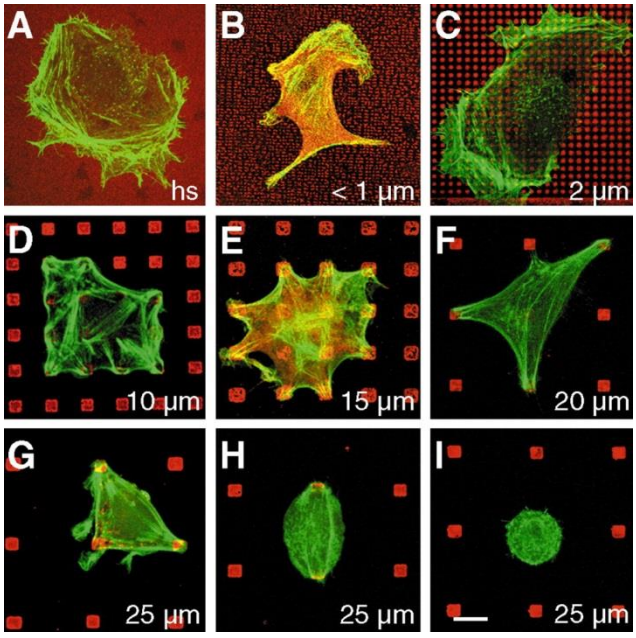

Figure 2-8 Influence of substrate geometry on cell morphology. Cells remain spread with micro pillar spacings of up to 2 μm (A-C). Increasing pillar spacing results in the formation of more defined stress fibres towards the centre of the cell (D-F). Beyond a critical pillar spacing, cells have difficulty spreading, resulting in more triangular or rounded shapes (G-I). (Lehnert *et al.*, 2004)

It can thus be seen that the close interaction between cell and matrix is key for maintaining physiologically relevant behaviour, whereby alterations can have profound consequences in terms of development and progression of disease. For instance, increased collagen content and highly aligned perpendicular fibres have been identified surrounding the stroma in breast tumours. This alignment of fibres guides the migration of cancerous epithelial cells away from the tumour resulting in further invasion of the surrounding tissue

and ultimately facilitating tumour metastasis via invasion of blood vessels (Hogrebe *et al.*, 2017b). Another example of altered fibrous architecture leading to disease progression is seen in osteoarthritis, whereby collagen fibril architecture is altered, becoming less aligned in the superficial zone compared to healthy individuals. This can amplify local tissue strain in response to loading, leading to further damage and cell death (Saarakkala *et al.*, 2010). The formation of regions within tissue with inappropriate stiffness can also have profound impact on correct tissue function. The formation of fibrotic tissue typically increases stiffness, with this promoting irregular accumulation of cells via durotaxis, which can lead to the development of cardiovascular diseases and many types of cancer (Kai, Laklai, & Weaver, 2016).

Tissue architecture can thus be seen to be integral in mediating correct, tissue appropriate function, and therefore considerable scrutiny must be applied for the development of safe and effective TE strategies for tissue regeneration. In the following sections, the role of tissue architecture in mediating cell behaviour will be reviewed with a focus on MSCs and musculoskeletal tissues, and strategies by which researchers have investigated and developed defined architectures for TE applications will be discussed.

2.5.2 Role of architecture in mediating MSC mechanobiology

MSCs play an important role in the formation and regeneration of tissues, with the architecture in which they reside controlling these functions. While signalling factors also play a role in stem cell behaviour and can be used to induce differentiation independent of stiffness and architecture, it is the mechanical constraints of the matrix which guide and maintain the long term physiologically desired phenotype of the cells (Engler *et al.*, 2006). It is therefore important to understand how stem cells behave in different materials and architectures, and the mechanisms by which these altered behaviours manifest.

In a study by Engler *et al.*, it was demonstrated that MSCs are sensitive to matrix stiffness, which can be used alone to drive differentiation of cells towards specific lineages. MSCs were cultured on several substrates ranging in stiffness from 0.1 – 40 kPa, with microarray profiling of transcripts identifying three distinct groups of upregulated markers for neurogenic, myogenic and osteogenic differentiation at low, medium and high stiffnesses respectively (Engler *et al.*, 2006). Further fluorescent imaging demonstrated the stiffness specific distribution of differentiation markers, illustrating the capacity for stiffness mediated stem cell lineage commitment compared to more terminally differentiated myoblasts and osteoblasts (Figure 2-9). One identified mechanism which may account for the mechanosensing ability of MSCs is non-muscle myosin II, which when inhibited by blebbistatin treatment, attenuated the differentiation capacity of the cells. This protein is known to promote focal adhesion assembly, which as previously discussed, are key components in cell adhesion and how they interact with their substrate.

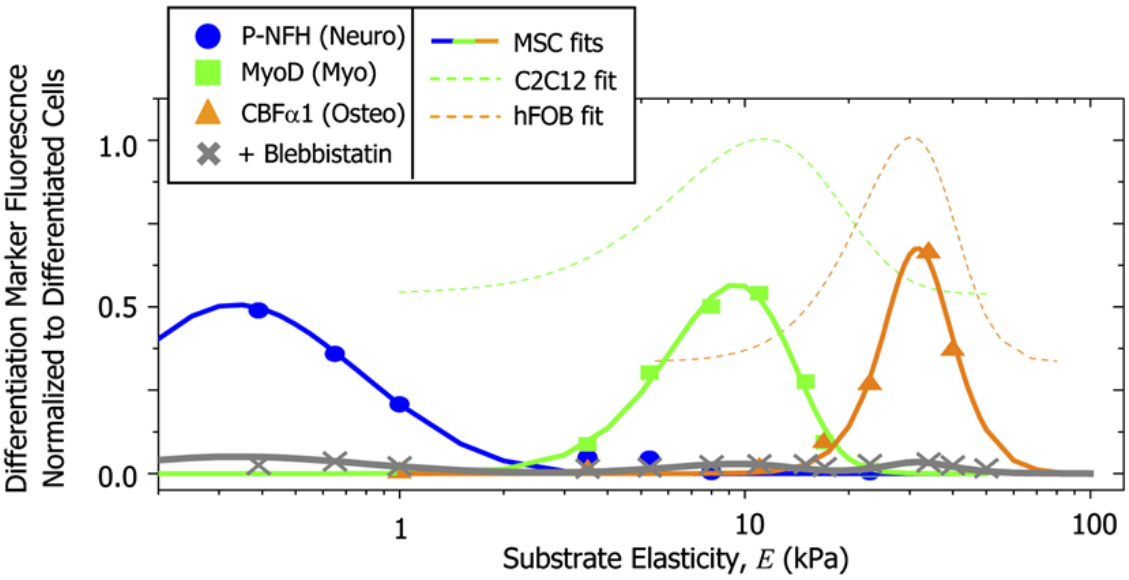

Figure 2-9 Stiffness dependent distribution of MSC differentiation markers. Neurogenic (Neuro), myogenic (Myo) and osteogenic (osteo) markers are upregulated in a stiffness dependent manner, with a role for non-muscle myosin II in mediating mechanosensation being demonstrated via its inhibition with blebbistatin. Marker distribution in control myobloast (C2C12) and osteoblast (hFOB) cells cultured on different stiffnesses demonstrate their more terminally specific differentiation capacity compared to MSCs.

This above work demonstrates MSC differentiation potential in tissues with widely varying function and elastic moduli, with further work by Olivares-Navarrete *et al.* demonstrating how stiffness mediates differentiation into the more closely related chondrogenic and osteogenic lineages (Olivares-Navarrete *et al.*, 2017). As previously demonstrated, MSCs were cultured on substrates of varying stiffness in the absence of exogenous stimuli, with chondrogenic and osteogenic lineage commitment investigated via mRNA and protein markers. It was shown that chondrogenic mRNA markers were upregulated in softer substrates of stiffness 0.8 MPa. These substrates also resulted in elevated levels of RUNX2, which is known to be involved in both osteogenic and chondrogenic differentiation, while other markers including ALP activity, osteocalcin (OCN) and osteoprotegerin being elevated on an increased stiffness of 4.7 MPa. Interestingly, these markers decreased when cells were cultured on even stiffer substrates, indicating an optimal stiffness range for osteogenic differentiation above which these affects are attenuated. Possible mechanisms behind these findings were also investigated, with the expression of several integrins, proteins which are part of the structure of focal adhesions, being investigated in MSCs as a function of matrix stiffness. Integrin ITGA5 and ITGB1 mRNA levels displayed a trend of greater expression on softer substrates, while ITGB3 displayed an inverse trend and ITGA2 and ITGAV displayed greatest expression at 4.7 MPa, the optimal stiffness of osteogenic differentiation. These varying trends illustrate the complex biology behind MSC matrix mechanosensing and the key role of integrins in this process, with a knockout of ITGB1 resulting in overall reduced sensitivity of MSCs to matrix stiffness, with attenuation of both chondrogenic and osteogenic differentiation. Interestingly, these changes in integrin expression were much more pronounced in MSCs compared to osteoblasts and chondrocytes, indicating the greater capacity of MSCs to sense matrix stiffness and differentiate in response.

The geometry of the matrix within which cells reside also provides cues to mediate stem cell behaviour, with a ground-breaking study by McBeath *et al.* demonstrating the role of MSC shape in driving lineage commitment, and investigating the molecular mechanisms driving this effect (McBeath *et al.*, 2004). In this study, it was first demonstrated that cell density influences lineage commitment, with greater adipogenic differentiation at higher densities and greater osteogenic differentiation at lower densities, with the authors hypothesising that this was due to difference in cell spreading. To further investigate this, MSCs were cultured on islands of three different sizes, where it was confirmed that greater cell spreading on larger islands was correlated with greater osteogenesis, and the inverse effect seen with adipogenesis (Figure 2-10A-B). Cells were also treated with a proliferation inhibitor to demonstrate that this affect is due to cell shape and occurs independently of proliferation (Figure 2-10C).

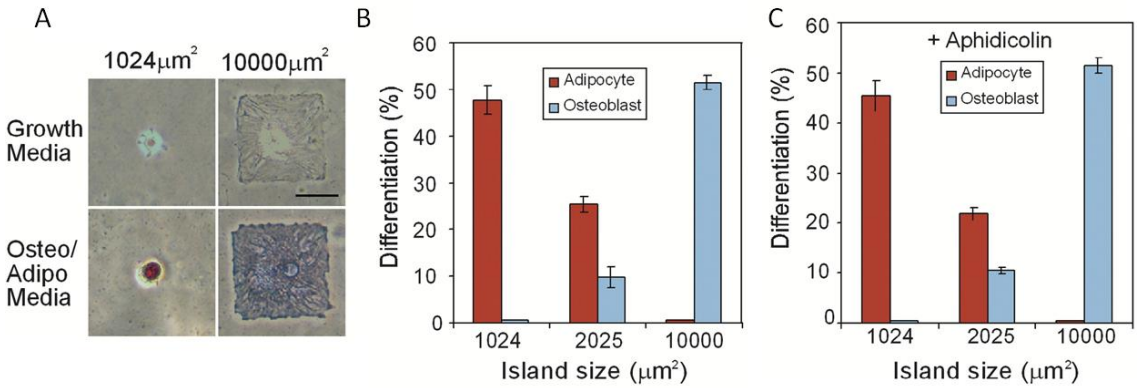

Figure 2-10 Role of cell shape in MSC commitment. Brightfield image of MSCs on small and large islands (A). Osteogenic and adipogenic differentiation on different island sizes (B), with aphidicolin treatment to inhibit proliferation demonstrating the same trend (C).

A recent paper by Dupont *et al.* was pivotal in understanding the mechanisms behind matrix mediated MSC differentiation and identified the fundamental role of YAP/TAZ in cellular mechanotransduction (Dupont *et al.*, 2011). YAP (Yes-associated protein, also known as YAP) and TAZ (transcriptional coactivator with a PDZ-binding domain) are both downstream effectors of the Hippo pathway, which has the primary functions of regulating tissue growth in adults, and mediating proliferation, migration and

differentiation in organ development (Z. Meng, Moroishi, & Guan, 2016). Many of the functions of YAP and TAZ are closely linked, with YAP being a negative regulator of TAZ which can compensate for changes in YAP abundance (Finch-Edmondson *et al.*, 2015), and thus these proteins will be referred to from here on as either YAP/TAZ or YAP depending on the nomenclature used by the author. In the work by Dupont *et al.*, MSCs were cultured on hydrogels of different stiffnesses and on islands of various sizes before investigating YAP/TAZ expression within the cells. It was found that both ECM stiffness and cell shape regulated YAP/TAZ expression, which was predominantly cytoplasmic on soft substrates and small islands and localised to the nucleus on stiffer substrates and more spread cells on larger islands (Figure 2-11A). To further investigate if this is mediated by cell contact area with the ECM, MSCs were cultured on a close array of micropillars, which resulted in a comparable cell area to cells cultured on large islands while limiting the contact area for cell-ECM interaction to 10% of the cell projected area. Interestingly, it was found that nuclear YAP/TAZ expression in micropillar cultured cells was identical to cells cultured on large islands, revealing that the primary regulator for YAP/TAZ is the degree of cell spreading imposed by the ECM.

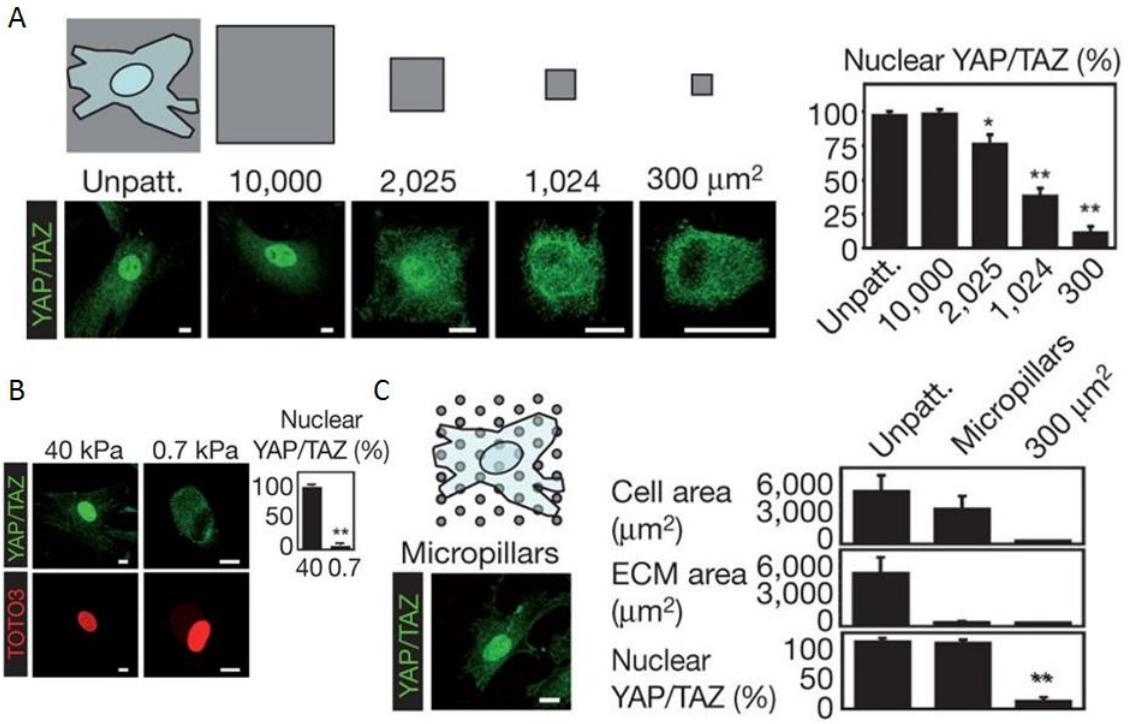

Figure 2-11 Role of cell spreading and stiffness on nuclear localisation of YAP/TAZ. MSCs cultured on islands of decreasing size resulted in less cell spreading and reduced nuclear YAP/TAZ expression (A). Influence of substrate stiffness on nuclear YAP/TAZ expression, with nuclei stained via TOTO3 (B). MSCs cultured on micropillars allowed cell spreading and reduced cell contact area, with comparable nuclear YAP/TAZ expression revealing the role of ECM regulated cell spreading in this response (C). Scale bars = 15 μm. Adapted from (Dupont *et al.*, 2011)

The authors then investigated the role of the RhoA pathway, previously demonstrated as a key component in MSC shape driven lineage commitment, in YAP/TAZ expression. Inhibition of Rho and Rho-associated protein kinase (ROCK) significantly reduced nuclear YAP/TAZ expression, while disruption of microtubules did not, revealing the role of the actin cytoskeleton in maintaining mechanosensing via YAP/TAZ and indicating the cytoskeletal tension is required for YAP/TAZ localisation. The authors have thus identified YAP and TAZ as mechanosensors of ECM elasticity and cell morphology, and next aimed to further understand if the expression of these proteins can in turn trigger cellular responses. To investigate this, MSCs were cultured on soft and stiff substrates, and as expected, differentiated towards the adipogenic and osteogenic lineages respectively. Next, YAP/TAZ was depleted via siRNA transfection, which resulted in inhibition of osteogenic differentiation on hard substrates, and remarkably, also allowed adipogenic

differentiation on hard substrates. Remarkably, overexpression of YAP with lentiviral infection rescued osteogenic differentiation of MSCs cultured on soft substrates or treated with a Rho inhibitor. These results demonstrate that YAP/TAZ is a key component involved in ECM mediated MSC differentiation.

Surface topography is also known to play a fundamental role in driving MSC behaviour, with recent work developing biomimetic scaffold models with various hierarchical structures and investigating their role in MSC mechanobiology (Pan *et al.*, 2017). In this study, MSCs were cultured on either polished titanium (PT), macroporous titanium (MT), or macroporous titanium with nanowire topography (MNT). Cells were round on PT, elongated on MT, and highly spread on MNT, with an increasing trend of osteogenesis towards MNT. A comparable trend was also seen with nuclear YAP, which was greatest in the MNT group, while knockdown of YAP inhibited osteogenesis on the nanowire topography. As in previous studies, the role of ROCK and non-muscle myosin II in this process was confirmed via treatment with Y-27632 and blebbistatin, resulting in significant downregulation of nuclear YAP in all groups. This study thus highlights the important role of controlling hierarchical structure when designing advanced biomimetic materials, indicating that nanoscale topography enhances MSC osteogenic differentiation via mediating cell mechanosignalling.

In summary, MSC behaviour is mediated by the architecture and stiffness of their surrounding matrix. Understanding the mechanisms by which this occurs is important for the development of tissue regeneration strategies, whereby synthetic matrices may be fabricated and tuned to guide MSC osteogenesis and enhance bone tissue regeneration.

2.6 Controlling architecture for bone regeneration

2.6.1 Fibre architecture

The increased appreciation of the importance of scaffold architecture in TE has seen the emergence of many studies aiming to optimise architecture for specific applications. This work is ongoing across a large range of scaffold manufacturing techniques, including electrospinning, freeze drying and 3D printing approaches among many others, as well as further methods to modify and optimise surface topography. To gain an appreciation for the techniques employed and processes followed to discover effective TE architectures for regeneration, previous work by several researchers with this objective will be discussed below with a focus on work in the field of bone TE.

Fused deposition modelling (FDM) is a commonly used 3D printing technique in TE, with previous work investigating different scaffold geometries and their effect on osteogenic and chondrogenic differentiation (Di Luca *et al.*, 2016). Different filament alignments between layers from 15 - 90° were investigated, as well as a gradient pattern with changing alignment. In the gradient scaffold, more rhomboidal regions supported greater MSC osteogenesis as seen by ALP activity, while chondrogenesis was enhanced in regions with square pores. However, in scaffolds with a consistent alignment pattern, there were little changes in terms of osteogenic gene expression or ALP activity between different alignments. This may be due to the average fibre diameter of 150 μm, which in comparison to the scale of a cell, acts more like a curved 2D surface regardless of filament alignment (Hogrebe *et al.*, 2017b). This is a major limitation of FDM, which make it difficult to use for the creation of microenvironments to influence cell behaviour. A range of other 3D printing techniques have been used for TE engineering, such as stereolithography, digital light processing and two photon polymerisation. Two photon polymerisation is of particular interest due to the fine microarchitectures which may be

fabricated. In this technology, the focal point of a laser can be controlled within a resin bath to cause controlled polymerisation in 3D via absorption of two near infrared photons. This technology has been used to investigate various honeycomb-like microarchitectures for bone regeneration (Irina Alexandra *et al.*, 2018). Interconnected microtubes of heights up to 20 μm were fabricated, and seeded with osteoblasts to investigate osteogenic differentiation capacity. It was found that a layer separation, corresponding to microtube height, of between 2 and 10 μm was optimal, with cells unable to interconnect between layers for heights above this range, which in turn limited mineralisation. Another study which uses this technology fabricated a biomimetic trabecular structure, which was demonstrated to enhance osteogenic differentiation as seen by hydroxyapatite deposition compared to flat control surfaces (Marino *et al.*, 2014). Two of the major limitations of 2PP however are fabrication time and construct size. While it can be used to create structures with exceptional resolution, the small focal point of the laser results in long fabrication times, which are also prohibitive in making high resolution constructs on the millimetre scale (Olsen, Larsen, & Hjortø, 2013).

Electrospinning is a technology which has been extensively used for the creation of 3D culture platforms and TE scaffolds, due to its capability of creating micron to nano-scale fibres which are a good model for the fibrous nature of many human tissues. In its most common form, a polymer melt or solution is passed through a needle, also termed the spinneret, at which point a high voltage typically in the kilovolt range is applied. This high voltage results in the electrical charging of material at the tip of the needle, which when great enough, results in the electrostatic forces in the material overcoming its surface tension resulting in the stretching of the material. At the point, termed the Taylor cone, a fine stream of material erupts away from the needle and is deposited on a grounded collector offset at given distance from the needle (Figure 2-12). This configuration can also be rotated 90° to deposit fibres on an underlying plate. In solvent electrospinning, the

solvent evaporates as the fibre travels towards the collector, and eventually travels with a whipping motion resulting in the deposition of fibres in a random orientation if the collector is static. Fibres can also be deposited on to a rotating mandrel or micropatterned surfaces, to give a degree of control over fibre alignment. Further control can be gained via electrospinning writing with solvent solutions, which aim to deposit the fibre within the stable region allowing for controlled deposition via a translating collector (D. Sun, Chang, Li, & Lin, 2006; G. H. Yang, Mun, & Kim, 2016), however, due to the limited distance for the solvent to evaporate, it is difficult to fabricate consistent, high quality fibres beyond several layers. A further degree of control which overcomes these limitations while also omitting harsh solvents from the process can be attained via MEW, which will be discussed in section 2.7.

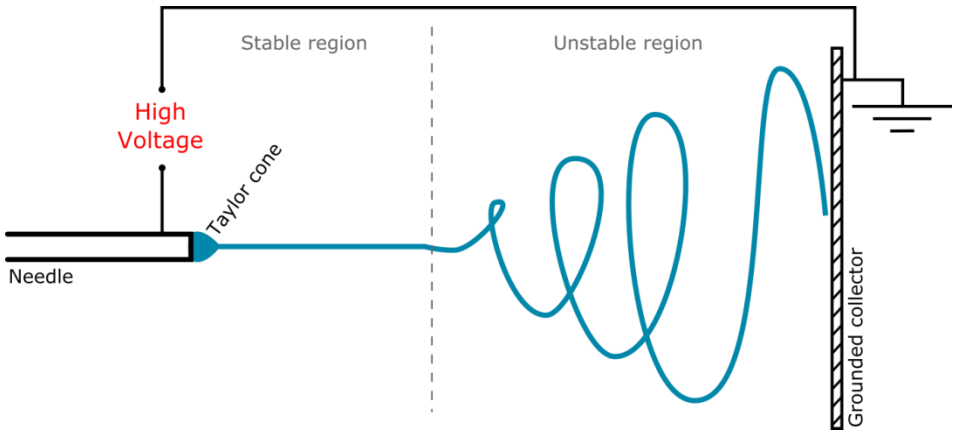

Figure 2-12 Schematic of typical solvent electrospinning process

A host of studies have utilised electrospun scaffolds for bone TE (Prabhakaran, Venugopal, & Ramakrishna, 2009), with many others also investigating the effect of scaffold architecture on cell behaviour and differentiation. These studies typically compare random and aligned fibrous scaffolds, where it is widely agreed across several independent studies that aligned architectures enhance tensile strength, and are optimal in terms of proliferation, guided cell growth and osteogenic differentiation of osteoblasts and MSCs (Doustgani, Vasheghani-Farahani, & Soleimani, 2013; Guo *et al.*, 2015; H. Li, Wong, *et al.*, 2012; Z. X. Meng *et al.*, 2010; Yazhou *et al.*, 2009). Another study further compared

aligned fibres with cross aligned fibres, with the latter being achieved by collecting fibres on a glass coverslip attached to a rotating mandrel for a given time, and then rotating the coverslip 90° to collect fibres perpendicularly to the initial layer (Jui-Chih *et al.*, 2013). Scaffolds were created with fibres at low and high density for both groups, where it was found that lower densities resulted in greater MSC spreading as seen by cell area, and high densities resulting in more aligned cells. Overall, it was found that aligned scaffolds resulted in greater osteogenic gene expression than cross aligned scaffolds. Another study used time lapse imaging to demonstrate greater MSC mobility on aligned scaffolds compared to random (Gugutkov *et al.*, 2017). The authors further developed a 3D environment via a sandwich configuration with multiple electrospun scaffolds, which exhibited enhanced mineralisation compared to single aligned scaffolds. Other variables of scaffold architecture which have also been investigated are fibre size and porosity, with one study investigating the effect of various fibre diameters from 2 – 42 μm on osteogenic differentiation of MSCs, while also studying scaffold porosity (Takahashi & Tabata, 2004). A trend of increasing seeding efficiency with larger fibre diameter was demonstrated, with a plateau at 22 μm. While little influence of porosity was seen in initial seeding efficiency, cell proliferation up to 28 days was significantly enhanced with higher porosity at all fibre sizes. Differentiation at this time was quantified by ALP activity and osteocalcin content, both of which were found to be greatest with a fibre diameter of 9 -12 μm.

2.6.2 Mineral architecture

As previously discussed, a significant proportion of natural bone tissue is comprised of a mineral component which is fundamental to its structure. *In vitro* experiments have shown that CaP based minerals enhance cellular adhesion, proliferation and differentiation, while *in vivo* studies demonstrate enhanced osteointegration and bone formation on CaP coated implants (Surmenev, Surmeneva, & Ivanova, 2014). These materials are also excellent as carriers for delivery of therapeutics (W. Habraken, Habibovic, Epple, &

Bohner, 2016), and can stabilise bound proteins for centuries (Yu *et al.*, 2017). An expansive range of CaP materials and coatings have thus been developed to exploit their favourable characteristics for biomedical applications, including cements for synthetic bone grafting, fracture stabilisation or implant fixation, materials for scaffold fabrication and coatings for orthopaedic implants (W. Habraken *et al.*, 2016). Coatings in particular are widely used due to the highly brittle nature of CaP, with the underlying material providing the desired mechanical properties, in addition to allowing materials or implants to be modified in post-processing with minimal influence on their initial manufacturing process. A range of methods to achieve this have been used, including physical deposition methods (such as plasma spraying, thermal spray processes and laser deposition) and wet chemical methods (which entail surface modification to enhance nucleation of CaP to the substrate) (Surmenev *et al.*, 2014). Wet precipitation, a type of wet chemical method, is particularly interesting due to the low processing temperatures, range of nano-scale shapes which can be manufactured, and general mild processing conditions, allowing the further incorporation of organic materials to form biocomposites (Mobasherpour, Heshajin, Kazemzadeh, & Zakeri, 2007; Surmenev *et al.*, 2014).

Particle size can easily be controlled with wet precipitation techniques. One commonly used method is the use of a simulated body fluid (SBF) solution containing ions similar to those present in blood plasma (including calcium, phosphate and magnesium ions among others), within which samples are soaked to allow precipitation (Kokubo, Kushitani, Sakka, Kitsugi, & Yamamuro, 1990). This coating method typically produces hydroxyapatite with a plate like morphology, which may be arranged into “rosette” like structures (Tas & Bhaduri, 2011). Altering the carbonate concentration allows particle size to be controlled with this method, with higher concentrations yielding smaller particle sizes (Yu *et al.*, 2017). Another wet chemical method for forming CaP entails the co-precipitation of separate calcium and phosphate solutions, whereby crystals of various

morphologies can be formed via partial substitution of calcium by magnesium (Kumta, Sfeir, Lee, Olton, & Choi, 2005). One co-precipitation method describes the formation of rod/needle shaped crystals, and demonstrates that particle size may be controlled via the concentration of the initial calcium and phosphate solutions to yield particles ranging in size from 83 – 3350 nm (Cunniffe, O'Brien, *et al.*, 2010). This method has been used for the creation of nHA particles which may be subsequently incorporated into scaffolds (Cunniffe, Dickson, Partap, Stanton, & O'Brien, 2010) in addition to being loaded with biological components for enhanced therapeutic effects (Curtin *et al.*, 2012).

As with micro and nano-fibrous architecture, the architecture and topography of CaPs has also been shown to influence cell behaviour, with nano-structured CaP being shown to be highly promising due to high surface to volume ratios, enhanced protein adsorption, and great capacity to support MSC proliferation and differentiation (P. Wang *et al.*, 2014; Hongjian Zhou & Lee, 2011). While these particles do not typically influence cell alignment due to their non-uniform distribution, they provide a useful source of calcium and phosphate ions for mineralisation, while the surface topography they confer can significantly enhance cell interaction with the scaffold due to the increased binding sites they provide and their influence in activating cell membrane receptors and mechanotransduction pathways.

In a study by Cai *et al.*, spherical nano-HA particles with sizes from 20 – 80 nm were fabricated and compared to larger crystals with average width and length of 55 nm and 350 nm respectively (Cai *et al.*, 2007). It was found that smaller particle sizes facilitated greater viability and proliferation of MSCs, with evidence of internalisation of smaller particles by cells being a possible contributing factor to this effect. Bone osteosarcoma cells were also cultured on these particles, where remarkably it was discovered that growth of these cells was inhibited by smaller particle sizes, illustrating further potential applications for the regeneration of bone following tumour ablation. The

therapeutic potential of smaller particles was confirmed in a later study which also investigated the influence of particle morphology on malignant melanoma cells, where it was found that smaller particles inhibit melanoma cell growth regardless of having a rod-like or ellipse-like morphology (B. Li, Guo, Fan, & Zhang, 2008). Particle morphology was found to influence MSC behaviour in a later study however, with sphere-like particles being shown to be better than rod-like particles at promoting osteogenic differentiation of MSCs (H. Yang *et al.*, 2014). The role of HA particle size has also been investigated in composite PCL-HA blends which have been developed for scaffold fabrication via FDM (Domingos, Gloria, Coelho, Bartolo, & Ciurana, 2016). In agreement with previous studies, it was found that nano-particle modified PCL scaffolds enhanced proliferation and ALP activity of MSCs compared to scaffolds with micro-scale particles.

In conclusion, scaffold architecture on the scale of micro and nano-fibrous meshes can significantly alter cell morphology, in turn mediating cell migration, proliferation and differentiation. Coupling this with the enhanced capacity for cell binding and differentiation which nanostructured CaP materials provide, a significant level of control over cell behaviour can be attained to enhance the regenerative and therapeutic potential of engineered scaffolds.

2.7 MEW

2.7.1 Introduction

MEW is a recently developed technology which utilises electrospinning and 3D printing techniques to form fibres on the nano to micron scale and control their deposition in three dimensions. This technology is thus revolutionising these already powerful and extensively used biofabrication technologies for the fabrication of TE scaffolds with precise microarchitectures. The technology was developed and described for the first time in 2011 (Brown *et al.*, 2011), and has grown exponentially since with an extensive range of

solutions developed for a wide range of applications including these in tissue engineering (Brown, Dalton, & Hutmacher, 2016).

In the first paper describing this technology, a method by which PCL pellets were placed in a syringe, melted using circulating heated water, and extruded through a needle via a syringe pump is outlined. A voltage of 12 kV was applied to the needle, with a grounded collector plate controlled via programmable translating linear slides being placed at a distance of 30 mm below. Due to the offset between the source of the extruded fibre and the collector, the controlled deposition dynamics of MEW differ significantly from FDM, as described in the paper. One such consequence is that the collector speed must be equal to or greater than the speed at which the fibre is extruded, with coiling of the fibre occurring if this is not the case, as explained by considering the relationship between the jet speed (S_j) and collector speed (S_c) (Figure 2-13A). If the collector is stationary ($S_c = 0$), the compressive force downwards will cause the fibre to buckle, causing the point of deposition to diverge away from the point directly below the needle and resulting in coiling of the fibre. As translation speed is increased such that the collector speed is equal to the jet speed ($S_c = S_j$), which in later work has been described as the "critical translation speed", the moving collector applies a tensile force which balances with the downward compressive force of the jet, resulting in a reduced "heel" region with deposition directly below the needle. Further increasing the speed of the collector ($S_c > S_j$) results in a greater tensile force being exerted by the plate, resulting in a catenary fibre profile with the point of deposition lagging behind the needle, at which point straight fibres begin to be deposited. Further increasing speed again ($S_c >> S_j$) results in greater lag and a more pronounced catenary profile, as well as stretching of the jet which forms fibres of smaller diameters. This is illustrated by depositing fibres at various collector speeds, which when increased, results in less fibre coiling and the eventual writing of straight fibres (Figure 2-13B). Optimising these deposition parameters can allow for the fabrication of highly precise

micro-fibrous architectures, and fires can be closely stacked to create larger porous structures (Figure 2-13C-D), or offset between layers to form an interconnected micro-porous structure (Figure 2-13E-F).

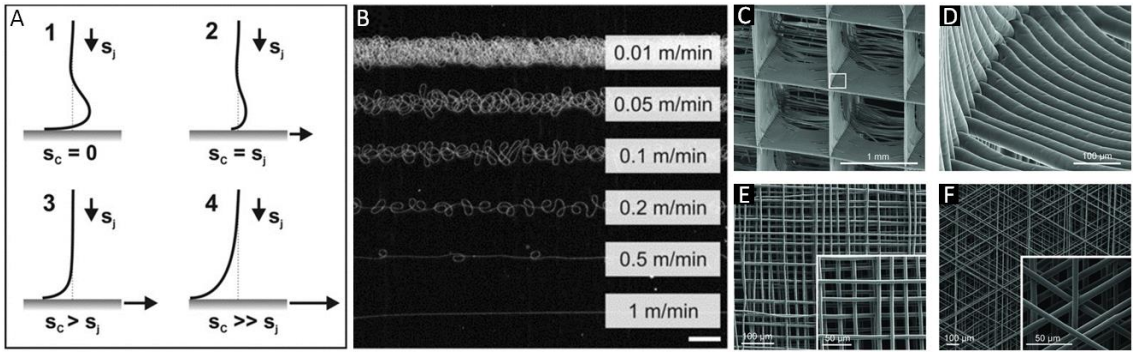

Figure 2-13 MEW Deposition characteristics and scaffolds. Collector speed must be precisely optimised to draw straight fibres (A). At collector speeds below the jet speed, fibre coiling occurs, and when increased allows for the deposition of straight fibres (B). The precise stacked architectures (C-D) and offset architectures (E-F) achievable with MEW. Adapted from (Brown *et al.*, 2011)

These deposition dynamics, along with several other challenges of using this technology, greatly complicate the scaffold fabrication process. The Dalton and Hutmacher research labs in particular have placed considerable focus on developing the technology to improve its functionality and accessibility and enable the fabrication of effective precision controlled scaffold architectures for a vast range of TE applications. Several of these key contributions to advancing MEW technology will be discussed in the following section.

2.7.2 Development of MEW technology

There are a large number of instrument parameters in MEW, including flow rate/pressure, temperature, voltage, collector distance and needle gauge among others, with a study by Brown *et al.* aiming to further characterise these parameters and their influence on fibre deposition (Brown *et al.*, 2014). The primary means by which to control fibre diameter is flow rate/pressure, however the importance of voltage in particular in maintaining consistent fibre formation was highlighted. Greater flow rates require a greater voltage to overcome the reduced surface charge density of the increased material, and voltage must be sufficiently high to establish a Taylor cone, while even further increasing

the voltage was shown to reduce fibre diameter. Collection distance must also be considered, with greater distances resulting in a power law reduction in electric field strength. It is of note that the manner in which voltage is used in MEW differs from solvent electrospinning, in which high voltage and resulting electrical instabilities result in fibre whipping and drawing of the fibre to its final dimensions. In MEW, voltage is used to stabilise fluid flow and prevent Plateau-Raleigh instabilities to form a continuous liquid column, and it is thus the maintained jet stability at extremely low flow rates which allows low fibre diameters (Paul D. Dalton, 2017). In the paper by Brown *et al.,* fibre writing characteristics were also investigated. It was demonstrated that lower flow rates and reduced fibre diameters result in an increase of electrospinning jet speed, requiring greater write speeds to form straight fibres. One of the main limitations of MEW in the maximum achievable scaffold height was also discussed. Initially, it is relatively simple to stack fibres directly on top of one another, with the reduced distance from the needle to a fibre elevated above the collector surface offering a shorter distance for the jet to a lower potential surface. However, there is also an added element of the fibres containing residual charge as they solidify, with the collective residual charge increasing with scaffold height and eventually deflecting the electrospinning jet and resulting in reduced fibre placement accuracy.

Lower fibre diameters are easier to achieve using solvent electrospinning, with melt electrospun fibres typically being on the micron scale or greater. A significant development in the field of MEW was the demonstration that sub-micron fibres could be fabricated while still maintaining precise deposition (Hochleitner *et al.*, 2015). Through optimising instrument parameters and writing characteristics, fibres as small as 817 nm could be placed on top of one another 50 layers high in a box structure with fibre spacing of 100.6 μm. The optimised parameters to allow controlled deposition of these fibres included a low collector distance of 1.5 mm, voltage of 2.9 kV and needle gauge of 33, with PCL being

extruded at a temperature of 84 °C at the needle with air pressure of 2.8 bar. Also, of note is the introduction of turning loops to aid in fibre placement (Figure 2-14B), overcoming the limited turning radius of MEW and facilitating the close fibre spacing of 100 µm.

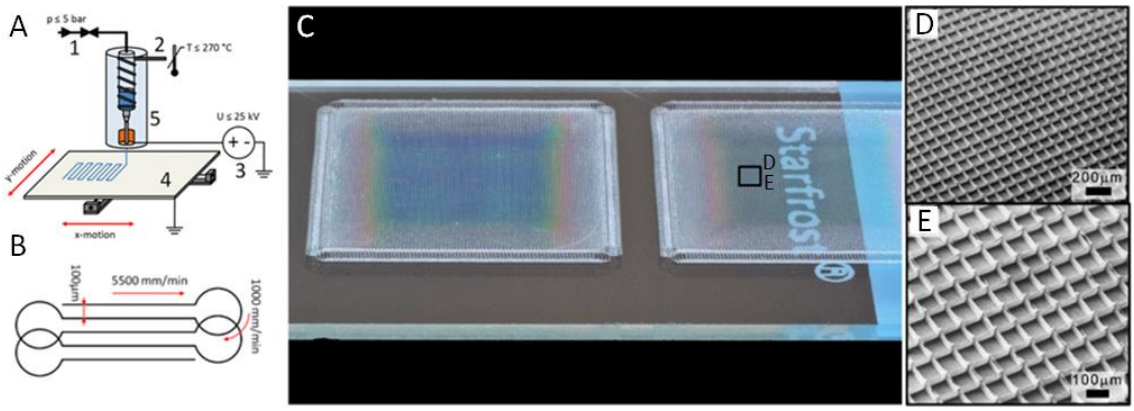

Figure 2-14 Fabricating sub-micron fibres with MEW. Experimental set-up (A), with turning loops enhancing fibre placement (B). The great accuracy achieved as demonstrated by SEM imaging (D,E). Adapted from (Hochleitner *et al.*, 2015)

Another significant study in the development of MEW technology was the characterisation of a phenomenon termed "fibre pulsing", with the researchers demonstrating how this may be overcome to improve fibre homogeneity (Hochleitner *et al.*, 2016). Fibre pulsing is the periodic oscillation of fibre diameter during deposition and occurs due to a sub-optimal balance between instrument parameters. While it may otherwise be tempting to accept a certain degree of fibre diameter variability, there are additional implications in terms of controlled deposition and placement accuracy which mean that tight fibre diameter distributions are fundamental to the MEW process. As previously stated, fibre diameter affects electrospinning jet speed, and the required translation speed as a result, with continuous fibre pulsing resulting in deviations from the programmed architecture (Figure 2-15), and in extreme cases, coiling of the fibre or dragging of larger diameter fibres across the scaffold which can destroy the print. Other possible outcomes are what have been termed "long bead defects", which is a significant increase in fibre diameter resulting from breakdown of the Taylor cone and formation of an elongated drop. It is thus in the researchers' best interests to limit pulsing to as great a

degree as possible. It has been demonstrated by Hochleitner *et al.* that voltage and pressure are particularly important for consistent deposition and must be optimised for fabrication of a given fibre diameter. Increasing pressure must be compensated for by increasing voltage to maintain sufficient charge on the material, however, excessive voltage results in arcing and electric field breakdown. There is thus a narrow usable voltage range for a given pressure and collector distance, which must be determined for consistent fibre formation.

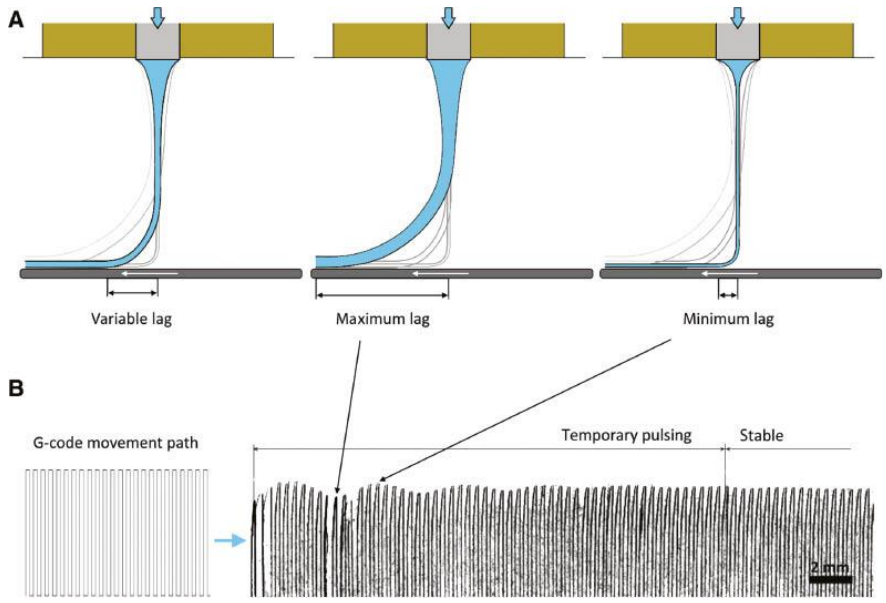

Figure 2-15 Influence of fibre pulsing on variable lag. Fibre pulsing results in altered fibre diameter during the print, which in turn influences fibre lag and optimal translation speed (A). This results in the programmed scaffold architecture (B) deviating from the printed scaffold (C), as evidenced by a wave-like pattern at the edges of the print.

More recently, the great degree of dynamic control over fibre diameter has been demonstrated by Hrynevich *et al.*, with alterations of instrument parameters during printing allowing the fabrication of complex gradient structures (Hrynevich *et al.*, 2018). In this study, it was demonstrated that fibres of diameter 2 – 50 µm could be fabricated by changing pressure and translation speed alone, with needle gauge, voltage, collector distance and temperature being maintained. Altering collector speed is an almost instantaneous method of changing fibre diameter without requiring any time for fibre diameter to equilibrate, however, placement accuracy can be compromised. Altering pressure allowed further increases in fibre diameter range, however, this required times of

approximately 2 – 5 min to allow for fibre diameter to equilibrate. Combining these methods allows for the fabrication of multiphasic MEW scaffolds, with complex features such as gradient pore sizes to aid in seeding efficiency, with another example illustrating how smaller "catching fibres" may be used to prevent adipose-derived stem cell spheroids from falling through the scaffold.

One significant limitation of MEW has previously been the limited print height which is achievable, due to increased charge build up and reduced accuracy of fibre placement. A recent study by Wunner *et al.* has significantly improved upon this however, demonstrating how large volume scaffolds with heights exceeding 7 mm may be fabricated (F.M. Wunner, Wille, *et al.*, 2018). To achieve this, the distance between the needle and the top of the scaffold was maintained via a z-axis, while the voltage was subsequently altered during the print to maintain a constant electrostatic force. Scaffolds were made with initial voltages 7, 8 and 9 kV, and interestingly it was found that the greatest height was achievable with the lowest starting voltage. This work greatly increases the attractiveness of MEW for biomedical applications and facilitates the fabrication of TE scaffolds with large volumes while maintaining precise control over micro-architecture.

MEW is a complex 3D fabrication technology, and process scalability has traditionally been an issue. Significant time is required for the optimisation of variables and fabrication of large scaffolds, however, these issue have recently been addressed in several recent studies by Wunner *et al*. In one study, a MEW system has been developed with advanced process monitoring capabilities, allowing variables to monitored in real time and facilitating the generation of large data sets to accurately characterise the influence of parameters on fibre deposition (Felix *et al.*, 2019). Systems such as this hold great importance for the translation of MEW from the research environment to a consistent, reproducible industrial manufacturing process. Another study reported the development of a high-throughput MEW device with eight print heads; four on each side of a vertically

mounted collector (Felix M. Wunner, Eggert, *et al.*, 2018), exploiting the previously demonstrated finding that MEW can successfully be carried out in different orientations (F.M. Wunner, Maartens, *et al.*, 2018).

Another significant innovation is the use of MEW in combination with a rotating collector to fabricate tubular scaffolds (Brown *et al.*, 2012; Jungst *et al.*, 2015), allowing the fabrication of scaffolds for vascular and neural TE applications among others. The addition of a rotating mandrel adds significant complexity to the MEW process, and the rotational and translational velocity must be tuned in close conjunction with the mandrel diameter and polymer jet speed to precisely deposit fibres in the desired architecture. Selecting these parameters has been made much more accessible with recent work from McColl *et al.* where the authors comprehensively characterised the process and developed a web-based application allowing other researchers to easily generate g-code to fabricate tubular MEW scaffolds (McColl *et al.*, 2018).

While the majority of researchers report using PCL for MEW, some have optimised the process for other polymers and composite materials to expand the potential range of TE applications. These include poly(2-ethyl-2-oxazoline) which has great potential for drug delivery (Hochleitner, Hümmer, Luxenhofer, & Groll, 2014), poly(L-lactide-co-ε-caprolactone-co-acryloyl carbonate), a photo-cross-linkable polymer which can be cross-linked with ultraviolet (UV) irradiation exhibiting high dynamic loading resistance and owing itself to potential connective tissue applications (F. Chen, Hochleitner, *et al.*, 2016), polypropylene, which has favourable mechanical properties and good long term stability (Haigh, Dargaville, & Dalton, 2017), poly(urea-siloxane), a thermoplastic elastomer which was demonstrated to have excellent placement accuracy and fibre stacking characteristics (Hochleitner, Fürsattel, *et al.*, 2018) and poly(vinylidene difluoride), an electroactive polymer with potential applications in cardiac and neural TE (Florczak *et al.*, 2018). MEW

scaffolds with composite PCL-HA (Bas *et al.*, 2018) and PCL-bioactive glass (Hochleitner *et al.*, 2017) blends have also been demonstrated, with potential applications in bone TE.

2.7.3 Applications of MEW in regenerative medicine

The first biomedical application for which MEW was investigated was skin TE, with the excellent cellular infiltration and highly controllable thin meshes guiding cell growth demonstrating the suitability of these scaffolds to this application (Farrugia BL, 2013). MEW has since been used for a large host of TE applications, as summarised in Table 2-1. A range of studies have used MEW for bone research applications in particular, towards which it is particularly suited due to its capability of fabricating hierarchical fibrous structures which may be combined with a mineral component to form composite scaffolds. Other relevant studies also involve interface TE, general TE strategies and vascularisation strategies, will be discussed below.

In a study by He *et al.*, the authors used MEW to fabricate relatively large structures on the scale of centimetres, with a microenvironment composed of 10 μm fibres (He, Xia, & Li, 2016). The authors investigated the effect of 100 μm and 250 μm fibre spacings on osteoblast behaviour, finding that cells proliferate and fill the pore region in the former, while cells are predominantly distributed on the fibres of the larger pore spacing group. Others have attempted to recapitulate the hierarchical structure of bone to an even greater extent, via modification with micro/nanoparticles or HA to mimic the mineral component of the tissue (Bas *et al.*, 2018; Hanßke *et al.*, 2017; Hochleitner *et al.*, 2017). Hanßke *et al.* described the development of an MgF2 nanoparticle-MEW scaffold composite, with the goal of promoting proliferation and differentiation of MSCs while also increasing scaffold stiffness (Hanßke *et al.*, 2017). It was found that scaffolds exhibited a steady release of Mg^{2+} ions, while EDX analysis following incubation in culture medium showed increases of Mg, F, Ca and P. This translated to enhanced cell behaviour, as demonstrated by increased proliferation and ALP activity on MgF2 scaffolds. Bas *et al.* developed a

multiphasic fibrous scaffold with a hydrogel matrix, and varying fibre architecture along its height (Bas *et al.*, 2018). This scaffold was developed for articular cartilage applications, however, also has applications in interface TE due to the inclusion of a HA functionalised layer for integration with the partially mineralised cartilage region connected to the underlying subchondral bone. A 5% w/w nano HA-PCL blend was used for electrowriting this layer, with a uniform distribution of HA being demonstrated throughout the fibres.

An innovation which is not only applicable to bone, but also to a vast range of TE applications, is the combination of bioprinting with MEW. It was demonstrated by de Ruijter *et al.* that these technologies can be combined to form mechanically and biologically stable constructs with great control over the spatial distribution of cells and fibres to form complex structures resembling native biological tissues (de Ruijter, Ribeiro, Dokter, Castilho, & Malda, 2018). By labelling MSCs with different fluorescent dyes, it was shown that spatial distribution of cells in converged MEW-bioprinting constructs could be controlled in both the x-y plane, and in the z-axis throughout the scaffold depth. Importantly, cell viability and metabolic activity was not affected due to the high voltages typically used in MEW. Scaffold fabrication time was a factor in cell viability however, which was decreased by 12%, 33%, 63%, and 80% after 15, 30, 45, and 60 min respectively, highlighting that fabrication time should be kept to a minimum, potentially reducing the size and complexity of scaffolds which can be manufacturing using this process.

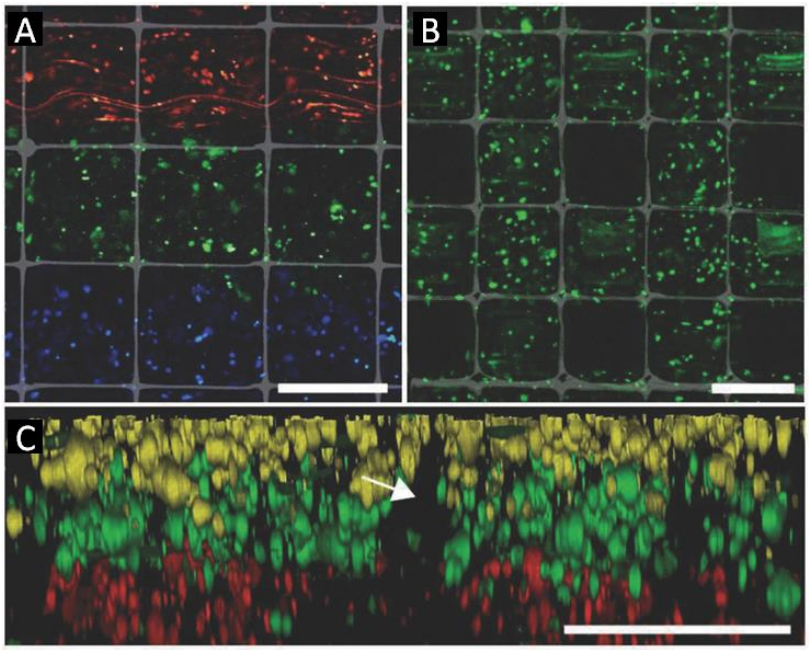

Figure 2-16 Convergence of MEW and bioprinting. Hierarchical structures can be fabricated with spatial control over cell distribution, as seen via labelling and controlled deposition of three difference cell groups (A). Calls can be selectively deposited within desired regions (B), and controlled deposition throughout the scaffold depth in the z-direction is also demonstrated (C). Arrow indicates location of MEW mesh. Scale = 400 µm. Adapted from (de Ruijter *et al.*, 2018).

Vascularisation of constructs is of great importance for a wide range of TE applications, and is vital for ensuring integration of the construct with native tissue and for transporting nutrients and wastes to and from the construct to facilitate tissue growth and regeneration. Cell-accumulation technology is a recently described method whereby single fibroblasts are coated in a fibronectin-gelatin (FN-G) film, and then seeded to a container along with HUVECs, where cells adhere to each other in 3D allowing the formation of vascularised tissues of width 1 cm and height 50 µm (Nishiguchi, Yoshida, Matsusaki, & Akashi, 2011). This was further improved upon via the addition of a MEW scaffold, allowing the formation of vascularised constructs up to a thickness of 100 µm (Bertlein *et al.*, 2017). Vessels were aligned predominantly along the fibres, which were shown to act as a guide for capillary formation. MEW scaffolds thus provide an ideal framework to guide vascularisation, and future TE approaches for a range of tissues would benefit from

incorporating this vascularisation approach into their regeneration strategy to facilitate integration of the scaffold with the native tissue.

MEW scaffolds have ideal properties for endosteal and periosteal regeneration, with these highly vascularised regions known to play significant roles in bone formation as a store of progenitor cells and growth factors (Arai *et al.*, 2009; N. Li *et al.*, 2016). These tissues, and the periosteum in particular, are known to be key regulators of bone healing following fracture, and thus mimicking these tissues via TE constructs has great potential for the enhancement of fracture repair (Roberts, van Gastel, Carmeliet, & Luyten, 2015). Muerza-Cascante *et al.* demonstrated that MEW constructs seeded with osteoblasts form a dense ECM which mimics human endosteum (Muerza-Cascante *et al.*, 2016), while another study by Baldwin *et al.* used MEW scaffolds for periosteal tissue engineering (Baldwin *et al.*, 2017). In the latter study, a multiphasic construct with a tubular MEW scaffold base was constructed. The authors investigated a cell free construct with Star-PEG heparin hydrogel at the outer and inner surfaces, a second construct with MSCs within the inner hydrogel layer and a third construct with MSCs within the inner hydrogel layer and human umbilical vein endothelial cells (HUVECs) within the outer hydrogel layer. Small circular defects of 0.5mm diameter were introduced into the femurs of mice, extending deep enough to expose the bone marrow, and scaffolds were wrapped around the bone. It was found that MSCs remained undifferentiated, perhaps due to being contained within a hydrogel, while the scaffold with HUVECs underwent greater vessel formation and connected with the host vasculature. The detection of multinucleated giant cells (MGCs) indicated initiation of a foreign body reaction, with this likely being due to the PCL scaffold, as others have seen with the use of slow degrading polyesters (Baldwin *et al.*, 2017). There is thus a need to develop and investigate the *in vivo* response of new materials which can be processed via MEW.

Several studies have developed humanized bone models via tubular MEW scaffolds to study cancer metastasis to and from bone (Holzapfel *et al.*, 2014; Martine *et al.*, 2017; Thibaudeau *et al.*, 2014; Wagner *et al.*, 2016). In these studies, humanised tissue engineering bone constructs are created from tubular scaffolds, human cells, osteogenic factor rhBMP-7 and fibrin glue, before being implanted subcutaneously in non-obese diabetic severe combined immunodeficient (NOD-SCID) mice. This powerful model results in the formation of a human bone niche within mice with many potential applications in the study of cancer metastases, drug testing and the study of physiological and pathological development pathways in bone (Martine *et al.*, 2017). For example, Thibaudeau *et al.* demonstrates that following injection of a human breast cancer cell line into the blood circulation of mice, metastases to the humanised bone is detected via bioluminescent imaging, along with osteolysis of the bone (Thibaudeau *et al.*, 2014), while Wagner *et al.* demonstrated how this model can also be used to detect metastases of human osteosarcoma cells from the humanised bone to other organs such as the lung (Wagner *et al.*, 2016).

In summary, MEW allows significant control over scaffold architecture via the precise deposition of fibres, and allows for the development of 3D environments with highly specific microarchitectures. This technology thus has great potential for the fabrication of scaffolds to intricately guide MSC behaviour and drive osteogenesis for applications in bone tissue regeneration.

Table 2-1 Applications of MEW in biomedical engineering

Biomedical application	**Description**	**Source**
Bone	Bioactive glass incorporated within fibres with potential applications in bone TE	(Hochleitner *et al.*, 2017)
Bone	MgF2 nanoparticle-MEW scaffold composite, MSC *in vitro* model	(Hanßke *et al.*, 2017)
Bone (endosteum)	*In vitro* model for endosteum	(Muerza-Cascante *et al.*, 2016)
Bone (periosteum)	Multiphasic construct recapitulating osteogenic and vascular niche *in vivo*	(Baldwin *et al.*, 2017)
Bone, general	Tubular MEW scaffolds demonstrating growth of osteoblasts and mesothelial cells	(Brown *et al.*, 2012)
Bone, general	Hierarchical scaffolds facilitating osteoblast growth and alignment	(He *et al.*, 2016)
Bone tumour model	Humanised bone model to study bone tumour metastasis *in vivo*	(Wagner *et al.*, 2016)
Bone tumour model	Humanised bone model to study bone tumour metastasis *in vivo* (protocol)	(Martine *et al.*, 2017)
Breast cancer model	Humanised bone model to study breast cancer metastasis *in vivo*	(Thibaudeau *et al.*, 2014)
Cancer immunotherapy	Antibody bound scaffolds for T cell therapy	(Delalat *et al.*, 2017)
Cardiac	Composite MEW constructs for guiding cardiac progenitor cell growth	(M. Castilho *et al.*, 2017)
Cardiac (myocardium)	Hexagonal ultrastretchable MEW heart patch, with minimally invasive *in vivo* delivery	(Miguel Castilho, Mil, *et al.*, 2018)
Cartilage	Fibre reinforced hydrogels with *in vitro* chondrocyte study	(Visser *et al.*, 2015)
Cartilage	Fibre reinforced hydrogels supporting chondrocyte differentiation *in vitro*	(Bas, De-Juan-Pardo, *et al.*, 2017)
Cartilage	Multiphasic MEW-hydrogel scaffold with mineral component for subchondral bone	(Bas *et al.*, 2018)
Cartilage, general	Convergence of MEW and bioprinting, demonstrating chondrocyte differentiation *in vitro*	(de Ruijter *et al.*, 2018)
General	Fibre reinforced hydrogels for enhancement of structural integrity	(Bas *et al.*, 2015)
General	MEW fibres used as sacrificial template for hydrogel scaffolds	(Haigh *et al.*, 2016)
General	MEW out-of-plane printed fibres to improve shear properties of hydrogel composites	(de Ruijter *et al.*, 2017)
In vitro model	Investigation into role of structural confinement on fibroblast behaviour	(F. Tourlomousis *et al.*, 2017)
In vitro model	Investigation into cell-matrix interactions with fibroblasts	(Filippos Tourlomousis & Chang, 2017)
Ligament, tendon	Crimped scaffolds with non-linear behaviour to recapitulate native tissue properties	(Hochleitner, Chen, *et al.*, 2018)
Prostate cancer model	Humanised bone model to study prostate cancer metastasis *in vivo*	(Holzapfel *et al.*, 2014)
Skin	*In vitro* study with fibroblast seeded constructs	(Farrugia BL, 2013)
Soft tissue	Stretchable fibrous-hydrogel composites	(Bas, D'Angella, *et al.*, 2017)
Soft tissue	Finite element and experimental models to characterise MEW-hydrogel composites for TE	(Miguel Castilho, Hochleitner, *et al.*, 2018)
Vascularisation	Scaffold vascularisation with cell accumulation technology	(Bertlein *et al.*, 2017)

2.8 Summary

This literature review has demonstrated the highly complex hierarchical architecture of bone tissue, which is composed of fibrous collagens, mineral nanocrystals, growth factors, and a range of cells communicating to one another to build and maintain its complex structure. While completely replicating this structure for regenerative and research applications is an unattainable goal with present technology, constructing a simplified yet highly precise and intricate structure to recapitulate the fundamental components of bone and form a highly effective tissue regeneration strategy is within our means. Achieving this however, requires a closely-knit collaboration between the current state-of-the-art in biofabrication techniques and understanding of cell mechanobiology. The importance of cell signalling in response to the external environment has been highlighted, with an emerging appreciation for the key role of EVs in this process. More specifically, the key role of the osteocyte mechanosignalling in guiding MSC behaviour, and the importance for this for continuous tissue regeneration, has been highlighted. The fundamental nature of architecture in mediating MSC behaviour and function, which is only recently beginning to be appreciated, has also been discussed in detail in this literature review.

There is still a need to further understand how cells communicate with one another in the dynamic environment of bone and how they respond to their surrounding fibrous micro-environment. Achieving this will not only further our understanding of cell behaviour, but will also allow for the development of improved therapies and regeneration strategies which exploit the natural behaviour of cells in bone. Combining both indirect biophysical/biochemical (mechanosignalling) and direct biophysical (architectural) cues has the potential for creating an immensely powerful framework to intricately guide cell behaviour with extensive applications in regenerative medicine.

Chapter 3

Osteocytes regulate human bone marrow mesenchymal stem cell behaviour via mechanically activated osteocyte-derived extracellular vesicles (MAEVs)

3.1 Introduction

Osteocytes are the most abundant cell type in bone and are known as the primary sensing and metabolism controlling cells within the tissue. Osteocytes are key to directing the processes of bone formation and resorption via the secretion of various signalling factors which act upon bone forming osteoblasts and resorbing osteoclasts and their progenitors, skeletal and haematopoietic stem cells (Dallas *et al.*, 2013). The implications of this can be seen in the highly debilitating and life threatening disease that is osteoporosis, which has been linked to osteocyte apoptosis (Bonewald, 2004) and reduced osteocyte numbers in affected patients (Qiu, Rao, Palnitkar, & Parfitt, 2003). This results in a significant drop in quality of life, increased risk of additional complications due to immobilisation, and significantly increased mortality rates due to fracture and secondary causes (Center, Nguyen, Schneider, Sambrook, & Eisman, 1999; Rachner, Khosla, & Hofbauer, 2011). Not only do osteocytes have key functions in bone, they have also been shown to be involved in a large range of other major functions throughout the body (Bonewald, 2017), including regulation of lymphoid organs (M. Sato *et al.*, 2013), influencing heart (Bonewald & Wacker, 2013; Touchberry *et al.*, 2013), muscle (Brotto & Bonewald, 2015; Huang J; Mo, Romero-Suarez, Bonewald, Johnson, & Brotto, 2012) and liver function (Singh *et al.*, 2016), and suppressing breast cancer growth and metastasis in

bone (J. Z. Zhou *et al.*, 2016). This highlights the critical role of the osteocyte in human health, and the importance of better understanding osteocyte signalling factors for the development of therapeutics to treat orthopaedic and systemic disease.

A prime example of osteocyte sensing and coordination of bone physiology is in mechanoadaptation, with mechanical loading leading to enhanced bone formation and unloading leading to bone loss (Bonewald, 2011; Mitchell B. Schaffler, Cheung, Majeska, & Kennedy, 2014a; Tatsumi *et al.*, 2007). In response to macroscale deformation of bone, resident osteocytes sense the micro-mechanical environment consisting of oscillatory fluid flow induced shear stress (Corrigan *et al.*, 2018; Johnson *et al.*, 2018; Mitchell B. Schaffler & Kennedy, 2012; Weinbaum *et al.*, 1994) and relay this biophysical signal to effector cells (Brady *et al.*, 2015; Tan *et al.*, 2007). Mechanically stimulated osteocytes can enhance the bone forming capacity of osteoblasts via direct cell-cell contact (Suswillo *et al.*, 2017; Taylor *et al.*, 2007), in addition to secreted factors as demonstrated by conditioned media experiments (Brady *et al.*, 2015; Hoey *et al.*, 2011). Furthermore, this same mechanically activated osteocyte conditioned media was also shown to inhibit osteoclast formation (Tan *et al.*, 2007; You *et al.*, 2008). Due to the non-proliferative state and short lifespan of mature bone cells, continuous bone formation requires the replenishment of the exhausted osteoblast from a stem cell population (J. C. Chen, Hoey, Chua, Bellon, & Jacobs, 2016a; Park *et al.*, 2012). Interestingly the osteocyte has also been shown to coordinate bone marrow MSC behaviour, with conditioned media from mechanically stimulated osteocytes enhancing stem cell proliferation, recruitment and osteogenic differentiation, demonstrating the far reaching influence of this cell type, particularly in response to a mechanical stimulus (Brady *et al.*, 2015; Hoey, Chen, & Jacobs, 2012).

The means by which osteocytes coordinate this mechanoadaptation of bone is of great interest, with several key factors having been identified which play a role in this regard and therefore targeted as a therapeutic. There has been a plethora of studies

investigating various osteocyte derived factors released in response to fluid shear, including nitric oxide (NO) (Klein-Nulend *et al.*, 1995), prostaglandin E_2 (Cheng *et al.*, 2001; Cherian *et al.*, 2005), ATP (Genetos *et al.*, 2007), RANKL (Nakashima *et al.*, 2011), OPG and macrophage colony-stimulating factor (M-CSF) (Zhao *et al.*, 2002). One factor that has gained much interest is sclerostin (SOST) which is released by osteocytes and inhibits Wnt-mediated bone formation (Moester *et al.*, 2010). SOST expression is inhibited following mechanical loading (Shu *et al.*, 2017) and inhibition of this protein has been shown to stimulate bone formation, with anti-sclerostin therapy currently in the advanced phase of clinical trials (Lewiecki, 2014). To gain a greater understanding of the factors expressed by physically stimulated osteocytes, others have taken a more global approach, utilising microarrays to study global gene expression in osteocytes subjected to cyclic compressive forces (W. Chen *et al.*, 2010) and osteocytes isolated from murine trabecular bone following vertebrae loading (Wasserman *et al.*, 2013). Furthermore, a proteomic analysis has been combined with a transcriptomic analysis of osteocytes subjected to fluid shear to investigate protein as well as gene expression information and reveal novel interactions between them (P. M. Govey *et al.*, 2014). These studies reveal the altered proteome of the osteocyte due to fluid flow stimulation and identified a range of proteins which may be involved in mechanotransduction, including Nucleoside diphosphate kinase and Calcyclin, which are of interest due to their roles in ATP and calcium binding respectively. However, to date, the full secretome protein signature of the osteocyte and how this is altered in response to mechanical stimulation is unknown.

A specific route of cell-cell communication which has garnered much attention of late is via EVs. EVs are spherical bi-layered proteolipids secreted from cells by exocytosis and are engulfed by neighbouring cells facilitating cell-cell communication. EVs transfer genetic information incorporated into lipids, proteins and nucleic acid (mRNA, miRNA) from one cell to another, thereby influencing the recipient cell function (Yanez-Mo *et al.*,

2015). Interestingly, it has recently been shown that bone cells release EVs and utilise these vesicles as a mechanism to mediate osteoblast and stem cell osteogenesis (Cui, Luan, Li, Zhou, & Han, 2016; Davies *et al.*, 2017b; Q. Li, Huang, Wang, & Huang, 2018; Jess Morhayim, Rudjito, van Leeuwen, & van Driel, 2016; Qin *et al.*, 2017; Mari Sato *et al.*, 2017). Moreover, osteocyte derived EVs contain microRNAs (miRNAs) known to mediate osteoblast function, highlighting a potential non-protein based role in bone cell communication (Qin *et al.*, 2017; Mari Sato *et al.*, 2017). Bone derived EVs may also be exploited as a potential therapy for various diseases, as well as having potential for treatment of critical size bone defects (Gimona, Pachler, Laner-Plamberger, Schallmoser, & Rohde, 2017). Isolated osteoblast EVs loaded with bisphosphonates could inhibit osteoclast activity both *in vitro* and *in vivo* (Cappariello *et al.*, 2017), revealing their potential as as powerful drug delivery method. Interestingly, the release of EVs and potentially the content of EVs may also be altered by mechanical loading, with EV release into plasma increasing following exercise, with a proteomic analysis demonstrating differential protein expression in EVs from subjects after exercise compared to those at rest (Whitham *et al.*, 2018). Therefore, a potential mechanism of osteocyte mediated mechanoadaptation in bone may be facilitated by MAEVs.

While several factors released by osteocytes have been investigated, as well as the protein expression of cell lysates being uncovered via proteomic analysis, the specific composition and factors implicated in mechanically mediated osteocyte paracrine signalling are yet to be elucidated. Thus, the aim of this study is to further understand the means by which osteocytes mediate bone mechanoadaptation, with this being achieved by constructing, for the first time, a complete map of the osteocyte secretome protein signature. The ability of the osteocyte secretome to induce a chemotactic and osteogenic response in hMSCs using a parallel plate flow chamber approach to mechanically stimulate osteocytes was first validated. A proteomic analysis on the osteocyte secretome via mass

spectrometry was then conducted to identify all proteins released by cells after both static and dynamic culture. Enrichment of gene ontology terms was investigated to elucidate the primary cellular components and processes with which the osteocyte secretome is involved, with further analysis comparing the altered protein release and most differentially expressed proteins released by mechanically stimulated cells. This lead to the discovery of MAEVs, which were subsequently isolated from the mechanically activated osteocyte secretome, characterised, and found to elicit identical trends in MSC recruitment and osteogenesis to that seen with conditioned media, demonstrated a key role for osteocyte EVs in mediating hMSC behaviour, identifying a novel mechanism by which osteocytes coordinate loading-induced bone formation. Moreover, pro-osteogenic osteocyte derived MAEVs represent a potential cell-free therapy to enhance bone regeneration and repair in diseases such as osteoporosis.

3.2 Materials and methods

3.2.1 Cell culture

MLO-Y4 osteocyte like cells (Kerafast) (Kato *et al.*, 1997) were maintained as previously described (Rosser & Bonewald, 2012) in α-MEM growth medium with 2.5% FBS, 2.5% CS, 1% Penicillin/Streptomycin (PS) and 1% L-glutamine during static culture and fluid shear stimulation. For conditioned medium studies, cells were cultured in α-MEM with 1% PS and 1% L-glutamine. Human bone marrow stem cells (hMSCs) were isolated from bone marrow (Lonza), characterised by trilineage differentiation, and maintained with 10% FBS and 1% PS unless otherwise stated.

3.2.2 Mechanical stimulation and conditioned medium collection

48 h prior to fluid shear application, 75 x 38 mm glass slides were coated with 0.15mg/ml type I collagen (Sigma C3867) for one hour and washed with PBS, after which osteocytes were seeded at a density of 1.16×10^4 cells/cm^2. Glass slides were transferred to

custom made parallel plate flow chambers (PPFC) as previously described (Stavenschi, Labour, & Hoey, 2017). Each glass slide was assembled within an individual PPFC under sterile conditions and incubated at 37°C and 5% CO_2. Cells in PPFCs were either subjected to a fluid shear stress of 1 Pa at a frequency of 1 Hz, or maintained in the PPFC under static conditions, with each condition completed in quadruplicate. After two hours of treatment, slides were transferred to culture dishes, washed with PBS, and 2.5 ml of serum free medium was applied. A control group consisting of collagen coated glass slides with no cells was also incubated with 2.5 ml of serum free medium. Cells were incubated for 24 h and medium was collected from cells which had undergone fluid shear (CM-F), statically cultured cells (CM-S) and from cell free slides with collagen coating (Medium). Samples were centrifuged at 3,000g for 10 mins at 4°C to remove debris, after which the supernatant was collected. Samples were stored at -80°C prior to use.

3.2.3 Effect of osteocyte conditioned media on hMSC recruitment

Chemotaxis of stem cells was assessed using Boyden chambers with a pore size of 8 μm (Merck Millipore, PIEP12R48). Cells were seeded on the upper membrane in serum free α-MEM medium at a density of 30,000 cells/cm^2 and allowed to adhere 4 h before being transferred to the wells containing chemotactant (CM-S, CM-F, 10% FBS). Cells were then cultured for a further 18 h, fixed with 10% formalin solution and stained with haematoxylin. Light microscopy was used to determine the number of migrated cells, which was then normalised to Medium for each group.

3.2.4 Effect of osteocyte conditioned media on hMSC osteogenesis

hMSC cells were seeded in 6-well plates at a density of 6,500 cells/cm^2 and cultured for 24 h. Osteocyte CM (CM-S, CM-F) was then applied and hMSCs were cultured for a further 24 h after which time cells were lysed with tri-reagent (Sigma Aldrich) and mRNA isolated as per the manufacturer's protocol. RNA concentration was measured using a Nanodrop spectrophotometer and sample purity was checked via 260/280

and 260/230 absorbance ratios, and 200 ng RNA was reverse transcribed to cDNA using a High-Capacity cDNA Reverse Transcription Kit (Applied Biosystems). Commercially available primers were used to determine levels of cyclooxygenase 2 (COX2), osteocalcin (OCN), osteopontin (OPN), runt-related transcription factor 2 (RUNX2) and osterix (OSX) (Table S1). Quantitative RT-PCR was performed using a reaction volume of 20 µl containing 10 µl SYBR green PCR MasterMix (Invitrogen Ltd, Paisley, UK), 0.8 µl of each forward and reverse primer, and 8.4 µl DNase free water. Plates were run on an ABI 7500 Fast real-time PCR system (Life Technologies, Carlsbad, CA, USA).

3.2.5 Sample preparation for mass spectrometric (MS) analysis

Protein precipitation was carried out with 1ml of each sample using Trichloroacetic Acid (TCA), and the pellet re-suspended with 6M urea in 50mM ammonium bicarbonate. Samples were reduced with 5 mM dithiothreitol for 30min at 60°C and alkylated with 10mM iodoacetamide for 30min at room temperature in the dark, after which ammonium bicarbonate was added to bring the concentration of urea to 1.8M. The reduced and alkylated proteins were then digested overnight with trypsin at a ratio of 1:50 w/w trypsin to protein at 37°C and 350 rpm on a Thermomixer. Digestion was then stopped with hydrochloric acid. Peptides were bound and desalted using C18 ZipTips (Merck Millipore) and washed with 0.1% trifluoroacetic acid (TFA) before being re-suspended in 10 µl elution solution (50% acetonitrile in 0.1% TFA). Samples were concentrated using a SpeedVac vacuum concentrator until roughly 4 µl remained, before being re-suspended in 20 µl 0.5% acetic acid.

3.2.6 Liquid chromatography tandem mass spectrometry (LC MS/MS)

Biological samples (n=3) were run with two technical replicates on a Thermo Scientific Q Exactive mass spectrometer connected to a Dionex Ultimate 3000 (RSLCnano) chromatography system. Each sample was loaded onto a fused silica emitter (75 µm ID, pulled using a laser puller (Sutter Instruments P2000)), packed with UChrom C18 (1.8 µm)

reverse phase media (nanoLCMS Solutions LCC) and was separated by an increasing acetonitrile gradient over 47/60 minutes at a flow rate of 250 nL/min. The mass spectrometer was operated in positive ion mode with a capillary temperature of 320°C, and with a potential of 2300V applied to the frit. All data was acquired with the mass spectrometer operating in automatic data dependent switching mode. A high resolution (70,000) MS scan (300-1600 m/z) was performed using the Q Exactive to select the 8 most intense ions prior to MS/MS analysis using high-energy collision dissociation (HCD).

3.2.7 MS data analysis

Raw data from MS analysis was processed using MaxQuant software (J. Cox & Mann, 2008; Tyanova, Temu, & Cox, 2016) version 1.5.5.1 and spectra searched using the built in Andromeda search engine (J. Cox *et al.*, 2011) with the Uniprot FASTA validated Mus musculus database being used as the forward database and the reverse for the decoy search being generated within the software. A minimum six amino acid length criteria was applied and the false discovery rate (FDR) was set to 1% at the peptide and protein level. Cysteine carbamidomethylation was included as a fixed modification and oxidation of methionine and protein N-terminal acetylation were set as variable modifications for the peptide search. The "match between runs" algorithm was used to transfer peptide identifications between MS runs where possible to increase total number of protein hits. At least one unique or razor peptide was required per protein group for identification. Label free quantification (LFQ) was carried out using the MaxLFQ algorithm (Jürgen Cox *et al.*, 2014) within the software, with Fast LFQ being disabled. Other settings were kept as default in the software.

3.2.8 Bioinformatics and statistical analyses

Bioinformatic analysis was performed using Perseus 1.5.5.3 (Tyanova, Temu, Sinitcyn, *et al.*, 2016) to analyse LFQ data from MaxQuant. Potential contaminants, proteins identified in the decoy reverse database and proteins identified only by site

modification were omitted. LFQ values were transformed using a $\log_2(x)$ function. For clustering and principal component analysis (PCA), imputation was carried out (width = 0.3, down shift = 1.8) where missing values were replaced by values from a normal distribution. For hierarchical clustering, log transformed intensities were normalised by z-score and clustered using the Euclidean distance method for both columns and rows. Pathway enrichment analysis of clusters was carried out using a Fisher's exact test with the Benjamini–Hochberg FDR threshold set to 5%, with gene ontology cellular component (GOCC), biological process (GOBP), molecular function (GOMF) and UniProt keywords being analysed for enrichment. A Student's T-Test with a permutation based FDR was carried out to identify significant differences in expression of proteins between groups, and volcano plots constructed with difference (log2 fold change) on the x-axis and significance (-log10 transformed) on the y-axis. The difference on the x-axis corresponds to the difference between the mean expression values of log2 transformed data, where a difference of n corresponds to fold change of 2^n. Pathway enrichment analysis was carried out on these significantly upregulated proteins using the Fisher's exact test with Benjamini-Hochberg FDR cut-off of 5%. Results were represented as word clouds, with the size of the word representing degree of enrichment and colour representing FDR corrected p value. All terms with a minimum of 0.5 enrichment factor were included. StringDB (Szklarczyk *et al.*, 2015) was used to generate protein-protein interaction networks of differentially expressed proteins and perform functional enrichment analysis of gene ontology and protein family (Pfam) terms. For further analysis between CM-S and CM-F groups, only proteins which were identified in all three biological replicates in at least one of the groups were considered for further analysis.

3.2.9 Extracellular vesicle isolation from conditioned media

Medium from statically and dynamically cultured osteocytes was collected and centrifuged at 3000 g for 10 min to remove debris. Medium was then filtered through a 0.45

μm pore filter and total protein content was determined via BCA assay. Medium was ultracentrifuged at 110,000 g for 75 min at 4°C, using an SW32.Ti swing bucket rotor. Collected EV pellets were washed in PBS and the ultracentrifugation process was repeated.

3.2.10 Characterisation of EVs

3.2.10.1 TEM imaging

Imaging was conducted via a JEOL JEM1400 transmission electron microscope (TEM) coupled with an AMT XR80 digital acquisition system. Samples were physiosorbed to 200 mesh carbon coated copper formvar grids and negatively stained with 1% Uranyl acetate.

3.2.10.2 Immunoblotting

For immunoblotting, cell pellets and EVs were lysed using cell extraction buffer (Invitrogen, Carlsbad, CA, USA) supplemented with protease inhibitor cocktail (Roche, Basel, Switzerland). Protein quantification was performed using Bio-Rad protein assay (Bio-Rad, Hercules, CA, USA). Cellular and EV protein (8μg) were resolved on 10% SDS gels and transferred to PVDF membranes (BioRad). Blots were incubated at 4°C overnight with primary antibodies to GRP-94 (Cell Signalling, 1:2000 dilution), TSG101 (Abcam, 1:1000 dilution) and PDC6I/ALIX (Abcam, 1:1000 dilution). Secondary antibodies were incubated for 1hr at room temperature and developed using Immobilon Western Chemiluminescent HRP substrate (Millipore, MA, USA).

3.2.10.3 Quantification of EV content in conditioned medium

Protein contents were measured using a BCA protein assay kit (Thermo Scientific, 23227). BSA standards (10 μl) were added to a 96 well plate after which 200 μl of working reagent was added (50:1 ratio of reagents A & B). EV samples were diluted in CST lysis buffer (Cell Signaling Technology, 9803), vortexed, and incubated for 1 hr on ice. 10 μl of sample lysates were added to the plate and mixed with 200 μl of working reagent. The plate

was incubated for 30 min at 37°C and absorbance read on a spectrophotometer at 562 nm. BCA assay results combined with the volume of the isolate were used to calculate the total quantity of protein in the EV isolates and this value was used to calculate the original concentration of EV protein in the conditioned medium.

3.2.10.4 Particle size analysis

Particle size analysis was performed on EVs with the NTA NS500 system (NanoSight, Amesbury, UK) to determine particle size based on Brownian motion. EV samples were diluted 1:50 in PBS and injected into the NTA system, which obtained 4 x 40 second videos of the particles in motion. Videos were then analysed with the NTA software to determine particle size.

3.2.11 Uptake of EVs by MSCs

For fluorescent labelling, 2 µg of EVs were incubated with 2 µM PKH26 dye solution (PKH26GL, Sigma) for 5 mins, after which staining was inhibited via addition of 1% BSA solution for 1 minute. Labelled EVs were pelleted, the excess dye solution aspirated, and washed twice with culture medium. hMSCs were seeded at a density of 10,000 cells/cm^2 to Nunc glass bottomed dishes (150680, Thermo Fisher) and cultured for 24 h. Cells were washed before being incubated with either PKH26-labelled EVs or a dye control containing no EVs. Cells were fixed after 18 h and stained with Alexa Fluor 488 phalloidin (1:40) (A12379, Thermo Fisher) and DAPI (1:2000) (D9542, Sigma) to label the actin cytoskeleton and nuclei before being mounted with Fluoroshield (F6182, Sigma) and imaged using confocal microscopy.

3.3 Results

3.3.1 Osteocytes regulate human MSC recruitment and osteogenesis in response to fluid shear

hMSCs were cultured in conditioned medium collected from statically and dynamically cultured osteocytes, with recruitment and osteogenic gene expression being investigated (Figure 3-1A). There is a trend of increased hMSC recruitment towards CM-S compared to control medium however this was not significant. CM-F did however enhance MSC recruitment, which was significantly greater than both medium ($p < 0.001$, $n = 9$) and CM-S ($p < 0.01$, $n = 9$) with fold changes of 3.2 and 1.8 respectively, indicating the enhanced chemotaxis displayed by MSCs towards mechanically stimulated osteocytes. The role of osteocyte paracrine signalling in driving osteogenesis was also investigated by treating hMSCs with CM-S and CM-F for 24 h and investigating expression of osteogenic genes COX2, OCN, OPN, RUNX2 and OSX (Figure 3-1B). Treatment with CM-S did not significantly alter expression of any of the investigated genes in hMSCs compared to medium. hMSCs cultured in CM-F resulted in consistent increasing trends of gene expression in all genes, with significant fold changes of 4.6 in COX2, 5.4 in OPN and 3.4 in RUNX2 compared to medium ($p < 0.001$, $n = 4$-6). These genes were also significantly upregulated compared to CM-S with fold changes of 3.0, 2.2 and 2.3 respectively ($P < 0.01 – 0.001$, $n = 4$-6). There was a near-significant 3.1 fold increase in OSX compared to medium ($p = 0.07$, $n = 4$-6), in addition to a 2.5 fold increase in OCN expression in CM-F compared to CM-S. In summary, CM-S elicits marginal increases in MSC osteogenesis, with significant increases following CM-F treatment, demonstrating the importance of mechanical loading in mediating osteocyte-MSC mechanosignaling.

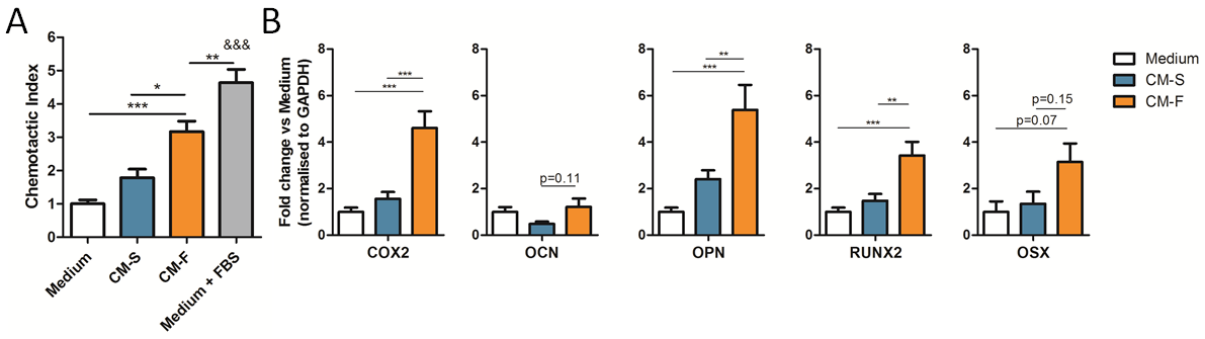

Figure 3-1 Migration of MSCs towards osteocyte conditioned medium and normalised to Medium, showing significant increases in chemotactic index towards CM-F medium when compared to CM-S (n=9) (A). qPCR analysis of COX-2, OCN, OPN, RUNX2 and OSX expression in hMSCs treated with osteocyte medium from CM-S and CM-F (n=4-6) (B). Statistical analysis using using one-way ANOVA and Bonferroni's multiple comparison post-test for chemotactic index (*p<0.05, **p < 0.01, ***p < 0.001, &&& p < 0.001 vs Medium and EV-S).

3.3.2 Overview of identified proteins within the osteocyte sectretome

Analysis of the osteocyte secretome revealed a total of 393 proteins across all groups. Within these groups, over 300 proteins were identified in CM-S and CM-F groups, with 112 being identified in Medium control (Figure 3-2C), with all proteins being listed in "supplementary table 1.xslx". Pearson correlations comparing all biological replicates to one another show that there is a high average correlation between replicates in the CM-S (0.92) and CM-F (0.90) group (Figure 3-2D). When comparing CM-S and CM-F to one another, an average correlation of 0.90 is seen, revealing a significant degree of similarity in protein expression between osteocytes cultured in static and dynamic conditions. In contrast, when comparing CM groups to Medium, an average correlation of 0.33 is seen between them, revealing the difference in the osteocyte secretome and osteocyte culture media validating the release of proteins into culture medium from the osteocyte.

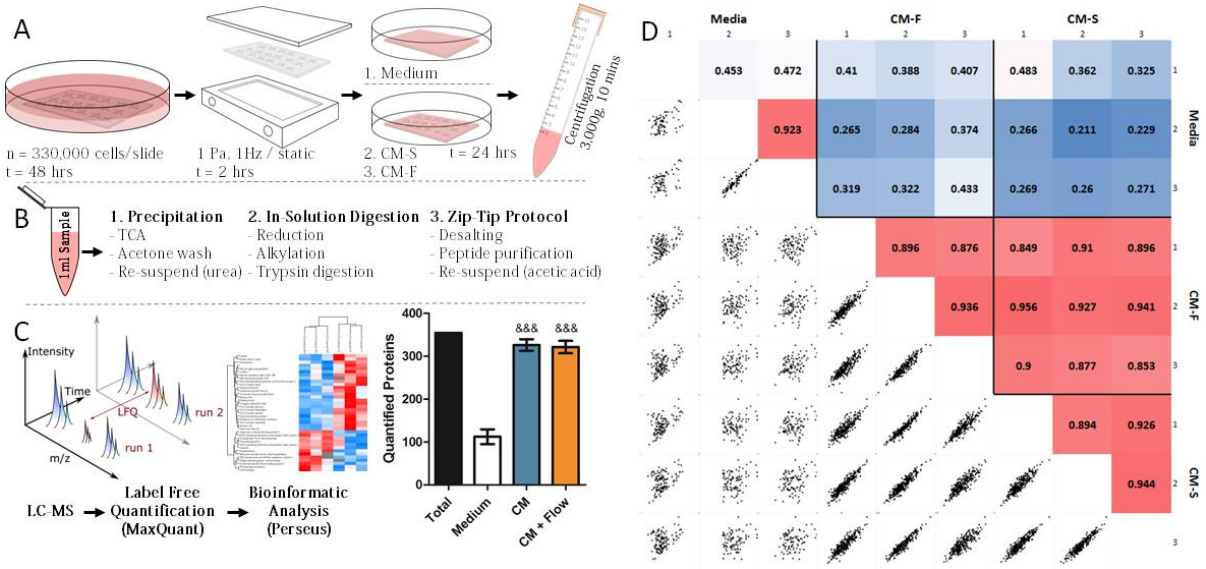

Figure 3-2 Outline of experiment procedure. MLO-Y4 cells were seeded to collagen coated glass slides and cultured for 48 hours (A), before being transferred to parallel plate flow chambers for dynamic (OFF, 1Pa, 1Hz, 2hrs) or static culture. The slides were then transferred to culture dishes and 2.5ml of serum free medium was applied, with a control group being present with collagen coated glass slides without cells. The serum free medium was collected and centrifuged to remove debris. 1ml of each sample was collected, and proteins were precipitated and digested in solution before being purified via C18 stage tips (B). Samples were analysed via LC-MS, and label free quantification was carried out in MaxQuant before a bioinformatic analysis was completed in Perseus (&&& $p < 0.001$ vs Medium using one-way ANOVA and Bonferroni's multiple comparison post-test)(C). Pearson correlations between technical replicates, biological replicates and sample groups were determined, with correlations between biological replicates with combined technical replicates shown (D).

3.3.3 Proteomic analysis of the osteocyte secretome reveals enrichment of proteins associated with EVs

Hierarchical clustering revealed three primary groups of protein expression within the samples. CM-S and CM-F groups comprise one of the main clusters (Figure 3-3A), where it can be seen that there is considerable similarity of protein expression in terms of LFQ intensity within these groups. Medium samples comprise the remaining column clusters, where the reduced number and expression of proteins are more apparent when considering data without imputation (Figure 3-3B). Due to the similarity between osteocyte conditioned medium groups, also verified via PCA (Figure S 3-2), an analysis was first undertaken by combining CM-S and CM-F (termed CM), and comparing to Medium to

reveal the proteins which comprise the osteocyte secretome. The results of this reveal the presence of 97 proteins which have significant differential expression in CM, indicated in red in Figure 3-3C. Within these proteins, significant enrichment (enrichment factor > 1.7, $p < 10^{-4}$) of several "extracellular" GOCC terms was revealed in comparison to the total 393 identified proteins using Fisher's exact test, with enrichment of UniProt keywords "secreted" and "signal" (enrichment factor > 1.6, $p < 10^{-5}$) also being revealed (Figure 3-3D). This validates the successful isolation of proteins released by the osteocyte into their surrounding environment, with evidence for further downstream signalling functions. Functional enrichment within CM proteins of GOCC terms with reference to the whole Mus musculus genome further revealed the significant enrichment of membrane bound vesicles and exosomes in the secretome (Table 3-1), revealing a potential role for EVs, and in particular exosomes (FDR < 10^{-40}), in transporting signalling factors released by osteocytes. Functional enrichment of GOBP, GOMF and Pfam terms was also investigated, revealing significant roles for these proteins in mechanosensing and mechanosignaling, as evidenced by the most significantly enriched terms "response to stress" (FDR < 10^{-6}) and "protein complex binding" (FDR < 10^{-8}). The interaction network between identified proteins in the osteocyte secretome reveals a highly significant degree of protein-protein interaction ($p < 10^{-16}$) as illustrated in Figure S 3-1. Enrichment analyses was also conducted on proteins more abundantly expressed in control samples using Fisher's exact test (Figure S 3-3) and functional enrichments (Table S 3-2), revealing enrichment of muscle and cytoskeletal terms. These associations are likely due to the release into the medium of proteins from rat tail collagen type 1 used for coating glass slides.

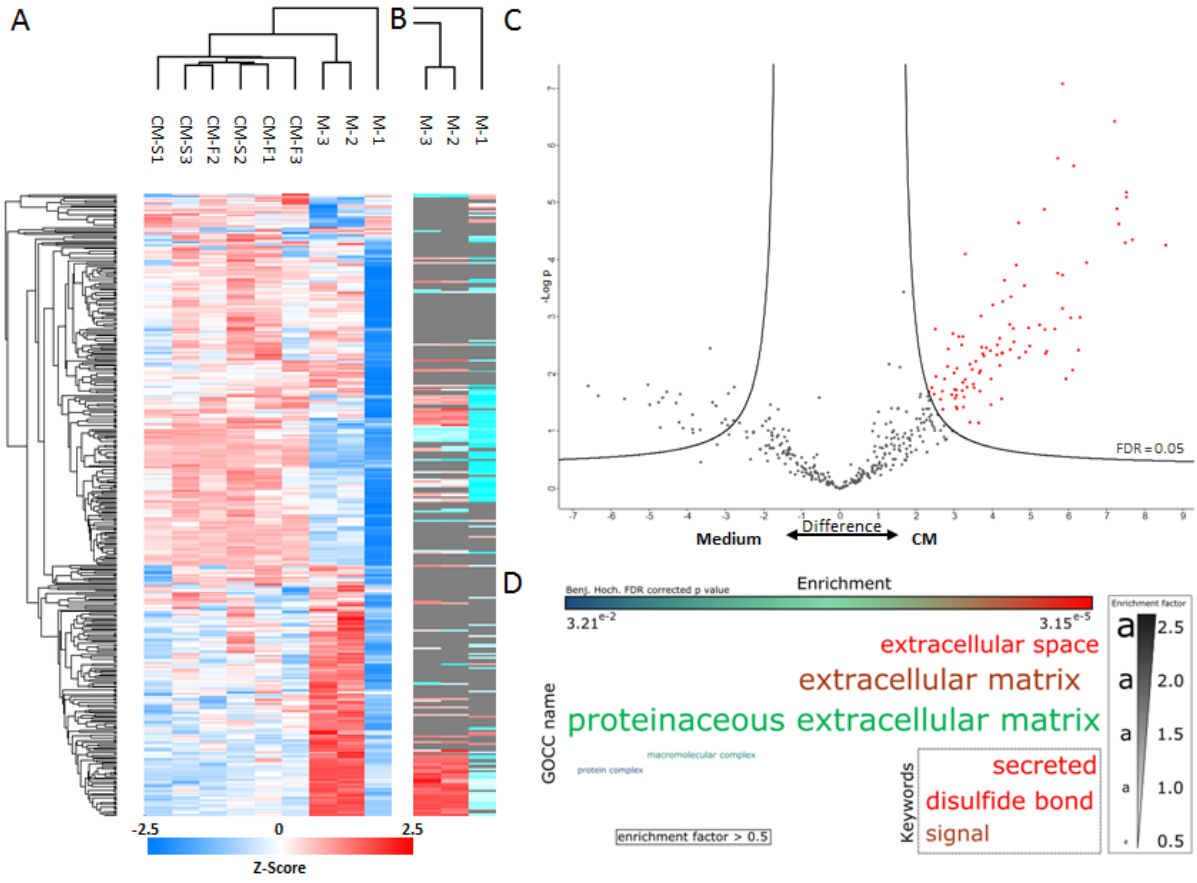

Figure 3-3 Hierarchical clustering of all samples with imputed data (A) and hierarchical clustering in the control samples without imputation of data (B). Volcano plot illustrating proteins significantly upregulated proteins marked in red in CM-S and CM-F groups compared to the control (C). Enrichment analysis of GOCC terms and Uniprot keywords in upregulated proteins using Fisher's exact test represented as a word cloud (D). The size of the word represents enrichment of terms, while colour represents FDR corrected p value. All terms with a minimum of 0.5 enrichment factor and 0.05 FDR corrected p value were included.

Table 3-1 Functional enrichments in CM proteins indicated in Figure 3C using String DB, with observed gene count out of a total of 105 genes and FDR cut-off of 2%. (note: 105 genes were identified from 97 proteins)

Pathway description	Observed gene count	False discovery rate (FDR)
GOCC		
extracellular exosome	71	1.72E-41
extracellular region part	76	5.05E-39
extracellular region	77	1.20E-35
membrane-bounded vesicle	70	2.07E-34
extracellular space	47	7.88E-32
extracellular matrix	26	9.57E-22
proteinaceous extracellular matrix	22	5.85E-18
cytoplasmic membrane-bounded vesicle	26	1.80E-12
cytoplasmic vesicle	24	9.53E-10

myelin sheath	12	9.48E-09
GOBP		
response to stress	36	6.92E-07
antigen processing and presentation of peptide antigen via MHC class I	6	4.09E-06
protein folding	10	8.52E-06
response to wounding	13	2.05E-05
regulation of biological process	63	5.41E-05
pyruvate metabolic process	6	1.73E-04
extracellular matrix organization	9	1.73E-04
biological regulation	63	1.99E-04
glycolytic process	5	2.85E-04
response to endogenous stimulus	19	2.85E-04
GOMF		
protein complex binding	20	7.80E-09
protein binding	52	7.85E-09
binding	73	5.31E-08
RNA binding	26	3.35E-07
poly(A) RNA binding	23	3.35E-07
isomerase activity	9	9.02E-06
macromolecular complex binding	21	1.05E-05
receptor binding	20	1.22E-05
calcium ion binding	15	1.22E-05
peptide binding	9	1.90E-05

3.3.4 Mechanical stimulation alters the protein release characteristics in osteocytes

Further analysis separating the CM-S and CM-F groups reveal the differential expression of proteins between statically cultured and mechanically stimulated osteocytes, highlighting the role of external mechanical forces in regulating the osteocyte secretome. The more stringent criteria of only considering proteins identified in all three biological replicates in at least one of the groups reduced the total number of proteins of interest to 317. A total of 34 proteins were identified with varying degrees of significance and differential expression between groups (Table 3-2), with 32 of these indicated on a volcano plot (Figure 3-4A), and a further 2 not present on the plot due to being present in only one of the CM groups. LFQ intensities of some of the most differentially expressed proteins with greater expression in CM-S (Figure 3-4B-D) and CM-F (Figure 3-4E-F) are

highlighted. Of note is the enrichment of 14-3-3 proteins, all of which are upregulated in CM-F (log2 fold change = 1.43 – 2.33). Also of particular interest are annexin A5 (log2 fold change = 2.39), which is associated with EVs and blood microparticles suggesting a role in systemic signalling, and histone H4 (log2 fold change = 2.00) which is associated with osteogenic growth peptide (OGP) and known to stimulate osteoblast activity (Bab *et al.*, 1992).

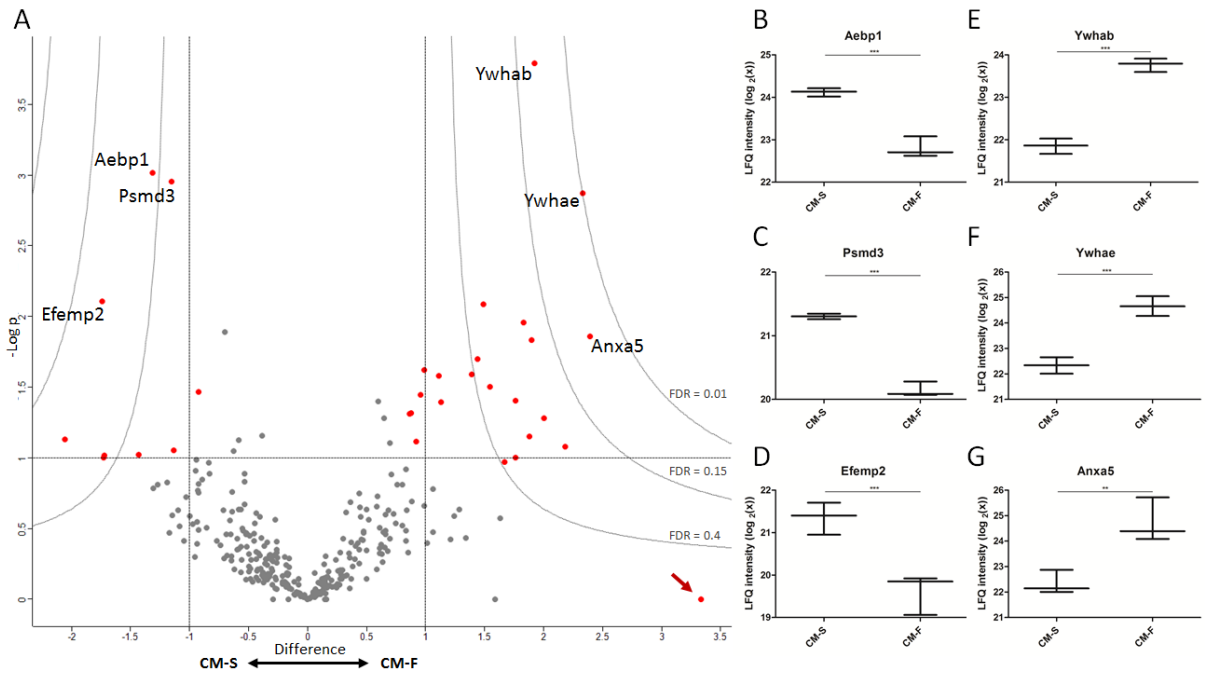

Figure 3-4 Volcano plot (A), illustrating upregulation with flow to the right and downregulation to the left. The y-axis displays the $-\log_{10}$ of p-value, where the horizontal line corresponding to a p-value of 0.1. Vertical lines indicate a $\log_2$ fold change of ±1. Curves illustrate indicated FDR values with S0 parameter set to 2. Whisker plots of three significantly upregulated proteins in the presence of fluid flow are indicated (B-D). The arrow indicates a protein which displays low significance due to being present in only one of the CM replicates.

Table 3-2 Differentially expressed proteins between CM-S and CM-F groups, where *p<0.1, **p<0.05, ***p<0.01 and + indicates proteins with only a single or no detection in CM-S group (top of table) and no detection in CM-F group (bottom of table) where p-value cannot be defined.

Gene Name	Protein	Mol. Weight [kDa]	Difference [Log_2 fold change]	p-value summary
Rpl8	60S ribosomal protein L8	28.024	0	+
Clic4	Chloride intracellular channel protein 4	28.729	3.328	+
Anxa5	Annexin A5	35.752	2.390	**
Ywhae	14-3-3 protein epsilon	29.174	2.327	***

Rps18	40S ribosomal protein S18	12.483	2.177	*
Hist2h4	Histone H4	11.367	2.001	*
Ywhab	14-3-3 protein beta/alpha	28.086	1.917	***
Ywhaz	14-3-3 protein zeta/delta	27.771	1.892	**
Dbi	Acyl-CoA-binding protein	10.000	1.878	*
Ywhag	14-3-3 protein gamma	28.302	1.827	**
Try10	MCG140784	26.221	1.762	**
Igf2	Insulin-like growth factor II	11.107	1.760	*
Hist1h2bk	Histone H2B	13.920	1.666	
Ptms	Parathymosin	11.430	1.541	**
Sh3bgrl3	SH3 domain-binding glutamic acid-rich-	10.477	1.489	***
Ywhaq	14-3-3 protein theta	32.221	1.434	**
Tmsb10	Thymosin beta-10	5.026	1.387	**
Erh	Enhancer of rudimentary homolog	12.259	1.126	**
Ftl1	Ferritin;Ferritin light chain 1;Ferritin	20.772	1.110	**
Inhba	Inhibin beta A chain	47.392	0.986	**
Myl12b	Myosin regulatory light chain 12B	19.895	0.954	**
Myl6	Myosin light polypeptide 6	16.930	0.918	*
Col1a2	Collagen alpha-2(I) chain	129.560	0.874	**
Cfl1	Cofilin-1	18.559	0.861	**
Gsn	Gelsolin	85.941	-0.925	**
Pgm1	Phosphoglucomutase-1	61.417	-1.135	*
Psmd3	26S proteasome non-ATPase regulatory	60.718	-1.158	***
Aebp1	Adipocyte enhancer-binding protein 1	128.360	-1.319	***
C1ra	Complement C1r-A subcomponent	80.072	-1.437	*
Thbs2	Thrombospondin-2	129.880	-1.723	*
Efemp1	EGF-containing fibulin-like extracellular	54.952	-1.732	*
Efemp2	EGF-containing fibulin-like extracellular	49.425	-1.743	***
Mdh2	Malate dehydrogenase, mitochondrial	35.611	-2.056	*
Npm1	Nucleophosmin	28.385	0	+

Subsequently, functional enrichment in differentially expressed proteins was investigated to help further elucidate their collective biological relevance in mechanically mediated osteocyte signalling (Table 3-3). The top four enriched GOCC terms; extracellular region, membrane-bounded vesicle, extracellular region part and extracellular exosome are associated with EV proteins with a highly significant false discovery rate (FDR < 10^{-10}) and 65 – 76% of all differentially expressed proteins being associated with these terms. This confirms that EVs are not only implicated in the osteocyte secretome as demonstrated above but are a key component of mechanically mediated signalling. Also of significant interest is the enrichment of the top two GOMF terms “calcium ion binding” (FDR < 0.01) and “phosphoserine binding” (FDR < 0.05), revealing the potential role of mechanically activated osteocyte EVs as sites of mineralisation via binding of calcium and phosphate components. A String DB network was constructed to further investigate any

potential interactions between proteins associated with EVs (Figure 3-5) revealing a significant degree of protein-protein interaction ($p < 10^{-3}$). Interestingly, there are several interactions between positively and negatively regulated proteins, including an interaction path between Anxa5 and Ywhab/Ywhae which are associated with calcium ion binding and phosphoserine binding respectively. Between these nodes are gelsolin and cofilin, the former of which is calcium sensitive and both of which have been shown to regulate changes in the actin cytoskeleton (Southwick, 2000), as well as being previously identified in vesicles from mineralising osteoblasts (Thouverey *et al.*, 2011).

Table 3-3 Functional enrichments in network using String DB with observed gene count out of a total of 34 genes and FDR cut-off of 2%.

Pathway description	Observed gene count	False discovery rate (FDR)	Associated proteins in network
GOCC			
extracellular region	26	1.16E-11	Aebp1,Anxa5,C1ra,Cfl1,Clic4,Col1a2,Dbi,Efemp1,Efemp2,Ftl1, Gsn,Hist1h2bk,Hist2h4,Igf2,Inhba,Mdh2,Myl12b,Myl6,Pgm1, Psmd3,Sh3bgrl3,Thbs2,Ywhab,Ywhae,Ywhag,Ywhaz
membrane-bounded vesicle	24	1.16E-11	Aebp1,Anxa5,C1ra,Cfl1,Clic4,Col1a2,Dbi,Efemp1,Efemp2,Ftl1, Gsn,Hist2h4,Igf2,Mdh2,Myl12b,Myl6,Pgm1,Psmd3,Sh3bgrl3, Thbs2,Ywhab,Ywhae,Ywhag,Ywhaz
extracellular region part	25	1.16E-11	Aebp1,Anxa5,C1ra,Cfl1,Clic4,Col1a2,Dbi,Efemp1,Efemp2,Gsn, Hist1h2bk,Hist2h4,Igf2,Inhba,Mdh2,Myl12b,Myl6,Pgm1,Psmd3,Sh3bgrl3,Thbs2,Ywhab,Ywhae,Ywhag,Ywhaz
extracellular exosome	22	1.16E-11	Aebp1,Anxa5,C1ra,Cfl1,Clic4,Col1a2,Dbi,Efemp1,Efemp2,Gsn, Hist2h4,Igf2,Mdh2,Myl12b,Myl6,Pgm1,Psmd3,Sh3bgrl3,Ywhab,Ywhae,Ywhag,Ywhaz
focal adhesion	9	2.88E-07	Anxa5,Cfl1,Gsn,Npm1,Rpl8,Ywhab,Ywhae,Ywhag,Ywhaz
extracellular space	12	3.20E-06	Aebp1,Anxa5,C1ra,Cfl1,Col1a2,Dbi,Efemp1,Gsn,Hist1h2bk,Igf2, Inhba,Ywhaz
cytosol	13	2.65E-05	Cfl1,Clic4,Gsn,Npm1,Pgm1,Ptms,Rpl8,Rps18,Ywhab,Ywhae, Ywhag,Ywhaq,Ywhaz
cytoplasmic vesicle part	7	1.04E-04	Clic4,Ftl1,Ywhab,Ywhae,Ywhag,Ywhaq,Ywhaz
cytoplasmic membrane-bounded vesicle	9	3.24E-04	Clic4,Dbi,Ftl1,Thbs2,Ywhab,Ywhae,Ywhag,Ywhaq,Ywhaz
cytoplasmic vesicle membrane	6	5.14E-04	Clic4,Ywhab,Ywhae,Ywhag,Ywhaq,Ywhaz
blood microparticle	4	6.77E-04	Anxa5,C1ra,Gsn,Ywhaz
cell junction	9	1.06E-03	Cfl1,Clic4,Gsn,Npm1,Rpl8,Ywhab,Ywhae,Ywhag,Ywhaz
macromolecular complex	16	4.47E-03	Clic4,Col1a2,Ftl1,Gsn,Hist1h2bk,Hist2h4,Inhba,Myl12b,Myl6, Npm1,Psmd3,Rps18,Ywhab,Ywhae,Ywhaq,Ywhaz
extracellular matrix	5	1.21E-02	Aebp1,Col1a2,Efemp1,Efemp2,Thbs2
protein complex	14	1.21E-02	Clic4,Col1a2,Ftl1,Gsn,Hist1h2bk,Hist2h4,Inhba,Myl12b,Myl6, Psmd3,Ywhab,Ywhae,Ywhaq,Ywhaz
GOBP			
regulation of biological quality	14	1.60E-02	Anxa5,Cfl1,Clic4,Col1a2,Dbi,Ftl1,Inhba,Myl12b,Thbs2,Tmsb10, Ywhab,Ywhae,Ywhag,Ywhaz

GOMF			
calcium ion binding	8	4.03E-03	Anxa5,C1ra,Efemp1,Efemp2,Gsn,Myl12b,Myl6,Thbs2
phosphoserine binding	2	2.65E-02	Ywhab,Ywhae
rRNA binding	3	4.06E-02	Npm1,Rpl8,Rps18
protein domain specific binding	6	4.06E-02	Gsn,Ywhab,Ywhae,Ywhag,Ywhaq,Ywhaz
Pfam			
14-3-3 protein	4	5.84E-08	Ywhab,Ywhae,Ywhag,Ywhaq

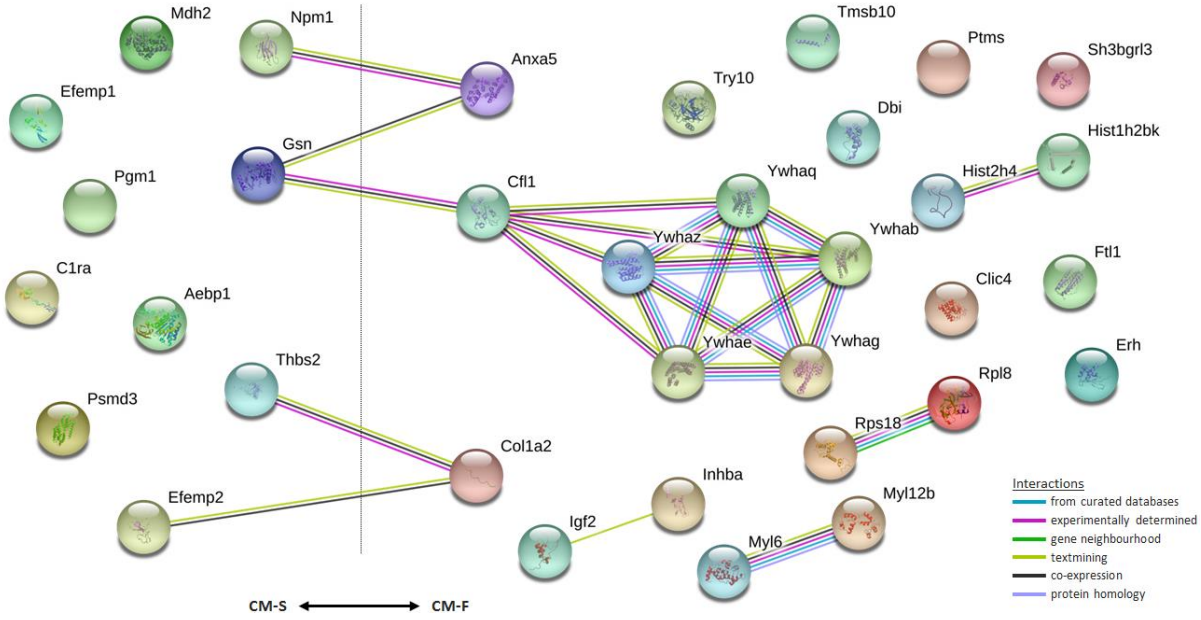

Figure 3-5 String DB network illustrating interactions between mechanically regulated proteins, with significant degree of protein-protein interaction ($p < 10^{-3}$).

3.3.5 EVs are present within the osteocyte secretome and EV morphology and size distribution is not altered by mechanical stimulation

Given the identification of EV-associated proteins within the osteocyte secretome, it was next investigated whether osteocytes release EVs in culture and whether EV characteristics were altered following mechanical stimulation. EVs were isolated from osteocyte CM using ultracentrifugation and the presence of EVs was confirmed by TEM imaging and immunoblotting. TEM imaging confirmed the presence of EVs of typical morphology and size (Figure 3-6A-B). The presence of EVs was further confirmed via

immunoblotting, with no detection of negative marker GRP-94, and detection of positive markers TSG101 and ALIX (Figure 3-6C). EV concentration was not significantly different between EVs isolated from the CM-S (EV-S) and EVs isolated from the CM-F (EV-F), both being within the range of 0.8 – 2.6 μg/ml, and with average values of 1.2 μg/ml and 1.5 μg/ml respectively (Figure 3-6D). It can be seen that there is a slight change in particle size distributions between EV-S and EV-F (Figure 3-6E), however, no changes in average particle size was detected, with values of 177 nm and 183 nm respectively (Figure 3-6F).

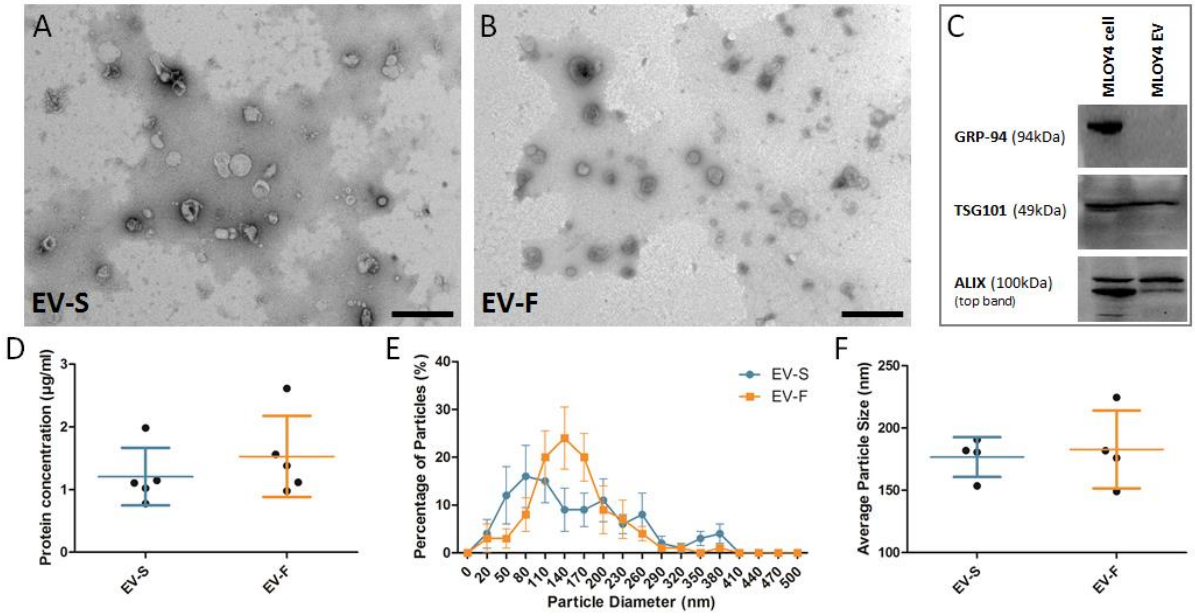

Figure 3-6 Characterisation of EVs. TEM image of EVs isolated from osteocyte CM-S (A) and CM-F (B) (Scale = 500nm). Immunoblots confirmed the presence of EVs via negative marker GRP-94 and positive markers TSG101 and ALIX (C). Protein concentration of EVs in conditioned medium groups (n=5) (D). Nanoparticle size analysis on EVs confirmed no significant difference in distribution (E) or average size (F) between groups (n=4).

3.3.6 Osteocytes regulate human MSC recruitment and osteogenesis in response to fluid flow shear via MAEVs

To determine whether mouse osteocyte derived EVs could be up taken by human MSCs, EVs were labelled with PKH26. Following 24 hr treatment, PHK26 labelled EVs were preferentially located within the cell as identified by the actin cytoskeleton, indicating uptake of EVs by human MSCs (Figure 3-7A). Control samples with no EVs are shown in

Figure S 3-4. A high density of EVs can be seen around the nuclear region in particular with minimal detection within the nuclear region itself.

Upon verifying EV uptake, further work was conducted on investigating the cellular response of hMSCs subjected to EV treatment isolated from static and mechanically stimulated osteocyte conditioned media. hMSCs were treated with EV-S and EV-F to investigate recruitment and osteogenic gene expression as previously demonstrated with CM. EV-S resulted in a slight non-significant increase in MSC recruitment (Figure 3-7B), while this response was significantly enhanced with EV-F, yielding a 3.7 fold increase compared to medium ($p < 0.001$, $n = 9$) and 2.3 fold increase compared to EV-S ($p < 0.01$, $n = 9$), a trend which closely mirrors that seen with conditioned media. Osteogenic gene expression was investigated (Figure 3-7C), with a consistent trend of marginally increased expression with CM-S treatment, which was further enhanced with CM-F. There was a near-significant increase of 1.5 in OPN ($p = 0.051$, $n = 17\text{-}18$) when comparing CM-S to medium. CM-F resulted in significant fold changes compared to medium of 2.0 in COX2 ($p < 0.05$, $n = 17\text{-}18$), 1.8 in OCN ($p < 0.05$, $n = 14\text{-}15$), 2.0 in OPN ($p < 0.001$, $n = 16\text{-}18$) and 1.5 in RUNX2 ($p < 0.05$, $n = 20$), with a near-significant increase of 2.6 in OSX ($p = 0.07$, $n = 21\text{-}23$). In addition, near-significant increases in OCN and OPN were detected comparing EV-F and EV-S. Moreover, orthology searches using the basic local alignment search tool BLAST (Altschul *et al.*, 1997) were performed for the human gene sequences (COX2, OCN, OPN, RUNX2, OSX) in the murine genome (version: Mus musculus GRCm38.p4). The bioinformatic tool, in silico PCR (UCSC Genome Browser), was used to confirm the lack of amplification of the human primer sequences in the murine genome (Kent *et al.*, 2002), confirming that amplified genes are human, and not due to possible transfer of murine mRNA from the MLO-Y4 cell line. In summary, there is a trend of increasing osteogenesis with EV-S treatment, however, this affect becomes significantly greater with EV-F treatment revealing a similar trend to that seen with CM and

demonstrates that MAEVs secreted by osteocytes are key drivers of stem cell recruitment and osteogenesis.

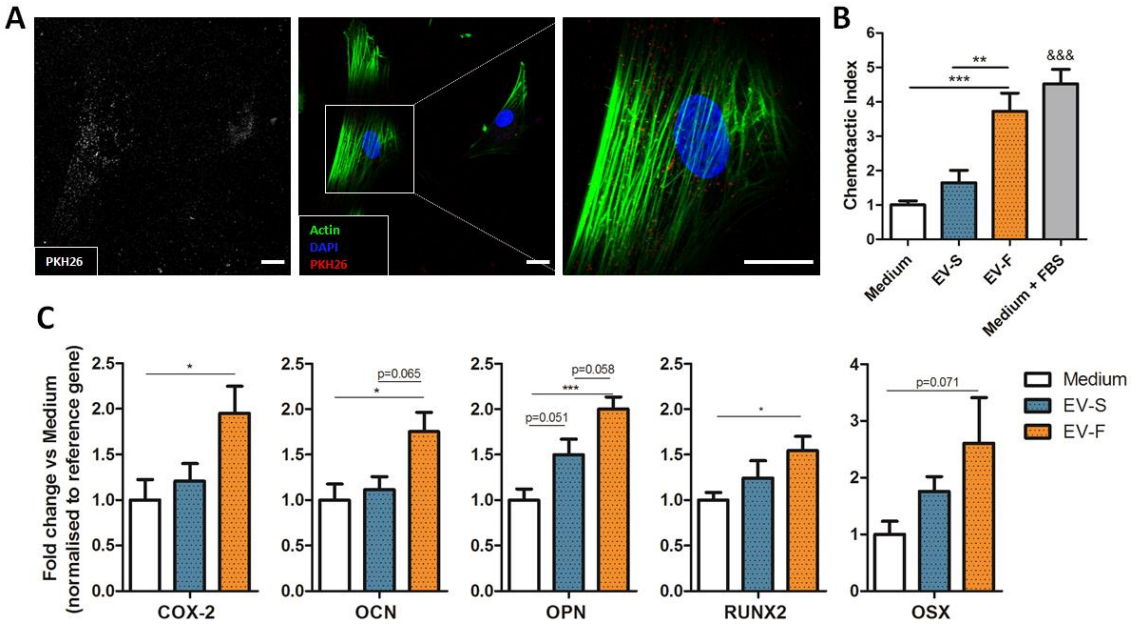

Figure 3-7 Immunofluorescent images illustrating osteocyte EV uptake by MSCs, as demonstrated by localisation of PKH26 labelled EVs within the cell body (Scale = 10µm) (A). Migration of MSCs towards EVs isolated from osteocyte conditioned medium and normalised to Medium, showing significant increases in chemotactic index towards CM-F medium when compared to CM-S (B). qPCR analysis of COX-2, OCN, OPN, RUNX2 and OSX expression in MSCs treated with EVs from osteocyte medium from CM-S and CM-F (C). Statistical analysis using using one-way ANOVA and Bonferroni's multiple comparison post-test (*p<0.05, **p < 0.01, ***p < 0.001, &&& p < 0.001 vs Medium and EV-S).

3.4 Discussion

Osteocytes are mechanosensitive cells which play a fundamental role in coordinating loading-induced bone formation via the secretion of paracrine factors which drive effector cell behaviour. One of the most important of these cells are MSCs, which are responsible for replenishing the bone forming osteoblast population. However, the exact mechanisms by which osteocytes relay mechanical signals to these cells are poorly understood. A greater understanding of these mechanisms would thus have profound implications for the development of therapies to treat the wide range of diseases with which the osteocyte has been linked, one of the most devastating of which is osteoporosis.

Therefore, this study aimed to demonstrate the potency of the mechanically stimulated osteocyte secretome in driving human MSC behaviour, and fully characterise its contents with the aim of identifying the key secreted factors regulating bone mechanobiology. Herein, it was demonstrated that osteocytes subjected to oscillatory fluid shear secrete factors that significantly enhance hMSC recruitment and osteogenesis. To uncover the osteocyte derived secreted factors which drive hMSC behaviour, a proteomic analysis of the osteocyte secretome was performed to uncover a complete map of proteins which are released both under static conditions and following mechanical stimulation. Over 300 proteins comprising the osteocyte secretome were identified with 34 proteins differentially expressed following mechanical stimulation. The osteocyte secretome was significantly enriched with proteins associated with EVs and exosomes indicating a role for secreted vesicles in mediated mechanically driven osteocyte-MSC communication. EVs were subsequently isolated from the mechanical activated osteocyte secretome, characterised, and found to elicit identical trends in MSC recruitment and osteogenesis to that seen with conditioned media, demonstrated a key role for osteocyte EVs in mediating hMSC behaviour.

Mechanically stimulated osteocytes secrete paracrine factors that recruit human MSCs and enhance osteogenesis. The ability of mechanically stimulated osteocytes to influence stem cell behaviour is in agreement with previous findings *in vivo* where mechanical loading of bone results in the recruitment and osteogenic differentiation of endogenous (Turner, Owan, Alvey, Hulman, & Hock, 1998) or transplanted exogenous osteoprogenitors (J. C. Chen, Hoey, Chua, Bellon, & Jacobs, 2016b). Furthermore a similar trend in recruitment has been shown in murine MSCs where a 128% increase in stem cell recruitment was observed following exposure to conditioned media collected from osteocytes cultured on a rocking platform (Brady *et al.*, 2015). Interestingly in the same study, mechanically activated osteocyte conditioned media was also been shown to induce

osteogenesis of MSCs as demonstrated by upregulation of Opn and Cox-2 gene expression and enhanced mineral deposition (Brady *et al.*, 2015; Hoey *et al.*, 2011). Herein, a comparable increase in COX-2 and OPN expression in human MSCs, as well as increases in OCN, OSX and RUNX2, were demonstrated. These findings, along with other previous work investigating the effect of the osteocyte secretome on osteoblast proliferation, migration and osteogenesis (Taylor *et al.*, 2007; Vezeridis *et al.*, 2006), further reinforce the importance of the osteocyte secretome and its contents in the indirect biophysical regulation of MSCs and loading-induced bone formation (P. M. Govey *et al.*, 2013; M. B. Schaffler, Cheung, Majeska, & Kennedy, 2014b).

To determine the mechanisms by which osteocytes coordinate stem cell recruitment and osteogenesis in response to loading, for the first time, a complete a map of the osteocyte secretome was identified via a mass spectrometry based proteomic analysis. Unsurprisingly, proteins in osteocyte CM revealed significant enrichment of several "extracellular" containing GOCC terms, validating the successful isolation of secreted proteins. Further bioinformatics investigation of these proteins revealed roles in protein, receptor and calcium ion binding, illustrating evidence for their mechanosignalling capacity. Interestingly, a number of key proteins, such as Sclerostin that is known to be secreted by osteocytes were not detected. Sclerostin secretion is downregulated following mechanical stimulation, reducing it suppression of osteogenic Wnt signalling in osteoprogenitors (P. M. Govey *et al.*, 2013). This may be due to the limitation of the MLO-Y4 osteocyte cell line, but given the pro-osteogenic effect of this mechanically activated osteocyte secretome, this opens up the possibility of identifying other novel factors regulating MSC behaviour. Despite this, several proteins from a previous proteomic analysis on osteocyte lysates have been identified (P. M. Govey *et al.*, 2014), including two proteins in particular which were previously highlighted: S100-A6 (Calcyclin) and NME2 (Nucleoside diphosphate kinase B), revealing potential roles for these proteins in cell

signalling. Further analysis sought to investigate the role of mechanical forces on the contents of the osteocyte secretome, with differential expression of a range of proteins being identified compared to statically cultured cells. One Pfam group of particular interest which are significantly enriched with fluid shear are the 14-3-3 proteins. These proteins belong to a family of seven regulatory protein isoforms present in almost all mammalian tissues, with many being modified by environmental signals via kinases and phosphatases and more than 50 signalling proteins being identified as 14-3-3- ligands (Fu, Subramanian, & Masters, 2000). One study reports that 14-3-3 beta has a negative effect on osteogenesis, with downregulation in calvaria organ cultures resulting in increased bone formation (Y. Liu, Ross, Bodine, & Billiard, 2007). 14-3-3 epsilon is released by osteoblasts/osteocytes in response to dynamic compression, inducing the release of catabolic factors in chondrocytes in a dose dependant manner, mimicking the effect of compression (Priam *et al.*, 2013). Interestingly, TAZ, a known mechanosensor and transcriptional modulator, has also been linked to 14-3-3 proteins, with decreased binding being shown to result in increased TAZ nuclear localisation (Rodan & Rodan, 2005), further indicating a role for 14-3-3 proteins in mechanically mediated signalling in bone. Other proteins of particular interest are histone H4 and annexin A5. The acetylation of histone H4 has been shown to promote the induction of osteocalcin gene expression in osteoblasts (Shen *et al.*, 2003), with histone deacetylase inhibition being shown to promote osteoblast differentiation (Dudakovic *et al.*, 2013) and increase mineralisation (Paino *et al.*, 2014). More specifically, the C-terminus of histone H4, termed osteogenic growth peptide (OGP), a circulating stimulator of osteoblast activity (Bab *et al.*, 1992), plays key roles in regulating the behaviour of bone residing cells, such as stimulating proliferation, phosphatase activity and mineralisation of osteoblasts and proliferation and osteogenic differentiation of MSCs (Pigossi, Medeiros, Saska, Cirelli, & Scarel-Caminaga, 2016). Annexin A5 has been shown to increase at the cell membrane in osteoblasts under fluid flow, with Ca^{2+} ion levels also being seen to

increase. It was found that the disruption of annexin A5 inhibited Ca^{2+} levels, implicating its role in calcium signalling (Haut Donahue, Genetos, Jacobs, Donahue, & Yellowley, 2004), with its knockdown in osteoblasts impairing proliferation, ALP expression and Runx2 expression (Genetos, Wong, Weber, Karin, & Yellowley, 2014). One downregulated protein of interest is thrombospondin 2. The knockdown of this protein in mice increases angiogenesis (Bornstein, Kyriakides, Yang, Armstrong, & Birk, 2000) with endosteal bone formation being shown in another study to increase as a result of increased bone marrow derived osteoprogenitors (Hankenson *et al.*, 2000). Thrombospondin 2 null mice have also demonstrated enhanced callus bone formation, vascularity and MSC proliferation following tibial fracture (Miedel *et al.*, 2013). A list of proteins released by the osteocyte have been identified, many of which are mechanically regulated, and have been linked to bone physiology. This therefore represents a database of proteins to help better understand the osteocyte coordination of bone anabolism and catabolism and provides a list of potential therapeutic targets to mimic this behaviour.

Functional enrichment analysis of the osteocyte secretome revealed a strong association with ‘extracellular exosome’ and ‘membrane bound vesicles’ with 66% of secreted proteins being linked to these cellular organelles. Moreover, in response to mechanical stimulation, 70% of the mechanically regulated proteins were associated with EVs. EVs were successfully isolated from osteocyte conditioned media and interestingly no changes in EV morphology or quantity between static and dynamic groups were detected, in contrast with previous work which has demonstrated an upregulation in EV number following fluid shear stimulation (Morrell *et al.*, 2018). In the present study, an almost identical trend in stem cell recruitment with CM and EVs, both of which are enhanced following fluid shear, provides evidence for the key role of osteocyte derived EVs in mediating this response. Similarly, the almost identical trends in MSC osteogenic gene expression treated with CM and EVs further provide evidence for the role of MAEVs in

facilitating cell-cell communication in bone. Given the similar concentrations of EVs between groups, it is expected that this pro-osteogenic effect is a result of EV content changing in response to mechanical stimulation. Many of the proteins identified in this paper have also been identified in a proteomic analysis of osteoblast released EVs (J. Morhayim *et al.*, 2015; Thouverey *et al.*, 2011). A previous *in vivo* study has suggested a role for EVs in systemic signalling, demonstrating altered miRNA expression in EVs isolated from the plasma of osteocyte ablated mice and wild-type mice (Mari Sato *et al.*, 2017), while other studies have demonstrated the potential for EVs in therapeutics to enhance osteogenic gene expression (C.-C. Huang *et al.*, 2016), the use of drug loaded EVs for osteoporosis therapies (Cappariello *et al.*, 2017), and the use of EVs for functionalisation of TE scaffolds to enhance bone regeneration (Diomede *et al.*, 2018; H. Xie *et al.*, 2017b). In addition to osteocyte derived MAEVs and the contents driving MSC osteogenesis, MAEVs may also act as sites for mineral nucleation, as has previously been demonstrated in osteoblast EVs (Davies *et al.*, 2017a; Golub, 2009). Of particular interest in this regard is the enrichment of calcium ion binding (such as annexin A5) and phosphoserine binding (such as 14-3-3 proteins Ywhae and Ywhab) proteins in osteocyte MAEVs, which have been shown to be linked in a protein interaction network. Annexin A5 is linked to the calcium sensitive protein gelsolin (Southwick, 2000), which in turn is linked to the 14-3-3 proteins via the phosphate regulating cofilin (Muhlrad, Pavlov, Peyser, & Reisler, 2006), both of which regulate changes in the actin cytoskeleton (Southwick, 2000). In addition to the known role of calcium ions in mineralisation, negatively charged amino acids such as phosphoserine are also known to play a key role in hydroxyapatite nucleation and growth (Tavafoghi & Cerruti, 2016). Therefore osteocyte EVs may promote mineralisation via delivery of calcium and phosphate interacting proteins through interaction with gelsolin and cofilin respectively. Taken together, it has been revealed that MAEVs are a key mechanism by which osteocytes communicate chemotactic and

osteogenic signals to osteoprogenitors in response to loading, highlighting these osteocyte derived MAEVs as a potential cell free therapy to mimic the beneficial effect of loading and enhance bone formation.

3.5 Conclusion

In summary this study presents evidence that the mechanically stimulated osteocyte secretes factors which coordinates MSC recruitment and osteogenesis demonstrating a mechanism required for loading-induced bone formation. Importantly, for the first time, the osteocyte protein secretome has been mapped, and how it is altered in response to mechanical stimulation has been determined, generating a database of potential factors mediating this mechanism. Lastly, this study also demonstrates the presence and fundamental role of MAEVs released by osteocytes in coordinating MSC recruitment and osteogenesis, identifying a novel mechanism by which osteocytes coordinate bone mechanobiology. Moreover, these pro-osteogenic osteocyte derived MAEVs represent a potential cell-free therapy to enhance bone regeneration and repair in diseases such as osteoporosis.

Chapter 4

Design and build of a melt electrowriting printer

4.1 Introduction

MEW is a recently developed technology, first described by Brown *et al.* in 2011, combining elements of melt electrospinning and 3D printing (Brown *et al.*, 2011). It is unique in its ability to generate ECM like fibres and control their deposition. It is thus an extremely powerful biofabrication tool, with recent studies exploring the use of MEW constructs for a range of biomedical applications, including scaffolds for skin (Farrugia BL, 2013), cartilage (Bas, De-Juan-Pardo, *et al.*, 2017; Bas *et al.*, 2018), bone (Baldwin *et al.*, 2017; Hanßke *et al.*, 2017; Muerza-Cascante *et al.*, 2016), cardiac (M. Castilho *et al.*, 2017; Miguel Castilho, Mil, *et al.*, 2018) and connective tissue applications (Hochleitner, Chen, *et al.*, 2018), as well as models for tumour metastasis (Holzapfel *et al.*, 2014; Thibaudeau *et al.*, 2014; Wagner *et al.*, 2016) and platforms for cancer immunotherapy (Delalat *et al.*, 2017). This technology is still in its infancy, with research groups traditionally building custom MEW printers and only three companies with commercially available options to date; RegenHU (Switzerland), Spraybase (Ireland) and GeSIM (Germany) (Paul D. Dalton, 2017).

Custom building a MEW apparatus is a lower cost option, and also bears the considerable advantage of allowing the user to develop an optimised system to achieve their specific requirements, with several advanced features such as dynamic pressure/voltage control and fibre collection on a rotating mandrel currently unavailable on commercial options. There are several key components for a MEW printer, including a heating system to melt the polymer, a method by which to safely introduce a high potential difference

between the depositing polymer and the collector, a means by which to control polymer flow, and a programmable collector to spatially control deposition of fibres. Several auxiliary features are also desirable, such as a safety enclosure and high magnification camera to monitor the process. There are key considerations for each of these components which must be understood to successfully implement a custom MEW printer.

Heating the polymer while maintaining a high potential difference is one of the main challenges when designing a MEW printer, with electrical interference and arcing likely to occur between the heating element and high voltage electrode at the needle if they are not adequately isolated from one another. Early MEW printers used circulating water jackets around a syringe to melt the polymer thus overcoming these issues (Brown *et al.*, 2011; Brown *et al.*, 2012; Farrugia BL, 2013). One limitation of this approach is the limited maximum temperature achievable, which may be an issue if processing of high melt temperature polymers is required, however circulating oil heaters may be used to overcome this (He *et al.*, 2016). A hot air gun has also been used (F. Tourlomousis, Babakhanov, Ding, & Chang, 2015), allowing greater melt temperatures to be achieved. Electrical heating elements have also extensively been used with more complex systems utilising separate heating systems for the syringe and needle, which may be isolated from the high voltage source via insulating tape (F. M. Wunner *et al.*, 2017). All manufacturers of commercially available MEW printers follow a different strategy of applying the high voltage source to the collector and grounding the needle, thus allowing the syringe to be heated as desired without encountering any difficulties with electrical interference. This approach however results in diminished charge available to maintain an electrospinning jet, and requires increased voltage to be used in order to achieve sufficient drawing force as the polymer must be charged from the collector across an air gap (Brown *et al.*, 2016).

Another important consideration is the polymer extrusion system, which must allow for extremely low and steady flow rates. Many designs have used syringe pumps to achieve

this (Bas *et al.*, 2015; Brown *et al.*, 2011; He *et al.*, 2016; Muerza-Cascante *et al.*, 2016), which allow for extremely low flow rates on the order of magnitude of μL/hr to be achieved. Many of the more recent publications report the use of air (Bas, D'Angella, *et al.*, 2017; M. Castilho *et al.*, 2017; Hochleitner *et al.*, 2016; Hrynevich *et al.*, 2018; F. M. Wunner *et al.*, 2017) or nitrogen (F. Chen, Hochleitner, *et al.*, 2016; de Ruijter *et al.*, 2017; Haigh *et al.*, 2017; Hochleitner *et al.*, 2014) pressure to extrude the polymer. This approach results in a more continuous extrusion force compared to the stepper motors typically used in syringe pumps. Finally, the collector design is also of key consideration, and must be capable of both achieving sufficient velocities to draw straight fibres for a range of fibre diameters, while also having a resolution and accuracy great enough for precise and repeatable deposition.

In the following chapter, the development process of a custom MEW printer for biofabrication applications will be outlined. The core of the design consists of a heated air assembly to safely control polymer temperature while overcoming an interference issues with the high voltage power supply. Other aspects of the design process will also be outlined, including development of the extrusion system, controlled deposition system, and safety components. Finally, the optimisation process to allow for precise scaffold fabrication will be outlined.

4.2 Materials and methods

4.2.1 Transient heat transfer analysis

In order to overcome limitations with solvent contamination during electrospinning for biological applications, an alternative approach is to melt the polymer. This is particularly important when collecting electrospun fibres over a short distance, where there is insufficient time for solvent evaporation. To investigate the feasibility of using air to heat and maintain polymers at elevated temperatures, a numerical heat transfer analysis was

conducted on the proposed system, using polycaprolactone (PCL) as the polymer of interest. First, the Biot number was calculated as the ratio of the heat transfer resistances inside of and at the surface of the body as follows:

$$Biot\ number = \frac{convective\ heat\ transfer}{conductive\ heat\ transfer} = \frac{hr_0}{k} \quad (1)$$

Where h is the heat transfer co-efficient, r_o is the characteristic length (in this case, the cylinder being heated), and k is the thermal conductivity. In the case of a low Biot number less than 0.1, conductive heat transfer significantly dominates and a simplified lumped system analysis can be conducted. However, in cases where convective heat transfer dominates with Biot numbers greater than 0.1, as is likely the case with a volume of PCL with relatively poor thermal conductivity, a transient heat analysis must be undertaken. To determine the transient thermal behaviour in a short cylinder which is representative of a volume of PCL being heated within a syringe, the analysis is done first on a wall of height L, and then on an infinite cylinder of radius r. A transformation is then conducted to determine the transient temperature behaviour in the cylinder of interest.

First the inverse Biot number for the centre of the wall is calculated as follows:

$$\frac{1}{Bi} = \frac{k}{hl} \quad (2)$$

Where l is half the length of the wall (Figure 4-1). The Fourier number is then calculated as follows:

$$\tau = \frac{\alpha t}{l^2} \quad (3)$$

Where α is the thermal diffusivity, and t is the time. Then using a Heisler chart for the two resulting values, the dimensionless temperature at the mid plane can be determined with the following notation:

$$\theta_{wall}(0,t) = \frac{T(0,t) - T_\infty}{T_i - T_\infty} \tag{4}$$

Where T(0,t) is the resulting temperature after time t, T_i is the initial temperature, and T_∞ is ambient temperature used to heat the material.

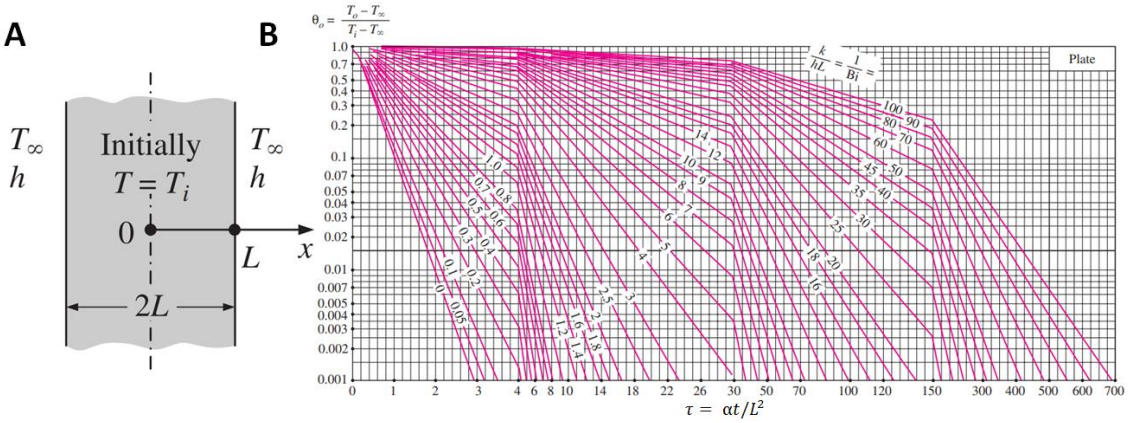

Figure 4-1 Notation for transient analysis in a plate (A). Heisler chart for calculating mid-point temperature in a plate (B). (Cengel, 2002) (from M. P. Heisler).

Next, the inverse Biot number for the centre of an infinite cylinder is calculated:

$$\frac{1}{Bi} = \frac{k}{hr} \tag{5}$$

Where r is the radius of the cylinder (Figure 4-2). The Fourier number is also calculated as follows:

$$\tau = \frac{\alpha t}{r^2} \tag{6}$$

With the dimensionless temperature at the centre of the infinite cylinder being determined using a Heisler chart with the following notation:

$$\theta_{\substack{infinite \\ cylinder}}(0,t) = \frac{T(0,t) - T_\infty}{T_i - T_\infty} \tag{7}$$

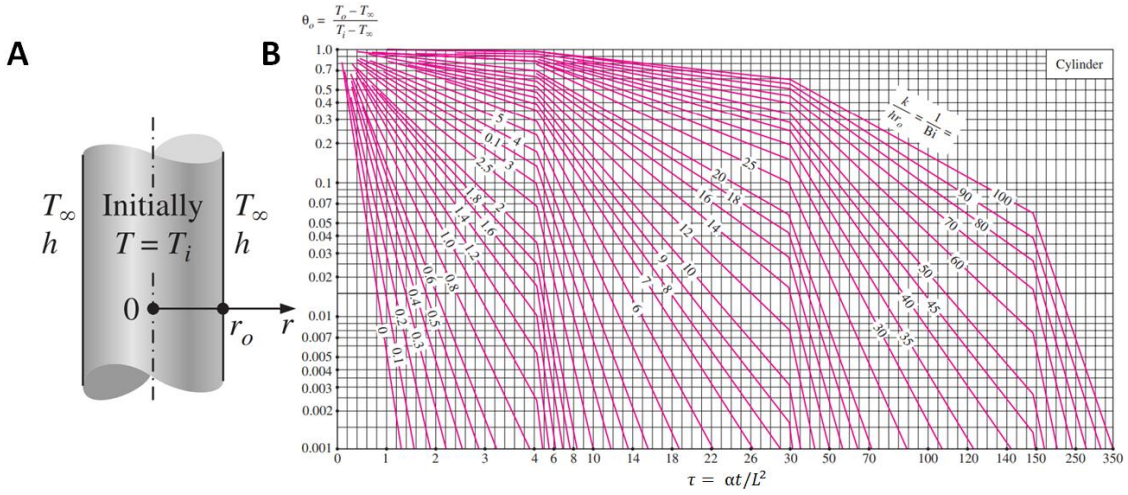

Figure 4-2 Notation for transient analysis in an infinite cylinder (A). Heisler chart for calculating centerline temperature in an infinite cylinder (B). (Cengel, 2002) (from M. P. Heisler).

The dimensionless temperature in the centre of the short cylinder can then be determined as follows (Figure 4-2A):

$$\left(\frac{T(0,t)-T_\infty}{T_i-T_\infty}\right)_{\substack{short\\cylinder}} = \theta_{wall}(0,t) \times \theta_{\substack{infinite\\cylinder}}(0,t) \tag{8}$$

The temperature in the centre of the cylinder is then calculated:

$$T(0,0,t) = T_\infty + \left(\frac{T(0,t)-T_\infty}{T_i-T_\infty}\right)_{\substack{short\\cylinder}} \times (T_i - T_\infty) \tag{9}$$

To determine the temperature at a given point x in the volume of interest, the ratio of the transformation over L is first calculated:

$$\frac{x}{L} \tag{10}$$

While the inverse Biot number is also calculated at this point:

$$\frac{1}{Bi} = \frac{k}{hl} \tag{11}$$

The dimensionless temperature at the point x of a plane wall is determined from the temperature distribution Heisler chart with notation as follows (Figure 4-3B):

$$\frac{T(L,t)-T_\infty}{T_i-T_\infty} \tag{12}$$

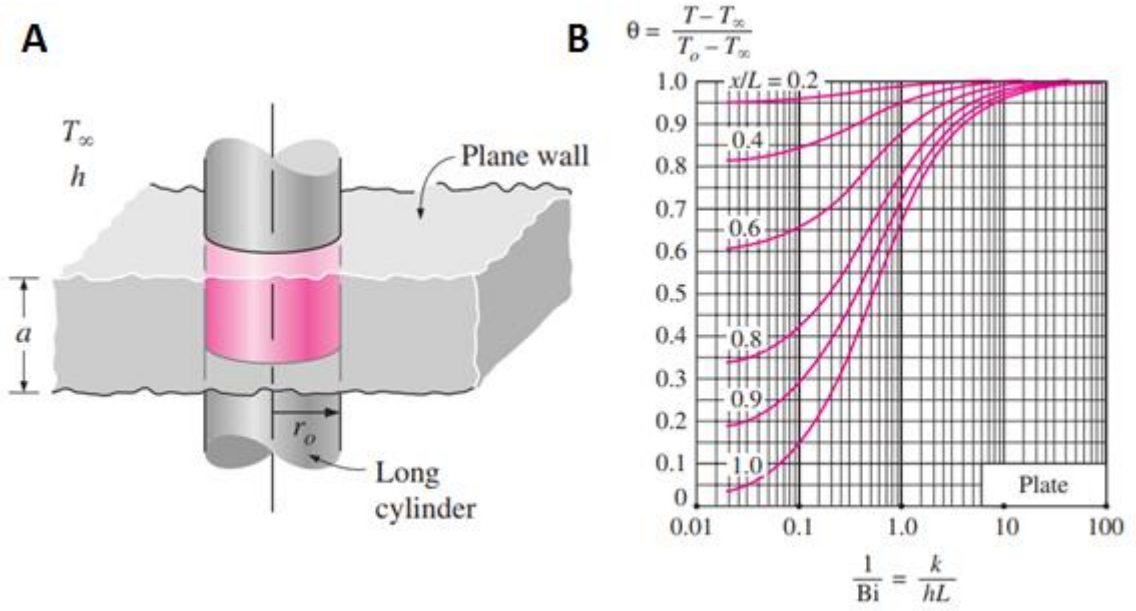

Figure 4-3 Performing transient analysis on a short cylinder, using previous analyses for plane wall and infinite cylinder (A). Temperature distribution in a plate (B). (Cengel, 2002) (from M. P. Heisler).

And by substituting the above value into the following formula:

$$\theta_{\substack{wall\\point}}(L,t) = \left(\frac{T(L,t)-T_\infty}{T_i-T_\infty}\right) \times \theta_{wall}(0,t) \tag{13}$$

The dimensionless temperature at the point of interest may then be calculated:

$$\left(\frac{T(L,0,t)-T_\infty}{T_i-T_\infty}\right)_{\substack{short\\cylinder}} = \theta_{\substack{wall\\point}}(L,t) \times \theta_{\substack{infinite\\cylinder}}(0,t) \tag{14}$$

After which the temperature at this point after the defined time is given as:

$$T(0,0,t) = T_\infty + \left(\frac{T(L,0,t)-T_\infty}{T_i-T_\infty}\right)_{\substack{short\\cylinder}} \times (T_i-T_\infty) \tag{15}$$

This analysis was used to calculate the change in temperature over time at the centre of the volume of PCL in a 1 ml BD Braun syringe, as well as the temperature change at the outlet of the syringe just before the PCL enters the needle. Variables were used as per Table 4-1. While in reality the proposed set-up consists of a volume of PCL bound within a

polycarbonate syringe, the problem was simplified by assuming a volume of PCL alone with diameter equal to the syringe diameter. Polypropylene has a thermal diffusivity of 2.6×10^{-7} m^2/s and thermal conductivity of 0.25 W/mK, both values of which are greater than those of PCL. Thus, assuming a homogenous volume of PCL gives a conservative estimate of the temperature increase in this analysis, with the actual temperature likely to increase at a faster rate. Upon completion of the heating system, these values were also calculated experimentally. This was achieved by melting a volume of PCL in the syringe and embedding a type K thermocouple within the centre or at the outlet before allowing the material to cool to room temperature. The PCL was then heated via air and temperature recorded every 10 s up to 20 min.

Table 4-1 Variables used for transient heat transfer analysis

symbol	*description*	*value*	*units*	*source*
T_∞	heating temp	90	°C	-
T_i	initial temp	27.2	°C	-
r_0	cylinder radius (syringe radius)	0.0045	m	-
l	wall length (PCL height in syringe)	0.02	m	-
α	thermal diffusivity PCL	1.30×10^{-7}	m^2/s	(Agari & Ueda, 1994)
k	thermal conductivity PCL	0.18	W/mK	(Agari & Ueda, 1994)
h	heat transfer coefficient of low speed air over a surface	10	W/m^2K	(Whitelaw, 2011)
1/Bi	Inverse Biot number centre plane wall	0.9	n/a	Eqn. 2
1/Bi	Inverse Biot number centre infinite cylinder	4	n/a	Eqn. 5
1/Bi	Inverse Biot number edge wall	0.9	n/a	Eqn. 11

4.2.2 Heating-voltage assembly

A prototype of the proposed heating system was first constructed and it was confirmed that the system could bring a PCL loaded syringe to the desired temperature of 90°C within 30 mins. The final system consists of a custom nylon chamber designed to

house a 1 ml BD Braun Luer-Lok syringe (Figure 4-4). Ambient air is passed through an in-line air heater, with the temperature being monitored by a type K thermocouple at the heater outlet, and maintained at the desired level via PID control. A second type K thermocouple is used to monitor ambient temperature around the printer. Heated air is passed through insulated PTFE tubing into the nylon heating chamber and passed directly across the needle, with an outlet bringing exhausted air away from the system. The end of a P200 pipette tip was used as a gasket to seal the heating chamber at the needle opening to prevent air from passing through the bottom of the chamber and disrupting the electrospinning jet. Voltage was controlled using a Genvolt (UK) 73030 power supply with maximum voltage of 30 kV. A port was placed in the side of the chamber to insert the high voltage cable, with the positive electrode being clamped around the needle using a grabber clip. The temperature drop between the heater outlet and chamber, specifically the point in the chamber between its inlet and the needle, was quantified to allow the chamber to be maintained at the desired temperature, with heater outlet temperatures of 70-110°C in increments of 5°C investigated. The temperature of PCL at the mid-point of its bulk and at the syringe outlet was also quantified and compared to the transient heat analysis above, with PCL temperature recorded every 10 s up to 20 mins at a chamber temperature of 90°C.

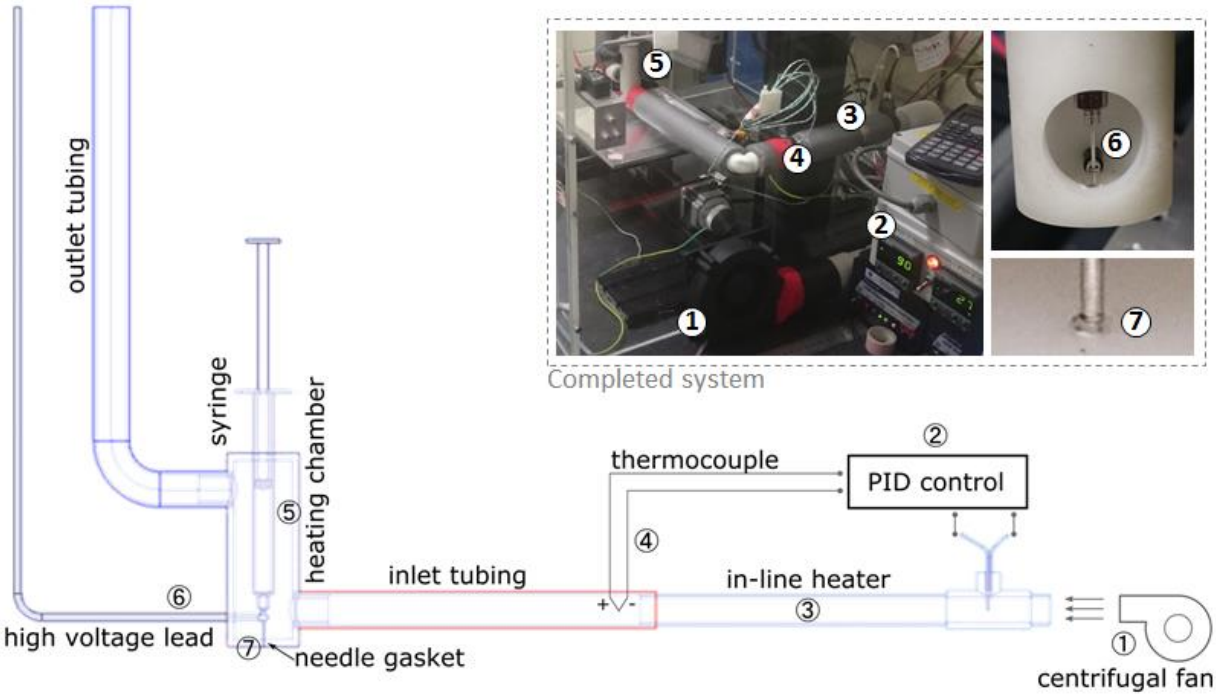

Figure 4-4 Schematic of the heating-voltage assembly design. Inset: completed system with key components labelled as per the schematic.

4.2.3 Polymer extrusion

Polymer extrusion was initially achieved via an NE-500 high pressure syringe pump (New Era Pump Systems, NY). The effect of flow rate on fibre diameter was investigated at 5, 10, 20, 30, 40 and 50 µL/hr, at all combinations of temperature 75, 85 and 95°C and voltage 13, 16 and 19 kV. A 21G needle at a distance of 30 mm from a grounded aluminium collector was used throughout these experiments. An air pressure based extrusion system was also implemented, with the influence of 10, 20, 30, 40, and 50 kPA feed pressure on fibre diameter investigated for all combinations of temperature 80, 90 and 100°C and voltage 8, 10 and 12 kV. In these experiments, a distance of 20 mm was used between the needle and the collector. The fibre was statically deposited for 2 min on a glass slide, after which the collector was moved and one of the variables was altered. A time of 15 min was allowed to elapse to allow the fibre to equilibrate before each experiment. Images were taken at a magnification of 40X using optical microscopy, which has previously been shown to be an accurate method for quantifying fibre diameter (Brown

et al., 2014), and a total of 20 measurements were taken for each sample using the FIJI distribution of ImageJ (Schindelin *et al.*, 2012).

4.2.4 Controlled deposition

An x-y stage was built by stacking two linear slides on top of one another and securing a 200 x 200 mm aluminium plate on top. Leadscrew pitch was chosen such that sufficient accuracy could be maintained over micron scale fibre placement while also allowing for great enough speeds to be reached to print straight fibres with a range of diameters. While a small leadscrew pitch gives greater print resolution, it also reduces the maximum translation speed achievable, and thus, an optimal leadscrew design must be chosen for the given application. For the x-y stage, XN10-0060-E02-21 (Velmex, USA) slides with travel of 152.4 mm and leadscrew pitch of 5.08 mm were used. This combination paired with PK264-03B NEMA 23 stepper motors with a 1.8° step angle and utilising half stepping gives 400 steps per revolution and a resulting resolution of 12.7 μm (Eqn. 16). Maximum speed is 101.6 mm/s at a stepping speed of 8,000 steps/second (Eqn. 17). For the z-axis on which the MEW print head is mounted, an XN10-0060-E25-21 slide was used, which has a travel of 152.4 mm and leadscrew pitch of 0.635 mm. This axis thus has a resolution of 1.5875 μm (Eqn. 16) and maximum speed of 12.7 mm/s (Eqn. 17). This reduced maximum speed would be too low for MEW of small diameter fibres, however on the z-axis which would only be translated upwards between layers this is not an issue and provides much greater resolution to travel upwards on the scale of an electrowritten fibre's diameter. A VXM-3 stepper motor controller (Velmex, USA) which utilised half-stepping was used to control slides in conjunction with the manufacturer's COSMOS software. This software is similar to g-code, with co-ordinates, speeds and accelerations of each slide manually programmed to define motion paths and fabricate scaffolds. Successive co-ordinates define the scaffold geometry, while speed, acceleration and pause commands are optimised for a given fibre diameter to give an optimal MEW jet profile. The final design of

the MEW printer with this deposition system and the previously discussed heating-voltage assembly is illustrated in Figure 4-5.

$$Resolution = \frac{screw\ pitch}{steps/revolution} \tag{16}$$

$$Speed = resolution \times stepping\ speed \tag{17}$$

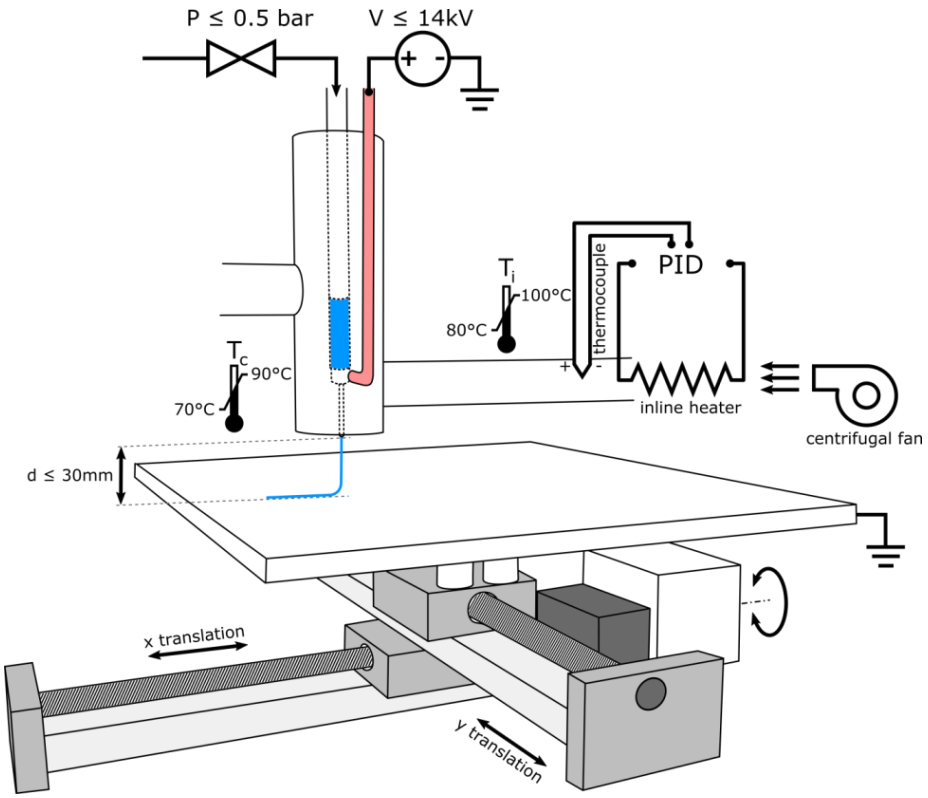

Figure 4-5 Schematic of final rig MEW printer design with range of parameters typically used for fibre fabrication. T_i = inlet temperature, T_c = chamber temperature.

4.2.5 Enclosure and safety

A custom gantry was built to mount the x-y stage for controlled deposition and the z-axis to secure all components of the print head, including the heating assembly and extrusion system. Electrically non-conductive anodised aluminium framing (MSX/MTX, Velmex USA) was used to limit any possible interference for unwanted grounding or arcing. The gantry was designed to allow for clearances of at least 30 mm at all sides of the x-y stage to make framing and enclosure strikes impossible and to limit potential pinch hazards. A custom 10 mm thick polycarbonate enclosure was built to house the printer,

consisting of separate wiring ports to isolate high voltage leads from all other general wiring of motors, controllers and heater components. A safety interlock was implemented between the door and high voltage power supply, such that the power supply is automatically disconnected from the mains electricity supply should the door be opened while it is turned on. A discharge rod was wired to the ground to discharge any potential residual charge from the needle after opening the enclosure door. A port and exhaust system was also included to allow for solvent electrospinning.

4.2.6 Process visualisation and monitoring

A Dino-lite AM4113TL long working distance USB microscope was used to easily visualise the electrospinning jet. This microscope gives a magnification of 20X and field of view of 19.6 x 15.6 mm at a distance of 151 mm. This set-up allows for the electrospinning jet to be easily visualised while keeping the microscope at a safe distance from the high voltage lead. The bright LED lights on the microscope also aid in easily visualising the fibre using the naked eye. In addition, a mobile phone connected to WiFi is used as an internet protocol (IP) camera to externally monitor the system. The "IP Webcam" android application is used to stream video and sound from the phone's camera to a private server and can be monitored live via the "Ivideon" application on another phone or computer.

4.3 Results

4.3.1 Completed MEW printer

A MEW printer was built with the key element of the design consisting of a semi-closed air heating assembly allowing air maintained at consistent high temperatures via PID control to be circulated around a syringe to melt the polymer (Figure 4-6). This also allows for simple application of high voltages to the needle of up to 30 kV with no interference from the isolated heating element. Air pressure was used to provide a consistent force for polymer extrusion, while controlled deposition was achieved via an x-y stage with a usable

print area of 152.4 × 152.4 mm and resolution of 12.7 μm. Z-axis height can also be controlled at a resolution of 1.5875 μm. The system is housed within a safety enclosure to protect from hazards such as moving components and high voltage, with a safety interlock also being incorporated to shut off the high voltage power supply should the door be opened while it is on.

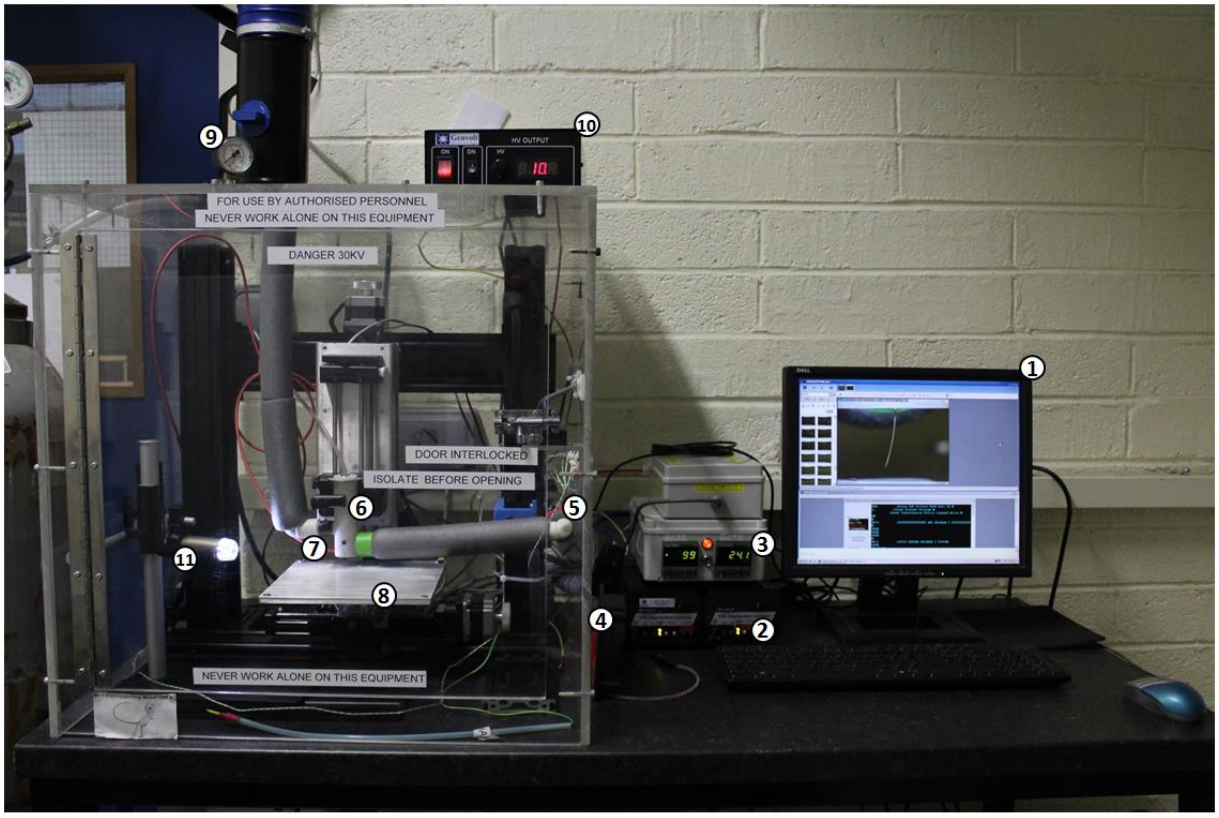

Figure 4-6 Photograph of completed MEW printer illustrating key components: 1. Workstation, 2. Stepper motor controller, 3. PID temperature controller, 4. Centrifugal fan, 5. In-line air heater, 6. Heating chamber, 7. High voltage cable, 8. Grounded collector, 9. Air pressure regulator, 10. High voltage power supply, 11. USB microscope.

4.3.2 Characteristics of heating assembly

For the range of temperatures tested, it was shown that there is a temperature drop of between 4 – 11°C between the air heater outlet and the chamber (Figure 4-7). While the trend looks linear, temperature drop increases with greater heater outlet temperatures, with the greatest drop of 11 °C at a heater temperature of 110 °C. Chamber temperature was shown to be consistently maintained for long periods, with no change after 1 hour of

heating, demonstrating that a syringe may be consistently heated at the desired temperature using the known temperature drop.

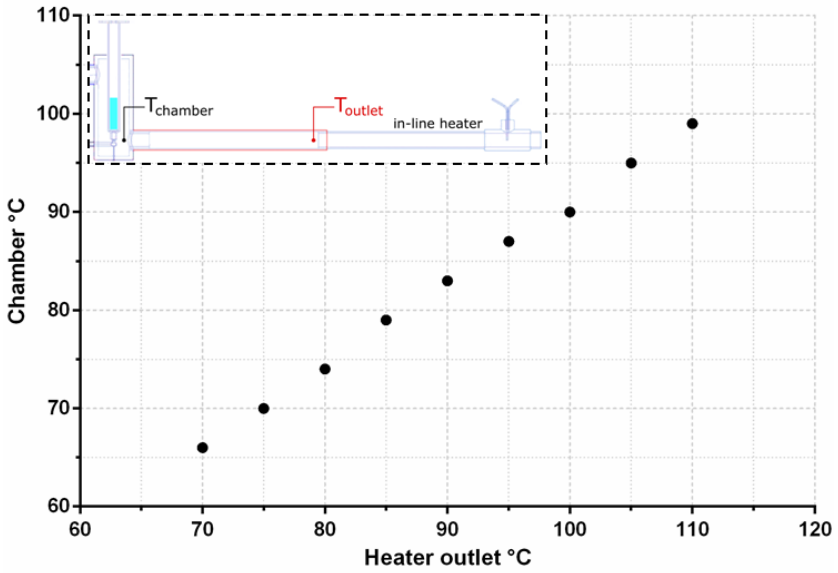

Figure 4-7 Relationship between heater outlet temperature and chamber temperature, illustrating drops of between 4 – 11 °C

It was found that at a chamber temperature of 90°C, the mid-point of the PCL reached 82°C. This is a slight deviation from the theoretically determined value of 88°C, however the transient temperature profiles between theoretical and experimental analyses correlate closely (Figure 4-8A). A possible contributing factor is temperature drop within the chamber itself, which was found to be approximately 2°C between its inlet and outlet, resulting in a gradient with lower temperatures towards the top of the chamber. After 20 min the temperature was found to be 87°C at the outlet, close to the theoretical value of 89°C (Figure 4-8B). While there are deviations in the theoretical approach, particularly between 60 - 85°C, it was found to closely match experimental readings in the initial and final heating stages. This is likely due to the approximate nature of Heisler charts which do not yield exact solutions, in addition to experimental errors, such as difficulty in accurately positioning the thermocouple. In addition, it is assumed that the surrounding temperature remains constant, however, the chamber was initially at ambient temperature and required approximately 20 s to reach the desired temperature of 90°C. Temperature within the

system enclosure was also characterised, and found to increase to a maximum of 31 °C over several hours due to dissipation from the heating system as well as heat from the stepper motors. Scaffolds could be fabricated with an enclosure temperature of 26–31 °C with no apparent influence on quality within this range. Relative humidity ranges between approximately 45–60%. The system has been shown to be capable of continuous fibre production for at least 24 hours.

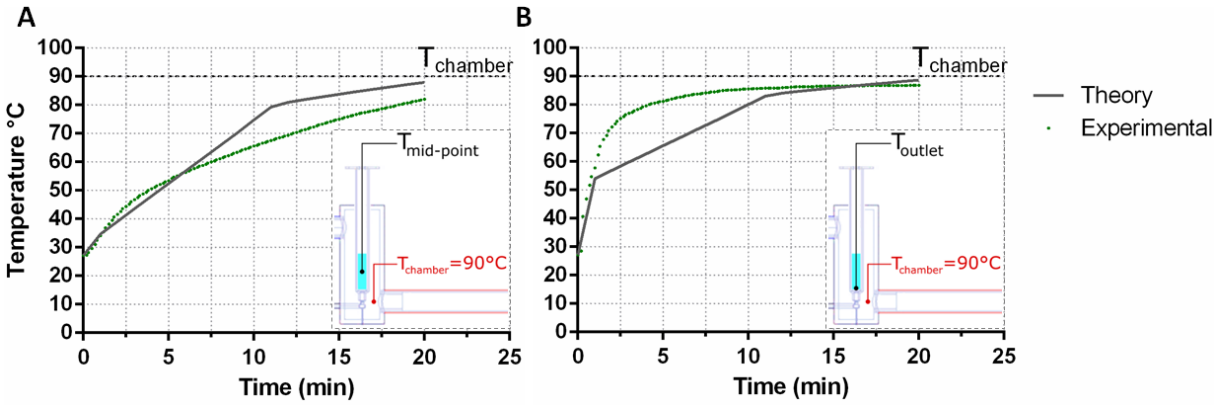

Figure 4-8 Theoretical and experimental temperature change at the mid-point (A) and outlet (B) of PCL within a 1 ml syringe at a chamber temperature of 90°C

4.3.3 Extrusion characteristics of syringe pump and pressure driven systems

Fibre diameter and printability are regulated to varying degrees by system variables including pressure, voltage and temperature, with the custom nature of the MEW apparatus requiring the study of these to generate consistent fibres for controlled deposition (Hochleitner *et al.*, 2016). As expected, increasing the flow rate or pressure results in a greater fibre diameter due to the increased flow of material through the needle, with this being the primary method by which fibre size may be controlled (Figure 4-9A-B). For the syringe pump system, fibre diameters below 25 μm could not be fabricated. Voltage did not influence fibre diameter at flow rates of 5 μL/hr, while there were varying trends at higher flow rates (Figure 4-9A). There were no apparent trends between fibre diameter and temperature. Overall, the syringe pump system was not found to be suitable for consistent fibre production and it was difficult to maintain an electrospinning jet for extended periods

of time. A likely cause is insufficient resolution of the syringe pump stepper motor, which did not exhibit continuous rotation and stepped forward approximately every 10 s to achieve low average flow rates, which in reality resulted in pulsed, stop-start extrusion. The pressure system was found to be much more consistent and also allowed for smaller diameter fibre production (Figure 4-9B). In this system, a trend of decreasing fibre diameter with increased voltage can be seen across all experiments, consistent with previous findings in the literature (Hrynevich *et al.*, 2018). Periodic breakdown of the Taylor cone was seen to occur in cases where voltage is insufficient for the material flow rate, as can be seen with the greater standard deviation using a pressure of 50 kPa at 8KV (average SD = 2.31) compared to 12 kV (average SD = 0.95). Temperature was not found to alter fibre diameter or consistency for the range of values studied. Overall, air pressure was shown to be a suitable method for fabricating consistent fibres at a range of diameters, while voltage must be optimised and generally increased in conjunction with increased pressure. The pressure based system has been shown to be capable of continuous fibre production for at least 24 h.

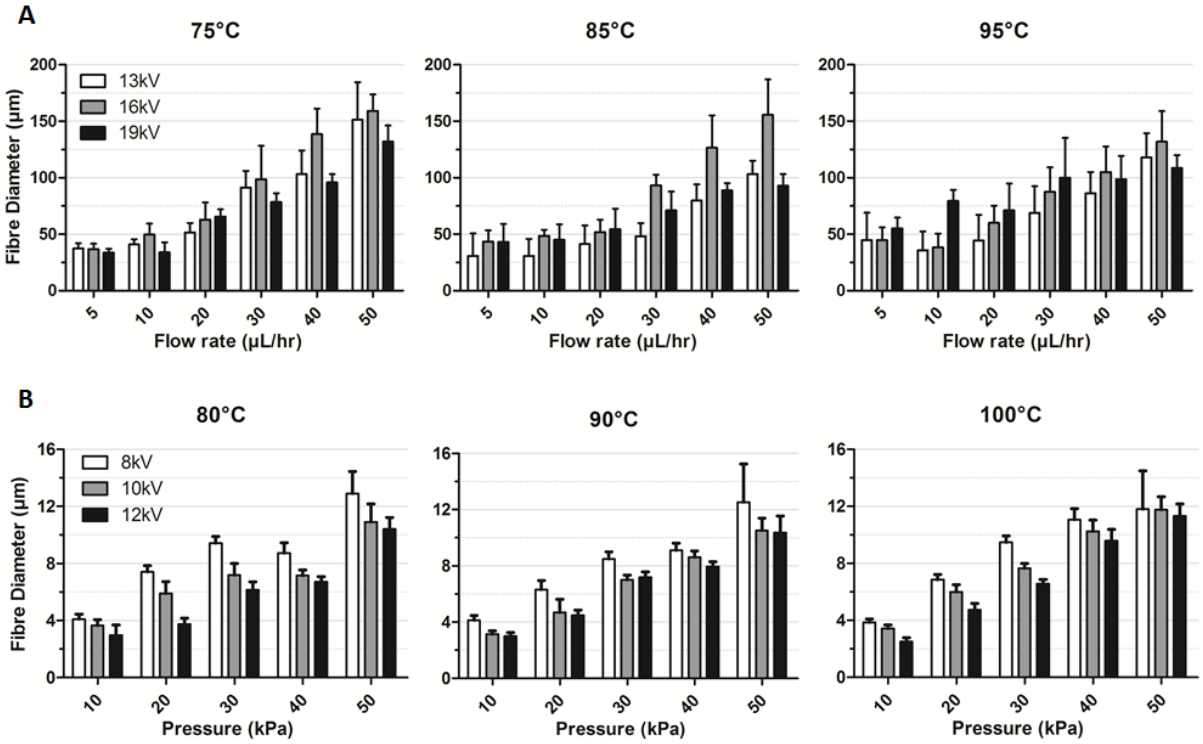

Figure 4-9 Influence of process parameters on fibre diameter for extrusion via syringe pump (A) and air pressure (B).

4.3.4 Control of fibre deposition

The collector speed must be optimised for a given fibre diameter. The critical translation speed (CTS) is the point at which the collector (S_c) and jet (S_j) speeds are equal (Figure 4-10A). Increasing collector speed slightly above the CTS yield an optimal catenary profile which gives the greatest accuracy of fibre deposition (Figure 4-10B). Further increasing S_c creates a greater lag between the needle and fibre contact point with the collector (Figure 4-10C), reduces fibre placement accuracy and stretches the jet resulting in marginally reduced fibre diameters. Characteristics of fibre deposition are demonstrated for a range of translation speeds (Figure 4-11A), where it can be seen that speeds significantly below the CTS result in a great degree of fibre coiling. Further increasing the speed such S_c is slightly below S_j means that the collector is not slow enough to allow for complete fibre coiling, resulting in a "wavy" fibre morphology. Further increasing the speed to just above the CTS, in this case S_c = 35.6 mm/s, allows for the writing of straight fibres.

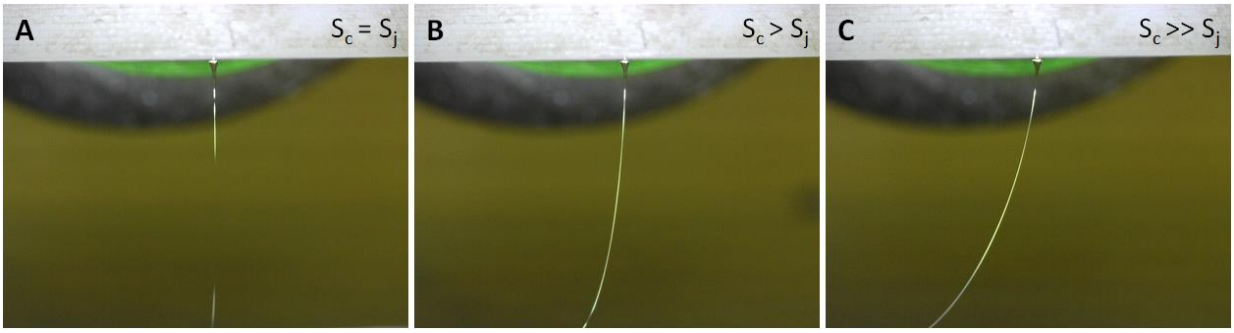

Figure 4-10 Relationship between collector speed (Sc) and jet speed (Sj). When equal, slight buckling of the fibre occurs (A), and when Sc is further increased, a catenary jet profile is observed (B). Further increasing Sc results in greater lag between the needle and the fibre contact point on the collector (C), and slight stretching of the jet with a reduction in fibre diameter.

The variables defining the turning region are also of great importance for controlled fibre deposition, with these including acceleration (and deceleration), pause commands and lateral speed. Ideally, a lower deceleration could be used before the turning region to allow the lag in the fibre to reach the end of the defined pattern, while greater acceleration would be used after the turn to avoid fibre coiling. With the VXM-3 stepper motor controller used in this study however, acceleration and deceleration cannot be controlled independently of one another and thus an optimal value is determined based on the fibre diameter and jet speed to partially allow fibre lag to reduce at the turning region while also ensuring coiling does not occur after turning. Lateral speed is then determined, which when too low, results in fibre coiling after the turning region (Figure 4-11B). Further increasing lateral speed overcomes this issue, however, it results in a loss of the square wave pattern programmed into the controller and premature turning of the fibre. Pause commands can be used to help restore the programmed pattern (Figure 4-11C), however, this can result in fibre coiling before the turning region if too long, or if lateral translation speeds are too low. It can be seen for this fibre that with a 0.1 s pause before turning and a lateral speed of at least 38.1 mm/s, the programmed pattern is beginning to be restored. It must be noted that reproduction of the exact square wave pattern is often not necessary, however, the variables

of the turning region should be optimised as much as necessary to avoid fibre coiling and premature turning of the fibre which reduces usable scaffold area.

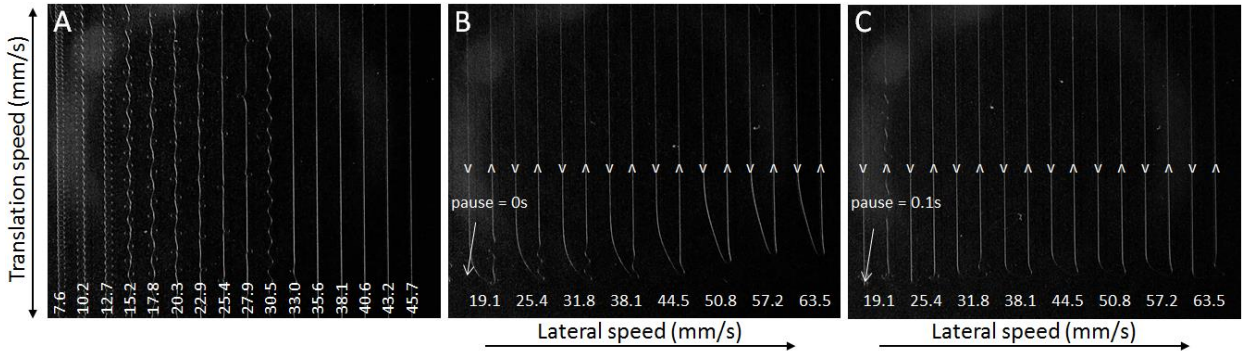

Figure 4-11 Effect of turning region variables on fibre deposition. Low translation speeds result in coiling or wavy fibre formation, with straight fibres being formed above the CTS at 35.6 mm/s (A). Low acceleration and lateral speeds can result in fibre coiling in the turning region, while excessive lateral speeds result in premature turning of the fibre (B). Pause commands may be introduced in conjunction with optimisation of acceleration/deceleration to restore deposition characteristics to more closely represent the defined geometry (C).

4.3.5 Scaffold fabrication

Optimisation of variables allowed for the fabrication of consistent, low-micron diameter fibres with precise controlled deposition. This was validated by fabricating scaffolds of various architectures based on previous studies, including designs with offset fibres between layers (Brown *et al.*, 2011), and designs with fibres stacked on top of one another which are commonly used to create larger pores which may be incorporated with hydrogels (Visser *et al.*, 2015). The former scaffold design was fabricated with a 90° angle offset between layers, fibre diameter of 5 μm and offset of 50 μm between subsequent layers (Figure 4-12A-B). This demonstrates the ability to precisely deposit fibres in close proximity to one another. Fibres may occasionally stack on top of one another if deposited too closely together, as the elevated fibres currently on the plate provide a shorter distance for the MEW jet to the ground. It is thus important to also consider fibre diameter when deciding the desired fibre offset (distance between central axes of two parallel fibres on the same layer), with larger diameter fibres being more difficult to closely deposit next to one

another due to the reduced distance between their outer circumferential surfaces. The ability to precisely deposit fibres on top of one another was also validated by fabricating porous box structure scaffolds with 1 mm pores (Figure 4-12C). Due to the greater height at the intersection of fibres compared to mid pore regions, the structure is characterised by peaks at these intersections, as seen in a 1 mm box structure scaffold composed of 10 μm diameter fibres (Figure 4-12D-F). As the scaffold is fabricated via deposition of 50 layers of fibres in each of the x and y directions, it is a total of 100 layers high from the perspective of the fibre intersections, and 50 layers high at mid pore regions, resulting in the characteristic peaks and troughs at the upper scaffold surface. As a result, some fibres bridge between adjacent peaks resulting in gaps between fibre layers (Figure 4-12E). This becomes more apparent at even greater scaffold heights, as seen in a scaffold of the same design, however, with fibres deposited a total of 200 layers high, 100 in each direction (Figure 4-12G-I). At greater layer heights, the offset in height between peaks and troughs also increases, resulting in further fibre bridging directly across peaks.

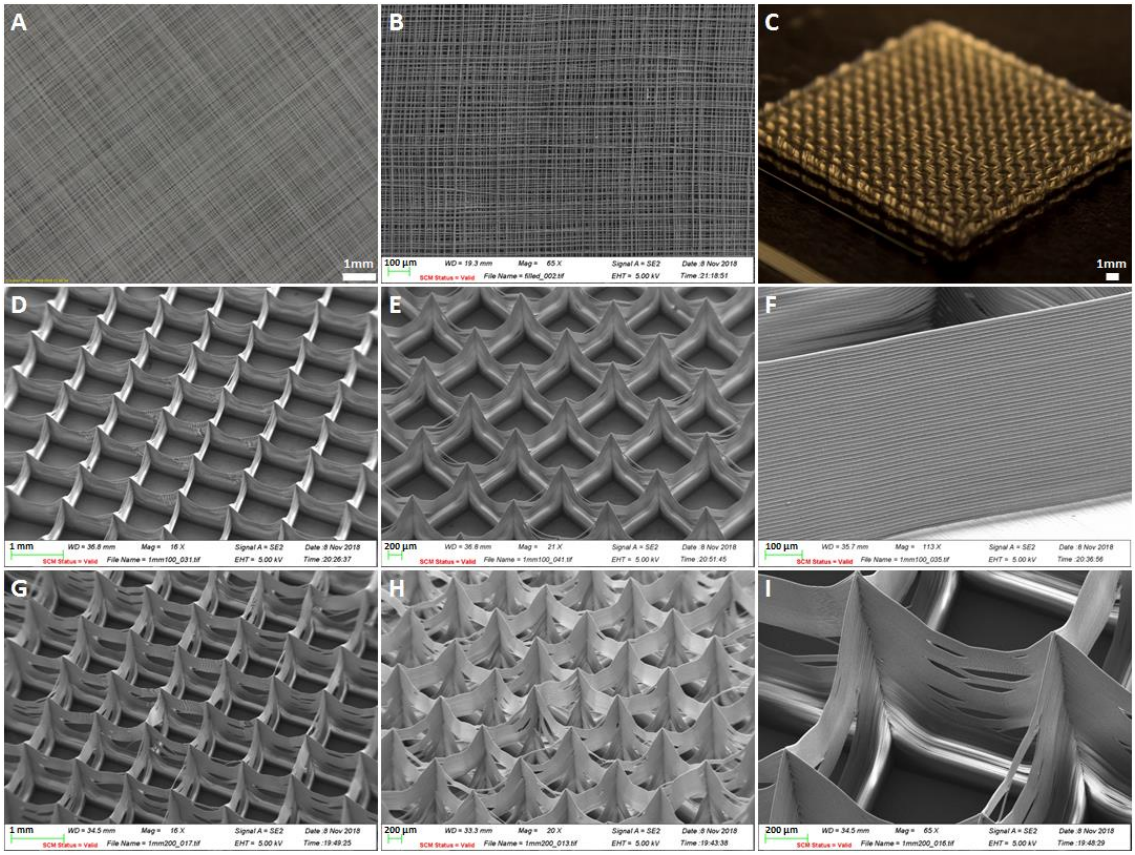

Figure 4-12 Precise controlled deposition using MEW. Fibres deposited with a 90° angle offset between layers (A-B). Photograph of box structure scaffold with 1 mm pores (B). SEM imaging illustrating controlled stacking of fibres 100 layers high (50 in each direction) (D-F) and 200 layers high (100 in each direction) (G-I).

4.4 Discussion

MEW is a powerful 3D printing technology with great potential for use in an extensive range of biomedical applications. Its capability of forming sub-micron scale controlled fibrous architectures to mimic native tissue makes it highly attractive for tissue engineering applications in particular. Here, the process followed for the design, build and optimisation of a custom MEW printer is described. The primary goal is to use this printer to fabricate micro-architectures to study their influence on cell behaviour, and further use this knowledge to develop scaffolds for tissue engineering applications.

The heating-voltage assembly is a key element of the technology, and one of the greatest challenges when designing a MEW printer due to potential interference between the heater and the high voltage electrode (Brown *et al.*, 2016; Muerza-Cascante, Haylock,

Hutmacher, & Dalton, 2015). Several strategies have been used to overcome interference between the high voltage system and heating system, including electrically isolating these two systems (Almoatazbellah, Scott, & Paul, 2017; Brown *et al.*, 2016; L. H. Zhang, Duan, *et al.*, 2016), using a heated water jacket (Brown *et al.*, 2011), or applying the high voltage to the collector plate while grounding the needle (He *et al.*, 2016; Lyons, Li, & Ko, 2004). Only one other group has used heated air for their MEW printer, which consists of a hot-air gun blowing air directly across a syringe in a large acrylic tunnel (F. Tourlomousis *et al.*, 2015). Using heated air has the advantages of eliminating interference should the heating element be kept at a great enough distance from the high voltage source, while also allowing greater temperatures than a circulating water set-up. Here a new approach has been employed, consisting of a semi-closed heating system comprising an inline heater with PID control to accurately control air temperature within a chamber in which a syringe is mounted. Upon characterisation of this system, a slight gradient was observed, with the defined temperature being reached at the bottom of the syringe and needle, and temperatures up to 2°C lower at the top of the syringe. It is believed that this gradient will not affect the process, with other groups using set-ups consisting of separate heaters for the needle and syringe (de Ruijter *et al.*, 2017; F. M. Wunner *et al.*, 2017), sometimes intentionally introducing gradients with reduced temperatures at the syringe heater (Bas, D'Angella, *et al.*, 2017). Importantly, using this air heating system, temperature can be defined close to the tip of the needle, such that the polymer temperature upon extrusion can be controlled with great accuracy.

The extrusion system is also a key component for precise fibre production. Of note is the fact that all early MEW studies used syringe pump systems, while the majority of the latest studies have used air or nitrogen pressure for extrusion, hinting at the current preference for the latter in the literature. The main findings from using both of these systems are that pressure based extrusion methods allow for fabrication of fibres with much

greater consistency, and allows fabrication of fibres with lower diameters to be more easily achieved. The inconsistent motor stepping in a syringe pump at low flow rates results in a pulsatile pumping force which is difficult to attenuate for consistent fibre production over long periods of time. In contrast, air pressure can be consistently applied, even at low values, allowing for a much more homogenous flow of material from the needle and a more consistent jet for MEW. This is of great importance for high quality (Hochleitner *et al.*, 2016) and sub-micron (Hochleitner *et al.*, 2015) fibre fabrication, the printing of highly complex scaffold geometries (Miguel Castilho, Mil, *et al.*, 2018; de Ruijter *et al.*, 2017; Hrynevich *et al.*, 2018; McColl *et al.*, 2018), and fabrication of large-volume scaffolds over extended periods of time (F.M. Wunner, Wille, *et al.*, 2018).

A characterisation study was carried out to investigate the effect instrument parameters on fibre diameter and deposition characteristics, with pressure being the primary means by which to control fibre diameter. Consistent with previous findings (Muerza-Cascante *et al.*, 2015), a higher voltage was found to consistently result in a decreased fibre diameter, with sufficiently high voltage required to overcome the surface tension of material at the tip of the needle to maintain a consistent Taylor cone and generate a uniform fibre diameter (Hochleitner *et al.*, 2016). Temperature was not seen to have a significant effect on fibre diameter, however previous studies have shown a slight reduction with greater temperatures (P. D. Dalton, Muerza-Cascante, & Hutmacher, 2015; R. Deng *et al.*, 2009; X. Li, Liu, Wang, & Li, 2012; Shimada, Ogata, Nakane, & Ogihara, 2012; H. Zhou, Green, & Joo, 2006). These deposition characteristics of MEW must be well understood and optimised to fabricate complex scaffold geometries. Additionally, unlike traditional 3D printing technologies such as FDM, the offset between the print head and the collector in MEW introduces a constant lag point between the needle and the point of fibre contact with the collector. This greatly complicates the process, and additional optimisation of deposition variables must be conducted to ensure that the final print matches the desired

architecture. Highly complex architectures may then be achieved, such as hexagonal porous structures (Miguel Castilho, Mil, *et al.*, 2018) and structures with variable fibre diameter (Hrynevich *et al.*, 2018). Indeed, the lag between needle and collector can be used to the researchers' advantage, where fibres can be intentionally deposited below their CTS to form well defined crimped structures for ligament and tendon TE (Hochleitner, Chen, *et al.*, 2018).

4.5 Conclusion

In conclusion, a custom MEW printer to allow for the fabrication of complex micro-architectures has been designed and built, and the key considerations when undertaking this process have been outlined. Just as important as the above is the full characterisation and optimisation of the process, with the large number of process parameters and complexities associated with direct writing requiring a great level of understanding to consistently deposit fibres to form a desired architecture. This allows for the fabrication of well-defined scaffolds and micro-architectures, with extensive applications for the study of cell behaviour and the development of optimised architectures for specific tissue engineering applications.

Chapter 5

Mediating human stem cell behaviour via defined fibrous architectures by melt electrowriting

5.1 Introduction

The architecture within which cells reside is fundamental to their function, and guides cell behaviour to elicit specific responses and maintain physiologically appropriate, tissue specific behaviour throughout the body (Frantz *et al.*, 2010; Rozario & DeSimone, 2010). This can be seen in the vastly differing microarchitectures seen in various tissues that contain similar collagen ECM makeup, such as the highly aligned nature of tendon tissue along the axis of loading and the circumferential distribution of fibres in the tunica media of arteries and veins. A range of architectures are also evident throughout bone tissue, where fibre organisation occurs in a load dependent manner (Foolen *et al.*, 2008). These architectures are not only important from a structural perspective, but also transmit important information via physical cues to surrounding cells about the external environment. The true importance of this is seen in the case of disease progression, where the development of abnormal architectures can have devastating outcomes on tissue function. For instance, increased collagen content and highly aligned perpendicular fibres have been identified surrounding the stroma in breast tumours, facilitating migration of cancerous cells, while conversely, the appropriate microenvironment is seen to suppress tumorigenic behaviour (Hogrebe *et al.*, 2017b). Another example is the altered collagen fibril architecture seen in osteoarthritis, which becomes less aligned in the superficial zone compared healthy individuals, which can in turn amplify local tissue strain in response to loading leading to further damage and cell death (Saarakkala *et al.*, 2010). These examples

highlight the importance of tissue microarchitecture for maintaining correct cellular function, with a greater understanding of how cells behave within particular architectures having great potential to aid in the development of therapeutics in cases where correct tissue structure is compromised, as well as facilitating the development of effective tissue engineering (TE) strategies to restore function in the case of trauma or disease (O'Brien, 2011).

A greater understanding of microarchitecture mediated biology has been facilitated via the use of *in vitro* cell culture platforms and cellular markers, with YAP being highlighted as a protein of particular interest in recent studies. Dupont *et al.* identified the mechanosensitive markers YAP and TAZ, revealing a role in signalling in response to cell shape, substrate stiffness and cytoskeletal tension via the use of micropatterned substrates (Dupont *et al.*, 2011). YAP is found to localise to the nucleus to a greater extent in cells that have a greater cytoskeletal tension, such are those that are more spread in response to the underlying architecture, or those that are cultured on stiff substrates. Aragona *et al.* investigated the influence of mechanical forces on YAP/TAZ, where greater activity was seen in more highly stressed cells, such as those located at corners of the substrate (Aragona *et al.*, 2013), again reinforcing the influence of architecture on cell signalling. YAP has also been implicated with the mediation of stem cell lineage commitment (Aragona *et al.*, 2013; Dupont *et al.*, 2011; Hong *et al.*, 2005; Karystinou *et al.*, 2015; Pan *et al.*, 2017; Zhong *et al.*, 2013), revealing its importance as not only a valuable tool for studying the influence of architecture on cell behaviour, but also as a key component in architecture mediated signalling and lineage commitment. A wide range of scaffold manufacturing techniques have been used for the study of cell behaviour and fabrication of TE scaffolds. 3D printing techniques are of particular interest due to the level of control over scaffold architecture (Hutmacher *et al.*, 2001). Pore shape in fused deposition modelling (FDM) scaffolds has been shown to influence stem cell differentiation, with

square pores facilitating chondrogenic differentiation and rhomboidal pores supporting osteogenic differentiation (Di Luca *et al.*, 2016). Achieving small fibre sizes is however a limitation of many 3D printing approaches, with cells on the often macroporous curved structures behaving similarly to those cultured in 2D (Hogrebe *et al.*, 2017b). Therefore these approaches are not appropriate for the study of physiologically relevant phenomena. Smaller fibre sizes which are more representative of the fibrous architecture in many native tissues are thus sought after, with electrospinning being an ideal technology to achieve this. Fibre diameter plays a role in influencing stem cell behaviour (Cardwell, Dahlgren, & Goldstein, 2014; Christopherson, Song, & Mao, 2009), with a fibre diameter of between 9-12μm being shown to be optimal for osteogenic differentiation (Takahashi & Tabata, 2004), while material choice is also an important consideration for guiding cell behaviour (Labour *et al.*, 2018; Nagarajan *et al.*, 2017). Microfibre alignment, achieved through collecting fibres on a rotating mandrel, has also been shown to influence stem cell differentiation (Doustgani *et al.*, 2013; Olvera, Sathy, Carroll, & Kelly, 2017). While fibre alignment can be achieved with electrospinning, there is a significant limitation to the degree of control which is achieved over fibre placement, thus limiting the suitability of this technique for the fabrication of fibrous micro-environments to study cell behaviour.

MEW is a recently developed technology which overcomes the above limitations of FDM and electrospinning, and facilitates the fabrication of controlled fibrous architectures reminiscent of those seen in native ECM. This process combines elements of melt electrospinning and 3D printing (Brown *et al.*, 2011; Hutmacher & Dalton, 2011), allowing the fabrication of micron to sub-micron (Hochleitner *et al.*, 2015) diameter fibres while controlling their orientation in three dimensions. While MEW has previously been limited in terms of the scaffold height achievable, the technology is constantly being developed, with large volume scaffolds with a thickness of greater than 7mm recently being achieved (F.M. Wunner, Wille, *et al.*, 2018). Studies have already begun to demonstrate its potential

for the fabrication of scaffolds for a wide range of biomedical applications (Almoatazbellah *et al.*, 2017; P. D. Dalton *et al.*, 2015), including models and scaffolds for skin (Farrugia BL, 2013), endosteum (Muerza-Cascante *et al.*, 2016), periosteum (Baldwin *et al.*, 2017), vascular (Bertlein *et al.*, 2017) and cardiac (M. Castilho *et al.*, 2017) applications. MEW fibres have also been collected on rotating collectors to create tubular scaffolds (Brown *et al.*, 2012; Jungst *et al.*, 2015) which have been used as a model for bone (Martine *et al.*, 2017), while others have also combined fibrous scaffolds with hydrogels to fabricate reinforced soft tissue models for applications such as cartilage TE (Bas, D'Angella, *et al.*, 2017; Bas, De-Juan-Pardo, *et al.*, 2017; Bas *et al.*, 2015; Bas *et al.*; Hochleitner *et al.*, 2014; Visser *et al.*, 2015). The vast range of potential applications for MEW scaffolds make it an ideal technology for the fabrication of controlled architectures for the study of cell behaviour, as well as the development of scaffolds for tissue engineering applications.

Herein, it is investigated how scaffold architecture of MEW fibrous ECM-like constructs influence cell behaviour. Scaffolds with various fibrous architectures were designed, fabricated and characterised, and how this affected hMSC behaviour in terms of cell geometry and YAP expression was studied. Finally, a long term study was undertaken to investigate the influence of architecture on stem cell osteogenesis. The resulting data demonstrates that MEW can be utilised to produce ECM-like cellular micro-environments, and demonstrates that architecture alone can drive cell shape, mechanosensing and osteogenic commitment of human stem cells in 3D fibrous constructs.

5.2 Materials and methods

5.2.1 Scaffold fabrication and characterisation

A custom MEW apparatus was used for the fabrication of scaffolds. Scaffolds were fabricated at a temperature of 90°C, pressure of 50kPa and voltage of 12kV. The spacing between fibres on each layer is 300μm, with a fibre offset of 50μm being present between

layers. This results in an apparent pore size of 50μm from a top view perspective, with the side view of the design showing the presence of larger channels formed as a result of the 300μm spacing between fibres on the same layer (Figure 5-1A). First the x-layer is laid down (1x fibres), followed by the first y-layer (1y fibres). Then the second x-layer is formed (2x), followed by the second y-layer (2y), with this process being continued for 6 x-layers and 6 y-layers, before the needle is brought back to the origin. This whole process is repeated 4 times for a total of 48 layers, with the first 24 layers being shown in Figure 5-1B. The fibre placement in the x-dimension is the same for the first three scaffold groups, with angle α of the fibres in every second layer being defined as 90° (S90), 45° (S45) or 10° (S10), maintaining the fibre spacing and apparent pore size between groups independent of alignment. The random scaffold (SR) was fabricated with the same program as S90, with the exception of the collector translation speed, which was halved to result in the coiling of fibres. Porosity was measured using a gravimetric method, whereby the mass of scaffolds of 8mm diameter was determined, while their thickness was measured using a micrometer (n=3 for each group). Porosity (Φ) was then calculated by comparing the total volume of PCL fibres (V_f) in the scaffold to the total bounding volume (V_t), as follows: $\Phi = 1 - \frac{V_f}{V_t}$. For SEM imaging, samples were prepared by sputter coating with gold/palladium for 60s at a current of 40mA.

5.2.2 Mechanical characterisation of scaffolds

Scaffolds were cut into rectangular sections of dimension 5 × 20mm, such that, with the exception of the random scaffold, the major axis was equiangular to each fibre and fibres were predominantly aligned along the length of the strip (Figure 5-2E). Samples were mounted in a Zwick Z005 with 5N load cell (A.S.T. – Angewandte System Technik GmbH) and pre-loaded to 0.002N at a speed of 1mm/min. Samples were held at this pre-load for 10s, and then tensile loaded at a speed of 30mm/min with a time save interval of 0.1s. Samples were loaded until a shutdown threshold force of 95% of the maximum was

reached. Load displacement graphs were constructed and used to determine scaffold properties including yield force, stiffness, and stiffness in the initial toe region. A total of four samples were tested for each group. In order to further investigate the local mechanical properties within scaffolds, their relative stiffness was characterised by determining the theoretical amount of fibre deflection as a result of cellular contractile forces when seeded to scaffolds. Based on previous experience of cell seeding on these scaffolds, MSCs span approximately 25μm from fibre junctions, with this being the point at which contractile forces were assumed to act. Fibre deflection was calculated up to this point using the beam deflection equation, $y = \frac{Pbx}{6lEI}(l^2 - x^2 - b^2)$, where P = load, E = Young's modulus, I = second moment of area and all other variables illustrated as per Figure 5-2F. Results are plotted as a function of P/EI, as the load applied by the cell is assumed to remain constant across groups, while the flexural rigidity component, EI, also remains constant due to equal fibre material and diameter between groups.

5.2.3 Cell culture and proliferation

Scaffolds were punched to a diameter of 8mm and mounted in stainless steel rings in 24-well plates to secure and elevate scaffolds above the bottom of the wells. Scaffolds were prepared similarly to a previously published method (Farrugia BL, 2013), where they were pre-wet in a graded ethanol series of 100%, 90% and 70% and washed three times in phosphate buffered saline (PBS) before being incubated overnight in normal media (NM) consisting of DMEM with 10% FBS. MSCs were isolated from human bone marrow (Lonza, US) and trilineage potentiality was verified. MSCs were seeded statically on top of each sample at a number of 10,000 cells per scaffold. After 3 days, scaffolds were transferred to new well-plates. Where applicable, culture with osteogenic medium (OM) began at day 3, with medium being supplemented with 100nM dexamethasone, 10mM β-glycerol phosphate and 50μg/ml ascorbic acid. Medium was changed every 3.5 days. For DNA content and ALP assays, scaffolds were added to 100μl lysis buffer in 1.5ml tubes

containing 0.2% Triton X-100, 1mM Tris pH8, with phenylmethylsulfonyl fluoride (PMSF) being added at a ratio of 1:200 just before use. Samples were sonicated for 60s, and subjected to three freeze-thaw cycles in liquid nitrogen before being stored on ice. DNA content was quantified using a Quant-iT™ PicoGreen™ dsDNA Assay Kit (Invitrogen, P7589), with excitation and emission wavelengths of 485nm and 528nm respectively.

5.2.4 Immunofluorescence and YAP expression

Cells were fixed in 10% formalin for 10 min and washed three times in PBS. Cell membranes were permeabilised with 0.1% Triton X-100 for 10 min, washed in PBS and incubated in 1% bovine serum albumin (BSA) blocking solution for 2 hrs at room temperature. For YAP nuclear localisation studies, cells were stained with YAP antibody (sc-101199, Santa Cruz Biotechnology) diluted in BSA at a concentration of 1:50 overnight at 4°C. Cells were washed three times in BSA, and incubated for 1 hr with Alexa Fluor 594 anti-mouse (A21203, ThermoFisher Scientific) at a concentration of 1:500 in BSA. Cells were stained for F-actin (Alexa Fluor 488 phalloidin, ThermoFisher A12379) at a concentration of 1:50 in BSA for 20 min at room temperature and washed in blocking solution, followed by incubation with DAPI (Sigma Aldrich, 32670) at a concentration of 1:1000 in PBS for 10 min. Scaffolds were washed in PBS, placed on 18mm diameter coverslips, and mounted on glass slides using Fluoroshield (Sigma Aldrich, F6182) mounting medium.

Fluorescent imaging was carried out using a Leica SP8 scanning confocal microscope with 20x objective. For nuclear YAP quantification, z-stacks with 10 steps and a total thickness of 15 μm were constructed, with two fields of view being imaged for each sample. For cells cultured on glass slides (G), the total thickness for z-stacks was 4.5 μm. These stacks were used to construct 3D objects of the nuclei using the DAPI channel, and the distribution of YAP throughout the cell using the YAP channel, via the 3D ImageJ suite (Ollion, Cochennec, Loll, Escudé, & Boudier, 2013) in the FIJI distribution of ImageJ.

Nuclear YAP was quantified by determining the integrated density of YAP bound within the volume defined by the DAPI channel, and normalising to the integrated density of total volume of YAP (Figure 5-4C). The 3D nucleus objects were also used to determine the elongation of nuclei, with this being calculated via the ratio of the major to second radii of the ellipsoids and being termed nuclear aspect ratio (NAR). Cell aspect ratio (CAR) and projected area was determined by manually drawing outlines around the f-actin channel on maximum projection stacks of cells and calculating the aspect ratio and projected area of the objects in FIJI.

5.2.5 Characterisation of osteogenic differentiation

5.2.5.1 Intracellular ALP

Intracellular ALP was quantified at days 7, 14 and 21 in NM and OM. Standard curves were constructed using serial dilutions of p-Nitrophenyl phosphate (pNPP, Sigma Aldrich, N1891) with 10µl of 43µM ALP enzyme (Sigma Aldrich, P6774) in 96-well plates. For test samples, 50µl of 5mM pNPP was added to each well, with 10µl cell lysate being added followed by 70µl ddH20. Samples were incubated for 1hr in the dark at room temperature, after which reactions were stopped using 20µl of 3M sodium hydroxide (NaOH) and the plate was read at 405nm. ALP activity was calculated as the amount of pNPP generated by samples, divided by sample volume and reaction time.

5.2.5.2 Collagen production

At D7, 14 and 21, scaffolds were collected to evaluate collagen production. Cell-scaffold constructs were rinsed in PBS and fixed in 10% neutral buffered formalin for 15 min before rinsing in PBS again. Scaffolds were cut in half on glass slides using 4mm square grid paper as a guide, with the second half being used to evaluate mineral production as described later. Scaffolds were stained for 1hr with shaking (150rpm) with 200µl of 1mg/ml of Direct Red 80 (Sigma Aldrich, 365548) in a saturated aqueous picric acid

solution, and washed twice with shaking with 0.5% acetic acid. Scaffolds were allowed to dry before imaging. They were then added to 500µl 0.5M NaOH in 1.5ml tubes and vortexed vigorously for 10s to dissolve the bound stain. Tubes were centrifuged at 14,000g for 10 min to pellet the scaffold and debris. Standards were made by adding red staining solution to 8µl of collagen I (Corning, #354249), before centrifuging and re-suspending the collagen in 500µl 0.5M NaOH. Samples and standards were added to a 96-well plate and the absorbance read at 490nm.

5.2.5.3 Mineral production

Alizarin red solution was made at a concentration of 10mg/ml of alizarin red S (Sigma Aldrich, A5533) in distilled water, with the pH being adjusted to between 4.1 - 4.3. 200µl of alizarin red solution was added to each sample for 20 min with shaking. Samples were then washed 5 times for 3 min with shaking in distilled water, and allowed to dry before imaging. They were then added to 400µl of 55% acetic acid in 1.5ml tubes and incubated for 18hrs with 150rpm shaking at room temperature. Tubes were vortexed vigorously for 30s, heated to 85°C for 10 min, transferred to ice for 5 min, and centrifuged at 20,000g for 15 min to pellet the scaffold and debris. 300µl of supernatant was transferred to new tubes and 120µl of ammonium hydroxide added. Standards were made with known dilutions of alizarin red solution in water with the pH for each standard adjusted to between 4.1 - 4.3. Samples and standards were added to a 96-well plate and the absorbance read at 405nm.

5.2.6 Statistical analysis

MEW validation and tensile testing data is presented in terms of average and standard deviation. All subsequent biological data is presented in terms of average and standard error of the mean. Statistical analysis was performed using one-way ANOVA and Tukey's multiple comparison post-test. For proliferation and osteogenic differentiation experiments, statistical analysis was performed as above for D1 and D3 time points, with

the remaining being analysed using two-way ANOVA (scaffold and culture medium) at each time point, and Bonferroni's post-test to compare scaffold groups.

5.3 Results

5.3.1 Fibrous cellular micro-environment design and imaging

The parameters used for the fabrication of scaffolds in this study were 90°C, 50kPa and 12kV, resulting in fibre diameters of 10.4 ± 2μm, with a corresponding translation speed of 11.5mm/s being used for the writing of fibres. Fibre diameter was quantified at this configuration via SEM, where comparable results to optical microscopy were obtained. Scaffolds were fabricated with angles between subsequent layers of 90°, 45°, 10° and random (Figure 5-1C), and were designed such that that fibre spacings (apparent and layer pore size) could be maintained irrespective of the angle between subsequent layers. Fabricating scaffolds in this way allows for cell behaviour to be studied at different fibre alignments while maintaining pore size and effective cell infiltration as a result, and is a significant advantage of the MEW biofabrication process. The controlled architecture groups have a porosity of 97.4 ± 0.2%, while the random scaffold has a porosity of 95.4%. The 48-layered scaffolds have a theoretical thickness of 480μm, while the measured thickness is approximately 300μm. A translation speed half of that used for S90 to fabricate SR results in initially organised coiled fibres at regular spacing from each other in the initial layer, which do not deposit evenly on top of one another between layers, resulting in the build-up of a random mesh of fibres. SEM images of the four groups are shown in Figure 5-2F.

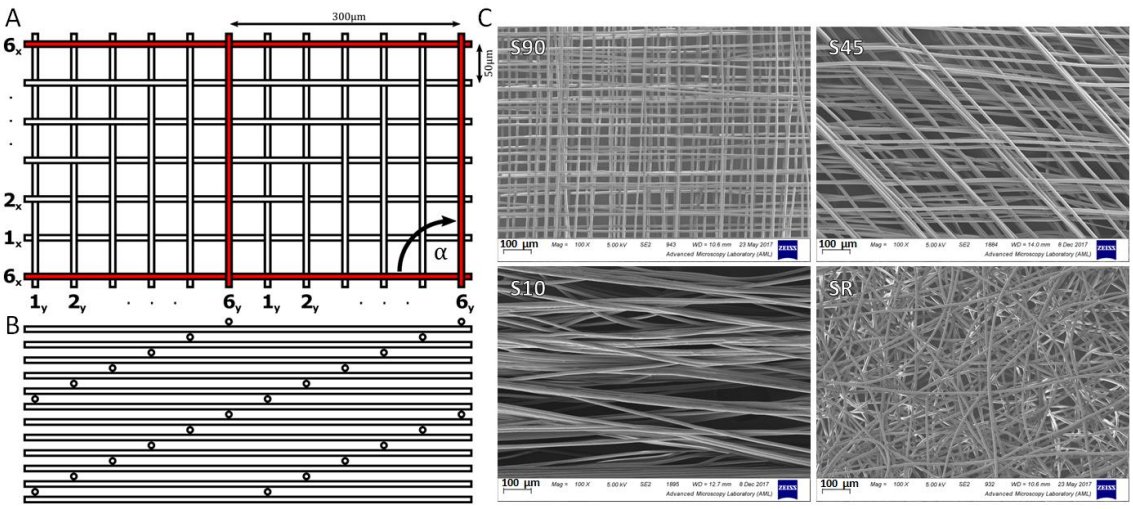

Figure 5-1 Design of scaffold architecture, which has repeating fibres on each layer in the x and y dimension with a spacing of 300µm (A). The x layer is first printed (1x), followed by the first y layer (1y). Each consecutive layer (2x, 2y etc.) is offset by 50µm, which is seen as the apparent pore size from the scaffold top view. The 300µm spacing forms larger channels through the depth of the scaffold, as can be seen in the scaffold side view (B). SEM images of all scaffold groups (C). Scale bar = 100µm.

5.3.2 Mechanical characterisation of fibrous cellular micro-environments

Overall, a trend of increasing yield force and stiffness from S90 - S45 - S10 was seen, however, an opposite trend with greatest local stiffness in S90 was demonstrated using an analytical model (Figure 5-2). Tensile testing (Figure 5-2A) revealed that yield force increases linearly with greater alignment, and increases in increments of 0.14N between S90 and S45, as well as between S45 and S10 (Figure 5-2B). Similar trends are also seen for stiffness and toe region stiffness, with a greater than 2-fold change between subsequent controlled deposition groups (Figure 5-2C-D). Interestingly, SR displayed the greatest toe region stiffness, while stiffness in the linear region was significantly lower than all other groups. This is likely due to the initial increased number of contact points between fibres in the random scaffold, which when disrupted; facilitate the straightening of fibres with minimal force. This experiment, however, provides information on scaffold properties when loaded in a single direction (Figure 5-2F), and fails to provide information on the local mechanical properties which are more relevant in terms of how cells perceive scaffold stiffness. Further investigation into these properties was carried out via an analytical model

(Figure 5-2F). While perpendicular fibre spacing is constant between groups, an inherent consequence of altering fibre angle on subsequent layers is the altered length of fibre sections between junctions, which in turn alters the bending stiffness of these fibres. i.e. In Figure 5-2F, "b" remains constant at 25µm, while "a" increases with more acute angles, resulting in reduced local stiffness in S45 and S10. This is demonstrated via calculating fibre deflection for a given force, where S10 is seen to deflect significantly more than S90 and S45, implying a lower bending stiffness (Figure 5-2G). Further focusing on the initial region, it can be seen for example that at a distance of 10µm from the fibre intersection, S90 has a stiffness 2-fold greater than S45 and 14-fold greater than S10, with these differences further increasing at greater distances along the fibre (Figure 5-2H).

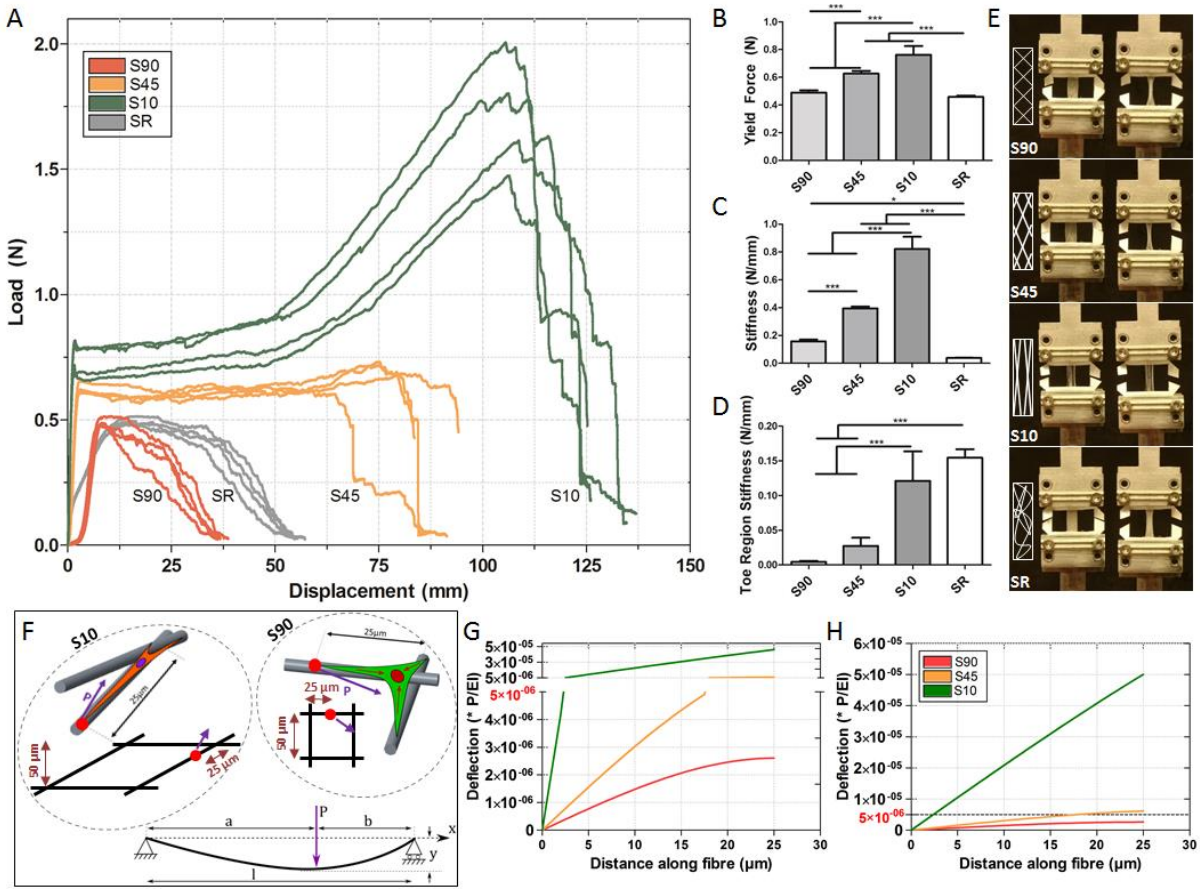

Figure 5-2 Mechanical characterisation of MEW scaffolds. The effect of geometry on scaffold behaviour under loading illustrated via load – displacement curves (n = 4 scaffolds) (A), yield force (B) and stiffness (C) which increase with greater fibre alignment, and stiffness of the toe region (D). Scaffolds before testing and after being loaded to approximately 50% of the yield strain (E). Local mechanical properties were investigated via an analytical beam bending model with contractile cellular forces assumed to act 25µm from fibre junctions

(F). Deflection as a function of length along fibres was plotted as a function of P/EI, which is assumed to remain constant across all groups (G). The same data was plotted with a focus on the initial region of each curve, showing the differences in deflection, and as a result, bending stiffness between groups (H).

5.3.3 Attachment and proliferation of human MSCs

MSCs attached to all scaffolds efficiently demonstrating early adhesion and infiltration of the constructs as demonstrated by DNA content at day 1 (Figure 5-3). Proliferation was studied up to 21 days, with significant increases first being detected by D7, at an average 4-fold increase compared to DNA at D3. Cells continued proliferating up to D21, however at a reduced growth rate, with a further 3-fold increase in DNA being seen between D7 and D21. Increased DNA content is seen in SR at most time-points, with this likely being due to the more dense random mesh of fibres resulting in a greater seeding efficiency and number of contact points for proliferation. Of note is also the lower DNA content in S45 across several experiments, however this is not significant compared to other controlled deposition groups with the exception of D14 OM. By D21, DNA content is similar between all controlled deposition groups suggesting little effect of fibrous architecture over long durations. There were no significant differences in DNA content between cells cultured in OM or NM groups at any time-point.

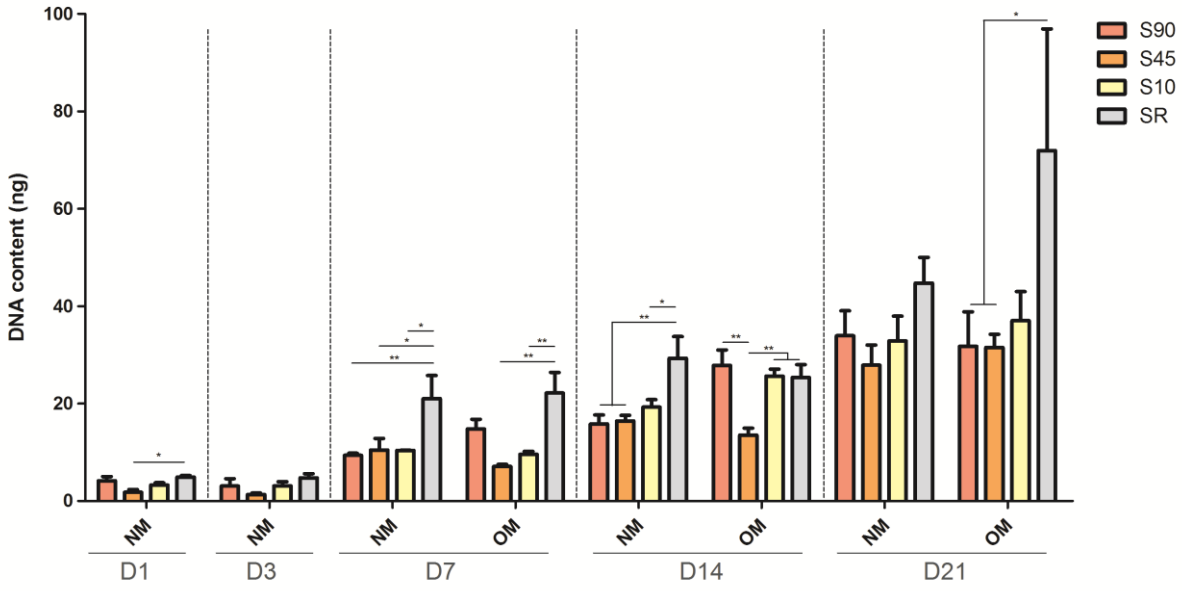

Figure 5-3 Proliferation quantified via DNA content in normal medium (NM) and osteogenic medium (NM) up to 21 days (n = 3 scaffolds).

5.3.4 Fibrous architecture mediates stem cell shape and mechano-signalling

Scaffold architecture can clearly be seen to influence cell behaviour, in terms of both shape and signalling (Figure 5-4). By D3, cells are distributed homogenously across the scaffolds with vastly altered morphology due to differences in their surrounding 3 dimensional fibrous environment (Figure 5-4A). In S90, a large proportion of cells branch around the corners of pores forming fillet-like features at fibre intersections. They can also be seen to branch between fibres with no contact at intersections, resulting in regions of cell processes being extended across open pore regions. Similar cell morphologies are seen in S45, however there is a greater degree of alignment as a result of the underlying architecture. Cell alignment is drastically increased in S10, with the majority of cells aligned in a single direction with minimal branching across pores. There are a variety of morphologies seen in the random scaffold, with some cells having several processes attaching to multiple fibres, and others aligning primarily along single fibres. CAR, NAR and cell area were quantified at D1 and D3 as indicators of cell morphology, and vary considerably depending on substrate architecture (Figure 5-4B). CAR is greatest in S10, with a fold change of 3 and 2 compared to S90 in days 1 and 3 respectively. NAR follows the same trend, with significantly greater values in S10 compared to S90. Projected cell area followed a trend inverse to aspect ratios, with area significantly increased in S90 compared to S10 at D3. The above markers of cell morphology in SR were similar to those in S90. As expected, cells on glass exhibit the lowest values of CAR and NAR, and greatest cell area due to their highly spread nature.

YAP was subsequently investigated as a marker of cell contractility and mechanosensing on scaffolds and expressed as the percentage of YAP contained within the nucleus, quantified as the integrated density of the YAP channel fluorescence bound within

the DAPI channel normalised to total cellular YAP integrated density (Figure 5-4C). There is a non-significant downward trend in YAP expression across groups as fibre alignment increases, with nuclear YAP being lowest in the random scaffold (Figure 5-4D). Similar findings are maintained at D3, with nuclear YAP expression being greatest in S90 and S45, however, it is seen to drop slightly at this time, perhaps due to greater cell number leading to greater cell-cell contact (Aragona *et al.*, 2013).

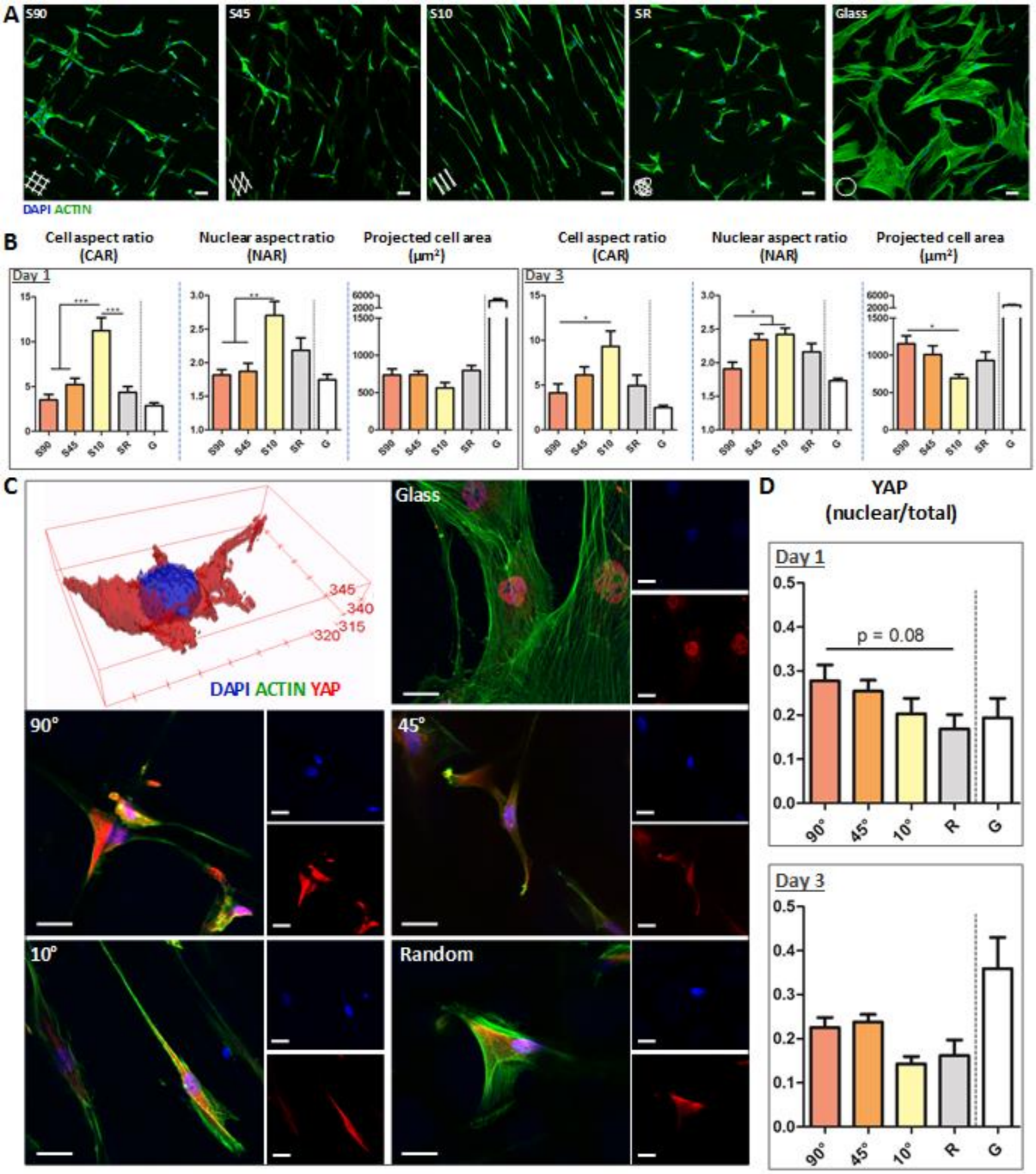

Figure 5-4 Effect of scaffold geometry on cell behaviour. Cells have a tendency to branch across fibres in the S90, S45 and SR scaffolds, while they align predominantly along single fibres in S10 (A) (Scale = 50μm). Cell aspect ratio (CAR), nuclear aspect ratio (NAR) and projected cell area quantified at days 1 and 3 (B) (n ≥ 18 cells per group). YAP was studied in terms of nuclear expression (C) (Scale = 20μm) and quantified by dividing nuclear YAP by total YAP (D) (n ≥ 65 cells per group).

5.3.5 Fibrous architecture directs human stem cell osteogenesis

5.3.5.1 ALP activity

Minimal ALP activity is detected at D7 in all groups, with notable increases appearing by D14, particularly in OM (Figure 5-5A). Considerably greater levels are seen by D21 in OM, with ALP activity being significantly greater in S90 and SR scaffolds compared to other groups, with a 2.5-fold increase in S90 compared to S45 and S10. The elevated levels detected in the random scaffold correlate to the higher cell number in these scaffolds by D21, however it is worth noting that irrespective of greater cell numbers in SR, total ALP activity is greatest in S90 indicating the influence of scaffold architecture on ALP expression. This is further shown by the normalisation of ALP activity to DNA content, revealing the vastly increased levels of ALP activity being released per cell in S90 and indicating the potential of this fibrous architecture for driving MSC osteogenic differentiation (Figure 5-5B).

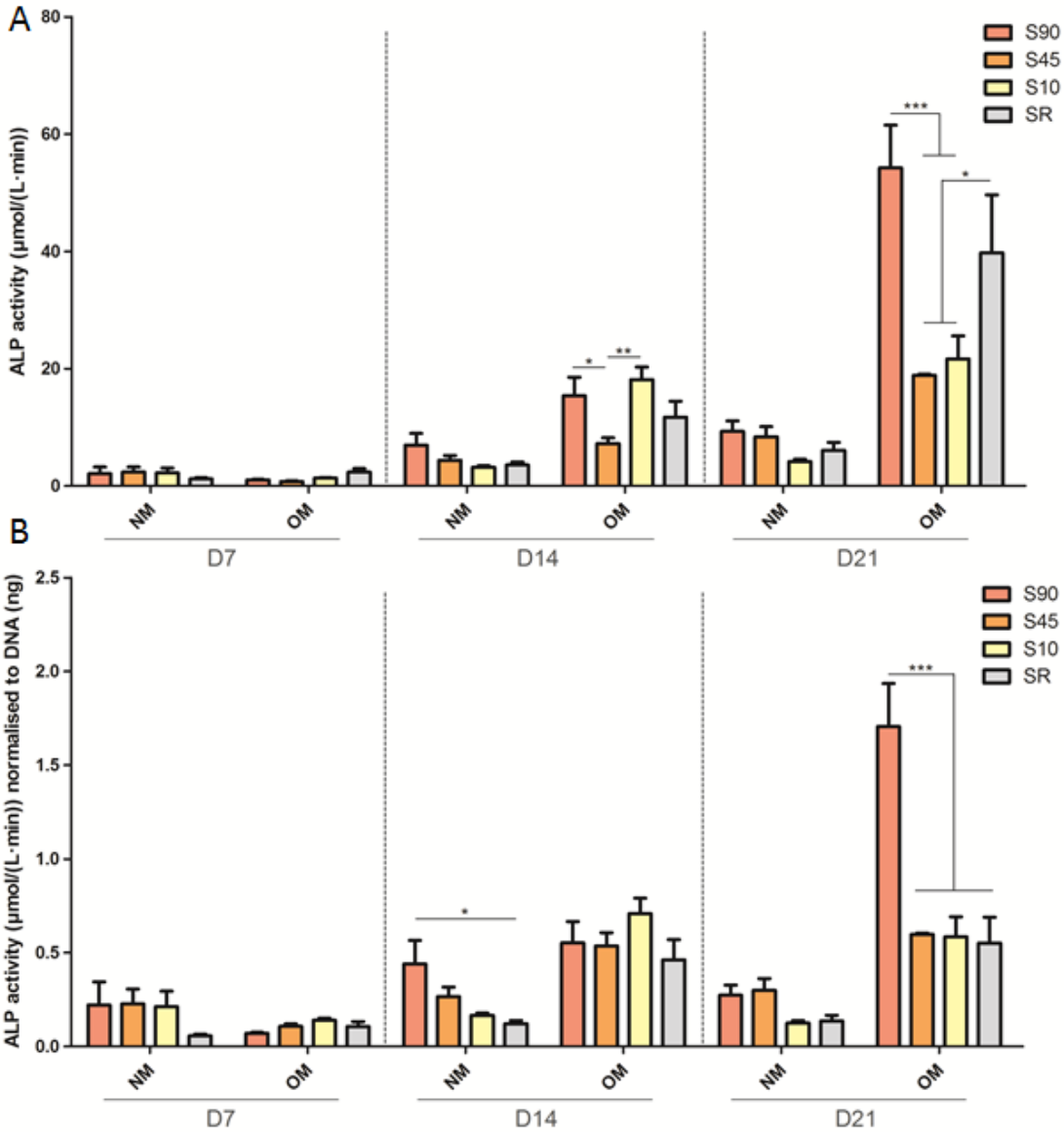

Figure 5-5 Total ALP activity in NM and OM (A), and ALP activity normalised to DNA (B). (n = 3 scaffolds).

5.3.5.2 Collagen production

Collagen production follows a similar trend to ALP activity after 21 days, with greatest levels in S90 and SR when cultured in OM. While difficult to visually differentiate collagen levels due to the 3D nature of scaffolds (Figure 5-6A), dissolution and quantification of the stain reveals relatively low levels of collagen detected at D7, with significant increases in collagen deposition detected by D14 in both NM and OM (Figure 5-6B). Collagen levels in S45 and S10 begin to plateau at D14, with further increases seen in S90 and SR by D21. Normalising this data to DNA content reveals elevated collagen in S45 by D14, however, this is influenced by the low amount of DNA measured in the

scaffolds at this time point, and no further increases are seen after 21 days. Collagen production per cell is greatest in S90 by D21 in OM, with this increase being significant compared to S10 and SR (Figure 5-6C).

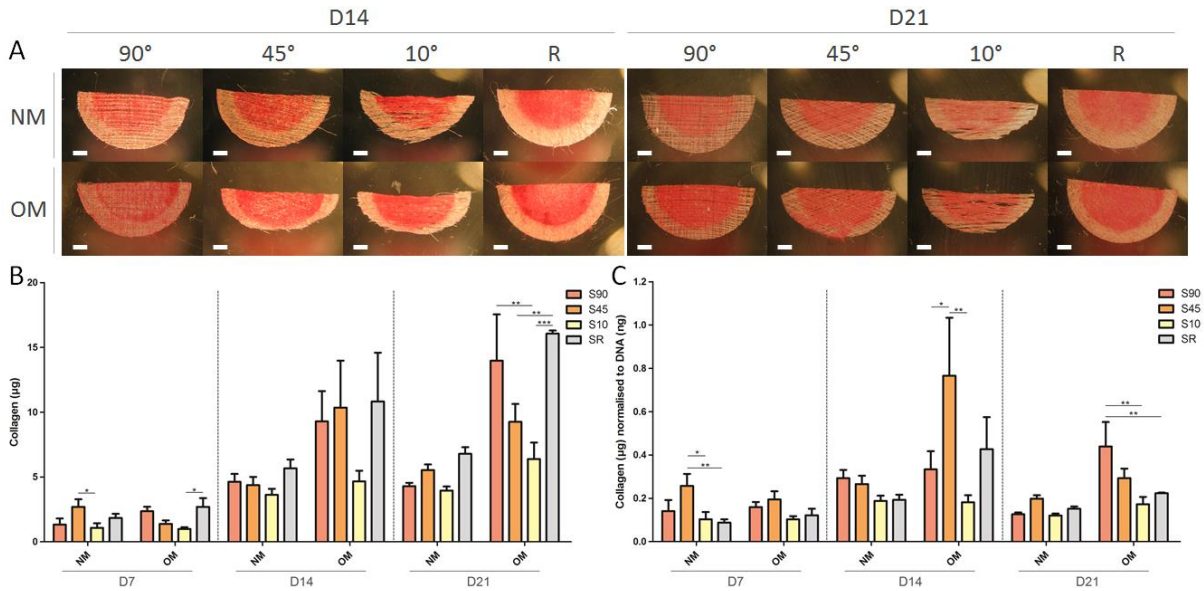

Figure 5-6 Collagen production in scaffolds at days 14 and 21 (A), and collagen quantified at days 7, 14 and 21 (B). Collagen content normalised to DNA (C). (n = 3 scaffolds). Scale = 1mm.

5.3.5.3 Mineral production

Finally, mineralisation was quantified via calcium production as a late marker of osteogenic differentiation, and as per previous markers, was found to be significantly enhanced in S90 constructs. Calcium was not detected at D7, with minimal levels being seen at D14 (Figure 5-7A). Calcium deposition increases rapidly between D14 and D21, with considerably enhanced staining being detected in OM at D21, shown via the total calcium levels per scaffold (Figure 5-7B). Mineralisation is greatest in S90, which can be seen to have significantly greater calcium deposition than S10 and SR, with fold changes of 2 and 3 respectively. When considering mineralisation data normalised to DNA content, increases can be seen in S45 at D14, however this plateaus with no further increases as before with ALP and collagen data (Figure 5-7C). In S90, however, further increases in calcium concentration per cell are seen by D21, with an almost 5-fold increase compared to SR. It is also of note that this increased mineralisation can be felt structurally when

removing the S90 OM scaffolds from their holders at D21. These scaffolds are considerably more rigid and can easily be handled (Figure 5-7C, inset), compared to earlier time-points where they wrap around forceps and are unable to support their own weight when wet.

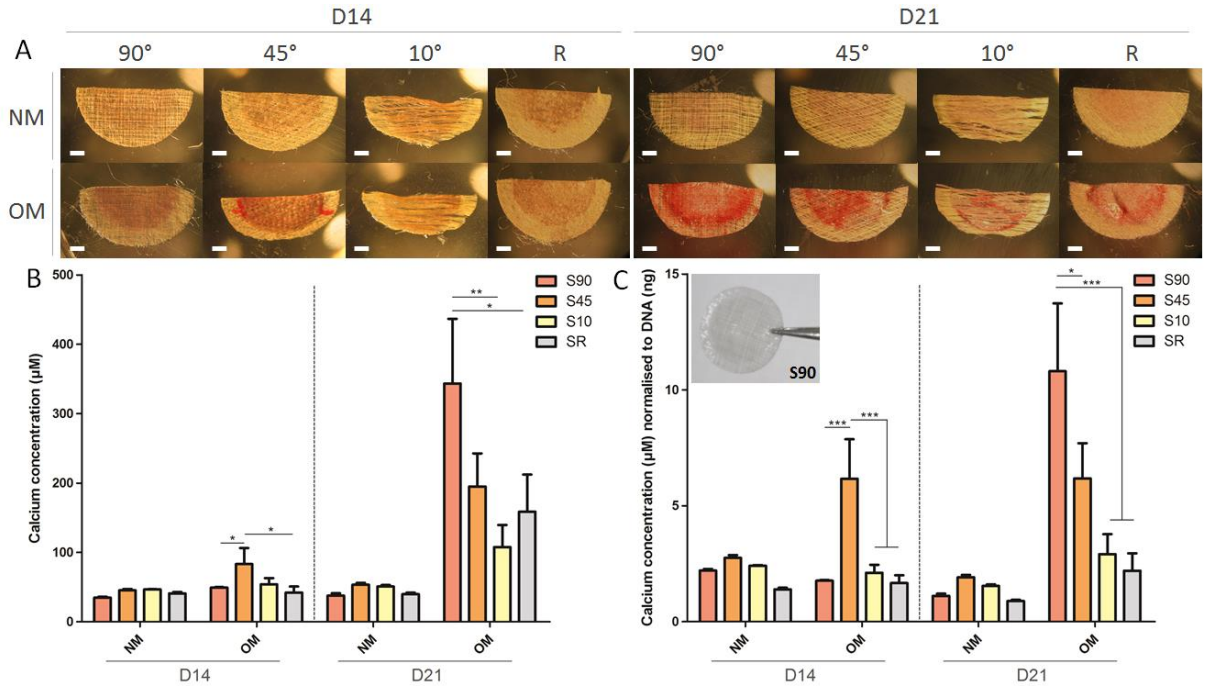

Figure 5-7 Mineralisation in scaffolds at days 14 and 21 (A), and quantification of calcium concentration (B). Calcium concentration normalised to DNA (C). (n = 3 scaffolds). Scale = 1mm.

5.4 Discussion

Tissue architecture is fundamental to dictating cellular function via physical cues eliciting specific responses and maintaining physiologically appropriate tissue specific behaviour (Frantz *et al.*, 2010; Rozario & DeSimone, 2010). Alterations in this architecture, independent of biochemical makeup, can initiate and drive disease. However, delineating the influence of biophysical from biochemical cues *in vivo* is currently not possible, while *in vitro* models of fibrous ECM-like cellular environments are limited by current biofabrication techniques. Therefore, as a means by which to study the effect of fibrous architecture on cell behaviour *in vitro*, MEW was utilised due to its unique ability to form microscale fibres and control their orientation in three dimensions. The custom-built apparatus was optimised to form consistent micron scale fibres and fabricate cell culture

platforms with varying degrees of fibre alignment to study the influence of fibrous architecture on MSC behaviour in a controlled 3-dimensional setting. It was demonstrated that a 90° fibre orientation resulted in the increased spreading and branching of cells compared to 45° and 10°, leading to increased cytoskeletal tension and nuclear YAP from as early as 24 hours post seeding. Furthermore, it was then demonstrated that this spread morphology and enhanced mechanosignalling, dictated by structural features alone, led to long term osteogenic lineage commitment of MSCs as measured by ALP expression, collagen production and mineralisation over 21 days. These findings clearly demonstrate that critical influence of 3D fibrous ECM-like architecture on stem cell behaviour which has implications for both tissue engineering strategies and disease progression.

Architecture mediated changes in cell behaviour were then investigated using MEW fabricated cell culture platforms, which were found to significantly alter cell shape and mechanosignalling. Tensile testing and analytical characterisation was carried out to assess the role of mechanical properties in mediating these changes. While tensile testing provided information on the global uniaxial tensile properties which varied significantly between groups, these findings are largely influenced by specimen orientation during testing. Rotating all specimens by 90°, it would be expected that stiffness is greatest in S90, with a downward trend towards S10. Further focus was thus placed on the local mechanical properties via an analytical model, demonstrating significantly greater bending stiffness in the fibre architecture of S90. The influence of architecture on local mechanical properties on cell behaviour was then investigated. Cell and nuclear aspect ratios were lowest in S90 and S45, which along with the greatest projected cell area in these groups, indicate spreading and branching of cells across two axes. This morphology suggests an increase in cytoskeletal tension (Driscoll, Cosgrove, Heo, Shurden, & Mauck, 2015), and results in greater nuclear YAP in these scaffolds. Greater YAP/TAZ activity has been shown to be associated with increased osteogenesis (Dupont *et al.*, 2011; Hong *et al.*, 2005), with

increased YAP expression in response to fluid shear also being shown to be in accordance with increases in Runx2 and ALP (Zhong *et al.*, 2013). Recent work has also shown a depression of osteogenic differentiation with the siRNA treatment of YAP (Pan *et al.*, 2017). It is believed that the greater YAP expression in S90 and S45 is primarily due to the greater cell spreading imposed by their architecture, indicated by low cell and nuclear aspect ratios and high cell area, as well as the greater local fibre stiffness in these scaffolds, with this finding being an early indication of the osteogenic potential of these scaffolds.

To determine whether this early architecture induced cell behaviour corresponded to long term lineage commitment, the osteogenic differentiation potential of fibrous constructs was investigated, with significant upregulation of ALP activity, collagen production and mineralisation in S90 being demonstrated after 21 days when compared to more aligned architectures. This architecture is similar to that seen in the outer layer of the periosteum, where collagen fibres have no predominant alignment and thus support isotropic tissue growth (Foolen *et al.*, 2008), which may be advantageous for bone formation. While ALP and collagen could be detected from D7 in all groups, values began to rise substantially by D14. At this time point, there was no indication of any group with potentially greater osteogenic potential. Calcium production was seen to rapidly increase from D14, with mineralisation being observed to a much greater extent at D21. At this point, there was a consistent trend seen across the three osteogenic markers, which were all shown to be significantly upregulated in the S90 scaffold, reinforcing its greater osteogenic potential above all other scaffold groups. Due to the consistent porosity and fibre spacing between groups, excluding SR, this upregulation is seen solely due to the altered fibre architecture and corresponding pore shape. This leads to greater cellular contractility as evidenced by increased nuclear YAP expression after as early as 24hr post seeding, followed by an increase in ALP activity and collagen production and finally leading to a significant upregulation in mineral deposition. It is widely known that greater substrate

stiffness enhances stem cell osteogenesis (Engler *et al.*, 2006), however the structure and chemistry of the matrix are also of key relevance (Reilly & Engler, 2010). As with nuclear YAP expression, the osteogenic potential of scaffolds is primarily a result of the geometry dependant limitations imposed on cells by the scaffold architecture as well as the local stiffness variations as a result of fibre architecture.

5.5 Conclusion

In summary, via utilising innovative biofabrication techniques, the means by which biophysical cues dictated by ECM-like fibrous architecture can drive human stem cell behaviour independent of biochemical signals has been demonstrated. While previous studies have investigated this mechanism in random and aligned fibrous scaffolds, this is the first study which has investigated the effect of a range of fibrous architectures (on the scale of microns) on human stem cell behaviour, with fibre orientation dictating cell morphology, mechanosignalling and lineage commitment in 3 dimensions. As fibrous scaffold architecture can be easily tailored using MEW, this technique represents a powerful tool for the fabrication of scaffolds due to the possibility to create high porosity, fibrous constructs with precision tailored architectures, allowing for the optimisation of architecture to control cell mechanobiology and tissue specific behaviour. This study therefore demonstrates the importance of fibre architecture on directing stem cell behaviour, highlighting the need for characterising and optimising scaffold architecture for tissue specific applications.

Chapter 6

Melt electrospun written scaffolds with tailored fibrous and mineral architectures to enhance protein delivery and human MSC osteogenesis for bone regeneration

6.1 Introduction

Autografts are the gold standard for bone defect repair due to their osteoconductive, osteoinductive and immunocompatible properties, but unfortunately are limited in supply (Yaszemski, Payne, Hayes, Langer, & Mikos, 1996). Due to technology advancements and an improved understanding of the physiological mechanisms of bone repair, synthetic tissue engineering approaches have demonstrated great progress in developing bioinspired materials that can promote bone formation (Winkler, Sass, Duda, & Schmidt-Bleek, 2018). These approaches continue to fall short of the gold standard however, therefore, continued development is required. Bone is a complex, hierarchical multi-phasic organ comprised primarily of mineralised collagen fibrils spanned by additional continuous, cross-fibrillar mineral units (Reznikov *et al.*, 2018; Margaret Tzaphlidou, 2008). It was only recently identified that the first fundamental component in this hierarchy is composed of needle-shaped mineral units of base 5 nm and length 50 – 100 nm, which merge to form platelets and mineral stacks and aggregate to form irregular 3D structures of size 200 – 300 nm which are crossfibrillar in nature (Reznikov *et al.*, 2018). It is the combination of collagen and mineral with specific topographies, working in unison in this hierarchical structure, which gives the bone both its excellent biological and mechanical properties. Moreover, this mineral nano-topography identified in bone is believed to be a key contributor to non-

collagenous protein binding and stabilisation, preserving proteins for centuries within the tissue without denaturation (Asara, Schweitzer, Freimark, Phillips, & Cantley, 2007). This therefore provides a potential strategy for therapeutic delivery in regenerative medicine (Yu *et al.*, 2017). Recapitulating this unique multiscale architecture may represent an innovative approach to develop effective bioinspired materials to promote bone repair.

Bone formation occurs following MSC osteogenic differentiation into an osteoblast, which begins laying down collagen fibrils and enriching the surrounding environment with alkaline phosphatase and osteocalcin to promote mineral deposition within the collagen template (Alford, Kozloff, & Hankenson, 2015; Rutkovskiy, Stensløkken, & Vaage, 2016). The resulting nano-crystals are initially formed within collagen fibrils, eventually nucleating to fill the voids forming a composite structure of mineral and collagen fibres approximately 10 μm in diameter (Kane & Ma, 2013). The underlying collagen fibrillar template is thus crucial in dictating cellular behaviour in bone and many other tissues, with dysregulation of this unique structure leading to undesirable outcomes including cell death, abnormal differentiation and tumour development (Bonnans, Chou, & Werb, 2014; P. Lu, Takai, Weaver, & Werb, 2011). Through the advent of new technology such as 3D printing, precise control of scaffold architecture is now achievable (Hutmacher *et al.*, 2001). Fused deposition modelling (FDM) can produce scaffolds with defined fibre architecture creating pores of differing shapes (Di Luca *et al.*, 2016) in addition to facilitating mineral incorporation (Bergmann *et al.*, 2010; S. C. Cox, Thornby, Gibbons, Williams, & Mallick, 2015; Daly *et al.*, 2017; Fierz *et al.*, 2008; Inzana *et al.*, 2014), which in turn drives MSC differentiation down specific lineages. However, FDM is limited in that fibre diameters below 100 μm are difficult to fabricate. These relatively large fibres result in a pseudo-3D environment at the scale of the cell (Hogrebe, Reinhardt, & Gooch, 2017a). Electrospinning is a common fabrication technique to produce physiological fibre diameters on the nano/micron scale which have been utilised in bone tissue engineering strategies

(Labour *et al.*, 2018; P. Zhou *et al.*, 2018). However, due to the unstable "whipping" motion of the electrospinning jet during fibre deposition, there is limited control over fibre architecture using this approach. Melt Electrospinning Writing (MEW) is a recently developed 3D printing technology which overcomes the above limitations of FDM and electrospinning, being capable of fabricating and controlling the deposition of micron-scale fibres (Brown *et al.*, 2011; Hochleitner *et al.*, 2015; F. M. Wunner *et al.*, 2017). This facilitates the manufacture of complex fibrous micro-architectures (Miguel Castilho, Mil, *et al.*, 2018; de Ruijter *et al.*, 2017; Hochleitner, Chen, *et al.*, 2018) consistent with that seen in native ECM including that of bone. MEW was previously utilised to fabricate scaffolds with bone inspired fibre diameters of 10 µm, and it was investigated whether the fibre architecture in terms of degrees of alignment could influence stem cell behaviour (chapter 5). Interestingly, the combination of fibre diameter and alignment had significant impact on cell shape, cell signalling and ultimately MSC osteogenesis, with a 90° fibre architecture mediating a 4-fold increase in stem cell mineralization when compared to 10° aligned architectures or a traditional random electrospun scaffold, demonstrating the critical role of fibrillar architecture in mediating stem cell behaviour and highlighting MEW as a powerful tool to fabricate physiological bioinspired environments for tissue engineering strategies.

In bone tissue, the mineral component makes up 60-70% of its dry weight, and is composed primarily of non-stoichiometric apatite along with other loosely bound ions including Ca^{2+}, HPO_4^{2-}, CO_3^{2-} and Mg^{2+} in a hydrated layer at the surface (Rey *et al.*, 2009). As with fibrillar architecture, the mineral structure in bone plays a key role in mediating cell behaviour, with deficiencies or changes in mineral composition contributing to diseases such as osteoporosis (Boskey, 2013). This has been exploited in a host of strategies for orthopaedic and dental applications, where materials and surfaces have been modified with CaPs with the aim of creating biomimetic materials which promote osseointegration and tissue regeneration. This includes coatings for implant fixation, cements and adhesives for

orthopaedic and dental implants, and synthetic bone grafts (W. Habraken *et al.*, 2016). A wide range of commercially available materials have been investigated, including hydroxyapatite (HA), calcium deficient apatite (CDA), α- and β tricalcium phosphate (TCP) and biphasic calcium phosphates such as HA + TCP, with a range of other materials including dicalcium phosphate (DCP) and Tetracalcium phosphate (TTCP) also being investigated (Lc, 2009). As with fibrillar architecture, an ever increasing appreciation for the importance of the architecture and particle size of the mineral phase is being gained, which defines surface topography and thus has a considerable influence on cell behaviour and scaffold performance (Hongjian Zhou & Lee, 2011). When cultured on nano-scale HA (nHA) films with varying particles sizes from 20 – 80 nm in diameter, MSCs exhibit a trend of greater viability and proliferation with smaller particle sizes (Cai *et al.*, 2007). The osteogenic capacity of nHA has been further demonstrated in a range of studies where cells have been cultured in nHA suspensions with particles of size between 20 – 100 nm, with cells demonstrating uptake of particles and exhibiting enhanced osteogenic differentiation (YuKan Liu *et al.*, 2008; Remya, Syama, Gayathri, Varma, & Mohanan, 2014; X. Yang, Li, Liu, Zhang, & Feng, 2018). The role of HA particle size has also been investigated in the 3D printing of composite PCL-HA blends, with enhanced proliferation and alkaline phosphatase (ALP) activity of MSCs seen with nano-particles compared to micro-particles (Domingos *et al.*, 2016). Remarkably, particle size has not only been shown to be an important cue for MSC osteogenesis, but also plays a role in suppressing undesired cellular outcomes in bone. This has been demonstrated via osteosarcoma inhibition (Cai *et al.*, 2007) and reduced melanoma proliferation (B. Li *et al.*, 2008) with nHA compared to larger particles, further reinforcing the therapeutic potential of nano-scale particles for additional applications such as bone regeneration following tumour ablation.

Bone tissue also houses non-collagenous proteins and growth factors embedded within its composite matrix, which are remarkably resolute and can be preserved for

centuries due to the great stability provided by the mineral structure (Asara *et al.*, 2007). It is thus of no surprise that the great binding affinity to HA of a host of biological and synthetic components has been exploited for therapeutic benefits. HA has been extensively used as a delivery mechanism for BMP2 protein with proven success in a number of *in vivo* models (Dellinger, Eurell, & Jamison, 2005; Notodihardjo, Kakudo, Kushida, Suzuki, & Kusumoto, 2012; Xiong *et al.*, 2015), while nHA particles have also been used for non-viral gene delivery of BMP2 to enhance MSC osteogenesis (Curtin *et al.*, 2012; Gonzalez-Fernandez *et al.*, 2017). Anti-tumour drugs have also been combined with nHA as a delivery vector, with potential applications in osteosarcoma chemotherapy (Palazzo *et al.*, 2007) and the development of targeted drug delivery methods (Wen Sun *et al.*, 2018). Interestingly, protein binding and stabilization is closely related to the nanoscale structural features of the mineral coatings (Yu *et al.*, 2017), demonstrating the importance of controlling this nHA architecture. In addition to the already pro-osteogenic capabilities of biomimetic nHA, there is great potential to exploit its natural affinity to further advance treatments by facilitating therapeutic delivery providing an extensive range of enhanced regenerative benefits.

In this study, the aim was to recapitulate the native structure of bone via the development of a biomimetic tissue regeneration strategy comprised of a micro-fibrous matrix spanned by an intrafibrillar nano-needle mineral phase stabilising bound protein for enhanced tissue regeneration. Herein, MEW technology was used to create fibrous 3D PCL micro-architectures. These scaffolds were further modified with an extrafibrillar coating of plate shaped micron-sized calcium phosphate (pHA) crystals, or with a novel extrafibrillar coating of nano-needle hydroxyapatite (nnHA) crystals. A third scaffold was developed whereby nano-sized crystals were placed intrafibrillarly during the MEW process (iHA). Along with vastly differing surface topographies, surface chemistry was also altered, with calcium/phosphate ratios within the range seen in healthy native bone. Biological

characterisation demonstrated significantly enhanced human stem cell mineralisation with extrafibrillar coatings, with a needle topography producing the most robust bone formation, demonstrating the importance of bone mimetic architectures. Given the protein stabilising properties of mineral, these materials were further functionalised with BMP2. Extrafibrillar coatings of nano-needles facilitated a controlled release of BMP2 from the scaffold which further enhanced mineral deposition by stem cells. This study thus outlines a method for fabricating scaffolds with precise fibrous micro-architectures and bone mimetic nnHA extrafibrillar coatings which significantly enhance MSC osteogenesis and therapeutic delivery and thus holds great promise for bone tissue regeneration.

6.2 Materials and methods

6.2.1 Scaffold fabrication

6.2.1.1 MEW of PCL

Fibrous scaffolds with a fibre diameter of 10 μm, square apparent pore size of 50 μm, and layer offset of 300 μm were fabricated on a custom built MEW apparatus as previously described (chapter 4-5), where it has been demonstrated that this fibrous scaffold architecture is optimal for MSC osteogenesis. Briefly, heated air at a temperature of 90°C was circulated around a syringe to melt PCL (Sigma Aldrich 440744, average Mn 80,000), with air pressure being used to extrude the polymer through a 21G needle with high voltage applied at a distance of 15 mm from a grounded aluminium collector plate. Fibres were deposited with a 90° offset between subsequent layers to result in a square pore shape. Scaffolds for control (C) groups were used without further mineral modification.

6.2.1.2 pHA coating

This coating was carried out via a saturated SBF solution, as described by Martine *et al.* (Martine *et al.*, 2017). Reactions were carried out in 50ml conical tubes, with reagent

volumes being maintained at 40 ml at each step of the process and 6 scaffolds of dimension 3 x 3 cm being processed per tube. Scaffolds were immersed in 70% ethanol for 15 min under vacuum and treated with 2M NaOH for 45 min at 37°C following a 5 min vacuum treatment to remove air bubbles. Scaffolds were rinsed 5 times in MilliQ water and immersed in 10x SBF, previously brought to a pH of 6 for 30 min at 37°C following a 5 min vacuum treatment. The coating step in 10x SBF was repeated a further two times minus the vacuum treatment. Scaffolds were then treated with 0.5M NaOH for 30 min at 37°C, rinsed 5 times in MilliQ water and allowed to dry overnight.

6.2.1.3 Nano-needle hydroxyapatite (nnHA) coating

A nano-hydroxyapatite coating method was developed to coat scaffolds with nano-needle mineral units. Sample pre- and post-processing was carried out as per the CaP coating procedure, with the 10x SBF treatment step being substituted for alternative calcium and phosphate solutions (Cunniffe, O'Brien, *et al.*, 2010; Kumta *et al.*, 2005). The calcium solution was made with 0.05M calcium chloride dihydrate (Sigma Aldrich C7902) in MilliQ water. The phosphate solution was made with 0.03M sodium phosphate tribasic dodecahydrate (Sigma Aldrich S7778) and 0.01M NaOH in MilliQ water. The entire coating procedure is outlined as below. Scaffolds were immersed in 70% ethanol for 15 min under vacuum and treated with 2M NaOH for 45 min at 37°C following a 5 min vacuum treatment to remove air bubbles. Scaffolds were rinsed 5 times in MilliQ water and added to 20 ml of the calcium solution. 20 ml of the phosphate solution was slowly added to the calcium solution, and scaffolds were incubated for 30 min at 37°C following a 5 min vacuum treatment. This coating procedure was repeated a further two times minus the vacuum treatment. Scaffolds were then treated with 0.5M NaOH for 30 min at 37°C, rinsed 5 times in MilliQ water and allowed to dry overnight. Scaffolds treated with this coating method are defined as nano-needle hydroxyapatite (nnHA).

6.2.1.4 Hydroxyapatite incorporated (iHA) PCL MEW

A nHA-PCL blend was created by incorporating a 3.5wt% of nano-hydroxyapatite (Sigma Aldrich 677418) into the polymer. PCL and nano-hydroxyapatite with a total mass of 1 g was added to a glass vial, with 10 ml of chloroform being added under stirring until dissolved. Particles were dispersed in the solution by sonication for 1 h, after which it was poured into a glass dish and left overnight for chloroform to evaporate. The resulting film was formed into pellets which were loaded into 1 ml BD-Braun syringes. The syringes were heated for 1 h at 110°C, and centrifuged at 4,000g for 60 s to remove air. The previous heating and centrifugation steps were repeated for a total of 8 cycles, or until a homogenous blend was present in the syringe with no air bubbles. MEW processing parameters were optimised to facilitate controlled deposition of PCL-nHA blends, with temperature increased to 110°C and voltage increased by approximately 0.5 kV. Scaffolds for this modification method are defined as fibre incorporated hydroxyapatite (iHA).

6.2.2 Scaffold characterisation

6.2.2.1 SEM imaging and Energy-dispersive X-ray spectroscopy

For SEM imaging, samples were prepared for imaging by coating with gold/palladium for 40 s at a current of 40 mA. For analysis with energy-dispersive X-ray spectroscopy (EDX), scaffolds were carbon coated and analysed at a voltage of 15kV in a Zeiss ULTRA plus SEM with an 80mm² Oxford Inca EDX detector. To investigate approximate calcium/phosphorus atomic ratios for each group, spectra were acquired on scaffolds for 30 s (n=6, 2 technical replicates per scaffold). Element maps were constructed by taking 2 frames at a resolution of 256 x 192 with map dwell of 4000 µs and linescan dwell of 2000 µs.

6.2.2.2 X-ray diffraction

To obtain powder samples for x-ray diffraction (XRD) analysis, 10 x SBF was allowed to precipitate in solution at a pH of 6, while for the nnHA group, calcium and phosphate solutions were mixed together and allowed to precipitate. Solutions were centrifuged at 5,000g for 40 min to collect the precipitate, which was then placed in dishes and dried for 4h at 50°C in an oven. The resulting mineral was ground into a powder using a mortar and pestle. The hydroxyapatite powder used for iHA was used for XRD analysis without any further processing. Samples were loaded in a Brucker D8 ADVANCE powder diffractometer and run for 1 h from 5 - 80° in the 2θ range with a monochromatic Cu-Kα radiation source. Values for crystallinity and crystallite size were calculated using DIFFRAC.SUITE EVA 4.1.1. Crystallite size was calculated from taking 5 measurements of the (211) peak in pHA and iHA groups. In the iHA group, crystallite size was calculated from the peak in the position of (211), (112) and (300), due to the broad peaks resulting in their merging.

6.2.2.3 Calcium staining

Samples were taken from scaffolds using a 2mm biopsy punch (n=5) and incubated with 1% alizarin red s (Sigma Aldrich, A5533) in distilled water for 10 min at a pH of between 4.1 – 4.3. Samples were rinsed 3 times with water and allowed to dry prior to imaging. To quantify bound stain, 400 µl of 10% acetic acid was applied and samples incubated at room temperature for 30 min while shaking at 150rpm. The acetic acid was added to 1.5 ml tubes, vortexed vigorously and heated to 85°C for 10 min. Tubes were transferred to ice for 5 min, centrifuged at 20,000g for 15 min, and 300 µl of the supernatant was added to new tubes along with 120 µl of 10% ammonium hydroxide. Standards were made with dilutions of alizarin red solution in distilled water, with the pH of each adjusted to between 4.1 – 4.3. Samples and standards were read at 405 nm in a 96-well plate.

6.2.2.4 Water contact angle

The water contact angle of all scaffold groups was quantified using a FTA125 contact angle analyzer (First Ten Angstroms Inc.). Samples were prepared using an 8mm biopsy punch (n=6-7). All measurements were taken 10 frames after contact of the water with the sample.

6.2.2.5 Tensile testing

Rectangular samples (n=4) of dimension 5 x 20 mm were taken from scaffolds and used for tensile testing in a Zwick Z005 with 5 N load cell (A.S.T. – Angewandte System Technik GmbH). Samples were pre-loaded to 0.002 N at a speed of 1 mm/min, and then loaded at a speed of 10 mm/min with a time save interval of 0.1 s. Load-displacement curves were graphed and used to determine the stiffness, toe region stiffness and yield force for each group.

6.2.3 hMSC Cell culture

Scaffolds were punched to a diameter of 8 mm and UV sterilised for 20 min on each side before being mounted in stainless steel holders and placed in 24-well plates. Scaffolds were then pre-wet in a graded ethanol series of 100%, 90% and 70% for 20 min each before being washed three times in PBS. They were then incubated overnight in DMEM with 10% FBS at 37°C. hMSCs were isolated from bone marrow (Lonza, US), trilineage potential verified, and seeded at a number of 10,000 cells per scaffold. Scaffolds were transferred to new well plates after 24 h, and cultured in osteogenic medium (OM) from day 3, which consisted of 10% FBS DMEM supplemented with 100 nM dexamethasone, 10 mM β-glycerol phosphate and 50 μg/ml ascorbic acid. Medium was changed every 3.5 days.

6.2.4 Proliferation

At days 1,7,14 and 21, scaffolds were added to 100 µl lysis buffer (n=4) containing 0.2% Triton X-100, 1 mM Tris pH8, with phenylmethylsulfonyl fluoride (PMSF) being added at a ratio of 1:200 just before use, and stored at -80°C. Before DNA quantification, samples underwent sonication for 60 s and subjected to three freeze-thaw cycles in liquid nitrogen before being stored on ice. DNA content was quantified using a Quant-iT™ PicoGreen™ dsDNA Assay Kit (Invitrogen, P7589), with excitation and emission wavelengths of 485 nm and 528 nm respectively. The DNA content in 10,000 MSCs seeded and pelleted in centrifuge tubes was also quantified to calculate the total number of cells present on scaffolds.

6.2.5 Characterisation of hMSC osteogenic differentiation

6.2.5.1 Intracellular alkaline phosphatase (ALP)

Intracellular ALP was quantified at days 14 and 21 (n=4). 50 µl of 5mM pNPP was added to wells along with 10 µl of cell lysate and 70µl MilliQ water in a 96-well plate. Standards were comprised of serial dilutions of p-Nitrophenyl phosphate (pNPP, Sigma Aldrich, N1891) with 10µl of 43µM ALP enzyme (Sigma Aldrich, P6774) being added to each. Plates were incubated for 1 h in the dark at room temperature, and reactions were then stopped using 20µl of 3M NaOH. Absorbance was read on plates at 405 nm, and ALP activity was calculated as the amount of pNPP generated as a function of sample volume and reaction time.

6.2.5.2 Collagen production

Scaffolds were cultured up to 21 days before evaluating collagen content. Cell-scaffold constructs were rinsed in PBS, fixed in 10% neutral buffered formalin for 15 min and rinsed again in PBS before storage at -20°C. Scaffolds were stained with 200µl of 1mg/ml of Direct Red 80 (Sigma Aldrich, 365548) in a saturated aqueous picric acid

solution for 1 h with shaking at 150 rpm. Scaffolds were then washed twice with 0.5% acetic acid and allowed to dry overnight before imaging. To quantify collagen content, 500µl 0.5M NaOH was added to wells under shaking until stain was dissolved, and solutions were added to 1.5 ml tubes. Tubes were centrifuged at 14,000g for 10 min to pellet debris. Standards were made by adding direct red staining solution to 8µl of collagen I (Corning, #354249) before centrifuging at 14,000g for 10 min and re-suspending the collagen in 500µl 0.5M NaOH. The absorbance of samples and standards were read at 490 nm in 96-well plates.

6.2.5.3 Calcium production

Cell-scaffold constructs were investigated for total calcium content after 21 days using 1% alizarin red S solution as previously described for calcium staining in scaffold characterisation. Cell-free scaffolds were also cultured up to 21 days to determine the contribution of total calcium from cell mineralisation versus the calcium present due to mineral modification of scaffolds.

6.2.6 BMP2 functionalisation of MEW scaffolds

6.2.6.1 BMP2 adsorption onto scaffolds

Scaffolds were prepared, sterilised and pre-wet in a graded ethanol series as previously described in section 3.3 before being washed three times in PBS. Recombinant human BMP2 (Peprotech 120-02) was diluted to 50 µg/ml in PBS, with 20 µl of solution containing a total of 1 µg BMP2 being placed on each scaffold and incubated for 4 h at room temperature. BMP2 was then removed and scaffolds were allowed to dry overnight.

6.2.6.2 BMP2 release kinetics

Scaffolds were placed in 48-well plates (n=4) and 200 µl of PBS added to each. At each time-point, PBS was removed and 1% BSA added to result in a final BSA concentration of 0.1%. 200 µl of fresh PBS was then added to each well. Samples were

stored at -80°C until BMP2 quantity was determined via ELISA (R&D Systems DY355-05). Cumulative BMP2 release was studied at time-points 1 h, 6 h, and days 1, 3, 7, 14 and 21.

6.2.6.3 Characterisation of osteogenic differentiation

After BMP2 adsorption, 10,000 hMSCs were seeded onto scaffolds (n=4), and cultured up to 21 days after which DNA content was investigated to determine total cell number. Scaffolds were also cultured up to 21 days to assess osteogenic potential in terms of ALP activity, collagen production and calcium production as described previously.

6.2.7 Statistical analysis

Tensile testing and material characterisation data is presented in terms of average and standard deviation. Subsequent biological data is presented in terms of average and standard error of the mean. Statistical analysis was performed using one-way ANOVA and Tukey's multiple comparison post-test. Data from the BMP2 loading study was analysed using two-way ANOVA and Bonferroni's multiple comparison test.

6.3 Results

6.3.1 MEW fibre topography is significantly altered by bulk and surface modification

The topography of 90° orientate fibrous MEW scaffolds was investigated following modification with CaP based materials, where significant changes were identified with minimal influence on macroscopic scaffold morphology. Control fibres have a diameter of 9.1 μm (SD = 1.0), with relatively featureless surface topography (Figure 6-1A). The pHA coating protocol yields a rosette-like arrangement of plates of average diameter 555.3 nm (SD = 193.2) and thickness 26.0 nm (SD = 8.6) (Figure 6-1B). Total fibre diameter including the coating is 13.5 μm (SD = 2.6), giving an average coating thickness in the pHA group of 2.2 μm. In stark contrast to this, the nnHA coating protocol results in the

formation of nano-needles on the fibre surface (Figure 6-1C), with a length and diameter of 100.0 nm (SD = 29.0) and 37.0 nm (SD = 7.1) respectively. These needles form occasional aggregates which range in diameter from 150 – 500 nm. Total fibre diameter shows a minimal increase compared to the control with a value of to 10.2 μm (SD = 1.0), yielding a total coating thickness in this group of 0.55 μm. The incorporation of HA within fibres in iHA during the MEW process yields minimal changes in surface topography, with the majority of visible particles being seen as bulges just below the fibre surface, while several can also be seen to protrude above the surface with no covering of PCL (Figure 6-1D). Particles have an average diameter of 147.2 nm (SD = 78.5), as measured within PCL fibres. The incorporation of HA also has an influence on the quality of the MEW process, with periodic pulsing of the Taylor cone resulting in a larger fibre diameter distribution (fibre diameter = 11.8 μm, SD = 4.2).

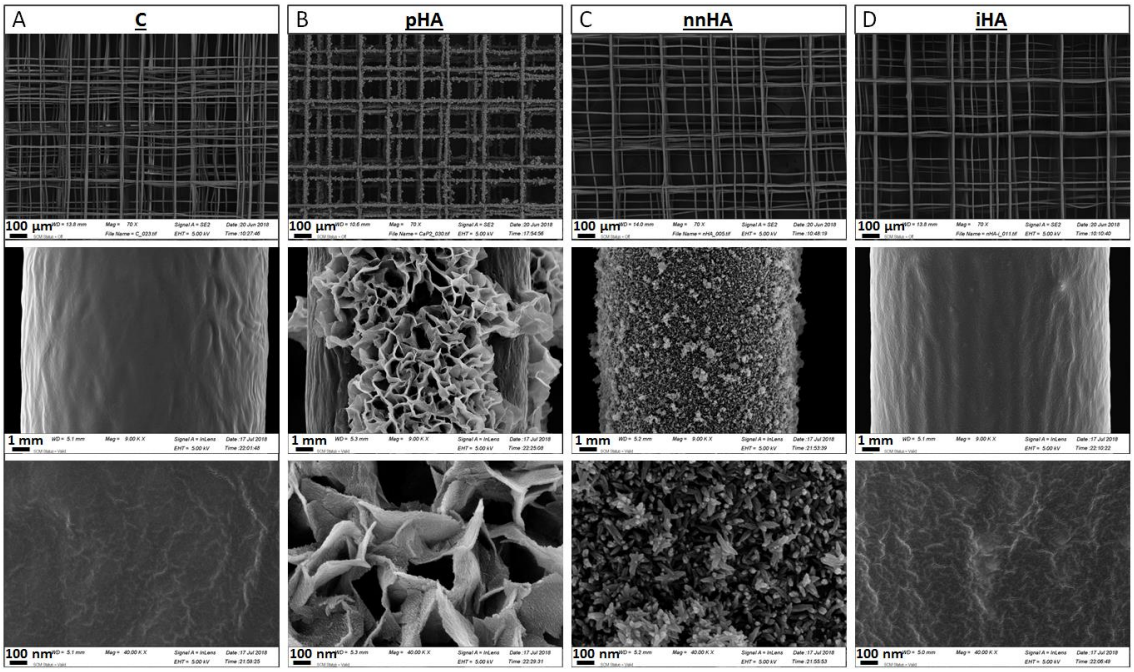

Figure 6-1 SEM imaging of scaffold groups illustrating the "plate" coating morphology in pHA, "needle" morphology in nnHA, and the presence of HA nanoparticles both within and protruding above the surface of the fibres in iHA.

6.3.2 CaP treatments modify surface chemistry

6.3.2.1 Element analysis

The coating chemistry and distribution in fibres was investigated via EDX analysis. The presence and distribution of calcium and phosphorous was first investigated via element mapping where, as expected, there was no detection in the control (Figure 6-2A). A consistent distribution of both elements was seen in pHA and nnHA coated fibres, while a sparse distribution in the iHA group confirmed the presence of HA particles within fibres. Carbon and oxygen were present in all groups from the PCL, as well as calcium and phosphorous as seen in the spectra of all groups except the control (Figure 6-2C, merge Figure 6-2D). A key difference in the pHA group was seen with the presence of sodium and magnesium in this coating. Ca/P ratios were investigated (Figure 6-2D) and were found to be close to stoichiometric hydroxyapatite with a ratio of 1.66 for the pHA group. The iHA group was investigated using both MEW scaffolds with HA incorporated, as well as the stock powder, with both having a resulting ratio of 1.76. The nnHA coating group deviated slightly from these findings, with a more calcium-rich HA with a ratio of 1.97 being identified.

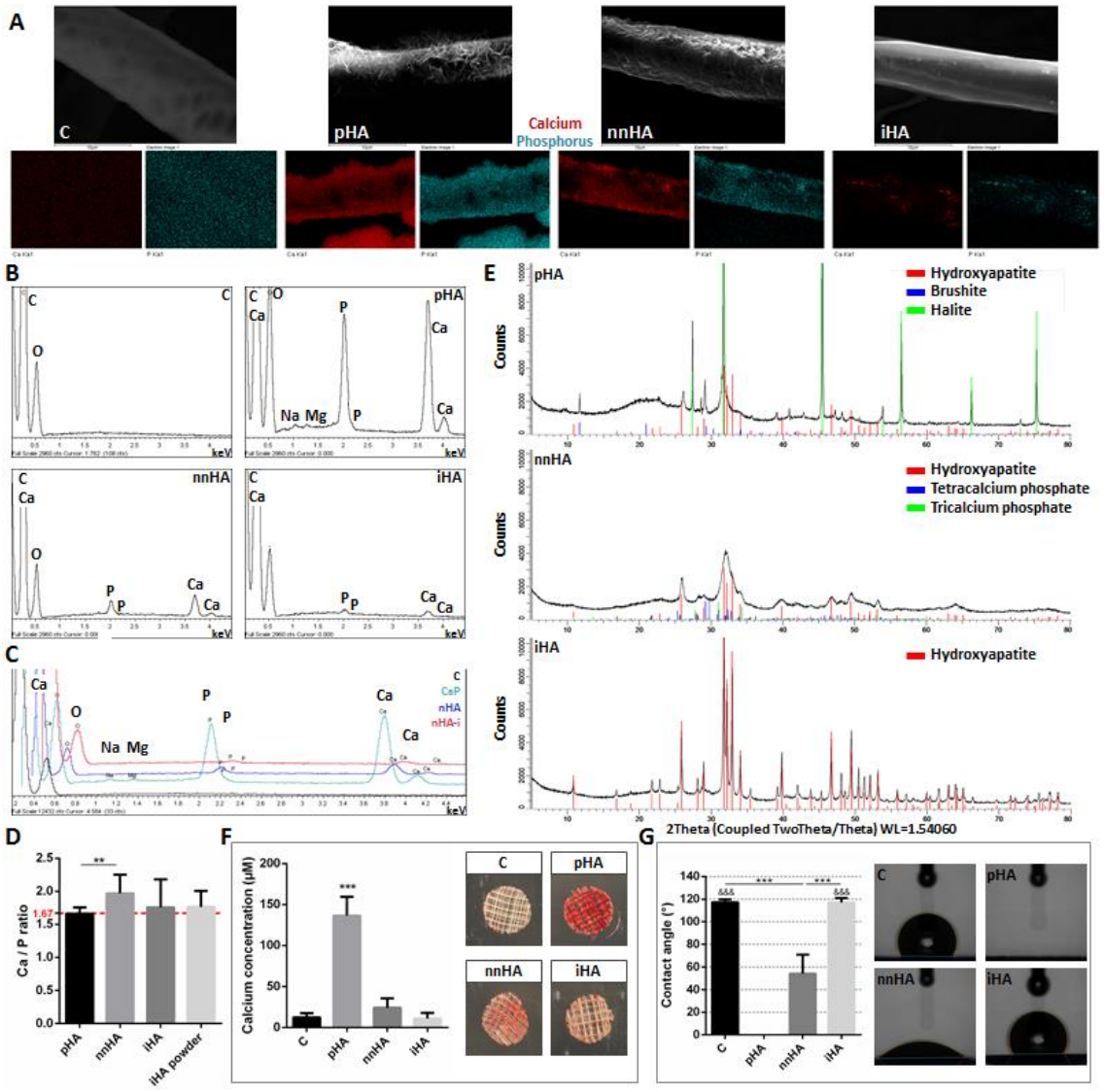

Figure 6-2 Chemical and physical characterisation of MEW-hydroxyapatite scaffolds. Element mapping of SEM images via EDX analysis illustrating the distribution of calcium and phosphorus in each group (A). Representative EDX spectra of all groups (B) and merge of spectra (C). Calcium to phosphorus ratios of EDX spectra (n=6 scaffolds, n=2 technical replicates) (D). XRD analysis of powder representative of CP, nnHA and iHA groups (E). Alizarin red staining of scaffolds (n=5) (F). Water contact angle illustrating increased hydrophilicity after hydroxyapatite coating (n=6-7) (G).

6.3.2.2 Crystal structure of surface and bulk modifications

XRD analysis was further conducted to characterise the crystal structure between groups (Figure 6-2E). Brushite, hydroxylapatite and halite were identified in the pHA group, in close agreement with previous literature (Vaquette, Ivanovski, Hamlet, & Hutmacher, 2013), with a crystallinity of 61.3%. The nnHA and iHA groups were both

shown to be composed of hydroxyapatite, with crystallinity of 52.5% and 69.3% respectively. The nnHA group was also shown to consist of tetracalcium phosphate (TTCP) and tricalcium phosphate (TCP) phases, among others. The broader peaks in the nnHA group are indicative of a smaller crystallite size, which was found to be 8.5 nm. This is in comparison to the larger crystallite sizes in pHA and iHA, which were measured at 105.8 nm and 75.0 nm respectively.

6.3.2.3 Calcium content of PCL modifications

The total calcium content as determined via quantification of alizarin red staining was investigated following scaffold modification with CaP minerals (Figure 6-2F). The calcium detected in C is minimal, and is due to slight background staining of the PCL. The greatest amount of calcium was found on pHA where nearly 150 µm was detected and was significantly greater than all other approaches. nnHA contained the second largest quantities of calcium but was still 6-fold less than that with pHA and was not significantly different to iHA. The calcium content detected in iHA is only marginally greater than that detected from background staining (C) due to the majority of HA particles being distributed throughout the bulk of the fibres.

6.3.2.4 Surface treatment enhances material hydrophilicity

The hydrophilicity of groups was investigated and found to correlate closely with their calcium content (Figure 6-2G). This is seen in the complete spreading of water on pHA, which has the greatest calcium content. The nnHA group also exhibited a significant degree of hydrophilicity, with a mean contact angle of 56.0°. The C and iHA groups were both shown to be hydrophobic in comparison, with contact angles of 117.3° and 117.1° respectively.

6.3.3 Mechanical properties are enhanced via HA-incorporation into PCL MEW fibres

Incorporation of HA into PCL in iHA is seen to increase its stiffness and yield force, while all coating protocols have minimal influence on mechanical behaviour (Figure 6-3A,B). Stiffness in the linear elastic region between 0.1 - 0.3 N is greatest in iHA scaffolds (Figure 6-3C), while stiffness in the toe region is not seen to be significantly altered between groups (Figure 6-3D). Yield force of iHA scaffolds is also significantly enhanced compared to all other groups, with an average fold increase of 1.4.

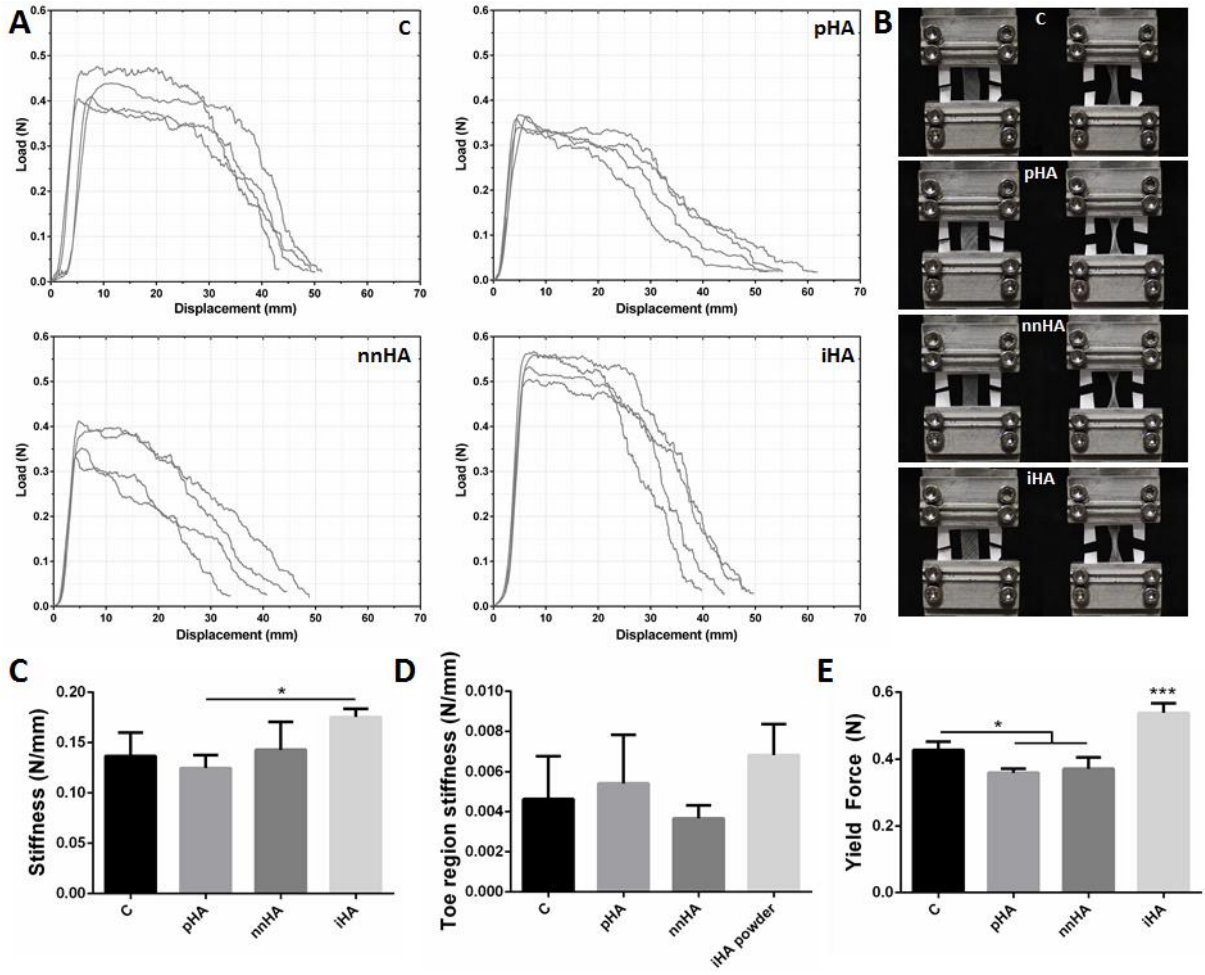

Figure 6-3 Mechanical characterisation of scaffolds via tensile testing. The incorporation of HA into fibres (iHA) can be seen to alter the mechanical properties of PCL micro-fibres (A). Scaffolds before tensile testing, and after being loaded to approximately 50% of the yield strain (B). Significant increases in stiffness seen in iHA (C), with no change in toe region stiffness (D). Yield force of iHA scaffolds is also significantly increased (E). (n=4).

6.3.4 Attachment and proliferation of hMSCs

Cells adhere to scaffolds with an average seeding efficiency of 25%, with approximately 1,100 – 3,400 cells remaining as quantified after 24 h post seeding. Adherent cells were found to branch across fibres resulting in elongated. Adherent hMSCs were commonly found branching across adjacent fibres as has been previously demonstrated with this fibre architecture (chapter 5). Interestingly the pHA coating resulted in a slightly altered cellular morphology will hMSCs adhering and spreading across the deposited mineral, masking the underlying fibre architecture (Figure 4A). The initial cell seeding efficiency is lowest in the coated scaffold groups; pHA and nnHA. This trend is seen to level off by D7 however, where cell number reaches the initial seeding quantity at a number of 10,000 per scaffold. Cells then proliferate 2-fold per week for the remainder of the study, with an average of 24,000 cells at D14 and 41,000 cells at D21. While there are no significant differences between groups at any time-point, a trend of reduced cell number in the pHA scaffold group is seen at D14 and D21.

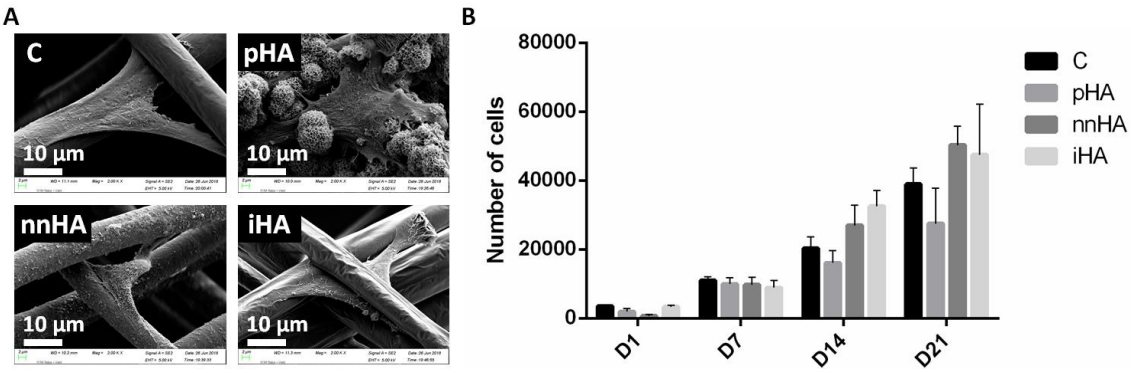

Figure 6-4 SEM imaging of cell seeded scaffolds after 24 h culture (A) Cell proliferation as quantified by DNA content. Proliferation in pHA scaffolds can be seen to be attenuated D14 compared to other scaffold groups (B). (n=4).

6.3.5 Surface treatment significantly enhances human stem cell osteogenesis

6.3.5.1 ALP activity

No significant trends were identified in hMSC ALP expression between each scaffold at D14 and D21. Total ALP activity can however be seen to be greater in nnHA and iHA groups at these time-points (Figure 6-5A). Of note is the 2.2-fold increase in ALP activity in nnHA at D21 compared to D14, in contrast with all other groups which remain constant between these time-points. Normalising these results to cell number reveals no further trends in ALP expression (Figure 6-5B), which remains relatively constant between groups.

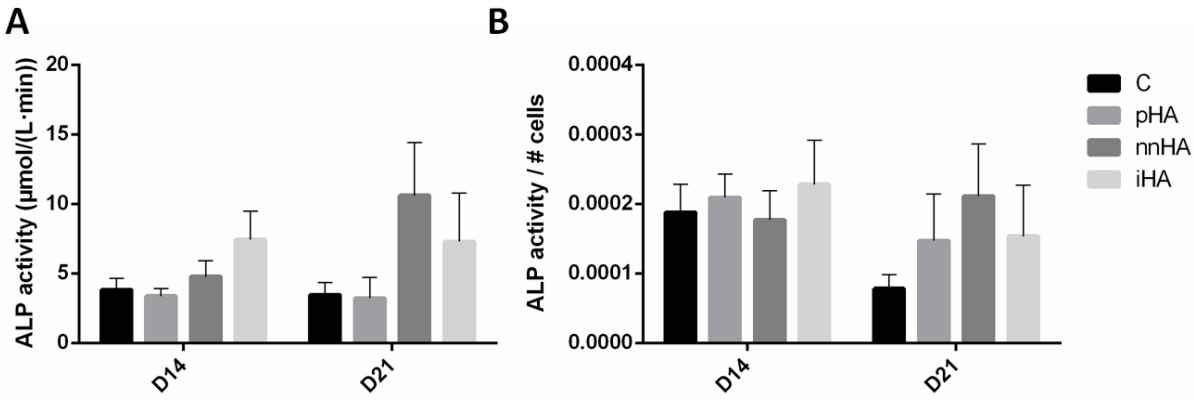

Figure 6-5 ALP activity in hMSCs at D14 and D21. No significant changes in total ALP activity (A) or ALP activity normalised to cell number (B) were identified. (n=3-4).

6.3.5.2 hMSC Collagen production

Collagen production is shown to be enhanced in coated scaffold groups (Figure 6-6). Total collagen quantity is greatest in pHA and nnHA at D21, with a 1.7 and 1.5-fold increase respectively compared to control scaffolds. This effect is further magnified in the pHA group when normalising results to cell number (Figure 6-6C), which is significantly greater than other groups. Collagen content per cell is 3.4-fold greater in pHA than control, and over 2.5-fold greater than nnHA and iHA groups.

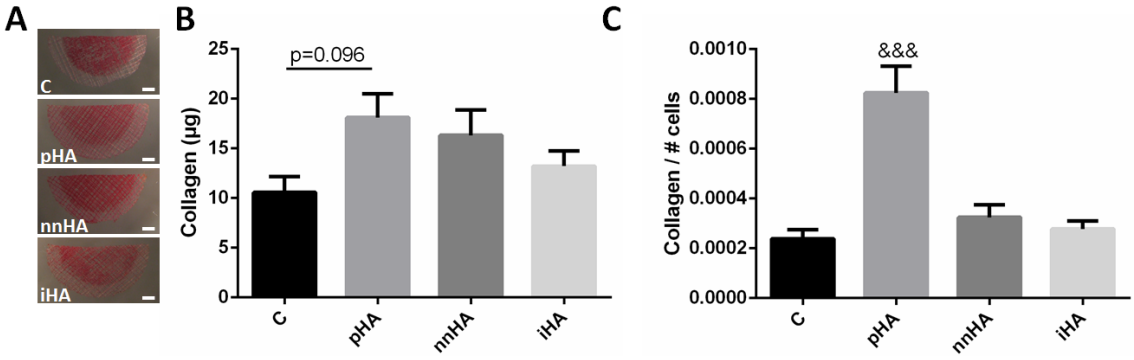

Figure 6-6 Collagen production at D21 (A). Total collagen is enhanced in the pHA group compared to C (scale = 1 mm) (A), while a significant increase compared to all groups is seen when collagen is normalised to cell number (B). (n=4). & = statistical significance compared to all other groups (&&& = p<0.001).

6.3.5.3 hMSC Calcium production

As with previous outputs of osteogenic differentiation, mineral production is seen to be enhanced in the coated scaffold groups (Figure 6-7A). These results encompass both mineralisation due to calcium production by cells, as well as the calcium present due to the treatments prior to cell seeding. Total mineral in pHA was 6.7-fold greater than C and iHA (Figure 6-7B). The greatest concentration following 21 days culture was found on scaffold nnHA, with this being over 12-fold greater than the calcium content in C and iHA and 1.8-fold greater than pHA. These findings are further enhanced when considering calcium due to cell mineralisation alone. The cell contribution to mineral in pHA was 59%, with the remainder the mineral from the scaffold coating. In stark contrast, 92% of the mineral in nnHA is contributed by the cells. Considering this cell mineralisation alone, nnHA is over 14-fold greater than C and 2.9-fold greater than pHA. When total calcium is normalised to cell number at D21 (Figure 6-6C), calcium in pHA and nnHA groups are seen to be significantly greater than others, with an over 10-fold increase in mineral production per cell in pHA and over 12-fold increase in nnHA when compared to untreated control PCL scaffolds.

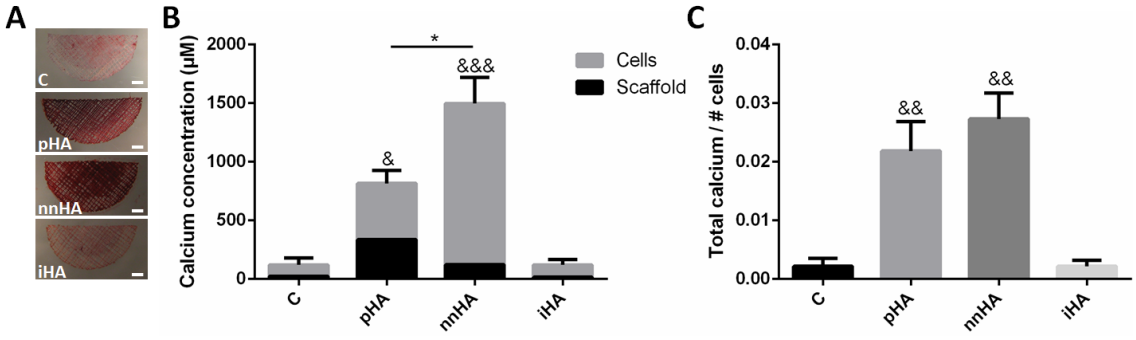

Figure 6-7 Calcium content at D21 with contributions from scaffold and cell mineralisation (scale = 1 mm) (A). Total calcium content is significantly enhanced in nnHA and pHA groups (B). Calcium content normalsied to cell number is also enhanced in these groups compared to C and iHA (C). (n=4). & = statistical significance compared to C and iHA groups (& = $p<0.05$, && = $p<0.01$, &&& = $p<0.001$). * = $p<0.05$.

6.3.6 Coating dissolution after long term culture

After 21 days in culture, the pHA coating was found to be largely intact as seen via SEM imaging, with minor changes seen in a more rough surface topography (Figure 6-8B) compared to at D1 (Figure 6-8A). In stark contrast to this, the nnHA coating is seen to have undergone considerable dissolution, with loss of the nano-needle topography and formation of a coating of nano-spheres with diameter of approximately 5-20 nm. Consistent fracturing of this coating can also be seen. The iHA group is also considerably altered, with extensive precipitates seen at the fibre surface in contrast to the relatively smooth fibre topography at D1.

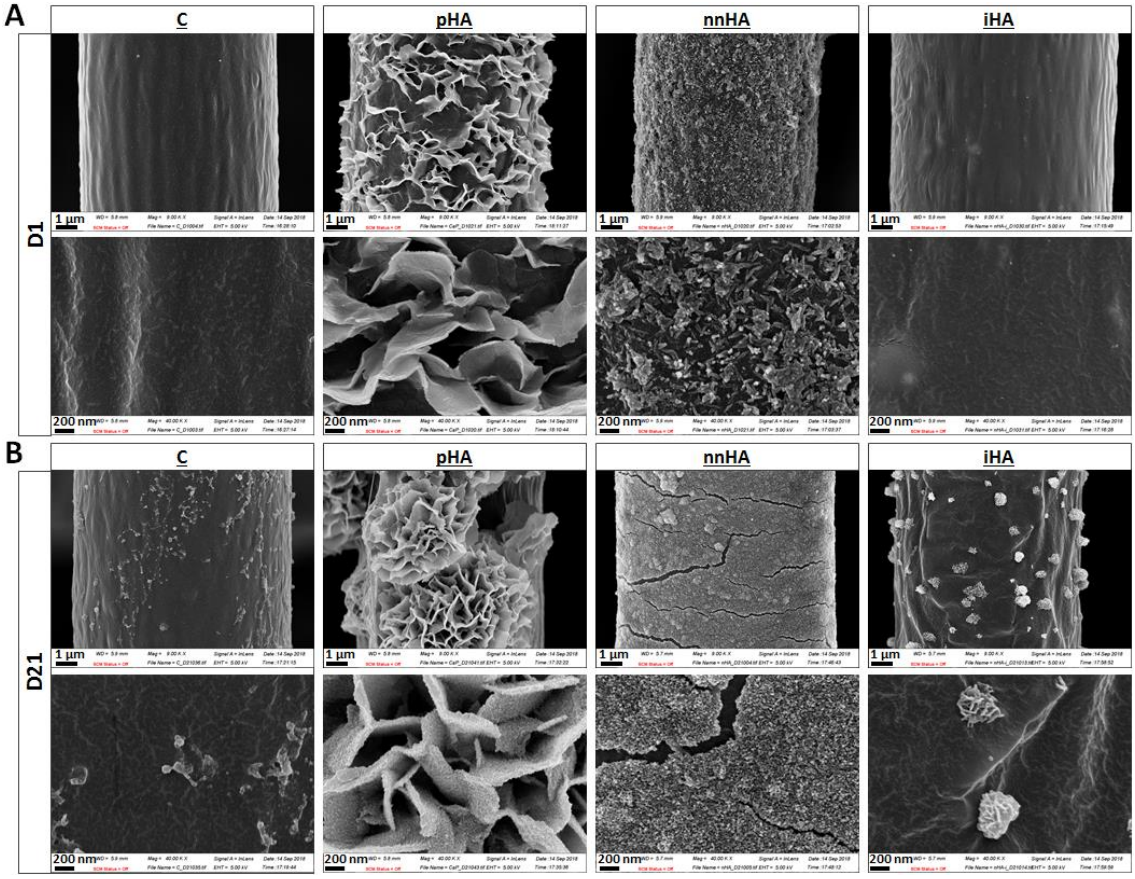

Figure 6-8 Fibre appearance after day 1 (A) and day 21 (B) in culture. Plates in the pHA group appear more rough at D21, with morphology otherwise unchanged. The nnHA coating is significantly altered, with the initial nano-needles becoming spherical and smaller in nature, and the coating exhibiting widespread fracturing. A greater amount of mineral precipitation on the fibre surface is seen in iHA at D21, where the near-surface HA appears to act as sites for mineral nucleation.

6.3.7 Mineral architecture mediates BMP2 controlled release and further enhances hMSC osteogenesis

In order to investigate the capacity of mineral architectures to bind, stabilise, and release growth factors, scaffolds were loaded with BMP2 and release kinetics and stem cell osteogenesis investigated. There is an initial burst release of BMP2 from the C, pHA and iHA materials, with a more sustained initial controlled release from nnHA (Figure 6-9A). The majority of the BMP2 is released by C after 7 days with a total amount of approximately 50%, where the curve is seen to plateau with minimal further release up to

day 21, indicating a lower level of adsorption of the protein with reduced affinity to the scaffold (Figure 6-9B). At 7 days, release percent from pHA and iHA is 65% and 61% respectively, in contrast to nnHA, with a value of 46%. Between D7 and D21, nnHA continues to maintain the greatest level of controlled release at a rate of 9.8% per week.

The controlled release of BMP2 from the MEW scaffolds is seen to enhance cell proliferation in each group. Of particular note is the significant 1.9-fold increase in cell number on the nnHA scaffolds at day 21 compared to control nnHA scaffolds, in addition to significantly enhanced DNA in BMP2 treated nnHA vs pHA, with a fold change of 2.9 (Figure 6-9C). The effect of BMP2 delivery on the osteogenic differentiation of hMSCs was investigated via ALP activity, collagen and mineral deposition as before. ALP increases were only seen in the C scaffolds, however as with all other groups, this was not significant (Figure 6-9D). Collagen content was also investigated, with the greatest increases in C and iHA compared to control scaffolds (Figure 6-9E). Overall collagen content was between 16-20 μg in all groups, with greatest collagen content in nnHA after 21 days. Finally, mineralisation is further enhanced in CP BMP2 functionalised scaffolds, with the greatest changes seen in the nnHA and iHA groups, with increases of 259 μM and 372 μM respectively (Figure 6-9F). In summary, the nnHA group exhibits the greatest potential for modification with additional factors, as seen by the greatest level of sustained protein release, significantly enhanced DNA content, and the greatest levels of collagen content and mineralisation content following 21 days in culture.

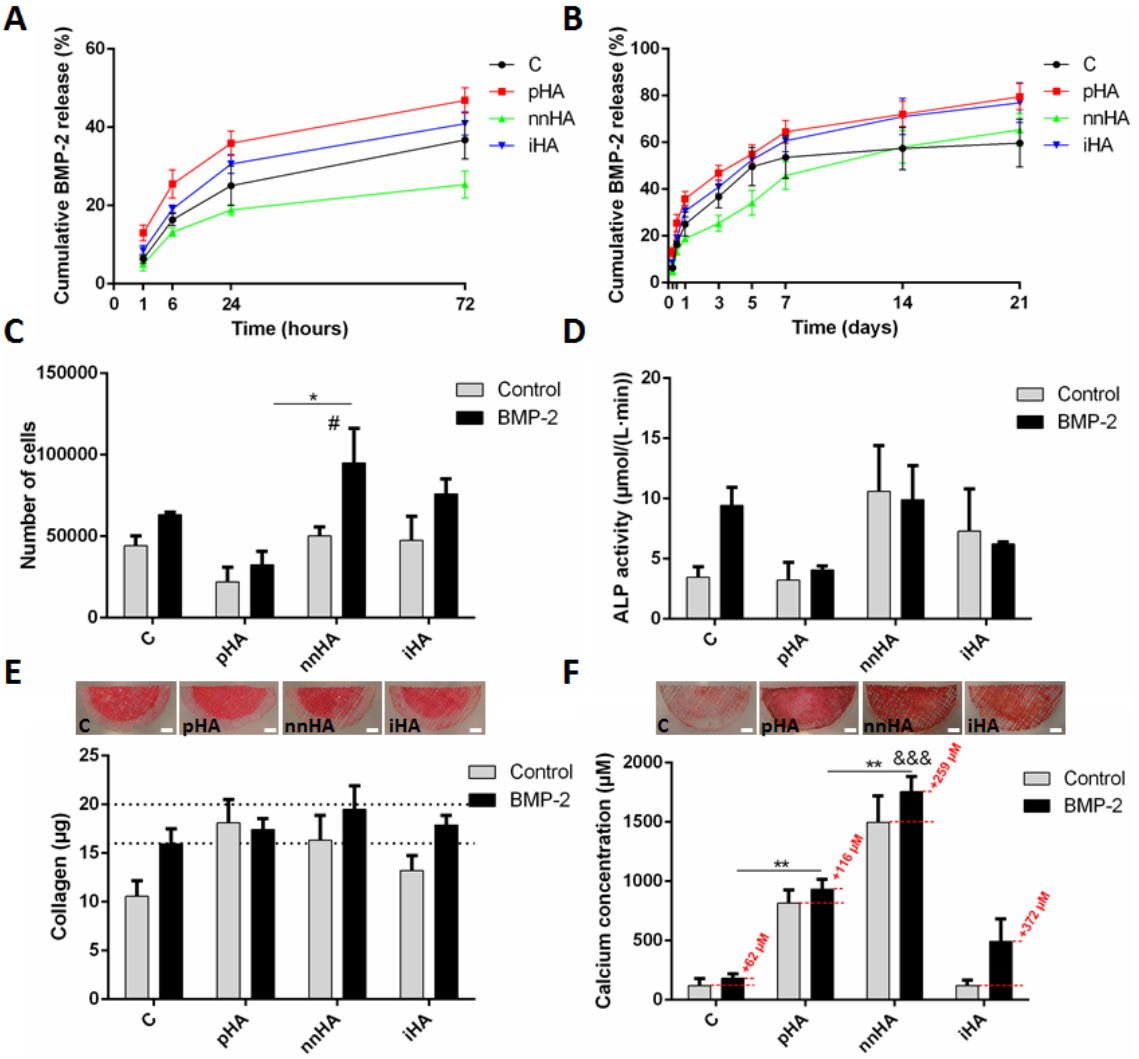

Figure 6-9 Cumulative BMP2 release up to D3 (A) and up to D21 (B) (n=4). Number of cells (C), ALP activity (D), collagen content (E) and calcium content (F) with BMP2 treatment at D21 compared to data from untreated scaffolds as presented in previous figures (scale = 1 mm). * = statistical significance via one-way ANOVA and Tukey multiple comparison test within BMP2 group only. & = statistical significance vs C and iHA groups with same method as previously. # = statistical significance between Control and BMP2 in the nnHA group via two-way ANOVA and Bonferroni's multiple comparison test.

6.4 Discussion

Due to a lack of bone autograft supply, bioinspired synthetic alternative materials are required to enhance bone regeneration in critically sized defects. Cell behaviour and function are mediated by microenvironmental biophysical and biochemical cues, with the architecture and chemistry of the surrounding ECM being fundamental in this regard. Bone

at a cellular level consists of arranged fibres with a cross-fibrillar mineral phase made up of curved nano-sized needle shaped crystals. Recapitulating this unique multiscale architecture may represent an innovative approach to develop effective bioinspired materials to promote bone regeneration. In this study, a 90° fibrous MEW scaffold architecture which has previously been optimised for human MSC osteogenesis was utilised, and further built upon by developing biomimetic mineral functionalisation strategies consisting of either intrafibrillar or cross fibrillar configurations. Interestingly, using a novel coating approach, it was possible to grow nano-needle shaped HA (nnHA) crystals on the surface of the MEW fibres which closely mimic those found in bone. These bioinspired nnHA topographies significantly enhanced hMSC osteogenesis over traditional SBF based pHA coatings or iHA scaffolds. Moreover, given the protein stabilising properties of mineral, it was demonstrated that nnHA facilitated a controlled release of BMP2 from the scaffold which further enhanced mineral deposition by stem cells. This study thus outlines a method for fabricating scaffolds with precise fibrous micro-architectures and bone mimetic nano-needle HA extrafibrillar coatings which significantly enhance MSC osteogenesis and therapeutic delivery and thus hold great promise for bone tissue regeneration.

The microarchitecture/topography, material chemistry, and mechanical properties of each MEW scaffolds is altered followed CaP modifications. The concentrated SBF pHA coating technique resulted in the formation of plates arranged in a “cauliflower” or “rosette” like coating morphology, consistent with previously published findings using this approach (Kokubo, Kushitani, *et al.*, 1990; Tas & Bhaduri, 2011; Vaquette *et al.*, 2013) and typical of the plate or “petal-like” morphology of apatite formed via supersaturated solutions (Drouet, 2013). In contrast, the nnHA coating procedure which has been developed resulted in a vastly different morphology consisting of a fine, extrafibrillar, nano-needle coating which form occasional aggregates, closely mimicking the fundamental mineral units of bone in terms of morphology and composition (Reznikov *et al.*, 2018). The

incorporation of HA into PCL for MEW, does not have a significant influence on fibre surface morphology, as seen by SEM and water contact angle measurements, however, mechanical properties are enhanced with this approach. EDX analysis was further conducted to investigate the elemental distribution and composition of modified fibres. Of particular interest is the elevated Ca/P ratio in the nnHA group approaching 2, suggesting a calcium rich hydroxyapatite or presence of additional phases. Indeed, it is known that bone is similar to the nnHA coating in this regard, and is not solely comprised of stoichiometric hydroxyapatite, but is made up of several phases, including calcium ions and carbonate (Rey *et al.*, 2009), with the atomic Ca/P ratios typically varying between 1.34 – 2.17 with a median value of 1.69, as seen in samples from the femoral neck and the rib bones of healthy humans (M. Tzaphlidou & Zaichick, 2003; V. Zaichick & Tzaphlidou, 2002; Vladimir Zaichick & Tzaphlidou, 2003) (note: weight ratios in references were converted to atomic ratios). To further investigate the crystal structure of the scaffold groups, XRD analyses were conducted. Additional phases in the pHA group include brushite (a pre-cursor to hydroxyapatite), and halite. Additional phases in the nnHA group include TTCP and TCP, which are also extensively used for biomedical applications (W. Habraken *et al.*, 2016; Moseke & Gbureck, 2010). Therefore, a scaffold which closely mirrors the fibrous and mineral architectures of native bone has been developed.

Bone bioinspired architectures can significantly enhance stem cell mediated bone formation, as has been demonstrated via long term *in vitro* studies. Cell behaviour was investigated on modified scaffolds via proliferation and markers of osteogenic differentiation. Cell number was greatest in the nnHA group after 21 days, with the lowest number of cells in the pHA group. This is consistent with previous work demonstrating a trend of increased proliferation with reduced HA particle size (Cai *et al.*, 2007). A corresponding increase in ALP activity in nnHA has also been demonstrated, however, this result is not significant. It is known that osteoprogenitor cells initially produce ALP and

secrete collagen type I, with further mineralisation occurring on this matrix at later time-points (Birmingham *et al.*, 2012; Z. Huang, Nelson, Smith, & Goodman, 2007). It has previously been demonstrated that the fibrous architecture of scaffolds can have a significant influence on hMSC collagen production (chapter 5). However, the findings here indicate that HA surface topography does not augment collagen production. Further investigation of calcium deposition demonstrated highly significant upregulation, particularly with nnHA coating. The majority of the contribution towards total calcium content is seen to be due to cell-based mineralisation, indicating the significant influence of nano-scale needles in this extrafibrillar coating in driving stem cell osteogenic differentiation. There are several likely factors for this result, in addition to the influence of the nano-particle size as discussed previously. Greater dissolution of this coating, as demonstrated by SEM imaging after 21 days in culture will yield a greater release of calcium and phosphate ions into the medium which can interact with cells and allow for reprecipitation, enhancing mineralisation (Chang, Stanford, & Keller, 2000). In addition, an inverse relationship between crystallinity and mineralisation has also been shown (Morgan, Holtman, Keller, & Stanford, 1996), providing further evidence for the greater mineral on the nnHA group which has the lowest crystallinity. Another contributing factor is the greater Ca/P ratio in the nnHA group in addition to the presence of additional CaP phases. Stoichiometric HA is highly stable, with greater dissolution occurring in TCP and TTCP which were identified in the nnHA group, and increased dissolution rate correlated with the content of these more soluble components (Ducheyne, Radin, & King, 1993), again allowing for greater release of ions into the surrounding environment to enhance differentiation. This therefore suggests that the superior bone formation demonstrated with a nnHA coating is multifactorial, harnessing several mechanisms to maximise regeneration.

Nano-needle structured HA extrafibrillar coatings effectively bind, and slowly deliver stable BMP2, enhancing hMSC proliferation and bone formation. The protein

binding and release capacity of these scaffold modifications was investigated via a BMP2 adsorption study. Recent studies have demonstrated that mineral can stabilise bound proteins, preventing conformational changes, maintaining biological activity for weeks during release and that this stabilisation is enhanced within nanostructured coatings (Yu *et al.*, 2017). The nnHA group was shown to facilitate the most sustained release of BMP2 over 21 days. Interestingly, this resulted in significantly enhanced proliferation in this group demonstrating biological activity, while markers of osteogenic differentiation were also marginally increased. A previous study has reported similar results, where continuous supplementation of media with BMP2 resulted in enhanced proliferation of hMSCs without initiating osteogenic differentiation (Lysdahl, Baatrup, Foldager, & Bünger, 2014). However, many studies have also demonstrated the key role of BMP2 in stimulating osteogenesis (Beederman *et al.*, 2013; W. Huang *et al.*, 2004; C. Li, Vepari, Jin, Kim, & Kaplan, 2006). It is hypothesised that due to the high degree of mineralisation indicating late stage differentiation, day 21 may be too late to capture elevated ALP expression, which is an early differentiation marker. Consistent with previous findings in this paper, it is also believed that peak collagen levels in scaffolds is being reached, as seen by the attenuated difference between groups with BMP2 treatment compared to untreated scaffolds. While no significant increases in calcium content were identified, it must be noted that the levels in nnHA are already 14-fold greater than control scaffolds in the absence of BMP2 treatment, and the further increases in mineral with BMP2 treatment in nnHA and iHA groups represent a change several fold-times greater than basal calcium levels in untreated control scaffolds, which has previously been shown to represent significantly enhanced mineralisation compared to random scaffolds (chapter 5). In summary, scaffolds with nnHA coating are shown to significantly enhance stem cell differentiation, with the controlled release of BMP2 loaded scaffolds further contributing to this effect.

6.5 Conclusion

In conclusion, MEW technology was utilised to create fibrous 3D micro-architectures and further modified these templates with a novel bioinspired extrafibrillar coating of needle shaped nano-sized crystals (nnHA). This bone mimetic fibrous and mineral architecture significantly enhanced human MSC osteogenesis over more established plate like mineral coatings. Moreover, extrafibrillar coatings of nano-needles facilitated the binding, stabilisation, and controlled release of BMP2 from the material which further enhanced stem cell proliferation and bone formation. This study thus outlines a method for fabricating scaffolds with precise fibrous micro-architectures and bone mimetic nano-needle HA extrafibrillar coatings which significantly enhance MSC osteogenesis and therapeutic delivery and thus hold great promise for bone tissue regeneration.

Chapter 7

Mechanically activated osteocyte-derived extracellular vesicle functionalised melt electrowritten materials for bone regeneration: A mechanobiomimetic scaffold

7.1 Introduction

There are many cases where bone is unable to self-repair following damage to the tissue, including large defects and fractures following trauma or tumour growth (Moore, Graves, & Bain, 2001). The clinical challenges presented by this are significant, and there are no satisfactory solutions to date. Approximately 2,000,000 bone grafting procedures are undertaken each year (Campana *et al.*, 2014), with the majority of these utilising autografts. This approach to bone repair has many issues however, and there is a need for the development of alternative tissue regeneration strategies. Synthetic tissue engineering approaches are an attractive solution, and may yield a potentially limitless tissue source for unrestricted repair. Of fundamental consideration when developing this type of approach is the understanding of the cell's native environment, which is pivotal for mediating its behaviour and ensuring continuous tissue regeneration in addition to guiding repair. In bone, this environment is comprised of an intricate network of several cell types within a complex composite matrix, which collectively co-ordinate cell behaviour in response to the dynamic mechanical environment (Kane & Ma, 2013). A fundamental component within this system is the stem cell niche, which coordinates direct and indirect biophysical stimuli to expand stem cells and mediate their behaviour for continuous regeneration (Yin & Li, 2006). Two regions of particular interest are the endosteal and periosteal surfaces, each of

which house specific stem cell niches (Ferretti & Mattioli-Belmonte, 2014; Gattazzo, Urciuolo, & Bonaldo, 2014). These are closely mediated directly by the adjacent fibrous environment, and indirectly by mechanically induced cell signalling, each of which will be discussed below. Understanding and implementing an environment which mimics the native biophysical cues of the stem cell niche would provide a powerful strategy to expand stem cells and control their behaviour to guide tissue repair.

Direct biophysical regulation of stem cells occurs via the underlying fibrous micro architecture and mineral nano-topography of bone tissue. *In vivo,* the micro architecture of bone is composed of collagen fibres with diameters of 1 – 10 μm (Kane & Ma, 2013), at varying degrees of alignment depending on local tissue strain (Foolen *et al.,* 2008). These fibres are composed primarily of collagen, which comprises 90% of the total organic component of bone (M. F. Young, 2003). It is known that substrate architecture (McBeath *et al.,* 2004) and stiffness (Engler *et al.,* 2006) can have profound effects on cell behaviour, in turn influencing cell mechanosignaling and driving stem cell lineage commitment (Dupont *et al.,* 2011). It has been demonstrated that stem cell shape and mechanosignaling are significantly altered in response to fibrous architecture specifically (chapter 5). Here, a 90° architecture with fibres of 10 μm diameter significantly enhances stem cell osteogenesis over more aligned or random scaffolds, which ultimately occurs as a result of enhanced cell spreading and cytoskeletal tension being imposed by this architecture. A large proportion of bone is composed of inorganic mineral which is closely integrated with the collagen structure to form a composite matrix. The basic mineral unit consists of nano-scale needles with approximate dimensions of base 5 nm and length 50 – 100 nm (Reznikov *et al.,* 2018). These needles form platelets composed of partly merging crystals of the same base and diameter, with platelet widths of 20 – 30 nm, which in turn form stacks and aggregates with irregular 3D structures of size 200 – 300 nm. The scale and architecture of this nano structure is known to be important for stem cell proliferation and differentiation, with stem

cell behaviour being negatively affected when cultured on larger particles (Cai *et al.*, 2007). In addition, it has been demonstrated that fibres coated with nano-needle hydroxyapatite (nnHA) can have a profound influence on stem cell osteogenesis (chapter 6). Remarkably, cell mineralisation is enhanced over 14-fold on nnHA fibres compared to uncoated controls, and almost 3-fold greater than fibres coated with micron-scale hydroxyapatite with a plate architecture. In addition, this nano-topography facilitates enhanced protein adsorption and controlled release, mimicking the great protein stability provided by the needle-shaped mineral structure of native bone (Asara *et al.*, 2007). Thus, implementing defined nano-topographical mineral features is a promising strategy to form biomimetic scaffolds and further enhance osteogenesis.

Indirect biophysical regulation also provides important information to recruit, expand and mediate stem cell behaviour. In bone, paracrine signalling coordinated by the osteocyte is a key component to this effect, with the release of mechanically induced factors driving the behaviour of osteoblasts, osteoclasts and their progenitors (Dallas *et al.*, 2013). The important role of osteocyte mechanosignaling on stem cell behaviour in particular has been well documented, with conditioned medium from mechanically stimulated osteocytes enhancing the recruitment, proliferation and osteogenic differentiation of stem cells (Brady *et al.*, 2015; Hoey *et al.*, 2012). This is achieved via the release of a range of factors, with several of particular interest including sclerostin (Moester *et al.*, 2010) and RANKL (Nakashima *et al.*, 2011). It has been demonstrated via proteomic analyses that a large range of factors are released by osteocytes, with this secretome being altered in response to mechanical loading, and in turn, enhancing stem cell osteogenesis (chapter 3). It has become apparent that the means by which factors such as these are delivered is likely of equal importance, with EVs being shown by us and others to be implicated in cell signalling in bone as well as throughout the body. Bone cells, including osteocytes (Morrell *et al.*, 2018; Qin *et al.*, 2017; Mari Sato *et al.*, 2017), osteoblasts (Cui *et al.*, 2016; Davies *et*

al., 2017a; Jess Morhayim *et al.*, 2016) and stem cells (Q. Li, Huang, *et al.*, 2018) have been shown to release EVs, which efficiently target cells to deliver signalling components including proteins and miRNAs. In addition to the above, it has been shown that the loading of osteocytes via fluid shear forms MAEVs, which significantly enhance stem cell recruitment and osteogenic gene expression in a similar fashion to conditioned medium from mechanically stimulated cells (chapter 3). This further reinforces the key role of osteocyte EVs in indirect biophysical regulation of stem cells, and indicates the great promise of osteocyte EVs in the development of therapeutics and strategies for bone regeneration. Previous studies have already started to investigate the use of EVs for these purposes, which may be loaded with drugs for use as a delivery vector to treat osteoporosis (Cappariello *et al.*, 2017), or incorporated within scaffolds to enhance bone regeneration (Diomede *et al.*, 2018; H. Xie *et al.*, 2017b). The further use of MAEVs for scaffold functionalisation holds great promise, where they may be used to locally guide MSC behaviour and enhance regeneration.

In this study, the aim was to combine both direct and indirect biophysical cues present within the bone stem cell niche, and develop a fibrous scaffold incorporating a collagen component, mineral component and mechanobiological cues, to create a mechano-biomimetic bone tissue regeneration strategy. A previously developed, fibrous 90° scaffold architecture fabricated via melt MEW (chapter 4-5) was utilised as a foundation upon which to build this scaffold. This matrix is then coated with nano-needle hydroxyapatite (nnHA), which closely recapitulates the natural nano topography of bone to further enhance osteogenesis (chapter 6), after which the scaffold was further coated in a collagen matrix. In addition, osteocytes are mechanically stimulated and either conditioned medium or subsequently isolated MAEVs are used to further functionalise scaffolds via incorporation within the collagen coating to provide cues for indirect biophysical regulation (chapter 3) (Figure 7-1). Stem cells were then cultured on these scaffolds and their osteogenic capacity

investigated via various means, including alkaline phosphatase (ALP) activity, collagen production and mineralisation. It is demonstrated that MAEV functionalised scaffolds significantly enhance stem cell osteogenesis and highlight the synergistic potential of direct and indirect biophysical cues of the bone stem cell niche in driving regeneration.

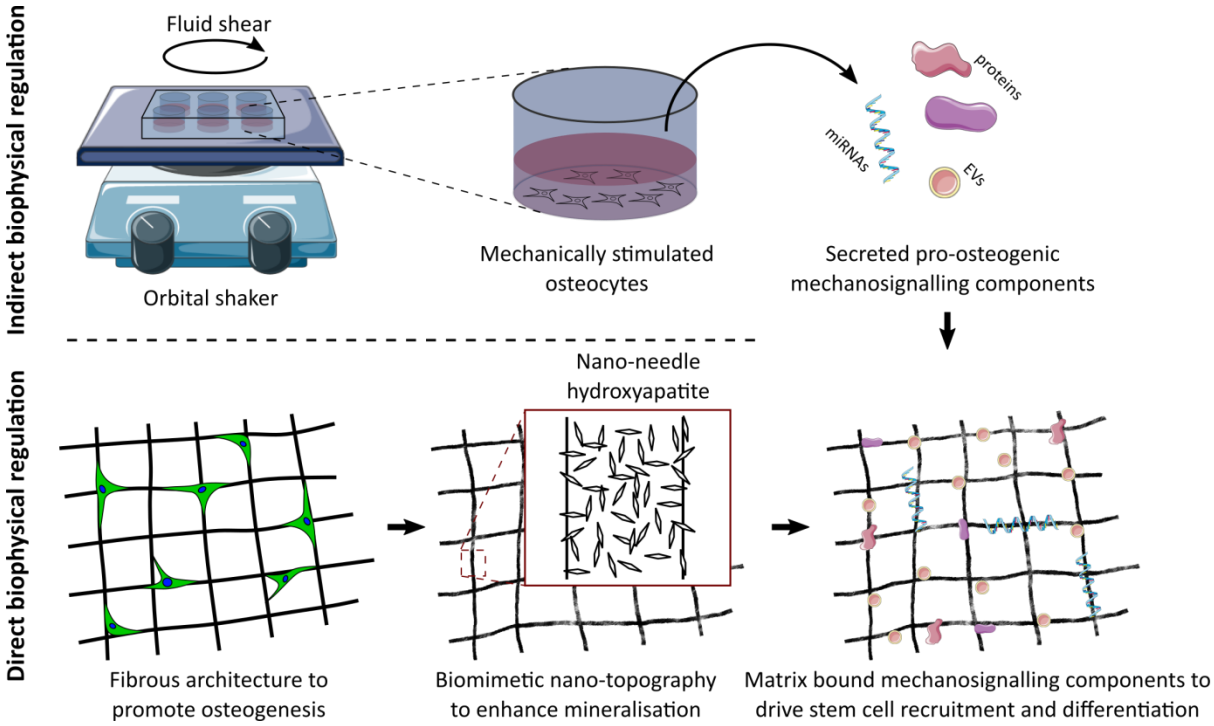

Figure 7-1 Development of biomimetic fibrous scaffolds to drive stem cell recruitment and osteogenesis

7.2 Materials and methods

7.2.1 MEW

Fibrous scaffolds with a fibre diameter of 10 µm, square apparent pore size of 50 µm, and layer fibre spacing of 300 µm were fabricated on a custom built MEW apparatus as previously described (chapter 5). Briefly, heated air at a temperature of 90°C was circulated around a syringe to melt PCL (Sigma Aldrich 440744, average Mn 80,000), with air pressure being used to extrude the polymer through a 21G needle with high voltage applied

at a distance of 15 mm from a grounded aluminium collector plate. Fibres were deposited with a 90° offset between subsequent layers to result in a square pore shape.

7.2.2 Nano-needle hydroxyapatite (nnHA) coating

A calcium solution was made with 0.05M calcium chloride dihydrate (Sigma Aldrich C7902) in MilliQ water. A phosphate solution was made with 0.03M sodium phosphate tribasic dodecahydrate (Sigma Aldrich S7778) and 0.01M NaOH in MilliQ water. Reactions were carried out in 50ml conical tubes, with reagent volumes being maintained at 40 ml at each step of the process and 6 scaffolds of dimension 3 x 3 cm being processed per tube. Scaffolds were immersed in 70% ethanol for 15 min under vacuum. They were then placed in 2M NaOH, vacuum applied for 5 min and incubated at 37°C for 45 min. Scaffolds were then rinsed 5 times in MilliQ water and added to 20 ml of the calcium solution. 20 ml of the phosphate solution was slowly added to the calcium solution, vacuum applied for 5 min and samples incubated in the calcium/phosphate solution for 30 min at 37°C. This coating procedure was repeated a further two times minus the vacuum treatment. Scaffolds were then treated with 0.5M NaOH for 30 min at 37°C, rinsed 5 times in MilliQ water and allowed to dry overnight.

7.2.3 Osteocyte cell culture

MLO-Y4 osteocyte like cells (Kerafast) (Kato *et al.*, 1997) were maintained as previously described (Rosser & Bonewald, 2012) in α-MEM growth medium with 2.5% fetal bovine serum (FBS), 2.5% calf serum (CS), 1% Penicillin/Streptomycin (PS) and 1% L-glutamine. 6-well plates were coated with 0.15mg/ml type I collagen (Sigma C3867) for one hour and washed with PBS, after which osteocytes were seeded at a density of 1.16 x 10^4 cells/cm^2 in 2 ml medium/well. After 48 h culture, plates were then placed on an orbital shaker for 2 h at a rotational speed of 100 rpm. This mechanical stimulation regime yields an average fluid shear stress of 0.28 Pa and maximum force of approximately 1 Pa across the bottom of the well (Salek, Sattari, & Martinuzzi, 2012). Cells were washed with PBS

and 833 µl of serum free medium (1% PS and 1% L-glutamine) was applied to each well. Cells were incubated for 24 h and conditioned medium (CM) was then collected. Samples were centrifuged at 3,000g for 10 mins at 4°C to remove debris, after which the supernatant was collected.

7.2.4 Extracellular vesicle isolation from conditioned media

Medium was filtered through a 0.45 µm pore filter and ultracentrifuged at 110,000 g for 75 min at 4°C, using an SW32.Ti swing bucket rotor. Pellets were washed in cold PBS and the ultracentrifugation process was repeated. EVs were then re-suspended in PBS and protein quantity determined via a NanoDrop spectrophotometer with absorbance of 280 nm. CM and EV particle size distribution was investigated via digital light scattering (DLS) on a Zetasizer Nano ZS. Samples were first diluted 1:50 in PBS and filtered using a 0.45 µm filter.

7.2.5 Functionalising MEW constructs with EVs and CM

Scaffolds were punched to a diameter of 8 mm and UV sterilised for 20 min on each side before being placed in 48-well plates. Scaffolds were then pre-wet in a graded ethanol series of 100%, 90% and 70% for 20 min each before being washed three times in sterile MilliQ water and allowed to dry overnight. Scaffolds were functionalised with EVs or CM within a collagen matrix to aid adhesion to fibres, and variables for collagen coating were optimised to obtain a coating which preserves the nano-topography of the mineral coating. The influence of time (1 hr and 24 hr) on collagen coating thickness was investigated at a collagen concentration of 100 µg/ml. The influence of collagen concentration (20 µg/ml and 100 µg/ml) on collagen coating thickness after 1 hr treatment was investigated. Final scaffold treatment methods are as follows. For the EV group, a 50 µl solution in PBS containing 1 µg collagen (20 µg/ml) and 1 µg EVs (20 µg/ml) was loaded on each scaffold. For the CM groups, a 50 µl solution of 88% CM containing 1 µg collagen (20 µg/ml) was loaded on to each scaffold. Control (C) scaffolds were loaded with

PBS, and collagen control (Col) scaffolds were loaded with 1 μg collagen. Scaffolds with above treatments were incubated for 1 h at 4°C and were then rinsed in PBS.

7.2.6 SEM imaging and EDX

For scanning electron microscope (SEM) imaging, samples were prepared for imaging by coating with gold/palladium for 40 s at a current of 40 mA. For EDX analyses, scaffolds were carbon coated and analysed at a voltage of 15kV in a Zeiss ULTRA plus SEM with an 80mm² Oxford Inca EDX detector. To investigate approximate calcium/phosphorus atomic ratios for each group, spectra were acquired on scaffolds for 120 s (n=5 technical replicates). Element maps were constructed at a resolution of 512 x 384 with map dwell of 4000 μs and linescan dwell of 2000 μs.

7.2.7 Immunofluorescent staining of MEW-EV constructs

Fluorescent membrane labelling was used to confirm the presence of EVs on functionalised scaffolds. Constructs were incubated with 1 μM PKH26 dye solution (PKH26GL, Sigma) for 5 min. Excess dye was then quenched by treatment with EV depleted FBS (3 x 5 min treatments). Constructs were then washed in PBS (3 x 5 min) and mounted to glass slides using Fluoroshield (Sigma Aldrich, F6182) mounting medium. Fluorescent imaging was carried out using a Leica SP8 scanning confocal microscope with 20x objective, where Z-stacks with 10 steps and a total thickness of 10 μm were constructed.

7.2.8 hMSC culture

hMSCs were isolated from bone marrow (Lonza, US), trilineage potential verified, and seeded at a number of 10,000 cells per scaffold. Scaffolds were transferred to new well plates after 24 h, and cultured in 300 μl osteogenic medium (OM)/well from day 3, which consisted of 10% FBS DMEM supplemented with 100 nM dexamethasone, 10 mM β-glycerol phosphate and 50 μg/ml ascorbic acid. Medium was changed every 3.5 days.

7.2.9 Proliferation

At days 1,7,14 and 21, scaffolds were added to 100 µl lysis buffer in 1.5 ml tubes (n=5) containing 0.2% Triton X-100, 1 mM Tris pH8, with phenylmethylsulfonyl fluoride (PMSF) being added at a ratio of 1:200 just before use, and stored at -80°C. Before DNA quantification, samples were subjected to three freeze-thaw cycles in liquid nitrogen and underwent sonication for 60 s. Samples were then vigorously vortexed before being stored on ice for processing. DNA content was quantified using a Quant-iT™ PicoGreen™ dsDNA Assay Kit (Invitrogen, P7589), with excitation and emission wavelengths of 485 nm and 528 nm respectively. The DNA content in 10,000 MSCs seeded and pelleted in centrifuge tubes was also quantified to calculate the total number of cells present on scaffolds.

7.2.10 Characterisation of hMSC osteogenic differentiation

7.2.10.1 Intracellular ALP

Intracellular ALP was quantified at days 14 and 21 (n=4). 50 µl of 5mM pNPP was added to wells along with 10 µl of cell lysate and 70µl MilliQ water in a 96-well plate. Standards were comprised of serial dilutions of p-Nitrophenyl phosphate (pNPP, Sigma Aldrich, N1891) with 10µl of 43µM ALP enzyme (Sigma Aldrich, P6774) being added to each. Plates were incubated for 1 h in the dark at room temperature, and reactions were then stopped using 20µl of 3M NaOH. Absorbance was read on plates at 405 nm, and ALP activity was calculated as the amount of pNPP generated as a function of sample volume and reaction time.

7.2.10.2 Collagen production

Scaffolds were cultured up to 21 days before evaluating collagen content. Cell-scaffold constructs were rinsed in PBS, fixed in 10% neutral buffered formalin for 15 min and rinsed again in PBS before storage at -20°C. Scaffolds were stained with 200µl of

1mg/ml of Direct Red 80 (Sigma Aldrich, 365548) in a saturated aqueous picric acid solution for 1 h with shaking at 150 rpm. Scaffolds were then washed twice with 0.5% acetic acid and allowed to dry overnight before imaging. To quantify collagen content, 500µl 0.5M NaOH was added to wells under shaking until stain was dissolved, and solutions were added to 1.5 ml tubes. Tubes were centrifuged at 14,000g for 10 min to pellet debris. Standards were made by adding direct red staining solution to 8µl of collagen I (Corning, #354249) before centrifuging at 14,000g for 10 min and re-suspending the collagen in 500µl 0.5M NaOH. The absorbance of samples and standards were read at 490 nm in 96-well plates.

7.2.10.3 Calcium production

Cell-scaffold constructs were investigated for total calcium content after 21 days. Cell-free scaffolds were also cultured up to 21 days to determine the contribution of total calcium from cell mineralisation versus mineral nucleation due to the presence of EVs. Scaffolds were incubated with 1% alizarin red S solution (Sigma Aldrich, A5533) in distilled water for 10 min at a pH of between 4.1 – 4.3. Samples were rinsed 3 times with water and allowed to dry prior to imaging. To quantify bound stain, 400 µl of 10% acetic acid was applied and samples incubated at room temperature for 30 min while shaking at 150rpm. The acetic acid was added to 1.5 ml tubes, vortexed vigorously and heated to 85°C for 10 min. Tubes were transferred to ice for 5 min, centrifuged at 20,000g for 15 min, and 300 µl of the supernatant was added to new tubes along with 120 µl of 10% ammonium hydroxide. Standards were made with dilutions of alizarin red solution in distilled water, with the pH of each adjusted to between 4.1 – 4.3. Samples and standards were read at 405 nm in a 96-well plate.

7.2.11 Statistical analysis

Subsequent biological data is presented in terms of average and standard error of the mean. For proliferation and ALP data, statistical analysis was performed using two-way

ANOVA and Tukey's multiple comparison post-test. For collagen and calcium data, statistical analysis was performed using one-way ANOVA and Tukey's multiple comparison post-test. For EDX data, statistical analysis was performed using unpaired Student's t-test.

7.3 Results

7.3.1 Fabrication of CM and EV functionalised scaffolds

The effect of collagen coating concentration after 1 h incubation on fibre topography was investigated via SEM imaging (Figure 7-2A). At a concentration of 100 μg/ml, the collagen almost completely covers the nnHA layer, with some needles partially visible through the collagen coating. At a concentration of 20 μg/ml, a thinner collagen coating is achieved with the nnHA layer largely visible. The influence of the above collagen concentrations in addition to 20 μg/ml of EVs on fibre topography was also investigated. As previously, the higher concentration results in a relatively thick collagen/EV coating which masks the needle topography of the nnHA layer. The lower concentration in addition to 20 μg/ml EVs yields a coating which partially covers the nnHA layer with needle topography largely maintained. The effect of coating time was also investigated, where 1 h and 24 h were compared, and was found to have no effect indicating that the coating process happens quickly. The lower collagen concentration at 1 h treatment was thus used for all study groups with the exception of the control (Figure 7-2B), with SEM images of all groups shown in (Figure 7-2C).

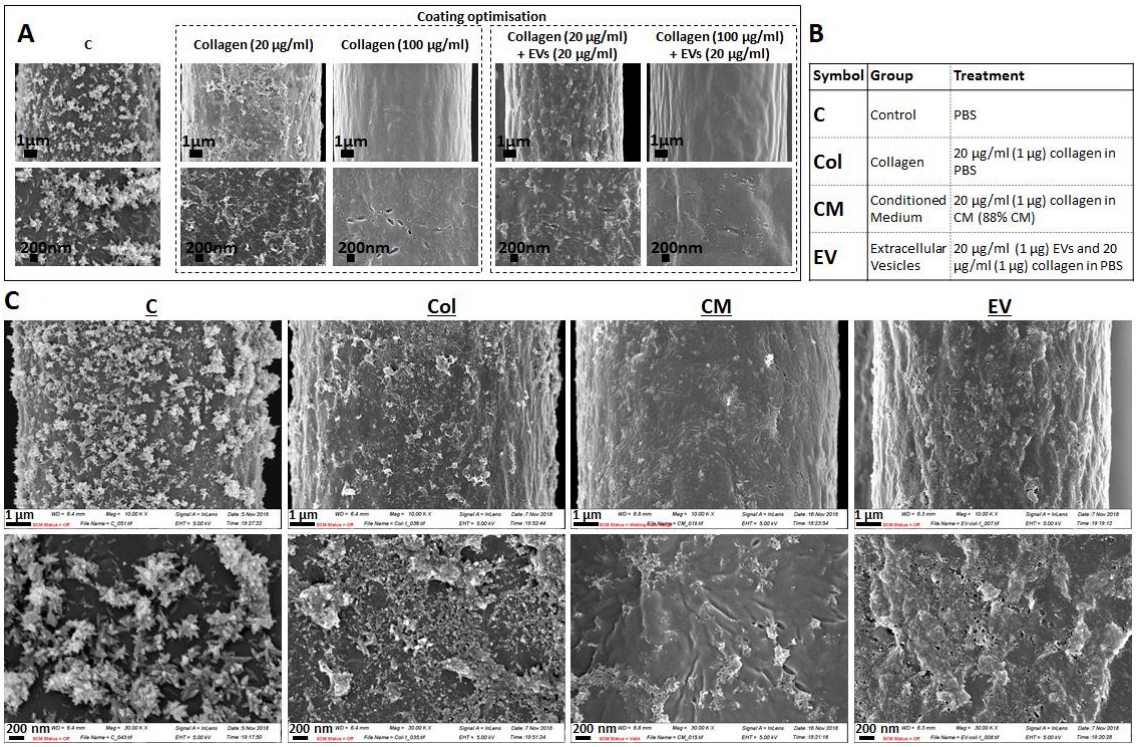

Figure 7-2 Development of scaffold coatings. Collagen concentration was optimised for the collagen and EV groups (A) with final concentrations listed in Table B. SEM images of final groups (C).

7.3.2 Characterisation of CM and EVs

Osteocyte derived CM and isolated EV samples were characterised by particle size analysis (n=3) and successful binding to scaffolds was investigated via fluorescent imaging. The primary peak in CM particle distribution, at an intensity of 60.33%, revealed an average particle size of 186.67 nm which is within the range typical of EVs (Figure 7-3A). A second peak with an intensity of 20% and average particle size of 0.72 nm is likely an experimental artifact, and is too low for the readings typically attained for protein size via DLS (Lorber, Fischer, Bailly, Roy, & Kern, 2012; Nobbmann). This may be caused by the presence of phenol red or other components within the DMEM culture medium in the CM group. As the sample was filtered prior to analysis via DLS, peak 3 is a likely contaminant. The primary peak in the EV group has an intensity of 87.83% and average particle size of 253.57 nm, which is also within the typical range for EVs (Figure 7-3B). As previously, the

peak below this is a possible artifact which is only present in 2 out of the 3 replicates, while the larger particle peak is a likely contaminant. Functionalised scaffolds were then stained with PKH26, a membrane dye used as a marker for EVs (Figure 7-3C). Background staining was detected in C and Col groups. In CM there was evidence of EV staining, however, at a relatively low intensity and concentration. In the EV group, PKH26 staining was more intense, with a consistent spread of high intensity point staining throughout the scaffold confirming successful binding of EVs.

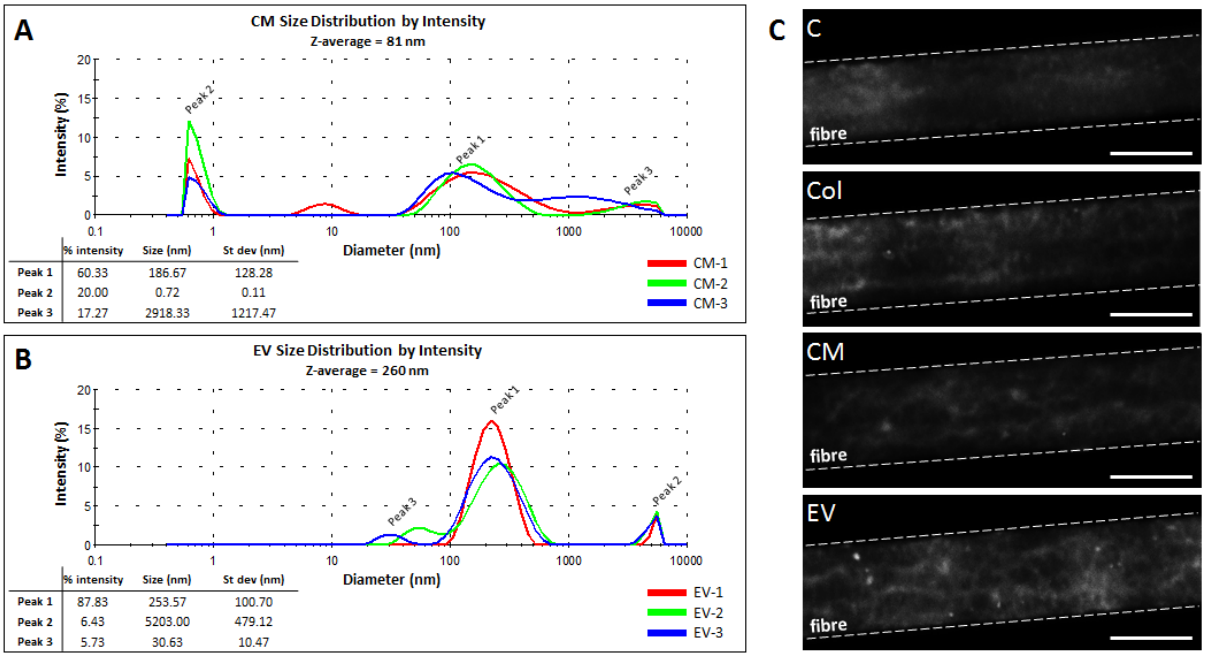

Figure 7-3 Particle size distribution in CM (A) and EVs (B) which both consisting of a primary peak at approximately 200 nm, and two minor peaks above and below this (n=3). PKH26 staining of functionalised scaffolds demonstrating successful EV binding in the CM and EV groups. Scale = 10 µm.

7.3.3 Attachment and proliferation of hMSCs

Seeding efficiency is not significantly altered between groups, which have an average cellular attachment of 46% after 24 h (n=5) (Figure 7-4). A greater difference in cell number between groups becomes apparent at D7, with DNA content lowest in C at this time and 2.7 fold greater in EV. This effect becomes more apparent at D14, with all groups significantly greater than C by more than 2 fold. Cell number in CM is also significantly

greater than Col and EV at this time. Interestingly, at D21 there was a reduction in the amount of DNA detected in Col, CM and EV groups, while DNA content increased in C. This is likely due to the development of a highly dense matrix after 21 days in culture, with constructs being noticeably much stiffer when handling compared to those at earlier time points. This made DNA extraction more difficult, with cells/matrix still partially visible on scaffolds after vigorous vortexing.

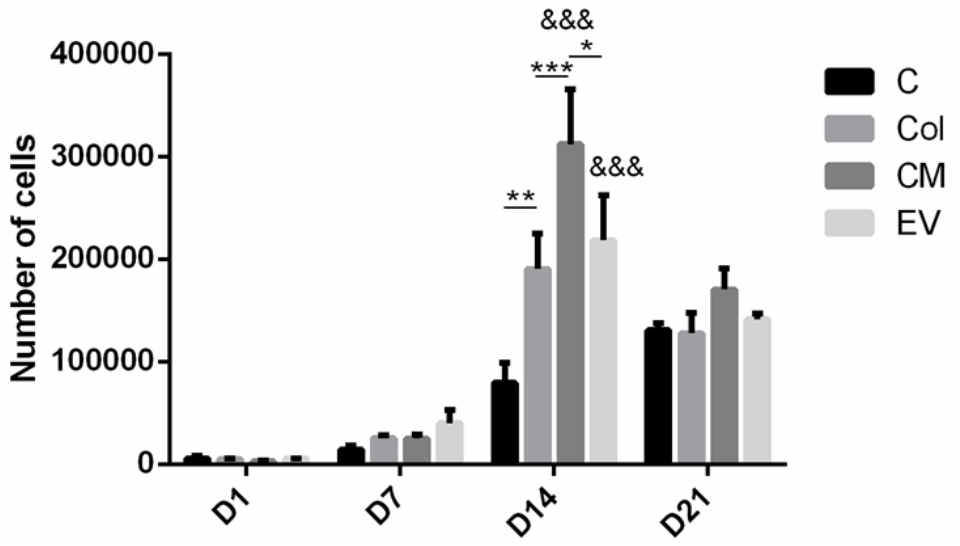

Figure 7-4 Proliferation quantified via DNA content. (n = 5). (& = statistical significance compared to C).

7.3.4 MSC osteogenesis

7.3.4.1 ALP activity

Total ALP activity was investigated at D14 and D21 (n=5) (Figure 7-5A). At D14, ALP is enhanced in the Col group compared to C, however this is not significant. The addition of mechanically activated osteocyte CM for scaffold functionalisation further enhances this effect, resulting in a significant 6.3-fold increase in ALP compared to C. ALP is also enhanced in the mechanically activated EV group, with a near-significant 4.9-fold increase vs C. At D21 the differences between groups are attenuated, with ALP activity greatest in the EV group at this time with a 1.6-fold increase vs C. ALP activity normalised to DNA was also investigated. As previously, values are lowest in C after 14 days. At D21,

ALP/DNA is greatest in the EV group, with a near-significant 1.8-fold change vs CM. In summary, the functionalisation of scaffolds with collagen enhances ALP activity compared to control scaffolds, however, the further functionalisation of scaffolds with CM or EVs greatly enhances these effects, indicating the potential of these biological components for further driving stem cell differentiation in fibrous micro-environments.

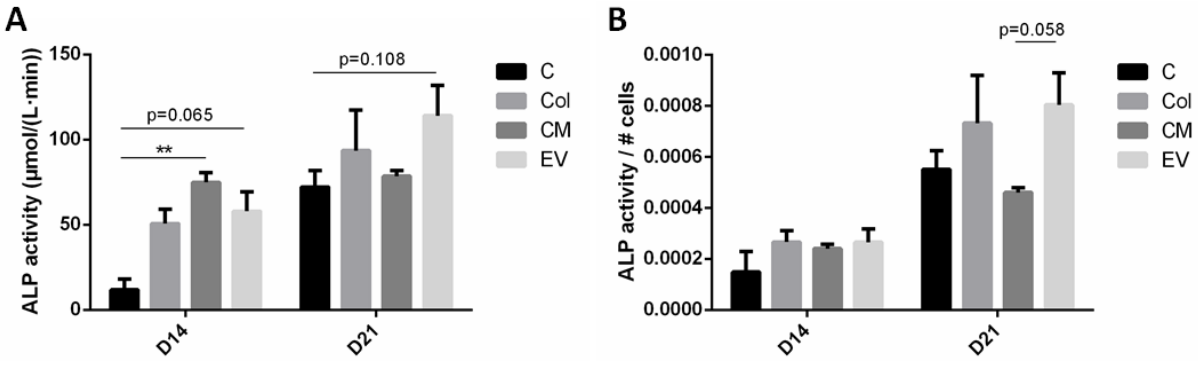

Figure 7-5 ALP activity in hMSCs at D14 and D21 (A), and ALP normalised to cell number (B). (n=5)

7.3.4.2 Collagen production

To further assess the osteogenic capacity of mechano-biomimetic scaffolds, the degree of collagen deposition was assessed (n=5). It can be visually seen that C has a less well developed collagen matrix than all other groups (Figure 7-6A). Quantifying total collagen reveals that all groups have at least 25% more collagen than C, with the greatest increases in the EV group with 36% more collagen at a total value of 30 µg (Figure 7-6B). Normalising to DNA content, both EV and Col groups have significantly more collagen compared to C and CM. In order to assess the contribution of collagen originally used for scaffold coating towards this result, cell-free scaffolds were cultured in the same conditions up to 21 days (n=5). There was visually no difference between groups which appeared to have a mild pink background stain, with this being confirmed upon further quantification (Figure 7-6D). As there are no differences between groups, including the control which originally contained no collagen. It can therefore be confirmed that none of the original collagen coating remained after 21 days in culture. In conclusion, collagen coating of

scaffolds enhances the deposition of collagen matrix by cells, with only this cell-synthesised collagen remaining after 21 days. Addition of EVs to the collagen coating yields further increases in collagen production by cells.

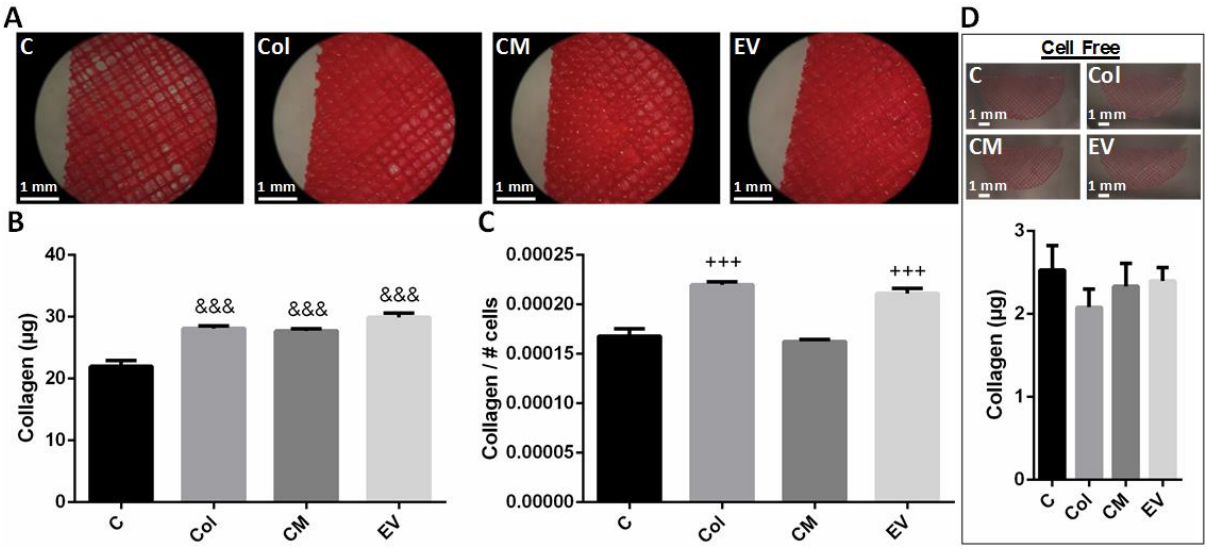

Figure 7-6 Collagen production at D21 (A). Total collagen is enhanced in Col, CM and EV compared to C (B), while a significant increase of Col and EV compared to C and CM is seen when collagen is normalised to cell number (n=5) (C). Collagen was quantified in cell-free scaffolds, with only background staining identified (D) (n=5), confirming that all collagen in cell-scaffold constructs is produced by the MSCs. (& = statistical significance compared to all other groups. + = statistical significance compared to C and CM).

7.3.4.3 Mineral production

Mineralisation was also assessed at D21 as a late-stage marker of osteogenic differentiation (n=5). As previously, visual differences could be seen between scaffold groups. In particular, C was covered in noticeably less mineral, with apparent patches with reduced staining (Figure 7-7A). In addition, the EV group appeared to have the most intense staining, with a dense, consistent matrix completely covering the scaffolds, that was noticeably stiffer following manual manipulation. Upon quantification, it was confirmed that C had the lowest level of mineral staining at 376 µM (Figure 7-7B). A marginal increase of 66 µM was seen in the Col group, with a further increase of 25 µM in CM. A further substantial increase of 231 µM was seen in the EV group compared to CM. This corresponds to a significant 1.9-fold increase in mineralisation in the EV group compared

to C, and a near-significant 1.6 fold increase vs Col. Similar trends are seen when normalising results to DNA, with significant increases in mineralisation in the EV group compared to C and CM (Figure 7-7C). While all groups are coated with the same quantity of mineral prior to cell culture, cell-free scaffolds were cultured to D21 (n=5) to investigate the hypothesis that EVs may act as sites of mineral nucleation in scaffolds, as has been previously demonstrated in 2D culture (Davies *et al.*, 2017a). No difference in mineral was seen between C and Col, both with 48 μM of mineral (Figure 7-7D). Marginal increases in CM and EV groups were identified, with values of 57 μM and 59 μM respectively. While difference in total mineral is not significant, this provides evidence that EVs, which are present in both the CM and EV groups, contain mineral components which may in fact act as sites of mineral nucleation in fibrous scaffolds in dependent of cells. In summary, EV functionalised scaffolds significantly enhance mineralisation after 21 days in culture, revealing their potential for driving stem cell osteogenic differentiation in fibrous 3D environments.

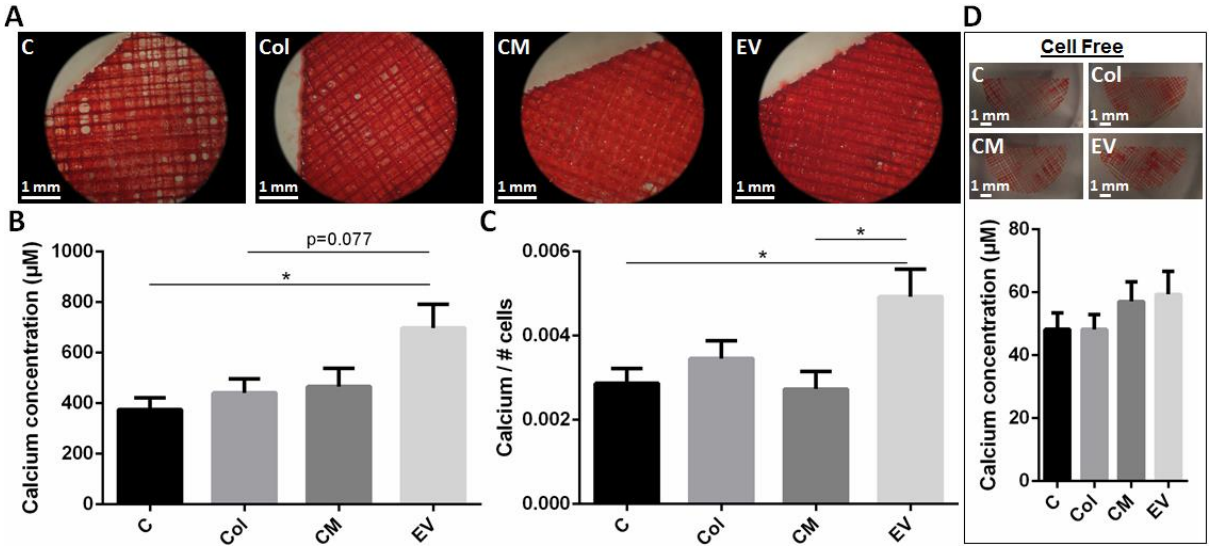

Figure 7-7 Calcium content at D21 (A). Total calcium content is significantly enhanced in the EV group compared to C (B). Calcium content normalised to cell number is also enhanced in this group (C) (n=5). Calcium was quantified in cell-free scaffolds with a trend towards greatest levels in CM and EV groups (n=4-5).

7.3.4.4 Mineral characterisation

SEM imaging and EDX analysis was conducted on C and EV groups at day 21 to further characterise the mineralised tissue, as these are the least and most osteogenic groups respectively. No differences were identified at low magnifications via SEM imaging, with both groups being completely covered in matrix (Figure 7-8A), and no observable difference in cellular organisation under high voltage imaging (Figure 7-8B). At higher magnifications, fibres were almost completely covered in cells, with spherical nodules present both on and adjacent to fibres (Figure 7-8C). In mid pore regions, greater numbers of these nodules are present in the EV group (Figure 7-8D). EDX analyses were conducted to further investigate the mineral structure of the C and EV groups, with minimal differences between them at low magnifications (Figure S 7-1). Sulfur, which is present in several amino acids and plays a role in collagen synthesis (Townsend, Tew, & Tapiero, 2004), was found to be spatially distributed to closely match the underlying cellular organisation. To further investigate the structure of nodules which are present in both groups, mapping was also done on clusters of nodules at high magnification. Calcium and phosphorus were found to have a greater intensity within these clusters (Figure 7-8E), indicating their potential role as sites of mineral nucleation. Ca/P ratios were investigated in cell-free constructs, with a value of 1.75 in C and a significantly greater Ca/P ratio of 1.91 the EV group (Figure 7-8F). This is likely due to the presence of minerals in EVs which may influence the mineral composition of the nnHA coating. Interestingly however, Ca/P ratios in cell-scaffold constructs were much lower, with values of 0.84 and 0.70 in C and EV groups respectively (Figure 7-8G). These values were recorded in mid-pore regions to investigate cell-produced mineral and limit influence from the nnHA coating on fibres.

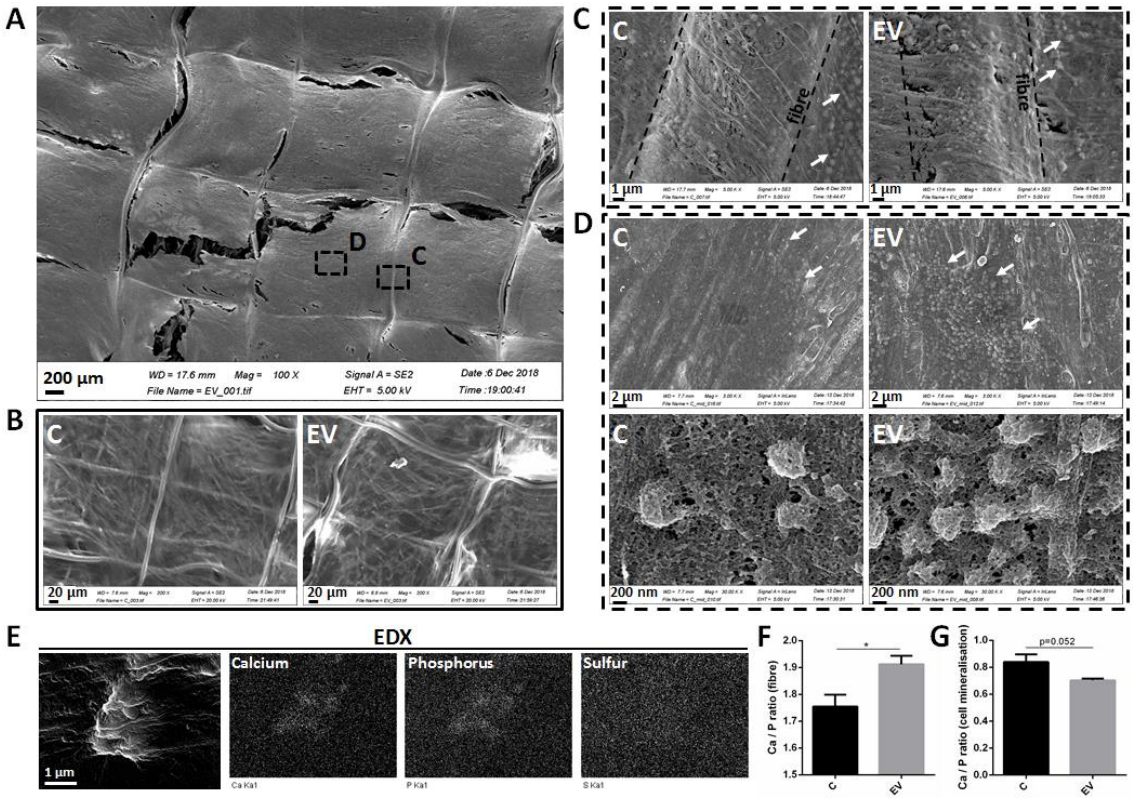

Figure 7-8 SEM imaging of C and EV constructs at D21. Both groups were enveloped in matrix (A), where two regions of interest, C and D are highlighted. High voltage imaging revealing the underlying cellular organisation (B). Superficial fibres in region C are almost completely covered, and the nHA coating can be seen through the matrix in addition to the presence of spherical nodules (white arrows) (C). Spherical nodules may also be seen in region D in the mid-pore regions (D), and are more numerous in the EV group. Element mapping was conducted on a cluster of nodules, where the greater intensity of calcium and phosphorus in this region confirms it as a site of mineral nucleation (E). Ca/P ratios were investigated in fibres of cell free constructs at D21 (n=5) (F) and were also investigated in cell-scaffold constructs at D21 (n=5) (G).

7.4 Discussion

Both direct and indirect biophysical regulation provide important cues to orchestrate cell behaviour and tissue adaptation in response to the continuously changing mechanical environment. Exploiting these cues by incorporation into regeneration strategies holds great promise for the repair of many tissues throughout the body. In this study, the development of a fibrous scaffold combining previously optimised direct and indirect biophysical cues which enhance stem cell osteogenesis to effectively guide bone tissue regeneration, is outlined. 10 µm diameter fibrous MEW scaffolds with defined 90°

fibre orientation were fabricated and modified with a biomimetic nnHA coating. Scaffolds were then functionalised with mechanically activated biochemical components released from stimulated osteocytes. It is shown that these components, namely whole conditioned medium and isolated MAEVs, both can enhance stem cell proliferation. It is further demonstrated that MAEV functionalisation further enhances osteogenic differentiation as seen by elevated ALP expression, collagen deposition and mineralisation of stem cells, and to a greater extent that has been previously shown with BMP2 functionalisation (chapter 6). This is further verified via SEM imaging and EDX analysis, where increased formation of mineralised nodules were seen in EV functionalised scaffolds. These findings demonstrate that indirect biophysical cues provide a powerful strategy for enhancing stem cell proliferation and mineralisation within 3D environments. Combined with the direct physical cues provided by the scaffold architecture and topography, this mechano-biomimetic approach has great potential to guide local bone tissue regeneration and repair.

Many strategies for bone tissue regeneration are comprised of engineered matrices which may be supplemented with potent factors such as bone morphogenic proteins (BMPs). While this has widely been demonstrated to significantly enhance *in vitro* osteogenesis and *in vivo* defect healing, there have recently been many concerns raised over the long-term safety of this approach. Adverse effects including osteolysis, ectopic bone formation and increased cancer risk have all been reported following *in vivo* use of BMPs (Hustedt & Blizzard, 2014; Tannoury & An, 2014; Vukicevic *et al.*, 2014). While these factors are naturally occurring within bone, the local imbalance caused by the high concentrations of an individual factor utilised in an engineered scaffold is likely the leading contributory factor to the adverse effects reported above (James *et al.*, 2016). This highlights the need for an alternative approach to stimulate bone repair in a more physiologically accurate manner. It is widely known that mechanical loading enhances the size and mineral content of bone (Kontulainen *et al.*, 2003), and exploiting the natural

means by which this occurs holds great promise for development of tissue regeneration strategies. It is now known that the osteocyte plays a key role in this process, sensing mechanical loads and communicating to other bone residing cells via biophysical cues to mediate their behaviour (Brady *et al.*, 2015; Hoey *et al.*, 2012; Mitchell B. Schaffler & Kennedy, 2012; You *et al.*, 2008). It has further been demonstrated that EVs are a primary means by which osteocytes deliver biophysical cues, with mechanical stimulation of osteocytes enhancing the recruitment and differentiation potential of released EVs (chapter 3). Furthermore, the great stability of the lipid membrane of EVs in addition to their specificity when delivering cargo to target cells (Maas, Breakefield, & Weaver, 2017) makes them a prime candidate for the delivery of indirect biophysical cues via engineered scaffolds to enhance bone repair in a safe and physiologically accurate manner.

One of the challenges of utilising EVs within engineering scaffolds entails securely binding them to the underlying structure. The majority of previous approaches have achieved this via loading an EV solution directly on to the scaffold before incubation to allow binding (de la Fuente *et al.*, 2015; Diomede *et al.*, 2018; W. Li, Liu, *et al.*, 2018; Narayanan, Huang, & Ravindran, 2016; Hui Xie *et al.*, 2017a; J. Zhang, Liu, *et al.*, 2016). One consideration with this method is the efficiency of EV binding. There is considerable work involved in the production of conditioned medium and isolation of EVs, and this loading method can result in a significant loss of these components depending on the scaffold material. Another method which has been reported entails suspending EVs within a gelatin solution before forming a hydrogel with EVs encapsulated inside (X. Liu *et al.*, 2017), which significantly reduces any loss of EVs. In the present study, scaffolds have been functionalised with a combinatory approach incorporating elements of both the above methods, with the foundation being a nHA coated scaffold. This mineral coating has nano-topographical features and a high surface area which stabilises proteins and enhances binding (Yu *et al.*, 2017). In addition to the enhanced binding properties provided by the

nHA mineral, CM and isolated EVs have further been re-suspended within a collagen solution, which is subsequently applied to scaffolds to further enhance binding efficiency. Membrane staining validated the presence of EVs on the fibre surface, both in CM, and to a greater extent, EV functionalised scaffolds. An important consideration in this work was to preserve the equally important direct biophysical cues provided by the micro-fibrous matrix and nano-topographical features of the mineral coating, both of which play important roles in driving stem cell osteogenesis (chapter 5-6), (Hongjian Zhou & Lee, 2011). Collagen concentration was thus optimised to preserve these features and provide a thin CM/EV enriched coating to further enhance these effects via indirect biophysical cues. This is the first study which has incorporated EVs with a defined micro-fibrous matrix to yield a scaffold which drives cellular behaviour via both direct and indirect biophysical cues.

The long term influence of CM and MAEV functionalised scaffolds on proliferation and osteogenesis was investigated by culturing scaffolds with MSCs. Consistent with previous findings which demonstrate that osteocyte CM enhances MSC proliferation (Heino, Hentunen, & Vaananen, 2004), it has been demonstrated here that CM, and to a lesser extent, MAEV functionalised scaffolds exhibit the same effect. Furthermore, the great capacity of MAEVs in driving MSC osteogenesis on fibrous scaffolds has been demonstrated through several osteogenic markers. Previous studies have reported on the capacity for EVs in promoting bone regeneration via immobilisation on scaffolds (Diomede *et al.*, 2018; W. Li, Liu, *et al.*, 2018; Hui Xie *et al.*, 2017a; J. Zhang, Liu, *et al.*, 2016). EVs from mechanically stimulated osteocytes have also been shown to enhance bone formation (Morrell *et al.*, 2018). However, this is the first report of osteocyte EVs being used for scaffold functionalisation, with the additional mechanical activation step providing significant benefits by exploiting the highly mechanosensitive nature of osteocytes to enhance mineralisation. Of particular interest is the means by which EVs enhance regeneration, and in particular, mineralisation. EVs are rich in annexin proteins and

membrane bound lipids which enhance calcification (Pokhrel, Gerstman, Hutcheson, & Chapagain, 2018). They have been shown to act as sites for mineral nucleation, and remarkably, to significantly enhance calcium deposition compared to BMP2 (Davies *et al.*, 2017a). In the present study, it is shown that mineralised nodules, closely resembling those previously identified in mineralising osteoblasts (Boonrungsiman *et al.*, 2012; Gough, Jones, & Hench, 2004), are present in both C and EV groups in close proximity to nnHA coated fibres. In mid pore regions, however, there are a greater number of nodules in the EV group indicating likely cellular uptake of EVs to globally enhance mineralisation. Also of particular interest is the Ca/P ratio of cells at day 21, which ranges between 0.70 – 0.84. This closely matches the value of 0.75 previously found for intracellular mineral-containing vesicles (Mahamid *et al.*, 2011) while also corresponding closely to the Ca/P ratio of amorphous calcium phosphate (W. Habraken *et al.*, 2016; W. J. E. M. Habraken *et al.*, 2013), a precursor phase which later transforms within collagen fibrils to hydroxyapatite (Mahamid *et al.*, 2011). Further from the significantly enhanced mineralisation in MSC seeded EV scaffolds, marginal increases in mineral content in cell-free EV scaffolds after 21 days has also been seen, in addition to elevated Ca/P ratios of the fibre mineral coating. This provides evidence that EVs alone may mineralise in culture. Taken together, it is evident that EVs play an important role in mineralisation, and enhance further mineral deposition by MSCs cultured on MAEV functionalised scaffolds. It is thus clear that EVs hold great promise not only as a means to recruit cells and drive behaviour via delivery of indirect biochemical cues, but also as sources of mineralisation, with promising applications for the functionalisation of scaffolds to guide bone regeneration in a biomimetic manner.

7.5 Conclusion

In summary, a scaffold which incorporates elements of direct biophysical stem cell regulation via a defined fibrous and mineral architecture, along with indirect biophysical regulation provided by mechanically activated EVs from stimulated osteocytes, has been developed for the first time. The capacity for EVs to enhance osteogenesis, and particularly mineralisation is clear, and this approach thus has great potential for applications in bone regeneration. In addition, this biomimetic approach overcomes the issues associated with using highly potent factors such as BMPs and has the potential to facilitate guided regeneration in a safe and physiologically appropriate manner.

Chapter 8

Discussion

The objective of this thesis was to investigate how direct and indirect biophysical cues drive MSC behaviour within bone, with this being used as a basis upon which to build therapies and tissue regeneration strategies to heal diseased or damaged bone (Figure 8-1). In stream 1 of this project, the indirect biophysically-induced biochemical cues which drive MSC behaviour were investigated. The osteocyte is known to act as the primary orchestrator of bone remodelling (Bonewald, 2011), and thus, the mechanisms behind mechanosignaling from the osteocyte to MSCs, and how this affects MSC behaviour, was investigated. It was found that osteocyte secreted EVs are largely responsible for delivering mechanically mediated signals to MSCs. EVs from mechanically stimulated osteocytes are significantly more potent in terms of driving MSC recruitment and osteogenesis, and have been termed here as MAEVs. MAEVs alone thus present themselves as a promising, biomimetic mechanotherapeutic for bone regeneration. In stream 2 of this project, the direct biophysical cues which drive MSC behaviour were investigated. On a microscopic level, bone tissue is fibrous in nature (Kane & Ma, 2013). The aim of this stream was to recapitulate the fibrous nature of the peri/endosteum, and develop various microarchitectures fabricated via MEW to investigate how fibrous architecture drives MSC behaviour. It was found that a 90° architecture enhanced cell spreading, mechanosignaling and osteogenesis as a result. The native mineral nanotopography was further recapitulated by developing a nano-needle hydroxyapatite coating, which was found to further significantly enhance MSC mineralisation. Finally, stream 1 and stream 2 were combined to develop a cell-free scaffold comprising direct and indirect biophysical cues to

synergistically drive MSC recruitment and osteogenesis. This biomimetic scaffold holds great promise for the effective regeneration of damaged or diseased bone.

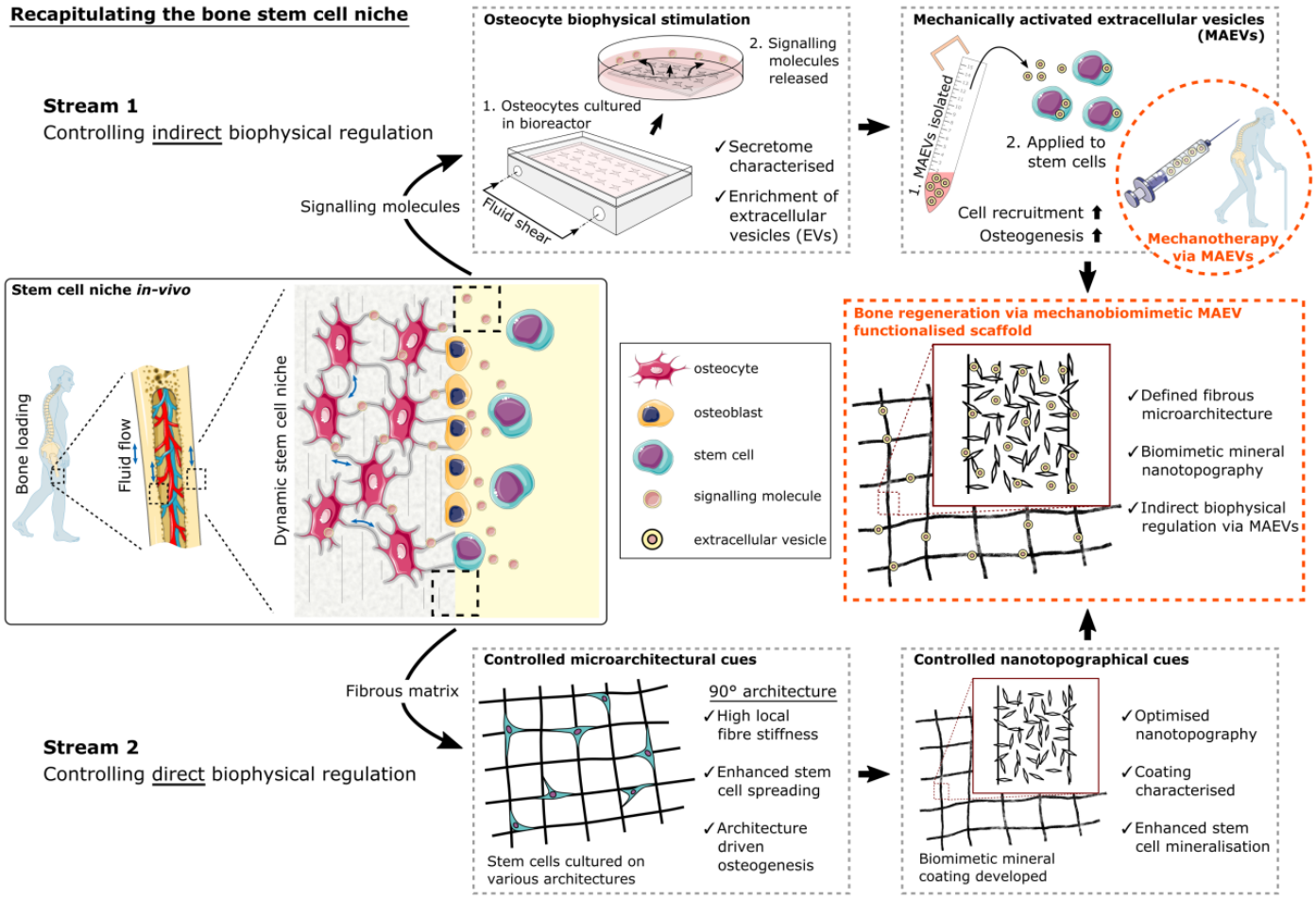

Figure 8-1 Outline of main results of thesis. Two project streams were undertaken to study and recapitulate the bone stem cell niche, with the final outcome of developing a mechano-biomimetic scaffold for bone regeneration.

8.1 Stream 1: Indirect cues for bone regeneration

This thesis begins with stream 1 (chapter 3), where mechanosignaling from the osteocyte to MSCs is investigated. It has previously been shown that conditioned medium (CM) from mechanically stimulated osteocytes enhances murine MSC recruitment and osteogenesis (Brady *et al.*, 2015; Hoey *et al.*, 2011). This was first verified in human MSCs, with enhanced recruitment and osteogenic gene expression being confirmed when treated with CM from mechanically stimulated osteocytes. The mechanisms behind this result have never thoroughly been investigated however, so a proteomic analysis on CM from statically cultured and mechanically stimulated osteocytes was conducted for the first time to yield a complete map of proteins in the osteocyte secretome. While the secretome was fundamentally similar for both cases, distinct differences were seen in the secretome of mechanically stimulated osteocytes, with upregulation of a range of proteins such as annexin A5 and histone H4, which have previously been positively correlated with enhanced osteogenesis (Genetos *et al.*, 2014; Shen *et al.*, 2003). Expression of several proteins was also negatively impacted by mechanical stimulation, such as thrombospondin 2, which has also been negatively correlated with bone formation *in vivo* (Hankenson *et al.*, 2000). Upon looking more globally at functional enrichments in mechanically regulated proteins however, several commonly recurring groups of proteins became apparent revealing further mechanisms behind osteocyte mechanosignaling. The most interesting of these was the significant enrichment of several extracellular vesicle and exosome related terms. This provided the first evidence that EVs are a fundamental component of osteocyte mechanosignaling. Also of great interest was the enrichment of both calcium and phosphate binding proteins in mechanically regulated proteins, further revealing likely roles of EV delivered proteins in driving mineralisation.

These results prompted further investigation into the role of EVs in osteocyte mechanosignaling to MSCs, with EVs being isolated from CM from statically and dynamically cultured osteocytes. It was first thought that EV quantity may increase following fluid shear stimulation of osteocytes, which was later demonstrated in another study (Morrell *et al.*, 2018). In the work presented in this thesis, an increase in EV quantity was also seen in mechanically stimulated osteocytes, however, this was not significant. This provided further evidence that EV quantity alone does not explain the enhanced recruitment and osteogenesis of MSCs cultured in CM from dynamically cultured osteocytes, but EV cargo is a likely contributing factor also, which is in agreement with the altered protein expression seen between groups in the proteomic analysis. As a result, EVs from mechanically cultured osteocytes have been termed MAEVs. MSCs were further treated with MAEVs and EVs from statically cultured osteocytes, and were shown to be taken up by MSCs. Remarkably, MSCs exhibited an almost identical trend of recruitment and osteogenic gene expression with MAEVs and static EVs to that seen with MSCs treated with CM from dynamically and statically cultured osteocytes. This further confirmed that EVs are a fundamental mechanism implicated in osteocyte mechanosignaling to MSCs. It is known that EVs both have great stability due to their lipid membrane, in addition to high specificity when delivering cargo to target cells (Maas *et al.*, 2017). This makes MAEVs a prime candidate for use as a systemic mechanotherapeutic due to their ability to specifically deliver biochemical cues in a safe and physiologically accurate manner. Furthermore, their stability highlights them as an ideal solution for the delivery of biochemical cues via synthetically fabricated scaffolds to guide local regeneration of damaged bone, leading to stream 2 of this thesis project.

8.2 Stream 2: Direct cues for bone regeneration

The aim of stream 2 of this project was to investigate how direct, architectural cues mediate MSC behaviour. Upon recruitment of MSCs *in vivo* they bind to the underlying fibrous matrix, where its architecture and stiffness further guide cell behaviour (Gattazzo *et al.*, 2014). Recapitulating this fibrous nature of bone, which is composed of fibrils arranged into fibres of diameter 1 – 10 μm (Kane & Ma, 2013), poses challenges in terms of scaffold fabrication. Traditional 3D printing approaches such as fused deposition modelling (FDM) cannot achieve this feature scale, while traditional electrospinning techniques have limited control over fibre placement to control scaffold architecture. As a result, it was decided to pursue the recently developed technology of MEW (Brown *et al.*, 2011), which overcomes both of the limitations with FDM and electrospinning above and allows the precise deposition of fibres of micron to sub-micron scale (Hochleitner *et al.*, 2015). MEW is a young technology which was only recently demonstrated for the first time in 2011, and at the commencement date of this project in 2014, there were no commercially available MEW printers. As a result, it was necessary to custom build a MEW printer (chapter 4), with this being based on the initial MEW work by Brown, Dalton and Hutmacher published in 2011, in addition to later developments by the Dalton and Hutmacher groups. While commercial options are available from 3 companies today, custom building a MEW printer still provides many advantages in terms of customisability and cost. This process took approximately 2 years before high quality scaffolds could consistently be fabricated, primarily due to the complications associated with combining high temperatures for polymer melting with a high voltage power supply. Early MEW printer configurations developed in this project had issues with electrical arcing between an electrical heating element and the high voltage electrode, while there were also issues with achieving consistent flow rates with syringe pump extrusion. The final design iteration consists of a semi-closed air heating configuration to eliminate interference between an isolated in-line

air heater and the high voltage at the needle. Air pressure is used to achieve consistent polymer flow through the needle. This system allowed the precise deposition of fibres necessary for subsequent work in stream 2 of this project.

The next step in this project was to investigate the role of fibrous scaffold architecture on MSC behaviour (chapter 5). While work has been done on the role of topography on MSC behaviour using micropatterned surfaces (Dupont *et al.*, 2011), with further work using FDM (Di Luca *et al.*, 2016) and solvent electrospun (H. Li, Wong, *et al.*, 2012) scaffolds, there are no studies which investigate the role of direct-written microfibrous geometries on MSC behaviour. To investigate this, random and highly aligned scaffolds (10° alignment in this study), which are commonly fabricated via solvent electrospinning for bone tissue engineering (Doustgani *et al.*, 2013; Guo *et al.*, 2015; H. Li, Wong, *et al.*, 2012; Z. X. Meng *et al.*, 2010; Yazhou *et al.*, 2009), were fabricated in addition to scaffolds with 90° and 45° fibre alignment using MEW. A 10 μm fibre diameter was used for this and all subsequent studies, with this being representative of the typical fibre diameters within native bone in addition to being within the range of 9 - 12 μm which was previously shown to be optimal for osteogenic differentiation out of a range of investigated diameters from 2 – 42 μm (Takahashi & Tabata, 2004). The four scaffold groups were mechanically characterised and investigated in terms of their influence on MSC behaviour and osteogenic differentiation. It was found that cells on the 90° scaffold exhibited greater spreading as demonstrated via lower cell aspect ratios and greater cell area. This, in conjunction with the greater fibre stiffness in this group contributed to greater nuclear YAP expression, a mechanosensitive marker for osteogenic differentiation (Dupont *et al.*, 2011). Interestingly, there was a downward trend in nuclear YAP from the 90° to 10° architecture, with lowest values in the random scaffold. Similar trends were seen through various markers of osteogenic differentiation, with mineralisation in particular giving a reliable indication to the osteogenic capacity of the 90° scaffold with lowest values in the

10° and random architectures. It can thus be seen that the traditionally used solvent electrospun random and aligned architectures can be further improved upon via the increased control achievable via MEW. Henceforth, the level of mineralisation in the random architecture will be used as the initial benchmark, to compare this and future results. Furthermore, the following studies will use as a control group the optimal scaffold from the preceding study, to demonstrate the iterative development of an effective strategy for applications in bone regeneration.

Following the development of a 90° scaffold architecture to guide MSC mechanosignaling and osteogenesis, work was done on developing a mineral component within the scaffold to further enhance these effects (chapter 6). A highly effective and commonly used approach to achieve this is via coating the substrate with a pHA coating using a highly concentrated SBF solution. This approach has a long history of use on bioactive glass (Kokubo, Ito, *et al.*, 1990; Kokubo, Kushitani, *et al.*, 1990), titanium (Kokubo & Takadama, 2006) and PCL (Oyane *et al.*, 2005; Vaquette *et al.*, 2013) to enhance osteogenesis, bonding to bone and facilitating bone formation. Scaffolds were coated using this approach as a benchmark. Another approach was developed as part of this project, which aimed to recapitulate the native nano-needle architecture of bone mineral (Reznikov *et al.*, 2018). This biomimetic approach using nanostructured CaPs has great capacity to support MSC proliferation and differentiation *in vitro* in addition to enhanced osseointegration and bone formation *in vivo* (P. Wang *et al.*, 2014; Hongjian Zhou & Lee, 2011). The nano-structure also facilitates enhanced protein adsorption which is advantageous for future biological functionalisation (Asara *et al.*, 2007). Developing a nnHA coating for fibrous scaffolds thus has great potential for enhancing bone regeneration. In addition, a composite PCL-hydroxyapatite blend was developed to fabricate micro-fibrous scaffolds via MEW with incorporated hydroxyapatite (iHA). The developed nnHA coating closely resembled the native nano-structure of bone mineral, and

vastly enhanced mineralisation 13-fold greater than the uncoated 90° scaffold and 2-fold greater than the pHA scaffold. It is also of note that almost half of the mineral on the pHA scaffold is from the mineral coating, while this contribution is much lower on the nnHA scaffold, with almost 90% of the total mineral being deposited by MSCs. Scaffolds were further loaded with BMP2, where it was shown that the nnHA coating facilitated a more sustained protein release which further enhanced mineralisation. Due to the significantly upregulated MSC osteogenesis and enhanced protein loading capacity, this scaffold was selected for further development to combine streams 1 and 2 of this thesis project.

8.3 Development of a bone mechano-biomimetic scaffold

The final aim of this project was to develop a mechano-biomimetic scaffold which recapitulates the bone stem cell niche as a strategy for tissue regeneration (chapter 7). As before, the optimal scaffold of the previous study modified with nnHA was used as the basis for this work, and used as a control to compare to scaffolds further functionalised with mechanically activated osteocyte CM and MAEVs. This aspect of the project posed several challenges, primarily of which entailed developing a strategy to securely bind proteins/EVs to the scaffold. While this was possible by simply soaking scaffolds in CM/EVs, further improvement was required to improve this and increase binding efficiency. This was achieved via a collagen coating method, with CM/EVs being re-suspended in collagen which then securely binds to the nnHA (Asara *et al.*, 2007) and forms a thin fibre coating. Collagen concentration and coating time were optimised such that a thin coating was attained to preserve the pro-proliferative and pro-osteogenic nature of the nnHA topography. Collagen coating alone was found to enhance further collagen deposition by MSCs, with further increases with MAEVs. CM was found to marginally increase mineralisation, with MAEV functionalised scaffolds demonstrating a significant, 2-fold increase in mineral deposition compared to the control nnHA scaffold. An increase in the

formation of mineralised nodules was also demonstrated in the MAEV group. Remarkably, the MAEV scaffold also demonstrated an almost 2-fold increase compared to BMP2 functionalised scaffolds. The implications of this result are profound, with BMP2 being the current gold standard for *in vivo* bone regeneration (Dellinger *et al.*, 2005; Notodihardjo *et al.*, 2012; Xiong *et al.*, 2015). In spite of this, long term *in vivo* studies with BMP2 use have reported a large number of severe adverse effects, including osteolysis, ectopic bone formation and increased cancer risk (Hustedt & Blizzard, 2014; Tannoury & An, 2014; Vukicevic *et al.*, 2014). Achieving the same or greater results via an alternative means, in this case via MAEVs, thus has substantial potential for the regeneration of bone in a safe, biomimetic manner. In addition, it is noteworthy that while this MAEV functionalised scaffold demonstrated an "only" 2-fold increase compared to control nnHA scaffolds, these scaffolds have already been systematically improved and optimised via several previous studies. The nnHA scaffold alone enhanced mineralisation 28-fold compared to the initial benchmark of the random scaffold. Further functionalisation with MAEVs brings this number to a 52-fold increase in mineralisation. The iterative development and improvements made to the scaffolds fabricated over the course of this thesis project are illustrated in Figure 8-2. Overall, this project has demonstrated that the synergistic combination of direct and indirect biophysical cues inspired by the native bone stem cell niche has significant potential for the generation of mechano-biomimetic strategies to effectively regenerate bone.

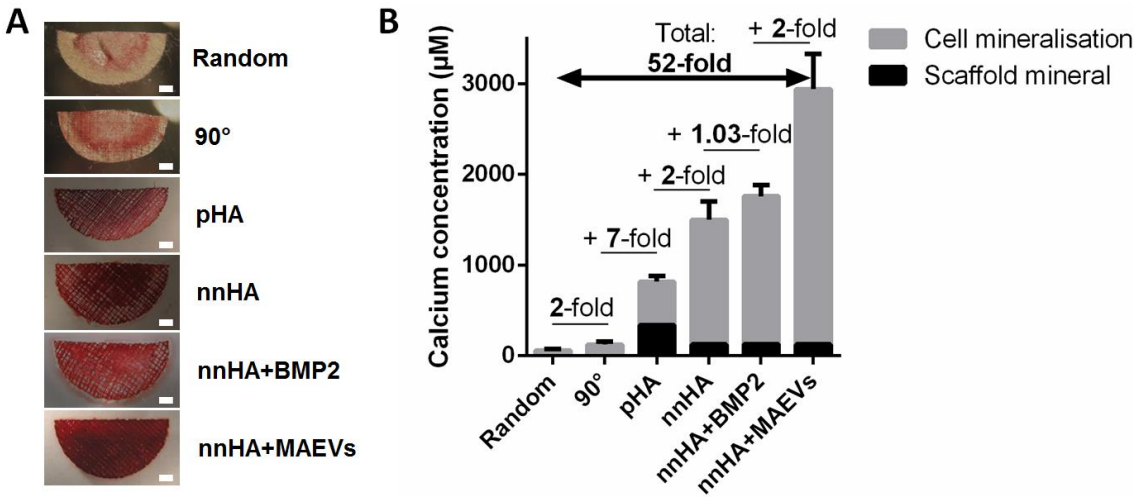

Figure 8-2 Iterative improvement of scaffold osteogenesis over the course of this thesis as shown via calcium staining (scale = 1 mm) (A) and further quantification of calcium concentration (B) in MSC cultured scaffolds after 21 days in culture. This resulted in a final 52-fold increase in mineral in the nnHA+MAEV functionalised scaffold compared to the initial random scaffold. Results are normalised to control samples to allow direct comparison between studies.

8.4 Limitations and future directions

In chapter 3 and 7, an osteocyte-like cell line, MLO-Y4, was used (Kato *et al.*, 1997). While these cells largely behave as osteocytes *in vivo*, releasing various characteristic signalling molecules and mediating bone cell behaviour (Cheng *et al.*, 2001; Zhao *et al.*, 2002), they lack several characteristics such as the typical absence of sclerostin expression and low DMP-1 expression (Shah *et al.*, 2016). Sclerostin is a mechanosignaling protein expressed by osteocytes, with reduced expression under osteocyte mechanical loading (Shu *et al.*, 2017). It has an inhibitory effect on bone formation and attenuates osteoblast proliferation and differentiation (Moester *et al.*, 2010). The MLO-Y4 line is thus not a perfect osteocyte model, with the proteomic analysis in chapter 3 not capturing the complete osteocyte secretome as would be present *in vivo*. Recently developed alternative osteocyte models include IDG-SW3 (Woo *et al.*, 2011) and OCY454 (Spatz *et al.*, 2015), both also of murine origin. There are also limitations with these cells however, including more complex culture protocols which require initial culture at 33ºC prior to being

maintained at 37ºC. This will likely facilitate the requirement for additional incubators dedicated to these cells, as incubators are typically maintained at 37ºC. Moreover, despite these limitations in terms of sclerostin expression, MAEVs isolated from MLO-Y4 CM elicited a pro-regenerative effect, indicating that additional factors, independent of sclerostin, regulate MSC behaviour. While the work in this thesis provided valuable insights to osteocyte mechanobiology, the challenges associated with more accurate cell lines are worth overcoming to gain a deeper understanding into osteocyte mechanobiology and signalling to neighbouring cells such as MSCs, and future work would greatly benefit from this.

Another limitation with this work is associated with the proteomic analysis. While this work yielded a large map of the proteins present in the osteocyte secretome, mass spectrometry does not detect all proteins. In this procedure, proteins are fragmented into peptides and ionised before conducting a mass analysis. The ability to detect a protein thus relies on how well the protein ionises, in addition to a range of other variables such as protein concentration and presence of other proteins or contaminants of similar masses which may interfere with its detection (Angel *et al.*, 2012). The use of other complimentary technologies, such as protein or gene microarrays, would thus prove valuable to both expand upon and validate the osteocyte secretome.

Collection of CM and isolation of MAEVs, which was also carried out as part of chapter 3 and 7, posed challenges in terms of experiment scaling. For chapter 3, cells were stimulated on glass slides of area 28.5 cm^2 within parallel plate flow chambers, with serum free medium subsequently being applied to glass slides before collecting the CM. The set-up and experimental protocol to conduct these experiments takes considerable time for the low yield of CM attained, approximately 2 ml per glass slide, with large volumes being required to further isolate appreciable quantities of MAEVs. In chapter 7, an orbital shaker was used to simplify this process and apply fluid shear to osteocytes in 6-well plates,

however, this also required significant time and consumables due to the high number of plates required to isolate the desired quantity of MAEVs. These problems are particularly manifested due to the requirement for fluid shear stimulation of cells, which is difficult to scale up. Nonetheless, developing methods to scale up these protocols would be considerably advantageous for the generation of large numbers of MAEVs, and would have valuable applications for both research and industrial MAEV production for the development of mechanotherapeutics.

There are several limitations of the MEW printer developed in chapter 4. One of the primary limitations is the VXM-3 stepper motor controller which is outdated in comparison to many other controllers currently available. Program size is severely limited, and commands are relatively basic limiting scaffolds to simple geometries. In addition, g-code is not supported, limiting the cross-transfer of programs and tools from other researchers, for example, the recently developed MEWTubes software to design tubular MEW structures (McColl *et al.*, 2018). While this was not an issue for the work undertaken as part of this thesis, future work would thus greatly benefit from an upgraded stepper motor controller, and a replacement system from Trio Motion Technology has already been ordered and is due to be implemented to achieve this. Another minor limitation of the current system is the air heating system. While this is effective for melting the polymer to facilitate a consistent MEW jet, it is believed that direct application of an electrical heater may provide a more consistent temperature. This would require further work to electrically insulate the heater from the high voltage electrode, such as via polyamide tape as used in other MEW systems (F. M. Wunner *et al.*, 2017). This would also provide a more elegant design with less tubing, in addition to eliminating the noise associated with the centrifugal fan required for the air heating system. Another limitation with MEW in general is the typically long print time required to fabricate scaffolds, however, other groups are currently

developing solutions to scale up the process and overcome this (Felix M. Wunner, Eggert, *et al.*, 2018).

In chapter 5, immunocytochemistry was used to assess cell morphology (via actin staining) and YAP expression on various scaffold architectures. It was difficult to precisely determine where, and to what degree, cells were binding to scaffolds however. This work could be expanded upon to include staining of focal adhesions, which would help to further elucidate the mechanisms behind the results seen in this chapter. In addition, the cell culture experiments in this chapter to assess long term osteogenic differentiation had a relatively low sample size (n=3 per group). This was offset however by the close agreement between outputs for osteogenic differentiation across three independent assays (ALP expression, calcium content and mineral content), which provided validation for these results in addition to being consistent with previous results for cell morphology and YAP expression.

In chapter 6, mineral modifications were developed for MEW scaffolds. Calcium/Phosphorus ratios were investigated as one means to characterise minerals on scaffolds. A limitation of this is that measurements taken using the EDX detector have limited accuracy. Increasing the accuracy of these measurements requires additional steps, including the use of accurate standards to allow fully quantitative analysis of samples. Another limitation was encountered in the XRD analysis. This requires the collection of a relatively large amount of powder sample, with this being achieved via precipitating the coating reagents in solution, centrifuging them and drying, before grinding the mineral into a powder. In reality, mineral is precipitated on to the scaffold in solution, and components in the reagents may bind to the scaffold to different degrees. The bulk isolated mineral for XRD analysis thus may not be fully representative of the coating which actually precipitates on to the scaffold. An attempt was made to precipitate mineral on flat PCL discs and scrape it off to yield a more representative precipitated mineral for XRD analysis. The required quantity of mineral could not be attained to successfully run an XRD analysis

however. Future work could look at optimising this process to more accurately characterise the scaffold precipitated mineral.

In chapter 7 of this thesis, scaffolds were functionalised with MAEVs. MAEVs were collected using an orbital shaker osteocyte stimulation method instead of parallel plate flow chambers, and thus, the flow regime is not exactly equal to that used in chapter 3. This was necessary due to the large number of MAEVs required for characterisation and scaffold functionalisation. In addition, scaffolds and MAEVs could not be characterised to the desired degree in this chapter due to time constraints. Further work would benefit from conducting immunoblotting to further validate the presence of EVs. In addition, quantification of EV release kinetics from scaffolds in addition to further immunofluorescence imaging to verify EV uptake by MSCs would be beneficial. Finally, *in vivo* evaluation of MAEVs and scaffolds is necessary to translate this research towards clinical applications.

8.5 Conclusions

- A MEW printer was designed, built, optimised and implemented within the laboratory for use within this thesis project and other PhD and masters projects.

- A map of the osteocyte secretome, both following static and dynamic culture, was created for the first time via mass spectrometry and a proteomic analysis revealing novel proteins and pathways implicated in osteocyte mechanosignaling.

- It was demonstrated that much of the effects of osteocyte mechanosignaling to MSCs were due to the presence of EVs, and it was shown that mechanically stimulated osteocytes release distinct MAEVs which enhance MSC recruitment and osteogenesis, with great potential for use as a potent systemic mechanotherapeutic.

- It was shown that a fibrous 90° scaffold microarchitecture significantly enhances MSC osteogenesis via direct biophysical cues which mediate cell behaviour.

- A new biomimetic nnHA coating was developed, and shown to significantly enhance MSC mineralisation and enhance protein adsorption compared to another commonly used coating protocol.

- A novel scaffold based mechano-biomimetic bone regeneration strategy was developed. This scaffold utilises direct biophysical (scaffold microarchitecture and mineral nanotopography) and indirect biophysical (MAEVs) cues based on the native bone stem cell niche to enhance osteogenesis in a physiologically relevant manner, with great potential as a more physiological and effective strategy to guide bone regeneration.

References

Agari, Y., & Ueda, A. (1994). Thermal conductivity of poly(vinyl chloride)/polycaprolactone blends. *Journal of Polymer Science Part B: Polymer Physics, 32* (1), 59-62.

Alford, A. I., Kozloff, K. M., & Hankenson, K. D. (2015). Extracellular matrix networks in bone remodeling. *The International Journal of Biochemistry & Cell Biology, 65*, 20-31.

Almoatazbellah, Y., Scott, J. H., & Paul, D. D. (2017). Additive manufacturing of polymer melts for implantable medical devices and scaffolds. *Biofabrication, 9* (1), 012002.

Altschul, S. F., Madden, T. L., Schaffer, A. A., Zhang, J., Zhang, Z., Miller, W., & Lipman, D. J. (1997). Gapped BLAST and PSI-BLAST: a new generation of protein database search programs. *Nucleic Acids Res, 25* (17), 3389-3402.

Angel, T. E., Aryal, U. K., Hengel, S. M., Baker, E. S., Kelly, R. T., Robinson, E. W., & Smith, R. D. (2012). Mass spectrometry-based proteomics: existing capabilities and future directions. *Chemical Society reviews, 41* (10), 3912-3928.

Aragona, M., Panciera, T., Manfrin, A., Giulitti, S., Michielin, F., Elvassore, N., Dupont, S., & Piccolo, S. (2013). A mechanical checkpoint controls multicellular growth through YAP/TAZ regulation by actin-processing factors. *Cell, 154* (5), 1047-1059.

Arai, F., Yoshihara, H., Hosokawa, K., Nakamura, Y., Gomei, Y., Iwasaki, H., & Suda, T. (2009). Niche regulation of hematopoietic stem cells in the endosteum. *Ann N Y Acad Sci, 1176*, 36-46.

Asara, J. M., Schweitzer, M. H., Freimark, L. M., Phillips, M., & Cantley, L. C. (2007). Protein sequences from mastodon and Tyrannosaurus rex revealed by mass spectrometry. *Science, 316* (5822), 280-285.

Bab, I., Gazit, D., Chorev, M., Muhlrad, A., Shteyer, A., Greenberg, Z., Namdar, M., & Kahn, A. (1992). Histone H4-related osteogenic growth peptide (OGP): A novel circulating stimulator of osteoblastic activity. *EMBO Journal, 11* (5), 1867-1873.

Baldwin, J. G., Wagner, F., Martine, L. C., Holzapfel, B. M., Theodoropoulos, C., Bas, O., Savi, F. M., De-Juan-Pardo, E. M., & Hutmacher, D. W. (2017). Periosteum tissue engineering in an orthotopic in vivo platform. *Biomaterials, 121*, 193-204.

Bas, O., D'Angella, D., Baldwin, J. G., Castro, N. J., Wunner, F. M., Saidy, N. T., Kollmannsberger, S., Reali, A., Rank, E., De-Juan-Pardo, E. M., & Hutmacher, D. W. (2017). An Integrated Design, Material, and Fabrication Platform for Engineering Biomechanically and Biologically Functional Soft Tissues. *ACS Applied Materials and Interfaces, 9* (35), 29430-29437.

Bas, O., De-Juan-Pardo, E., Meinert, C., D'Angella, D., Baldwin, J., Bray, L., Wellard, R., Kollmannsberger, S., Rank, E., Werner, C., Klein, T., Catelas, I., & Hutmacher, D. W. (2017). Biofabricated soft network composites for cartilage tissue engineering. *Biofabrication*.

Bas, O., De-Juan-Pardo, E. M., Chhaya, M. P., Wunner, F. M., Jeon, J. E., Klein, T. J., & Hutmacher, D. W. (2015). Enhancing structural integrity of hydrogels by using highly organised melt electrospun fibre constructs. *European Polymer Journal, 72*, 451-463.

Bas, O., Lucarotti, S., Angella, D. D., Castro, N. J., Meinert, C., Wunner, F. M., Rank, E., Vozzi, G., Klein, T. J., Catelas, I., De-Juan-Pardo, E. M., & Hutmacher, D. W. Rational design and fabrication of multiphasic soft network composites for tissue engineering articular cartilage: a numerical model-based approach. *Chemical Engineering Journal*.

Bas, O., Lucarotti, S., Angella, D. D., Castro, N. J., Meinert, C., Wunner, F. M., Rank, E., Vozzi, G., Klein, T. J., Catelas, I., De-Juan-Pardo, E. M., & Hutmacher, D. W. (2018). Rational design and fabrication of multiphasic soft network composites for tissue engineering articular cartilage: A numerical model-based approach. *Chemical Engineering Journal*.

Beederman, M., Lamplot, J. D., Nan, G., Wang, J., Liu, X., Yin, L., Li, R., Shui, W., Zhang, H., Kim, S. H., Zhang, W., Zhang, J., Kong, Y., Denduluri, S., Rogers, M. R., Pratt, A., Haydon, R. C., Luu, H. H., Angeles, J., Shi, L. L., & He, T.-C. (2013). BMP signaling in mesenchymal stem cell differentiation and bone formation. *Journal of biomedical science and engineering, 6* (8A), 32-52.

Bergmann, C., Lindner, M., Zhang, W., Koczur, K., Kirsten, A., Telle, R., & Fischer, H. (2010). 3D printing of bone substitute implants using calcium phosphate and bioactive glasses. *Journal of the European Ceramic Society, 30* (12), 2563-2567.

Bertlein, S., Hikimoto, D., Hochleitner, G., Hümmer, J., Jungst, T., Matsusaki, M., Akashi, M., & Groll, J. (2017). Development of Endothelial Cell Networks in 3D Tissues by Combination of Melt Electrospinning Writing with Cell-Accumulation Technology. *Small*.

Birmingham, E., Niebur, G. L., McHugh, P. E., Shaw, G., Barry, F. P., & McNamara, L. M. (2012). Osteogenic differentiation of mesenchymal stem cells is regulated by osteocyte and osteoblast cells in a simplified bone niche. *Eur Cell Mater, 23*, 13-27.

Bonewald, L. F. (2004). Osteocyte biology: its implications for osteoporosis. *J Musculoskelet Neuronal Interact, 4* (1), 101-104.

Bonewald, L. F. (2011). The amazing osteocyte. *Journal of Bone and Mineral Research, 26* (2), 229-238.

Bonewald, L. F. (2017). The Role of the Osteocyte in Bone and Nonbone Disease. *Endocrinology and Metabolism Clinics of North America, 46* (1), 1-18.

Bonewald, L. F., & Wacker, M. J. (2013). FGF23 production by osteocytes. *Pediatr Nephrol, 28* (4), 563-568.

Bonnans, C., Chou, J., & Werb, Z. (2014). Remodelling the extracellular matrix in development and disease. *Nat Rev Mol Cell Biol, 15* (12), 786-801.

Boonrungsiman, S., Gentleman, E., Carzaniga, R., Evans, N. D., McComb, D. W., Porter, A. E., & Stevens, M. M. (2012). The role of intracellular calcium phosphate in osteoblast-mediated bone apatite formation. *Proceedings of the National Academy of Sciences, 109* (35), 14170.

Bornstein, P., Kyriakides, T. R., Yang, Z., Armstrong, L. C., & Birk, D. E. (2000). Thrombospondin 2 modulates collagen fibrillogenesis and angiogenesis. *J Investig Dermatol Symp Proc, 5* (1), 61-66.

Boskey, A. L. (2013). Bone composition: relationship to bone fragility and antiosteoporotic drug effects. *BoneKEy Reports, 2*, 447.

Boyle, W. J., Simonet, W. S., & Lacey, D. L. (2003). Osteoclast differentiation and activation. *Nature, 423*, 337.

Brady, R. T., O'Brien, F. J., & Hoey, D. A. (2015). Mechanically stimulated bone cells secrete paracrine factors that regulate osteoprogenitor recruitment, proliferation, and differentiation. *Biochem Biophys Res Commun, 459* (1), 118-123.

Brotto, M., & Bonewald, L. (2015). Bone and muscle: Interactions beyond mechanical. *Bone, 80*, 109-114.

Brown, T. D., Dalton, P. D., & Hutmacher, D. W. (2011). Direct writing by way of melt electrospinning. *Adv Mater, 23* (47), 5651-5657.

Brown, T. D., Dalton, P. D., & Hutmacher, D. W. (2016). Melt electrospinning today: An opportune time for an emerging polymer process. *Progress in Polymer Science*.

Brown, T. D., Edin, F., Detta, N., Skelton, A. D., Hutmacher, D. W., & Dalton, P. D. (2014). Melt electrospinning of poly(ε-caprolactone) scaffolds: Phenomenological observations associated with collection and direct writing. *Materials Science and Engineering C, 45*, 698-708.

Brown, T. D., Slotosch, A., Thibaudeau, L., Taubenberger, A., Loessner, D., Vaquette, C., Dalton, P. D., & Hutmacher, D. W. (2012). Design and fabrication of tubular scaffolds via direct writing in a melt electrospinning mode. *Biointerphases, 7* (1-4), 1-16.

Cai, Y., Liu, Y., Yan, W., Hu, Q., Tao, J., Zhang, M., Shi, Z., & Tang, R. (2007). Role of hydroxyapatite nanoparticle size in bone cell proliferation. *Journal of Materials Chemistry, 17* (36), 3780-3787.

Campana, V., Milano, G., Pagano, E., Barba, M., Cicione, C., Salonna, G., Lattanzi, W., & Logroscino, G. (2014). Bone substitutes in orthopaedic surgery: from basic science to clinical practice. *Journal of Materials Science. Materials in Medicine, 25* (10), 2445-2461.

Caplan, A. I. (1991). Mesenchymal stem cells. *J Orthop Res, 9* (5), 641-650.

Caplan, A. I. (2017). Mesenchymal Stem Cells: Time to Change the Name! *STEM CELLS Translational Medicine, 6* (6), 1445-1451.

Cappariello, A., Loftus, A., Muraca, M., Maurizi, A., Rucci, N., & Teti, A. (2017). Osteoblast-derived extracellular vesicles are biological tools for the delivery of active molecules to bone. *J Bone Miner Res*.

Cardwell, R. D., Dahlgren, L. A., & Goldstein, A. S. (2014). Electrospun fibre diameter, not alignment, affects mesenchymal stem cell differentiation into the tendon/ligament lineage. *J Tissue Eng Regen Med, 8* (12), 937-945.

Castilho, M., Feyen, D., Flandes-Iparraguirre, M., Hochleitner, G., Groll, J., Doevendans, P. A. F., Vermonden, T., Ito, K., Sluijter, J. P. G., & Malda, J. (2017). Melt Electrospinning Writing of Poly-Hydroxymethylglycolide-co-ε-Caprolactone-Based Scaffolds for Cardiac Tissue Engineering. *Advanced Healthcare Materials, 6* (18).

Castilho, M., Hochleitner, G., Wilson, W., van Rietbergen, B., Dalton, P. D., Groll, J., Malda, J., & Ito, K. (2018). Mechanical behavior of a soft hydrogel reinforced with three-dimensional printed microfibre scaffolds. *Scientific reports, 8* (1), 1245.

Castilho, M., Mil, A., Maher, M., Metz, C. H. G., Hochleitner, G., Groll, J., Doevendans, P. A., Ito, K., Sluijter, J. P. G., & Malda, J. (2018). Melt Electrowriting Allows Tailored Microstructural and Mechanical Design of Scaffolds to Advance Functional Human Myocardial Tissue Formation. *Advanced Functional Materials, 0* (0), 1803151.

Cengel, Y. A. (2002). *Heat Transfer: A Practical Approach* (2 ed.). London, United States: McGraw-Hill Education - Europe.

Center, J. R., Nguyen, T. V., Schneider, D., Sambrook, P. N., & Eisman, J. A. (1999). Mortality after all major types of osteoporotic fracture in men and women: an observational study. *The Lancet, 353* (9156), 878-882.

Chan, C. K. F., Gulati, G. S., Sinha, R., Tompkins, J. V., Lopez, M., Carter, A. C., Ransom, R. C., Reinisch, A., Wearda, T., Murphy, M., Brewer, R. E., Koepke, L. S., Marecic, O., Manjunath, A., Seo, E. Y., Leavitt, T., Lu, W.-J., Nguyen, A., Conley, S. D., Salhotra, A., Ambrosi, T. H., Borrelli, M. R., Siebel, T., Chan, K., Schallmoser, K., Seita, J., Sahoo, D., Goodnough, H., Bishop, J., Gardner, M., Majeti, R., Wan, D. C., Goodman, S., Weissman, I. L., Chang, H. Y., & Longaker, M. T. (2018). Identification of the Human Skeletal Stem Cell. *Cell, 175* (1), 43-56.e21.

Chang, Y.-L., Stanford, C. M., & Keller, J. C. (2000). Calcium and phosphate supplementation promotes bone cell mineralization: Implications for hydroxyapatite (HA)-enhanced bone formation. *Journal of Biomedical Materials Research, 52* (2), 270-278.

Charbord, P. (2010). Bone marrow mesenchymal stem cells: historical overview and concepts. *Human Gene Therapy, 21* (9), 1045-1056.

Chen, F., Hochleitner, G., Woodfield, T., Groll, J., Dalton, P. D., & Amsden, B. G. (2016). Additive Manufacturing of a Photo-Cross-Linkable Polymer via Direct Melt Electrospinning Writing for Producing High Strength Structures. *Biomacromolecules, 17* (1), 208-214.

Chen, J. C., Hoey, D. A., Chua, M., Bellon, R., & Jacobs, C. R. (2016a). Mechanical signals promote osteogenic fate through a primary cilia-mediated mechanism. *Faseb Journal, 30* (4), 1504-1511.

Chen, J. C., Hoey, D. A., Chua, M., Bellon, R., & Jacobs, C. R. (2016b). Mechanical signals promote osteogenic fate through a primary cilia-mediated mechanism. *FASEB J, 30* (4), 1504-1511.

Chen, W., Qing, H., He, Y., Wang, J., Zhu, Z., & Wang, H. (2010). Gene expression patterns of osteocyte-like MLO-Y4 cells in response to cyclic compressive force stimulation. *Cell Biology International, 34* (5), 425-432.

Cheng, B., Kato, Y., Zhao, S., Luo, J., Sprague, E., Bonewald, L. F., & Jiang, J. X. (2001). PGE(2) is essential for gap junction-mediated intercellular communication between osteocyte-like MLO-Y4 cells in response to mechanical strain. *Endocrinology, 142* (8), 3464-3473.

Cherian, P. P., Siller-Jackson, A. J., Gu, S., Wang, X., Bonewald, L. F., Sprague, E., & Jiang, J. X. (2005). Mechanical strain opens connexin 43 hemichannels in osteocytes: A novel mechanism for the release of prostaglandin. *Molecular Biology of the Cell, 16* (7), 3100-3106.

Christopherson, G. T., Song, H., & Mao, H. Q. (2009). The influence of fiber diameter of electrospun substrates on neural stem cell differentiation and proliferation. *Biomaterials, 30* (4), 556-564.

Corrigan, M. A., Johnson, G. P., Stavenschi, E., Riffault, M., Labour, M.-N., & Hoey, D. A. (2018). TRPV4-mediates oscillatory fluid shear mechanotransduction in mesenchymal stem cells in part via the primary cilium. *Scientific reports, 8* (1), 3824.

Cox, J., Hein, M. Y., Luber, C. A., Paron, I., Nagaraj, N., & Mann, M. (2014). Accurate Proteome-wide Label-free Quantification by Delayed Normalization and Maximal Peptide Ratio Extraction, Termed MaxLFQ. *Molecular & Cellular Proteomics : MCP, 13* (9), 2513-2526.

Cox, J., & Mann, M. (2008). MaxQuant enables high peptide identification rates, individualized p.p.b.-range mass accuracies and proteome-wide protein quantification. *Nature Biotechnology, 26* (12), 1367-1372.

Cox, J., Neuhauser, N., Michalski, A., Scheltema, R. A., Olsen, J. V., & Mann, M. (2011). Andromeda: a peptide search engine integrated into the MaxQuant environment. *J Proteome Res, 10* (4), 1794-1805.

Cox, S. C., Thornby, J. A., Gibbons, G. J., Williams, M. A., & Mallick, K. K. (2015). 3D printing of porous hydroxyapatite scaffolds intended for use in bone tissue engineering applications. *Materials Science and Engineering: C, 47*, 237-247.

Cui, Y., Luan, J., Li, H., Zhou, X., & Han, J. (2016). Exosomes derived from mineralizing osteoblasts promote ST2 cell osteogenic differentiation by alteration of microRNA expression. *FEBS Lett, 590* (1), 185-192.

Cunniffe, G. M., Dickson, G. R., Partap, S., Stanton, K. T., & O'Brien, F. J. (2010). Development and characterisation of a collagen nano-hydroxyapatite composite scaffold for bone tissue engineering. *J Mater Sci Mater Med, 21* (8), 2293-2298.

Cunniffe, G. M., O'Brien, F. J., Partap, S., Levingstone, T. J., Stanton, K. T., & Dickson, G. R. (2010). The synthesis and characterization of nanophase hydroxyapatite using a novel dispersant-aided precipitation method. *J Biomed Mater Res A, 95* (4), 1142-1149.

Curtin, C. M., Cunniffe, G. M., Lyons, F. G., Bessho, K., Dickson, G. R., Duffy, G. P., & O'Brien, F. J. (2012). Innovative Collagen Nano-Hydroxyapatite Scaffolds Offer a Highly Efficient Non-Viral Gene Delivery Platform for Stem Cell-Mediated Bone Formation. *Adv Mater, 24* (6), 749-754.

Dallas, S. L., Prideaux, M., & Bonewald, L. F. (2013). The osteocyte: An endocrine cell . . . and more. *Endocrine Reviews, 34* (5), 658-690.

Dalton, P. D. (2017). Melt electrowriting with additive manufacturing principles. *Current Opinion in Biomedical Engineering, 2*, 49-57.

Dalton, P. D., Muerza-Cascante, M. L., & Hutmacher, D. W. (2015) Design and fabrication of scaffolds via melt electrospinning for applications in tissue engineering. *Vol. 2015-January. RSC Polymer Chemistry Series* (pp. 100-120).

Daly, A. C., Freeman, F. E., Gonzalez-Fernandez, T., Critchley, S. E., Nulty, J., & Kelly, D. J. (2017). 3D Bioprinting for Cartilage and Osteochondral Tissue Engineering. *Advanced Healthcare Materials, 6* (22), 1700298.

Davies, O. G., Cox, S. C., Williams, R. L., Tsaroucha, D., Dorrepaal, R. M., Lewis, M. P., & Grover, L. M. (2017a). Annexin-enriched osteoblast-derived vesicles act as an extracellular site of mineral nucleation within developing stem cell cultures. *Scientific reports, 7* (1).

Davies, O. G., Cox, S. C., Williams, R. L., Tsaroucha, D., Dorrepaal, R. M., Lewis, M. P., & Grover, L. M. (2017b). Annexin-enriched osteoblast-derived vesicles act as an extracellular site of mineral nucleation within developing stem cell cultures. *Sci Rep, 7* (1), 12639.

de la Fuente, A., Alonso-Alconada, L., Costa, C., Cueva, J., Garcia-Caballero, T., Lopez-Lopez, R., & Abal, M. (2015). M-Trap: Exosome-Based Capture of Tumor Cells as a New Technology in Peritoneal Metastasis. *J Natl Cancer Inst, 107* (9).

de Ruijter, M., Hrynevich, A., Haigh, J. N., Hochleitner, G., Castilho, M., Groll, J., Malda, J., & Dalton, P. D. (2017). Out-of-Plane 3D-Printed Microfibers Improve the Shear Properties of Hydrogel Composites. *Small*, 1702773-n/a.

de Ruijter, M., Ribeiro, A., Dokter, I., Castilho, M., & Malda, J. (2018). Simultaneous Micropatterning of Fibrous Meshes and Bioinks for the Fabrication of Living Tissue Constructs. *Advanced Healthcare Materials, 0* (0), 1800418.

Delalat, B., Harding, F., Gundsambuu, B., De-Juan-Pardo, E. M., Wunner, F. M., Wille, M.-L., Jasieniak, M., Malatesta, K. A. L., Griesser, H. J., Simula, A., Hutmacher, D. W., Voelcker, N. H., & Barry, S. C. (2017). 3D printed lattices as an activation and expansion platform for T cell therapy. *Biomaterials, 140*, 58-68.

Dellinger, J. G., Eurell, J. A. C., & Jamison, R. D. (2005). Bone response to 3D periodic hydroxyapatite scaffolds with and without tailored microporosity to deliver bone morphogenetic protein 2. *Journal of Biomedical Materials Research Part A, 76A* (2), 366-376.

Deng, L., Wang, Y., Peng, Y., Wu, Y., Ding, Y., Jiang, Y., Shen, Z., & Fu, Q. (2015). Osteoblast-derived microvesicles: A novel mechanism for communication between osteoblasts and osteoclasts. *Bone, 79* (Supplement C), 37-42.

Deng, R., Liu, Y., Ding, Y., Xie, P., Luo, L., & Yang, W. (2009). Melt electrospinning of low-density polyethylene having a low-melt flow index. *Journal of Applied Polymer Science, 114* (1), 166-175.

Di Luca, A., Lorenzo-Moldero, I., Mota, C., Lepedda, A., Auhl, D., Van Blitterswijk, C., & Moroni, L. (2016). Tuning Cell Differentiation into a 3D Scaffold Presenting a Pore Shape Gradient for Osteochondral Regeneration. *Advanced Healthcare Materials, 5* (14), 1753-1763.

Diomede, F., Gugliandolo, A., Cardelli, P., Merciaro, I., Ettorre, V., Traini, T., Bedini, R., Scionti, D., Bramanti, A., Nanci, A., Caputi, S., Fontana, A., Mazzon, E., & Trubiani, O. (2018). Three-dimensional printed PLA scaffold and human gingival stem cell-derived extracellular vesicles: a new tool for bone defect repair. *Stem Cell Research & Therapy, 9*, 104.

Domingos, M., Gloria, A., Coelho, J., Bartolo, P., & Ciurana, J. (2016). Three-dimensional printed bone scaffolds: The role of nano/micro-hydroxyapatite particles on the adhesion and differentiation of human mesenchymal stem cells. *Proc Inst Mech Eng H*, 954411916680236.

Doustgani, A., Vasheghani-Farahani, E., & Soleimani, M. (2013). Aligned and random nanofibrous nanocomposite scaffolds for bone tissue engineering. *Nanomedicine Journal, 1* (1), 20-27.

Driscoll, Tristan P., Cosgrove, Brian D., Heo, S.-J., Shurden, Zach E., & Mauck, Robert L. (2015). Cytoskeletal to Nuclear Strain Transfer Regulates YAP Signaling in Mesenchymal Stem Cells. *Biophys J, 108* (12), 2783-2793.

Drouet, C. (2013). Apatite Formation: Why It May Not Work as Planned, and How to Conclusively Identify Apatite Compounds. *BioMed Research International, 2013*, 490946.

Ducheyne, P., Radin, S., & King, L. (1993). The effect of calcium phosphate ceramic composition and structure on in vitro behavior. I. Dissolution. *Journal of Biomedical Materials Research, 27* (1), 25-34.

Dudakovic, A., Evans, J. M., Li, Y., Middha, S., McGee-Lawrence, M. E., van Wijnen, A. J., & Westendorf, J. J. (2013). Histone deacetylase inhibition promotes osteoblast maturation by altering the histone H4 epigenome and reduces Akt phosphorylation. *J Biol Chem, 288* (40), 28783-28791.

Dupont, S., Morsut, L., Aragona, M., Enzo, E., Giulitti, S., Cordenonsi, M., Zanconato, F., Le Digabel, J., Forcato, M., Bicciato, S., Elvassore, N., & Piccolo, S. (2011). Role of YAP/TAZ in mechanotransduction. *Nature, 474* (7350), 179-184.

Engler, A. J., Sen, S., Sweeney, H. L., & Discher, D. E. (2006). Matrix Elasticity Directs Stem Cell Lineage Specification. *Cell, 126* (4), 677-689.

Farrugia BL, B. T., Upton Z, Hutmacher DW, Dalton PD, Dargaville TR. (2013). Dermal fibroblast infiltration of poly(ε-caprolactone) scaffolds fabricated by melt electrospinning in a direct writing mode. *Biofabrication, 5* (2).

Felix, M. W., Pawel, M., Onur, B., Sebastian, E., Joachim Hendrik, M., Paul Donald, D., Elena, M. D.-J.-P., & Dietmar Werner, H. (2019). Printomics: the high-throughput analysis of printing parameters applied to melt electrowriting. *Biofabrication*.

Ferretti, C., & Mattioli-Belmonte, M. (2014). Periosteum derived stem cells for regenerative medicine proposals: Boosting current knowledge. *World journal of stem cells, 6* (3), 266-277.

Fierz, F. C., Beckmann, F., Huser, M., Irsen, S. H., Leukers, B., Witte, F., Degistirici, Ö., Andronache, A., Thie, M., & Müller, B. (2008). The morphology of anisotropic 3D-printed hydroxyapatite scaffolds. *Biomaterials, 29* (28), 3799-3806.

Finch-Edmondson, M. L., Strauss, R. P., Passman, A. M., Sudol, M., Yeoh, G. C., & Callus, B. A. (2015). TAZ Protein Accumulation Is Negatively Regulated by YAP Abundance in Mammalian Cells. *J Biol Chem, 290* (46), 27928-27938.

Florczak, S., Lorson, T., Zheng, T., Mrlik, M., Hutmacher, D., Higgins, M., Luxenhofer, R., & Dalton, P. (2018). *Melt Electrowriting of Electroactive Poly(vinylidene difluoride) Fibers*.

Florencio-Silva, R., Sasso, G. R. d. S., Sasso-Cerri, E., Simões, M. J., & Cerri, P. S. (2015). Biology of Bone Tissue: Structure, Function, and Factors That Influence Bone Cells. *BioMed Research International, 2015*, 421746.

Foolen, J., van Donkelaar, C., Nowlan, N., Murphy, P., Huiskes, R., & Ito, K. (2008). Collagen orientation in periosteum and perichondrium is aligned with preferential directions of tissue growth. *Journal of Orthopaedic Research, 26* (9), 1263-1268.

Frantz, C., Stewart, K. M., & Weaver, V. M. (2010). The extracellular matrix at a glance. *Journal of Cell Science, 123* (24), 4195.

Franz-Odendaal, T. A., Hall, B. K., & Witten, P. E. (2005). Buried alive: How osteoblasts become osteocytes. *Developmental Dynamics, 235* (1), 176-190.

Frost, H. M. (1994). Wolff's Law and bone's structural adaptations to mechanical usage: an overview for clinicians. *Angle Orthod, 64* (3), 175-188.

Fu, H., Subramanian, R. R., & Masters, S. C. (2000) 14-3-3 Proteins: Structure, function, and regulation. *Vol. 40. Annual Review of Pharmacology and Toxicology* (pp. 617-647).

Gattazzo, F., Urciuolo, A., & Bonaldo, P. (2014). Extracellular matrix: A dynamic microenvironment for stem cell niche. *Biochimica et Biophysica Acta (BBA) - General Subjects, 1840* (8), 2506-2519.

Genetos, D. C., Kephart, C. J., Zhang, Y., Yellowley, C. E., & Donahue, H. J. (2007). Oscillating fluid flow activation of gap junction hemichannels induces ATP release from MLO-Y4 osteocytes. *Journal of Cellular Physiology, 212* (1), 207-214.

Genetos, D. C., Wong, A., Weber, T. J., Karin, N. J., & Yellowley, C. E. (2014). Impaired osteoblast differentiation in annexin A2- and -A5-deficient cells. *PLoS ONE, 9* (9), e107482.

Giedraitis, A., Arnoczky, S. P., & Bedi, A. (2014). Allografts in Soft Tissue Reconstructive Procedures: Important Considerations. *Sports Health, 6* (3), 256-264.

Gilbert, S. (2000). *Developmental Biology*. Sunderland (MA): Sinauer Associates.

Gimona, M., Pachler, K., Laner-Plamberger, S., Schallmoser, K., & Rohde, E. (2017). Manufacturing of Human Extracellular Vesicle-Based Therapeutics for Clinical Use. *Int J Mol Sci, 18* (6).

Golub, E. E. (2009). Role of matrix vesicles in biomineralization. *Biochim Biophys Acta, 1790* (12), 1592-1598.

Gonzalez-Fernandez, T., Sathy, B. N., Hobbs, C., Cunniffe, G. M., McCarthy, H. O., Dunne, N. J., Nicolosi, V., O'Brien, F. J., & Kelly, D. J. (2017). Mesenchymal stem cell fate following non-viral gene transfection strongly depends on the choice of delivery vector. *Acta Biomaterialia, 55*, 226-238.

Gough, J. E., Jones, J. R., & Hench, L. L. (2004). Nodule formation and mineralisation of human primary osteoblasts cultured on a porous bioactive glass scaffold. *Biomaterials, 25* (11), 2039-2046.

Govey, P. M., Jacobs, J. M., Tilton, S. C., Loiselle, A. E., Zhang, Y., Freeman, W. M., Waters, K. M., Karin, N. J., & Donahue, H. J. (2014). Integrative transcriptomic and proteomic analysis of osteocytic cells exposed to fluid flow reveals novel mechano-sensitive signaling pathways. *J Biomech, 47* (8), 1838-1845.

Govey, P. M., Kawasawa, Y. I., & Donahue, H. J. (2015). Mapping the osteocytic cell response to fluid flow using RNA-Seq. *J Biomech, 48* (16), 4327-4332.

Govey, P. M., Loiselle, A. E., & Donahue, H. J. (2013). Biophysical regulation of stem cell differentiation. *Curr Osteoporos Rep, 11* (2), 83-91.

Grand View Research. (2017). Coronary Artery Bypass Graft (CABG) Market Analysis By Type (Saphenous Vein Grafts, Internal Thoracic Artery Grafts), By Surgical Procedures, By Technology (On-Pump CABG, Off-Pump CABG), And Segment Forecasts, 2014 - 2025 *www.grandviewresearch.com*.

Gugutkov, D., Awaja, F., Belemezova, K., Keremidarska, M., Krasteva, N., Kuyrkchiev, S., GallegoFerrer, G., Seker, S., Elcin, A. E., Elcin, Y. M., & Altankov, G. (2017). Osteogenic Differentiation of Mesenchymal Stem Cells using Hybrid Nanofibers with Different Configurations and Dimensionality. *Journal of Biomedical Materials Research Part A*, n/a-n/a.

Guo, Z., Xu, J., Ding, S., Li, H., Zhou, C., & Li, L. (2015). In vitro evaluation of random and aligned polycaprolactone/gelatin fibers via electrospinning for bone tissue engineering. *J Biomater Sci Polym Ed, 26* (15), 989-1001.

Habraken, W., Habibovic, P., Epple, M., & Bohner, M. (2016). Calcium phosphates in biomedical applications: materials for the future? *Materials Today, 19* (2), 69-87.

Habraken, W. J. E. M., Tao, J., Brylka, L. J., Friedrich, H., Bertinetti, L., Schenk, A. S., Verch, A., Dmitrovic, V., Bomans, P. H. H., Frederik, P. M., Laven, J., van der Schoot, P., Aichmayer, B., de With, G., DeYoreo, J. J., & Sommerdijk, N. A. J. M. (2013). Ion-

association complexes unite classical and non-classical theories for the biomimetic nucleation of calcium phosphate. *Nat Commun, 4*, 1507.

Hadjidakis, D. J., & Androulakis, II. (2006). Bone remodeling. *Ann N Y Acad Sci, 1092*, 385-396.

Haigh, J. N., Chuang, Y. M., Farrugia, B., Hoogenboom, R., Dalton, P. D., & Dargaville, T. R. (2016). Hierarchically Structured Porous Poly(2-oxazoline) Hydrogels. *Macromolecular Rapid Communications, 37* (1), 93-99.

Haigh, J. N., Dargaville, T. R., & Dalton, P. D. (2017). Additive manufacturing with polypropylene microfibers. *Materials Science and Engineering C, 77*, 883-887.

Han, Y., Cowin, S. C., Schaffler, M. B., & Weinbaum, S. (2004). Mechanotransduction and strain amplification in osteocyte cell processes. *Proceedings of the National Academy of Sciences of the United States of America, 101* (47), 16689-16694.

Hankenson, K. D., Bain, S. D., Kyriakides, T. R., Smith, E. A., Goldstein, S. A., & Bornstein, P. (2000). Increased marrow-derived osteoprogenitor cells and endosteal bone formation in mice lacking thrombospondin 2. *Journal of Bone and Mineral Research, 15* (5), 851-862.

Hanßke, F., Bas, O., Vaquette, C., Hochleitner, G., Groll, J., Kemnitz, E., Hutmacher, D. W., & Börner, H. G. (2017). Via precise interface engineering towards bioinspired composites with improved 3D printing processability and mechanical properties. *Journal of Materials Chemistry B, 5* (25), 5037-5047.

Haut Donahue, T. L., Genetos, D. C., Jacobs, C. R., Donahue, H. J., & Yellowley, C. E. (2004). Annexin V disruption impairs mechanically induced calcium signaling in osteoblastic cells. *Bone, 35* (3), 656-663.

He, J., Xia, P., & Li, D. (2016). Development of melt electrohydrodynamic 3D printing for complex microscale poly (epsilon-caprolactone) scaffolds. *Biofabrication, 8* (3), 035008.

Heino, T. J., Hentunen, T. A., & Vaananen, H. K. (2004). Conditioned medium from osteocytes stimulates the proliferation of bone marrow mesenchymal stem cells and their differentiation into osteoblasts. *Exp Cell Res, 294* (2), 458-468.

Hochleitner, G., Chen, F., Blum, C., Dalton, P. D., Amsden, B., & Groll, J. (2018). Melt electrowriting below the critical translation speed to fabricate crimped elastomer scaffolds with non-linear extension behaviour mimicking that of ligaments and tendons. *Acta Biomaterialia, 72*, 110-120.

Hochleitner, G., Fürsattel, E., Giesa, R., Groll, J., Schmidt, H. W., & P.D., D. (2018). Melt Electrowriting of Thermoplastic Elastomers. *Macromolecular Rapid Communications, 39* (10), 1800055.

Hochleitner, G., Hümmer, J. F., Luxenhofer, R., & Groll, J. (2014). High definition fibrous poly(2-ethyl-2-oxazoline) scaffolds through melt electrospinning writing. *Polymer, 55* (20), 5017-5023.

Hochleitner, G., Jüngst, T., Brown, T. D., Hahn, K., Moseke, C., Jakob, F., Dalton, P. D., & Groll, J. (2015). Additive manufacturing of scaffolds with sub-micron filaments via melt electrospinning writing. *Biofabrication, 7* (3).

Hochleitner, G., Kessler, M., Schmitz, M., Boccaccini, A. R., Teβmar, J., & Groll, J. (2017). Melt electrospinning writing of defined scaffolds using polylactide-poly(ethylene glycol) blends with 45S5 bioactive glass particles. *Materials Letters, 205*, 257-260.

Hochleitner, G., Youssef, A., Hrynevich, A., Haigh, J. N., Jungst, T., Groll, J., & Dalton, P. D. (2016). Fibre pulsing during melt electrospinning writing. *BioNanoMaterials*.

Hoey, D. A., Chen, J. C., & Jacobs, C. R. (2012). The primary cilium as a novel extracellular sensor in bone. *Frontiers in Endocrinology, 3* (JUN).

Hoey, D. A., Kelly, D. J., & Jacobs, C. R. (2011). A role for the primary cilium in paracrine signaling between mechanically stimulated osteocytes and mesenchymal stem cells. *Biochem Biophys Res Commun, 412* (1), 182-187.

Hogrebe, N. J., Reinhardt, J. W., & Gooch, K. J. (2017a). Biomaterial microarchitecture: a potent regulator of individual cell behavior and multicellular organization. *Journal of Biomedical Materials Research Part A, 105* (2), 640-661.

Hogrebe, N. J., Reinhardt, J. W., & Gooch, K. J. (2017b). Biomaterial microarchitecture: a potent regulator of individual cell behavior and multicellular organization. *Journal of Biomedical Materials Research - Part A, 105* (2), 640-661.

Holzapfel, B. M., Wagner, F., Loessner, D., Holzapfel, N. P., Thibaudeau, L., Crawford, R., Ling, M.-T., Clements, J. A., Russell, P. J., & Hutmacher, D. W. (2014). Species-specific homing mechanisms of human prostate cancer metastasis in tissue engineered bone. *Biomaterials, 35* (13), 4108-4115.

Hong, J. H., Hwang, E. S., McManus, M. T., Amsterdam, A., Tian, Y., Kalmukova, R., Mueller, E., Benjamin, T., Spiegelman, B. M., Sharp, P. A., Hopkins, N., & Yaffe, M. B. (2005). TAZ, a transcriptional modulator of mesenchymal stem cell differentiation. *Science, 309* (5737), 1074-1078.

Hrynevich, A., Elçi Bilge, Ş., Haigh Jodie, N., McMaster, R., Youssef, A., Blum, C., Blunk, T., Hochleitner, G., Groll, J., & Dalton Paul, D. (2018). Dimension-Based Design of Melt Electrowritten Scaffolds. *Small, 0* (0), 1800232.

Huang, C.-C., Narayanan, R., Alapati, S., & Ravindran, S. (2016). Exosomes as Biomimetic Tools for Stem Cell Differentiation: Applications in Dental Pulp Tissue Regeneration. *Biomaterials, 111*, 103-115.

Huang J, M. C., Bonewald L. Wnt3a potentiates myogenesis in C2C12 myoblasts through changes of signaling pathways including Wnt and NFkB. *ASBMR 2014 Annual Meeting, SU0190:s266. Houston (TX)*.

Huang, W., Carlsen, B., Wulur, I., Rudkin, G., Ishida, K., Wu, B., Yamaguchi, D. T., & Miller, T. A. (2004). BMP-2 exerts differential effects on differentiation of rabbit bone marrow stromal cells grown in two-dimensional and three-dimensional systems and is required for in vitro bone formation in a PLGA scaffold. *Experimental Cell Research, 299* (2), 325-334.

Huang, Z., Nelson, E. R., Smith, R. L., & Goodman, S. B. (2007). The sequential expression profiles of growth factors from osteoprogenitors [correction of osteroprogenitors] to osteoblasts in vitro. *Tissue Eng, 13* (9), 2311-2320.

Hustedt, J. W., & Blizzard, D. J. (2014). The controversy surrounding bone morphogenetic proteins in the spine: a review of current research. *The Yale journal of biology and medicine, 87* (4), 549-561.

Hutmacher, D. W., & Dalton, P. D. (2011). Melt Electrospinning. *Chemistry-an Asian Journal, 6* (1), 44-56.

Hutmacher, D. W., Schantz, T., Zein, I., Ng, K. W., Teoh, S. H., & Tan, K. C. (2001). Mechanical properties and cell cultural response of polycaprolactone scaffolds designed and fabricated via fused deposition modeling. *J Biomed Mater Res, 55* (2), 203-216.

Inzana, J. A., Olvera, D., Fuller, S. M., Kelly, J. P., Graeve, O. A., Schwarz, E. M., Kates, S. L., & Awad, H. A. (2014). 3D printing of composite calcium phosphate and collagen scaffolds for bone regeneration. *Biomaterials, 35* (13), 4026-4034.

Irina Alexandra, P., Roxana Cristina, P., Cosmin Catalin, M., Marian, Z., Bogdan Stefanita, C., Mona, M., Maria, D., Andrei, P., Diana, C., Mihai, S., & Catalin Romeo, L. (2018). Laser-direct writing by two-photon polymerization of 3D honeycomb-like structures for bone regeneration. *Biofabrication, 10* (2), 025009.

James, A. W., LaChaud, G., Shen, J., Asatrian, G., Nguyen, V., Zhang, X., Ting, K., & Soo, C. (2016). A Review of the Clinical Side Effects of Bone Morphogenetic Protein-2. *Tissue Eng Part B Rev, 22* (4), 284-297.

Johnson, G. P., Stavenschi, E., Eichholz, K. F., Corrigan, M. A., Fair, S., & Hoey, D. A. (2018). Mesenchymal stem cell mechanotransduction is cAMP dependent and regulated by adenylyl cyclase 6 and the primary cilium. *Journal of Cell Science, 131* (21).

Jui-Chih, C., Satoshi, F., Hiroyuki, T., Koichi, K., Hiroo, I., & Shan-hui, H. (2013). Cell orientation and regulation of cell–cell communication in human mesenchymal stem cells on different patterns of electrospun fibers. *Biomed Mater, 8* (5), 055002.

Jungst, T., Muerza-Cascante, M. L., Brown, T. D., Standfest, M., Hutmacher, D. W., Groll, J., & Dalton, P. D. (2015). Melt electrospinning onto cylinders: Effects of rotational velocity and collector diameter on morphology of tubular structures. *Polymer International, 64* (9), 1086-1095.

Kai, F., Laklai, H., & Weaver, V. M. (2016). Force Matters: Biomechanical Regulation of Cell Invasion and Migration in Disease. *Trends Cell Biol, 26* (7), 486-497.

Kane, R., & Ma, P. X. (2013). Mimicking the nanostructure of bone matrix to regenerate bone. *Materials Today, 16* (11), 418-423.

Karystinou, A., Roelofs, A. J., Neve, A., Cantatore, F. P., Wackerhage, H., & De Bari, C. (2015). Yes-associated protein (YAP) is a negative regulator of chondrogenesis in mesenchymal stem cells. *Arthritis Research & Therapy, 17* (1), 147.

Kato, Y., Windle, J. J., Koop, B. A., Mundy, G. R., & Bonewald, L. F. (1997). Establishment of an Osteocyte-like Cell Line, MLO-Y4. *Journal of Bone and Mineral Research, 12* (12), 2014-2023.

Kent, W. J., Sugnet, C. W., Furey, T. S., Roskin, K. M., Pringle, T. H., Zahler, A. M., & Haussler, D. (2002). The human genome browser at UCSC. *Genome Res, 12* (6), 996-1006.

Klein-Nulend, J., Semeins, C. M., Ajubi, N. E., Nijweide, P. J., & Burger, E. H. (1995). Pulsating fluid flow increases nitric oxide (NO) synthesis by osteocytes but not periosteal fibroblasts - correlation with prostaglandin upregulation. *Biochem Biophys Res Commun, 217* (2), 640-648.

Kokubo, T., Ito, S., Huang, Z. T., Hayashi, T., Sakka, S., Kitsugi, T., & Yamamuro, T. (1990). Ca,P-rich layer formed on high-strength bioactive glass-ceramic A-W. *J Biomed Mater Res, 24* (3), 331-343.

Kokubo, T., Kushitani, H., Sakka, S., Kitsugi, T., & Yamamuro, T. (1990). Solutions able to reproduce in vivo surface-structure changes in bioactive glass-ceramic A-W3. *Journal of Biomedical Materials Research, 24* (6), 721-734.

Kokubo, T., & Takadama, H. (2006). How useful is SBF in predicting in vivo bone bioactivity? *Biomaterials, 27* (15), 2907-2915.

Kontulainen, S., Sievänen, H., Kannus, P., Pasanen, M., & Vuori, I. (2003). Effect of Long-Term Impact-Loading on Mass, Size, and Estimated Strength of Humerus and Radius of Female Racquet-Sports Players: A Peripheral Quantitative Computed Tomography Study Between Young and Old Starters and Controls. *Journal of Bone and Mineral Research, 18* (2), 352-359.

Kumta, P. N., Sfeir, C., Lee, D.-H., Olton, D., & Choi, D. (2005). Nanostructured calcium phosphates for biomedical applications: novel synthesis and characterization. *Acta Biomaterialia, 1* (1), 65-83.

Labour, M.-N., Walsh, M., Cavaignac, M., Eichholz, K., deBarra, E., & Hoey, D. A. (2018). Electrospun Poly-D-L-Lactic Acid Fibrous Scaffolds as a Delivery Vehicle for Calcium Phosphate Salts to Promote In Situ Mineralisation and Bone Regeneration. *Journal of Biomaterials and Tissue Engineering, 8* (2), 206-217.

Lc, C. (2009). Next generation calcium phosphate-based biomaterials. *Dental materials journal, 28* (1), 1-10.

Lehnert, D., Wehrle-Haller, B., David, C., Weiland, U., Ballestrem, C., Imhof, B. A., & Bastmeyer, M. (2004). Cell behaviour on micropatterned substrata: limits of extracellular matrix geometry for spreading and adhesion. *Journal of Cell Science, 117* (1), 41.

Lewiecki, E. M. (2014). Role of sclerostin in bone and cartilage and its potential as a therapeutic target in bone diseases. *Therapeutic Advances in Musculoskeletal Disease, 6* (2), 48-57.

Li, B., Guo, B., Fan, H., & Zhang, X. (2008). Preparation of nano-hydroxyapatite particles with different morphology and their response to highly malignant melanoma cells in vitro. *Applied Surface Science, 255* (2), 357-360.

Li, C., Vepari, C., Jin, H.-J., Kim, H. J., & Kaplan, D. L. (2006). Electrospun silk-BMP-2 scaffolds for bone tissue engineering. *Biomaterials, 27* (16), 3115-3124.

Li, H., Wong, Y. S., Wen, F., Ng, K. W., Ng, G. K. L., Venkatraman, S. S., Boey, F. Y. C., & Tan, L. P. (2012). Human Mesenchymal Stem-Cell Behaviour On Direct Laser Micropatterned Electrospun Scaffolds with Hierarchical Structures. *Macromolecular Bioscience, 13* (3), 299-310.

Li, N., Song, J., Zhu, G., Li, X., Liu, L., Shi, X., & Wang, Y. (2016). Periosteum tissue engineering-a review. *4* (11), 1554-1561.

Li, Q., Huang, Q. P., Wang, Y. L., & Huang, Q. S. (2018). Extracellular vesicle-mediated bone metabolism in the bone microenvironment. *J Bone Miner Metab, 36* (1), 1-11.

Li, W., Liu, Y., Zhang, P., Tang, Y., Zhou, M., Jiang, W., Zhang, X., Wu, G., & Zhou, Y. (2018). Tissue-Engineered Bone Immobilized with Human Adipose Stem Cells-Derived Exosomes Promotes Bone Regeneration. *ACS Appl Mater Interfaces, 10* (6), 5240-5254.

Li, X., Liu, H., Wang, J., & Li, C. (2012). Preparation and characterization of poly(ε-caprolactone) nonwoven mats via melt electrospinning. *Polymer, 53* (1), 248-253.

Li, X., Ominsky, M. S., Warmington, K. S., Morony, S., Gong, J., Cao, J., Gao, Y., Shalhoub, V., Tipton, B., Haldankar, R., Chen, Q., Winters, A., Boone, T., Geng, Z., Niu, Q.-T., Ke, H. Z., Kostenuik, P. J., Simonet, W. S., Lacey, D. L., & Paszty, C. (2009). Sclerostin Antibody Treatment Increases Bone Formation, Bone Mass, and Bone Strength in a Rat Model of Postmenopausal Osteoporosis. *Journal of Bone and Mineral Research, 24* (4), 578-588.

Liu, X., Yang, Y., Li, Y., Niu, X., Zhao, B., & Wang, Y. (2017). Integration of stem cell-derived exosomes with in situ hydrogel glue as a promising tissue patch for articular cartilage regeneration. *9* (13), 4430-4438.

Liu, Y., Ross, J. F., Bodine, P. V., & Billiard, J. (2007). Homodimerization of Ror2 tyrosine kinase receptor induces 14-3-3(beta) phosphorylation and promotes osteoblast differentiation and bone formation. *Mol Endocrinol, 21* (12), 3050-3061.

Liu, Y., Wang, G., Cai, Y., Ji, H., Zhou, G., Zhao, X., Tang, R., & Zhang, M. (2008). In vitro effects of nanophase hydroxyapatite particles on proliferation and osteogenic differentiation of bone marrow-derived mesenchymal stem cells. *Journal of Biomedical Materials Research Part A, 90A* (4), 1083-1091.

Loong, C. K., Rey, C., Kuhn, L. T., Combes, C., Wu, Y., Chen, S. H., & Glimcher, M. J. (2000). Evidence of hydroxyl-ion deficiency in bone apatites: an inelastic neutron-scattering study. *Bone, 26* (6), 599-602.

Lorber, B., Fischer, F., Bailly, M., Roy, H., & Kern, D. (2012). Protein analysis by dynamic light scattering: methods and techniques for students. *Biochem Mol Biol Educ, 40* (6), 372-382.

Lu, P., Takai, K., Weaver, V. M., & Werb, Z. (2011). Extracellular Matrix Degradation and Remodeling in Development and Disease. *Cold Spring Harbor perspectives in biology, 3* (12), 10.1101/cshperspect.a005058 a005058.

Lu, Y., Yuan, B., Qin, C., Cao, Z., Xie, Y., Dallas, S. L., McKee, M. D., Drezner, M. K., Bonewald, L. F., & Feng, J. Q. (2011). The Biological Function of DMP-1 in Osteocyte Maturation Is Mediated by Its 57-kDa C-terminal Fragment. *Journal of Bone and Mineral Research, 26* (2), 331-340.

Lyons, J., Li, C., & Ko, F. (2004). Melt-electrospinning part I: processing parameters and geometric properties. *Polymer, 45* (22), 7597-7603.

Lysdahl, H., Baatrup, A., Foldager, C. B., & Bünger, C. (2014). Preconditioning Human Mesenchymal Stem Cells with a Low Concentration of BMP2 Stimulates Proliferation and Osteogenic Differentiation In Vitro. *BioResearch Open Access, 3* (6), 278-285.

Maas, S. L. N., Breakefield, X. O., & Weaver, A. M. (2017). Extracellular Vesicles: Unique Intercellular Delivery Vehicles. *Trends Cell Biol, 27* (3), 172-188.

Mahamid, J., Sharir, A., Gur, D., Zelzer, E., Addadi, L., & Weiner, S. (2011). Bone mineralization proceeds through intracellular calcium phosphate loaded vesicles: A cryo-electron microscopy study. *Journal of Structural Biology, 174* (3), 527-535.

Malone, A. M. D., Anderson, C. T., Tummala, P., Kwon, R. Y., Johnston, T. R., Stearns, T., & Jacobs, C. R. (2007). Primary cilia mediate mechanosensing in bone cells by a calcium-independent mechanism. *Proceedings of the National Academy of Sciences of the United States of America, 104* (33), 13325-13330.

Manolagas, S. C. (2000). Birth and Death of Bone Cells: Basic Regulatory Mechanisms and Implications for the Pathogenesis and Treatment of Osteoporosis*. *Endocrine Reviews, 21* (2), 115-137.

Marino, A., Filippeschi, C., Genchi, G. G., Mattoli, V., Mazzolai, B., & Ciofani, G. (2014). The Osteoprint: A bioinspired two-photon polymerized 3-D structure for the enhancement of bone-like cell differentiation. *Acta Biomaterialia, 10* (10), 4304-4313.

Marsell, R., & Einhorn, T. A. (2011). THE BIOLOGY OF FRACTURE HEALING. *Injury, 42* (6), 551-555.

Martine, L. C., Holzapfel, B. M., McGovern, J. A., Wagner, F., Quent, V. M., Hesami, P., Wunner, F. M., Vaquette, C., De-Juan-Pardo, E. M., Brown, T. D., Nowlan, B., Wu, D. J., Hutmacher, C. O., Moi, D., Oussenko, T., Piccinini, E., Zandstra, P. W., Mazzieri, R., Levesque, J.-P., Dalton, P. D., Taubenberger, A. V., & Hutmacher, D. W. (2017). Engineering a humanized bone organ model in mice to study bone metastases. *Nat. Protocols, 12* (4), 639-663.

McBeath, R., Pirone, D. M., Nelson, C. M., Bhadriraju, K., & Chen, C. S. (2004). Cell Shape, Cytoskeletal Tension, and RhoA Regulate Stem Cell Lineage Commitment. *Developmental Cell, 6* (4), 483-495.

McClung, M. R. (2017). Sclerostin antibodies in osteoporosis: latest evidence and therapeutic potential. *Therapeutic Advances in Musculoskeletal Disease, 9* (10), 263-270.

McColl, E., Groll, J., Jungst, T., & Dalton, P. D. (2018). Design and fabrication of melt electrowritten tubes using intuitive software. *Materials & Design, 155*, 46-58.

McMahon, J. M., Boyde, A., & Bromage, T. G. (1995). Pattern of collagen fiber orientation in the ovine calcaneal shaft and its relation to locomotor-induced strain. *Anat Rec, 242* (2), 147-158.

Meng, F., Murray, G. F., Kurgan, L., & Donahue, H. J. (2018). Functional and structural characterization of osteocytic MLO-Y4 cell proteins encoded by genes differentially expressed in response to mechanical signals in vitro. *Scientific reports, 8* (1), 6716.

Meng, Z., Moroishi, T., & Guan, K.-L. (2016). Mechanisms of Hippo pathway regulation. *Genes & Development, 30* (1), 1-17.

Meng, Z. X., Wang, Y. S., Ma, C., Zheng, W., Li, L., & Zheng, Y. F. (2010). Electrospinning of PLGA/gelatin randomly-oriented and aligned nanofibers as potential scaffold in tissue engineering. *Materials Science and Engineering: C, 30* (8), 1204-1210.

Mescher, A. L., & Junqueira, L. C. U. (2013). *Junqueira's basic histology: Text and atlas* (13 ed.). New York: McGraw Hill Medical.

Miedel, E., Dishowitz, M. I., Myers, M. H., Dopkin, D., Yu, Y. Y., Miclau, T. S., Marcucio, R., Ahn, J., & Hankenson, K. D. (2013). Disruption of thrombospondin-2 accelerates ischemic fracture healing. *Journal of Orthopaedic Research, 31* (6), 935-943.

Mo, C., Romero-Suarez, S., Bonewald, L., Johnson, M., & Brotto, M. (2012). Prostaglandin E2: from clinical applications to its potential role in bone- muscle crosstalk and myogenic differentiation. *Recent Pat Biotechnol, 6* (3), 223-229.

Mobasherpour, I., Heshajin, M. S., Kazemzadeh, A., & Zakeri, M. (2007). Synthesis of nanocrystalline hydroxyapatite by using precipitation method. *Journal of Alloys and Compounds, 430* (1), 330-333.

Moester, M. J. C., Papapoulos, S. E., Löwik, C. W. G. M., & van Bezooijen, R. L. (2010). Sclerostin: Current Knowledge and Future Perspectives. *Calcified tissue international, 87* (2), 99-107.

Moore, W. R., Graves, S. E., & Bain, G. I. (2001). Synthetic bone graft substitutes. *ANZ Journal of Surgery, 71* (6), 354-361.

Morgan, J., Holtman, K. R., Keller, J. C., & Stanford, C. M. (1996). In vitro mineralization and implant calcium phosphate-hydroxyapatite crystallinity. *Implant Dent, 5* (4), 264-271.

Morhayim, J., Rudjito, R., van Leeuwen, J. P., & van Driel, M. (2016). Paracrine Signaling by Extracellular Vesicles via Osteoblasts. *Current Molecular Biology Reports, 2* (1), 48-55.

Morhayim, J., van de Peppel, J., Demmers, J. A., Kocer, G., Nigg, A. L., van Driel, M., Chiba, H., & van Leeuwen, J. P. (2015). Proteomic signatures of extracellular vesicles secreted by nonmineralizing and mineralizing human osteoblasts and stimulation of tumor cell growth. *FASEB J, 29* (1), 274-285.

Morrell, A. E., Brown, G. N., Robinson, S. T., Sattler, R. L., Baik, A. D., Zhen, G., Cao, X., Bonewald, L. F., Jin, W., Kam, L. C., & Guo, X. E. (2018). Mechanically induced Ca2+ oscillations in osteocytes release extracellular vesicles and enhance bone formation. *Bone Res, 6* (1), 6.

Moseke, C., & Gbureck, U. (2010). Tetracalcium phosphate: Synthesis, properties and biomedical applications. *Acta Biomaterialia, 6* (10), 3815-3823.

Muerza-Cascante, M. L., Haylock, D., Hutmacher, D. W., & Dalton, P. D. (2015). Melt electrospinning and its technologization in tissue engineering. *Tissue Eng Part B Rev, 21* (2), 187-202.

Muerza-Cascante, M. L., Shokoohmand, A., Khosrotehrani, K., Haylock, D., Dalton, P. D., Hutmacher, D. W., & Loessner, D. (2016). Endosteal-like extracellular matrix expression on melt electrospun written scaffolds. *Acta Biomater*.

Muhlrad, A., Pavlov, D., Peyser, Y. M., & Reisler, E. (2006). Inorganic phosphate regulates the binding of cofilin to actin filaments. *Febs j, 273* (7), 1488-1496.

Murray, I. R., & Péault, B. (2015). Q&A: Mesenchymal stem cells — where do they come from and is it important? *BMC Biology, 13*, 99.

Nagarajan, S., Belaid, H., Pochat-Bohatier, C., Teyssier, C., Iatsunskyi, I., Coy, E., Balme, S., Cornu, D., Miele, P., Kalkura, N. S., Cavaillès, V., & Bechelany, M. (2017). Design of Boron Nitride/Gelatin Electrospun Nanofibers for Bone Tissue Engineering. *ACS Appl Mater Interfaces, 9* (39), 33695-33706.

Nakashima, T., Hayashi, M., Fukunaga, T., Kurata, K., Oh-Hora, M., Feng, J. Q., Bonewald, L. F., Kodama, T., Wutz, A., Wagner, E. F., Penninger, J. M., & Takayanagi, H. (2011). Evidence for osteocyte regulation of bone homeostasis through RANKL expression. *Nature Medicine, 17* (10), 1231-1234.

Narayanan, R., Huang, C.-C., & Ravindran, S. (2016). Hijacking the Cellular Mail: Exosome Mediated Differentiation of Mesenchymal Stem Cells. *Stem cells international, 2016*, 11.

Nishiguchi, A., Yoshida, H., Matsusaki, M., & Akashi, M. (2011). Rapid Construction of Three-Dimensional Multilayered Tissues with Endothelial Tube Networks by the Cell-Accumulation Technique. *Adv Mater, 23* (31), 3506-3510.

Nobbmann, U. Protein sizing by light scattering, molecular weight and polydispersity. Retrieved 15/12/18, 2018, from http://nanoparticles.org/pdf/nobbmann.pdf

Notodihardjo, F. Z., Kakudo, N., Kushida, S., Suzuki, K., & Kusumoto, K. (2012). Bone regeneration with BMP-2 and hydroxyapatite in critical-size calvarial defects in rats. *Journal of Cranio-Maxillofacial Surgery, 40* (3), 287-291.

O'Brien, F. J. (2011). Biomaterials & scaffolds for tissue engineering. *Materials Today, 14* (3), 88-95.

Olivares-Navarrete, R., Lee, E. M., Smith, K., Hyzy, S. L., Doroudi, M., Williams, J. K., Gall, K., Boyan, B. D., & Schwartz, Z. (2017). Substrate Stiffness Controls Osteoblastic and Chondrocytic Differentiation of Mesenchymal Stem Cells without Exogenous Stimuli. *PLoS ONE, 12* (1), e0170312.

Ollion, J., Cochennec, J., Loll, F., Escudé, C., & Boudier, T. (2013). TANGO: A generic tool for high-throughput 3D image analysis for studying nuclear organization. *Bioinformatics, 29* (14), 1840-1841.

Olsen, M. H., Larsen, N. B., & Hjortø, G. M. (2013). *Two-photon polymerization of immune cell scaffolds.* (PhD), Technical University of Denmark, Denmark.

Olvera, D., Sathy, B. N., Carroll, S. F., & Kelly, D. J. (2017). Modulating microfibrillar alignment and growth factor stimulation to regulate mesenchymal stem cell differentiation. *Acta Biomater, 64*, 148-160.

Oyane, A., Uchida, M., Yokoyama, Y., Choong, C., Triffitt, J., & Ito, A. (2005). Simple surface modification of poly(ϵ-caprolactone) to induce its apatite-forming ability. *Journal of Biomedical Materials Research Part A, 75A* (1), 138-145.

Paino, F., la Noce, M., Tirino, V., Naddeo, P., Desiderio, V., Pirozzi, G., De Rosa, A., Laino, L., Altucci, L., & Papaccio, G. (2014). Histone Deacetylase Inhibition with Valproic Acid Downregulates Osteocalcin Gene Expression in Human Dental Pulp Stem Cells and Osteoblasts: Evidence for HDAC2 Involvement. *Stem Cells (Dayton, Ohio), 32* (1), 279-289.

Palazzo, B., Iafisco, M., Laforgia, M., Margiotta, N., Natile, G., Bianchi, C. L., Walsh, D., Mann, S., & Roveri, N. (2007). Biomimetic Hydroxyapatite–Drug Nanocrystals as Potential Bone Substitutes with Antitumor Drug Delivery Properties. *Advanced Functional Materials, 17* (13), 2180-2188.

Pan, H., Xie, Y., Zhang, Z., Li, K., Hu, D., Zheng, X., Fan, Q., & Tang, T. (2017). YAP-mediated mechanotransduction regulates osteogenic and adipogenic differentiation of BMSCs on hierarchical structure. *Colloids Surf B Biointerfaces, 152*, 344-353.

Parekkadan, B., & Milwid, J. M. (2010). Mesenchymal stem cells as therapeutics. *Annu Rev Biomed Eng, 12*, 87-117.

Park, D., Spencer, J. A., Koh, B. I., Kobayashi, T., Fujisaki, J., Clemens, T. L., Lin, C. P., Kronenberg, H. M., & Scadden, D. T. (2012). Endogenous bone marrow MSCs are dynamic, fate-restricted participants in bone maintenance and regeneration. *Cell Stem Cell, 10* (3), 259-272.

Pigossi, S. C., Medeiros, M. C., Saska, S., Cirelli, J. A., & Scarel-Caminaga, R. M. (2016). Role of Osteogenic Growth Peptide (OGP) and OGP(10–14) in Bone Regeneration: A Review. *Int J Mol Sci, 17* (11), 1885.

Pokhrel, R., Gerstman, B. S., Hutcheson, J. D., & Chapagain, P. P. (2018). In Silico Investigations of Calcium Phosphate Mineralization in Extracellular Vesicles. *The Journal of Physical Chemistry B, 122* (14), 3782-3789.

Prabhakaran, M. P., Venugopal, J., & Ramakrishna, S. (2009). Electrospun nanostructured scaffolds for bone tissue engineering. *Acta Biomaterialia, 5* (8), 2884-2893.

Priam, S., Bougault, C., Houard, X., Gosset, M., Salvat, C., Berenbaum, F., & Jacques, C. (2013). Identification of soluble 14-3-3 as a novel subchondral bone mediator involved in cartilage degradation in osteoarthritis. *Arthritis Rheum, 65* (7), 1831-1842.

Qin, Y., Peng, Y., Zhao, W., Pan, J., Ksiezak-Reding, H., Cardozo, C., Wu, Y., Divieti Pajevic, P., Bonewald, L. F., Bauman, W. A., & Qin, W. (2017). Myostatin inhibits osteoblastic

differentiation by suppressing osteocyte-derived exosomal microRNA-218: A novel mechanism in muscle-bone communication. *J Biol Chem, 292* (26), 11021-11033.

Qiu, S., Rao, D. S., Palnitkar, S., & Parfitt, A. M. (2003). Reduced iliac cancellous osteocyte density in patients with osteoporotic vertebral fracture. *J Bone Miner Res, 18* (9), 1657-1663.

Rachner, T. D., Khosla, S., & Hofbauer, L. C. (2011). Osteoporosis: now and the future. *The Lancet, 377* (9773), 1276-1287.

Reilly, G. C., & Engler, A. J. (2010). Intrinsic extracellular matrix properties regulate stem cell differentiation. *J Biomech, 43* (1), 55-62.

Remya, N. S., Syama, S., Gayathri, V., Varma, H. K., & Mohanan, P. V. (2014). An in vitro study on the interaction of hydroxyapatite nanoparticles and bone marrow mesenchymal stem cells for assessing the toxicological behaviour. *Colloids and Surfaces B: Biointerfaces, 117*, 389-397.

Rey, C., Combes, C., Drouet, C., & Glimcher, M. J. (2009). Bone mineral: update on chemical composition and structure. *Osteoporosis international : a journal established as result of cooperation between the European Foundation for Osteoporosis and the National Osteoporosis Foundation of the USA, 20* (6), 1013-1021.

Reznikov, N., Bilton, M., Lari, L., Stevens, M. M., & Kröger, R. (2018). Fractal-like hierarchical organization of bone begins at the nanoscale. *Science, 360* (6388).

Roberts, S. J., van Gastel, N., Carmeliet, G., & Luyten, F. P. (2015). Uncovering the periosteum for skeletal regeneration: The stem cell that lies beneath. *Bone, 70*, 10-18.

Robling, A. G., Niziolek, P. J., Baldridge, L. A., Condon, K. W., Allen, M. R., Alam, I., Mantila, S. M., Gluhak-Heinrich, J., Bellido, T. M., Harris, S. E., & Turner, C. H. (2008). Mechanical stimulation of bone in vivo reduces osteocyte expression of Sost/sclerostin. *J Biol Chem, 283* (9), 5866-5875.

Robling, A. G., & Turner, C. H. (2009). Mechanical signaling for bone modeling and remodeling. *Critical reviews in eukaryotic gene expression, 19* (4), 319-338.

Rodan, G. A., & Rodan, A. R. (2005). The family of osteoblast transcription factors is growing. *IBMS BoneKEy, 2* (10), 12-15.

Rosser, J., & Bonewald, L. F. (2012). Studying osteocyte function using the cell lines MLO-Y4 and MLO-A5. *Methods Mol Biol, 816*, 67-81.

Rozario, T., & DeSimone, D. W. (2010). The Extracellular Matrix In Development and Morphogenesis: A Dynamic View. *Developmental Biology, 341* (1), 126-140.

Rutkovskiy, A., Stensløkken, K.-O., & Vaage, I. J. (2016). Osteoblast Differentiation at a Glance. *Medical Science Monitor Basic Research, 22*, 95-106.

Saarakkala, S., Julkunen, P., Kiviranta, P., Mäkitalo, J., Jurvelin, J. S., & Korhonen, R. K. (2010). Depth-wise progression of osteoarthritis in human articular cartilage: investigation of composition, structure and biomechanics. *Osteoarthritis and Cartilage, 18* (1), 73-81.

Salek, M. M., Sattari, P., & Martinuzzi, R. J. (2012). Analysis of fluid flow and wall shear stress patterns inside partially filled agitated culture well plates. *Ann Biomed Eng, 40* (3), 707-728.

Sato, M., Asada, N., Kawano, Y., Wakahashi, K., Minagawa, K., Kawano, H., Sada, A., Ikeda, K., Matsui, T., & Katayama, Y. (2013). Osteocytes regulate primary lymphoid organs and fat metabolism. *Cell Metab, 18* (5), 749-758.

Sato, M., Suzuki, T., Kawano, M., & Tamura, M. (2017). Circulating osteocyte-derived exosomes contain miRNAs which are enriched in exosomes from MLO-Y4 cells. *Biomedical Reports, 6* (2), 223-231.

Schaffler, M. B., Cheung, W.-Y., Majeska, R., & Kennedy, O. (2014a). Osteocytes: Master Orchestrators of Bone. *Calcified tissue international, 94* (1), 5-24.

Schaffler, M. B., Cheung, W. Y., Majeska, R., & Kennedy, O. (2014b). Osteocytes: master orchestrators of bone. *Calcif Tissue Int, 94* (1), 5-24.

Schaffler, M. B., & Kennedy, O. D. (2012). Osteocyte Signaling in Bone. *Current Osteoporosis Reports, 10* (2), 118-125.

Schindelin, J., Arganda-Carreras, I., Frise, E., Kaynig, V., Longair, M., Pietzsch, T., Preibisch, S., Rueden, C., Saalfeld, S., Schmid, B., Tinevez, J.-Y., White, D. J., Hartenstein, V., Eliceiri, K., Tomancak, P., & Cardona, A. (2012). Fiji: an open-source platform for biological-image analysis. *Nat Meth, 9* (7), 676-682.

Shah, K. M., Stern, M. M., Stern, A. R., Pathak, J. L., Bravenboer, N., & Bakker, A. D. (2016). Osteocyte isolation and culture methods. *BoneKEy Reports, 5*, 838-838.

Shen, J., Hovhannisyan, H., Lian, J. B., Montecino, M. A., Stein, G. S., Stein, J. L., & Van Wijnen, A. J. (2003). Transcriptional induction of the osteocalcin gene during osteoblast differentiation involves acetylation of histones H3 and H4. *Molecular Endocrinology, 17* (4), 743-756.

Shimada, N., Ogata, N., Nakane, K., & Ogihara, T. (2012). Spot laser melt electrospinning of a fiber bundle composed of poly(lactide)/poly(ethylene-co-vinyl alcohol) pie wedge fibers. *Journal of Applied Polymer Science, 125* (SUPPL. 2), E384-E389.

Shu, R., Bai, D., Sheu, T., He, Y., Yang, X., Xue, C., He, Y., Zhao, M., & Han, X. (2017). Sclerostin Promotes Bone Remodeling in the Process of Tooth Movement. *PLoS ONE, 12* (1), e0167312.

Singh, S., Grabner, A., Yanucil, C., Schramm, K., Czaya, B., Krick, S., Czaja, M. J., Bartz, R., Abraham, R., Di Marco, G. S., Brand, M., Wolf, M., & Faul, C. (2016). Fibroblast growth factor 23 directly targets hepatocytes to promote inflammation in chronic kidney disease. *Kidney Int, 90* (5), 985-996.

Solheim, E. (1998). Growth factors in bone. *International Orthopaedics, 22* (6), 410-416.

Southwick, F. S. (2000). Gelsolin and ADF/cofilin enhance the actin dynamics of motile cells. *Proceedings of the National Academy of Sciences, 97* (13), 6936.

Spatz, J. M., Wein, M. N., Gooi, J. H., Qu, Y., Garr, J. L., Liu, S., Barry, K. J., Uda, Y., Lai, F., Dedic, C., Balcells-Camps, M., Kronenberg, H. M., Babij, P., & Pajevic, P. D. (2015). The Wnt Inhibitor Sclerostin Is Up-regulated by Mechanical Unloading in Osteocytes in Vitro. *Journal of Biological Chemistry, 290* (27), 16744-16758.

Stavenschi, E., Labour, M.-N., & Hoey, D. A. (2017). Oscillatory fluid flow induces the osteogenic lineage commitment of mesenchymal stem cells: The effect of shear stress magnitude, frequency, and duration. *J Biomech, 55*, 99-106.

Sun, D., Chang, C., Li, S., & Lin, L. (2006). Near-Field Electrospinning. *Nano Letters, 6* (4), 839-842.

Sun, W., Fan, J., Wang, S., Kang, Y., Du, J., & Peng, X. (2018). Biodegradable Drug-Loaded Hydroxyapatite Nanotherapeutic Agent for Targeted Drug Release in Tumors. *ACS Appl Mater Interfaces, 10* (9), 7832-7840.

Sun, W., Zhao, C., Li, Y., Wang, L., Nie, G., Peng, J., Wang, A., Zhang, P., Tian, W., Li, Q., Song, J., Wang, C., Xu, X., Tian, Y., Zhao, D., Xu, Z., Zhong, G., Han, B., Ling, S., Chang, Y.-Z., & Li, Y. (2016). Osteoclast-derived microRNA-containing exosomes selectively inhibit osteoblast activity. *Cell Discovery, 2*, 16015.

Surmenev, R. A., Surmeneva, M. A., & Ivanova, A. A. (2014). Significance of calcium phosphate coatings for the enhancement of new bone osteogenesis – A review. *Acta Biomaterialia, 10* (2), 557-579.

Suswillo, R. F., Javaheri, B., Rawlinson, S. C., Dowthwaite, G. P., Lanyon, L. E., & Pitsillides, A. A. (2017). Strain uses gap junctions to reverse stimulation of osteoblast proliferation by osteocytes. *Cell Biochem Funct, 35* (1), 56-65.

Szklarczyk, D., Franceschini, A., Wyder, S., Forslund, K., Heller, D., Huerta-Cepas, J., Simonovic, M., Roth, A., Santos, A., Tsafou, K. P., Kuhn, M., Bork, P., Jensen, L. J., & Von Mering, C. (2015). STRING v10: Protein-protein interaction networks, integrated over the tree of life. *Nucleic Acids Res, 43* (D1), D447-D452.

Takahashi, Y., & Tabata, Y. (2004). Effect of the fiber diameter and porosity of non-woven PET fabrics on the osteogenic differentiation of mesenchymal stem cells. *J Biomater Sci Polym Ed, 15* (1), 41-57.

Tan, S. D., de Vries, T. J., Kuijpers-Jagtman, A. M., Semeins, C. M., Everts, V., & Klein-Nulend, J. (2007). Osteocytes subjected to fluid flow inhibit osteoclast formation and bone resorption. *Bone, 41* (5), 745-751.

Tannoury, C. A., & An, H. S. (2014). Complications with the use of bone morphogenetic protein 2 (BMP-2) in spine surgery. *Spine J, 14* (3), 552-559.

Tas, A. C., & Bhaduri, S. B. (2011). Rapid coating of Ti6Al4V at room temperature with a calcium phosphate solution similar to 10× simulated body fluid. *Journal of Materials Research, 19* (9), 2742-2749.

Tatsumi, S., Ishii, K., Amizuka, N., Li, M. Q., Kobayashi, T., Kohno, K., Ito, M., Takeshita, S., & Ikeda, K. (2007). Targeted ablation of Osteocytes induces osteoporosis with defective mechanotransduction. *Cell Metabolism, 5* (6), 464-475.

Tavafoghi, M., & Cerruti, M. (2016). The role of amino acids in hydroxyapatite mineralization. *Journal of the Royal Society Interface, 13* (123).

Taylor, A. F., Saunders, M. M., Shingle, D. L., Cimbala, J. M., Zhou, Z., & Donahue, H. J. (2007). Mechanically stimulated osteocytes regulate osteoblastic activity via gap junctions. *Am J Physiol Cell Physiol, 292* (1), C545-552.

Thibaudeau, L., Taubenberger, A. V., Holzapfel, B. M., Quent, V. M., Fuehrmann, T., Hesami, P., Brown, T. D., Dalton, P. D., Power, C. A., Hollier, B. G., & Hutmacher, D. W. (2014). A tissue-engineered humanized xenograft model of human breast cancer metastasis to bone. *Disease Models & Mechanisms, 7* (2), 299-309.

Thouverey, C., Malinowska, A., Balcerzak, M., Strzelecka-Kiliszek, A., Buchet, R., Dadlez, M., & Pikula, S. (2011). Proteomic characterization of biogenesis and functions of matrix vesicles released from mineralizing human osteoblast-like cells. *Journal of Proteomics, 74* (7), 1123-1134.

Touchberry, C. D., Green, T. M., Tchikrizov, V., Mannix, J. E., Mao, T. F., Carney, B. W., Girgis, M., Vincent, R. J., Wetmore, L. A., Dawn, B., Bonewald, L. F., Stubbs, J. R., & Wacker, M. J. (2013). FGF23 is a novel regulator of intracellular calcium and cardiac contractility in addition to cardiac hypertrophy. *Am J Physiol Endocrinol Metab, 304* (8), E863-873.

Tourlomousis, F., Babakhanov, A., Ding, H., & Chang, R. C. (2015). *A novel melt electrospinning system for studying cell substrate interactions.* Paper presented at the ASME 2015 International Manufacturing Science and Engineering Conference, MSEC 2015.

Tourlomousis, F., Boettcher, W., Ding, H., & Chang, R. C. (2017). *Investigation of cellular confinement in 3D microscale fibrous substrates: Fabrication and metrology.* Paper presented at the ASME 2017 12th International Manufacturing Science and Engineering Conference, MSEC 2017 collocated with the JSME/ASME 2017 6th International Conference on Materials and Processing.

Tourlomousis, F., & Chang, R. C. (2017). Dimensional Metrology of Cell-matrix Interactions in 3D Microscale Fibrous Substrates. *Procedia CIRP, 65* (Supplement C), 32-37.

Townsend, D. M., Tew, K. D., & Tapiero, H. (2004). Sulfur containing amino acids and human disease. *Biomedicine & Pharmacotherapy, 58* (1), 47-55.

Turner, C. H., Owan, I., Alvey, T., Hulman, J., & Hock, J. M. (1998). Recruitment and proliferative responses of osteoblasts after mechanical loading in vivo determined using sustained-release bromodeoxyuridine. *Bone, 22* (5), 463-469.

Tyanova, S., Temu, T., & Cox, J. (2016). The MaxQuant computational platform for mass spectrometry-based shotgun proteomics. *Nat Protoc, 11* (12), 2301-2319.

Tyanova, S., Temu, T., Sinitcyn, P., Carlson, A., Hein, M. Y., Geiger, T., Mann, M., & Cox, J. (2016). The Perseus computational platform for comprehensive analysis of (prote)omics data. *13* (9), 731-740.

Tzaphlidou, M. (2008). Bone Architecture: Collagen Structure and Calcium/Phosphorus Maps. *Journal of Biological Physics, 34* (1-2), 39-49.

Tzaphlidou, M., & Zaichick, V. (2003). Calcium, phosphorus, calcium-phosphorus ratio in rib bone of healthy humans. *Biol Trace Elem Res, 93* (1-3), 63-74.

van Niel, G., D'Angelo, G., & Raposo, G. (2018). Shedding light on the cell biology of extracellular vesicles. *Nature Reviews Molecular Cell Biology, 19*, 213.

van Oers, R. F. M., Wang, H., & Bacabac, R. G. (2015). Osteocyte Shape and Mechanical Loading. *Current Osteoporosis Reports, 13* (2), 61-66.

Vaquette, C., Ivanovski, S., Hamlet, S. M., & Hutmacher, D. W. (2013). Effect of culture conditions and calcium phosphate coating on ectopic bone formation. *Biomaterials, 34* (22), 5538-5551.

Verbruggen, S. W., Vaughan, T. J., & McNamara, L. M. (2014). Fluid flow in the osteocyte mechanical environment: a fluid-structure interaction approach. *Biomech Model Mechanobiol, 13* (1), 85-97.

Vezeridis, P. S., Semeins, C. M., Chen, Q., & Klein-Nulend, J. (2006). Osteocytes subjected to pulsating fluid flow regulate osteoblast proliferation and differentiation. *Biochem Biophys Res Commun, 348* (3), 1082-1088.

Visser, J., Melchels, F. P. W., Jeon, J. E., Van Bussel, E. M., Kimpton, L. S., Byrne, H. M., Dhert, W. J. A., Dalton, P. D., Hutmacher, D. W., & Malda, J. (2015). Reinforcement of hydrogels using three-dimensionally printed microfibres. *Nat Commun, 6*.

Vukicevic, S., Oppermann, H., Verbanac, D., Jankolija, M., Popek, I., Curak, J., Brkljacic, J., Pauk, M., Erjavec, I., Francetic, I., Dumic-Cule, I., Jelic, M., Durdevic, D., Vlahovic, T., Novak, R., Kufner, V., Bordukalo Niksic, T., Kozlovic, M., Banic Tomisic, Z., Bubic-Spoljar, J., Bastalic, I., Vikic-Topic, S., Peric, M., Pecina, M., & Grgurevic, L. (2014). The clinical use of bone morphogenetic proteins revisited: a novel biocompatible carrier device OSTEOGROW for bone healing. *International Orthopaedics, 38* (3), 635-647.

Wagner, F., Holzapfel, B. M., Thibaudeau, L., Straub, M., Ling, M. T., Grifka, J., Loessner, D., Levesque, J. P., & Hutmacher, D. W. (2016). A Validated Preclinical Animal Model for Primary Bone Tumor Research. *J Bone Joint Surg Am, 98* (11), 916-925.

Wang, P., Zhao, L., Liu, J., Weir, M. D., Zhou, X., & Xu, H. H. (2014). Bone tissue engineering via nanostructured calcium phosphate biomaterials and stem cells. *Bone Res, 2*, 14017.

Wang, Y., Von Euw, S., Fernandes, F. M., Cassaignon, S., Selmane, M., Laurent, G., Pehau-Arnaudet, G., Coelho, C., Bonhomme-Coury, L., Giraud-Guille, M.-M., Babonneau, F., Azaïs, T., & Nassif, N. (2013). Water-mediated structuring of bone apatite. *Nat Mater, 12*, 1144.

Wasserman, E., Webster, D., Kuhn, G., Attar-Namdar, M., Müller, R., & Bab, I. (2013). Differential load-regulated global gene expression in mouse trabecular osteocytes. *Bone, 53* (1), 14-23.

Weinbaum, S., Cowin, S. C., & Zeng, Y. (1994). A model for the excitation of osteocytes by mechanical loading-induced bone fluid shear stresses. *J Biomech, 27* (3), 339-360.

Wells, R. G. (2008). The role of matrix stiffness in regulating cell behavior. *Hepatology, 47* (4), 1394-1400.

Whitelaw, J. H. (2011, 9 February 2011). Convective heat transfer. Retrieved 22/10/2018, 2018, from http://thermopedia.com/content/660/

Whitham, M., Parker, B. L., Friedrichsen, M., Hingst, J. R., Hjorth, M., Hughes, W. E., Egan, C. L., Cron, L., Watt, K. I., Kuchel, R. P., Jayasooriah, N., Estevez, E., Petzold, T., Suter, C. M., Gregorevic, P., Kiens, B., Richter, E. A., James, D. E., Wojtaszewski, J. F. P., & Febbraio,

M. A. (2018). Extracellular Vesicles Provide a Means for Tissue Crosstalk during Exercise. *Cell Metab, 27* (1), 237-251.e234.

Winkler, T., Sass, F. A., Duda, G. N., & Schmidt-Bleek, K. (2018). A review of biomaterials in bone defect healing, remaining shortcomings and future opportunities for bone tissue engineering: The unsolved challenge. *Bone Joint Res, 7* (3), 232-243.

Woo, S. M., Rosser, J., Dusevich, V., Kalajzic, I., & Bonewald, L. F. (2011). Cell Line IDG-SW3 Replicates Osteoblast-to-Late-Osteocyte Differentiation in vitro and Accelerates Bone Formation in vivo. *J Bone Miner Res, 26* (11), 2634-2646.

Wopenka, B., & Pasteris, J. D. (2005). A mineralogical perspective on the apatite in bone. *Materials Science and Engineering: C, 25* (2), 131-143.

World Health Organisation. (2017). Burns: Fact sheet. *www.who.int*.

Wunner, F. M., Bas, O., Saidy, N. T., Dalton, P. D., Pardo, E. M. D., & Hutmacher, D. W. (2017). Melt Electrospinning Writing of Three-dimensional Poly(epsilon-caprolactone) Scaffolds with Controllable Morphologies for Tissue Engineering Applications. *J Vis Exp* (130).

Wunner, F. M., Eggert, S., Maartens, J., Bas, O., Dalton, P. D., De-Juan-Pardo, E. M., & Hutmacher, D. W. (2018). Design and Development of a Three-Dimensional Printing High-Throughput Melt Electrowriting Technology Platform. *3D Printing and Additive Manufacturing*.

Wunner, F. M., Maartens, J., Bas, O., Gottschalk, K., De-Juan-Pardo, E. M., & Hutmacher, D. W. (2018). Electrospinning writing with molten poly (ε-caprolactone) from different directions – Examining the effects of gravity. *Materials Letters, 216*, 114-118.

Wunner, F. M., Wille, M., T.G., N., Bas, O., P.D., D., E.M., D. J. P., & D.W., H. (2018). Melt Electrospinning Writing of Highly Ordered Large Volume Scaffold Architectures. *Adv Mater, 0* (0), 1706570.

Xie, H., Wang, Z., Zhang, L., Lei, Q., Zhao, A., Wang, H., Li, Q., Cao, Y., Jie Zhang, W., & Chen, Z. (2017a). Extracellular Vesicle-functionalized Decalcified Bone Matrix Scaffolds with Enhanced Pro-angiogenic and Pro-bone Regeneration Activities. *Scientific reports, 7*, 45622.

Xie, H., Wang, Z., Zhang, L., Lei, Q., Zhao, A., Wang, H., Li, Q., Cao, Y., Jie Zhang, W., & Chen, Z. (2017b). Extracellular Vesicle-functionalized Decalcified Bone Matrix Scaffolds with Enhanced Pro-angiogenic and Pro-bone Regeneration Activities. *Sci Rep, 7*, 45622.

Xiong, L., Zeng, J., Yao, A., Tu, Q., Li, J., Yan, L., & Tang, Z. (2015). BMP2-loaded hollow hydroxyapatite microspheres exhibit enhanced osteoinduction and osteogenicity in large bone defects. *International Journal of Nanomedicine, 10*, 517-526.

Yanez-Mo, M., Siljander, P. R., Andreu, Z., Zavec, A. B., Borras, F. E., Buzas, E. I., Buzas, K., Casal, E., Cappello, F., Carvalho, J., Colas, E., Cordeiro-da Silva, A., Fais, S., Falcon-Perez, J. M., Ghobrial, I. M., Giebel, B., Gimona, M., Graner, M., Gursel, I., Gursel, M., Heegaard, N. H., Hendrix, A., Kierulf, P., Kokubun, K., Kosanovic, M., Kralj-Iglic, V., Kramer-Albers, E. M., Laitinen, S., Lasser, C., Lener, T., Ligeti, E., Line, A., Lipps, G., Llorente, A., Lotvall, J., Mancek-Keber, M., Marcilla, A., Mittelbrunn, M., Nazarenko, I., Nolte-'t Hoen, E. N., Nyman, T. A., O'Driscoll, L., Olivan, M., Oliveira, C., Pallinger, E., Del Portillo, H. A., Reventos, J., Rigau, M., Rohde, E., Sammar, M., Sanchez-Madrid, F., Santarem, N., Schallmoser, K., Ostenfeld, M. S., Stoorvogel, W., Stukelj, R., Van der Grein, S. G., Vasconcelos, M. H., Wauben, M. H., & De Wever, O. (2015). Biological properties of extracellular vesicles and their physiological functions. *J Extracell Vesicles, 4*, 27066.

Yang, G. H., Mun, F., & Kim, G. (2016). Direct electrospinning writing for producing 3D hybrid constructs consisting of microfibers and macro-struts for tissue engineering. *Chemical Engineering Journal, 288*, 648-658.

Yang, H., Zeng, H., Hao, L., Zhao, N., Du, C., Liao, H., & Wang, Y. (2014). Effects of hydroxyapatite microparticle morphology on bone mesenchymal stem cell behavior. *Journal of Materials Chemistry B, 2* (29), 4703-4710.

Yang, X., Li, Y., Liu, X., Zhang, R., & Feng, Q. (2018). In Vitro Uptake of Hydroxyapatite Nanoparticles and Their Effect on Osteogenic Differentiation of Human Mesenchymal Stem Cells. *Stem cells international, 2018*, 2036176-2036176.

Yang, Y., Wang, K., Gu, X., & Leong, K. W. (2017). Biophysical Regulation of Cell Behavior—Cross Talk between Substrate Stiffness and Nanotopography. *Engineering (Beijing, China), 3* (1), 36-54.

Yaszemski, M. J., Payne, R. G., Hayes, W. C., Langer, R., & Mikos, A. G. (1996). Evolution of bone transplantation: molecular, cellular and tissue strategies to engineer human bone. *Biomaterials, 17* (2), 175-185.

Yazhou, W., Guixue, W., Liang, C., Hao, L., Tieying, Y., Bochu, W., James, C. M. L., & Qingsong, Y. (2009). Electrospun nanofiber meshes with tailored architectures and patterns as potential tissue-engineering scaffolds. *Biofabrication, 1* (1), 015001.

Yin, T., & Li, L. (2006). The stem cell niches in bone. *The Journal of clinical investigation, 116* (5), 1195-1201.

You, L., Temiyasathit, S., Lee, P., Kim, C. H., Tummala, P., Yao, W., Kingery, W., Malone, A. M., Kwon, R. Y., & Jacobs, C. R. (2008). Osteocytes as Mechanosensors in the Inhibition of Bone Resorption Due to Mechanical Loading. *Bone, 42* (1), 172-179.

Young, K. A., Wise, J. A., DeSaix, P., Kruse, D. H., Poe, B., Johnson, E., Johnson, J. E., Korol, O., Betts, J. G., & Womble, M. (2013). *Anatomy & Physiology* (1 ed.): OpenStax College.

Young, M. F. (2003). Bone matrix proteins: their function, regulation, and relationship to osteoporosis. *Osteoporosis International, 14* (3), 35-42.

Yu, X., Biedrzycki, A. H., Khalil, A. S., Hess, D., Umhoefer, J. M., Markel, M. D., & Murphy, W. L. (2017). Nanostructured Mineral Coatings Stabilize Proteins for Therapeutic Delivery. *Adv Mater, 29* (33).

Zaichick, V., & Tzaphlidou, M. (2002). Determination of calcium, phosphorus, and the calcium/phosphorus ratio in cortical bone from the human femoral neck by neutron activation analysis. *Appl Radiat Isot, 56* (6), 781-786.

Zaichick, V., & Tzaphlidou, M. (2003). Calcium and phosphorus concentrations and the calcium/phosphorus ratio in trabecular bone from the femoral neck of healthy humans as determined by neutron activation analysis. *Applied Radiation and Isotopes, 58* (6), 623-627.

Zhang, J., Liu, X., Li, H., Chen, C., Hu, B., Niu, X., Li, Q., Zhao, B., Xie, Z., & Wang, Y. (2016). Exosomes/tricalcium phosphate combination scaffolds can enhance bone regeneration by activating the PI3K/Akt signaling pathway. *Stem Cell Research & Therapy, 7* (1), 136.

Zhang, L. H., Duan, X. P., Yan, X., Yu, M., Ning, X., Zhao, Y., & Long, Y. Z. (2016). Recent advances in melt electrospinning. *RSC Advances, 6* (58), 53400-53414.

Zhao, S., Kato, Y., Zhang, Y., Harris, S., Ahuja, S. S., & Bonewald, L. F. (2002). MLO-Y4 osteocyte-like cells support osteoclast formation and activation. *Journal of Bone and Mineral Research, 17* (11), 2068-2079.

Zhong, W., Tian, K., Zheng, X., Li, L., Zhang, W., Wang, S., & Qin, J. (2013). Mesenchymal stem cell and chondrocyte fates in a multishear microdevice are regulated by Yes-associated protein. *Stem Cells Dev, 22* (14), 2083-2093.

Zhou, H., Green, T. B., & Joo, Y. L. (2006). The thermal effects on electrospinning of polylactic acid melts. *Polymer, 47* (21), 7497-7505.

Zhou, H., & Lee, J. (2011). Nanoscale hydroxyapatite particles for bone tissue engineering. *Acta Biomaterialia, 7* (7), 2769-2781.

Zhou, J. Z., Riquelme, M. A., Gu, S., Kar, R., Gao, X., Sun, L., & Jiang, J. X. (2016). Osteocytic connexin hemichannels suppress breast cancer growth and bone metastasis. *Oncogene, 35* (43), 5597-5607.

Zhou, P., Wu, J., Xia, Y., Yuan, Y., Zhang, H., Xu, S., & Lin, K. (2018). Loading BMP-2 on nanostructured hydroxyapatite microspheres for rapid bone regeneration. *International Journal of Nanomedicine, 13*, 4083-4092.

List of figures

List of tables

Supplementary figures and tables

Table S 3-1 Primer sequences and concentrations employed in quantitative PCR analysis.

Gene symbol	Tm (°C)	Primer concentration	Sequence	Amplicon size
18s	60	300 nM	ATCGGGGATTGCAATTATTC	130bp
			CTCACTAAACCATCCAATCG	
GAPDH	60	300 nM	ACAGTTGCCATGTAGACC	95bp
			TTTTTGGTTGAGCACAGG	
COX2	60	400 nM	AAGCAGGCTAATACTGATAGG	113bp
			TGTTGAAAAGTAGTTCTGGG	
OCN	65	400 nM	CACTCCTCGCCCTATTGGC	112bp
			CCCTCCTGCTTGGACACAAAG	
OPN	60	400 nM	GACCAAGGAAAACTCACTAC	84bp
			CTGTTTAACTGGTATGGCAC	
RUNX2	60	400 nM	GCAGTATTTACAACAGAGGG	112bp
			TCCCAAAAGAAGTTTTGCTG	
OSX	60	400 nM	TGAGGAGGAAGTTCACTATG	200bp
			CATTAGTGCTTGTAAAGGGG	

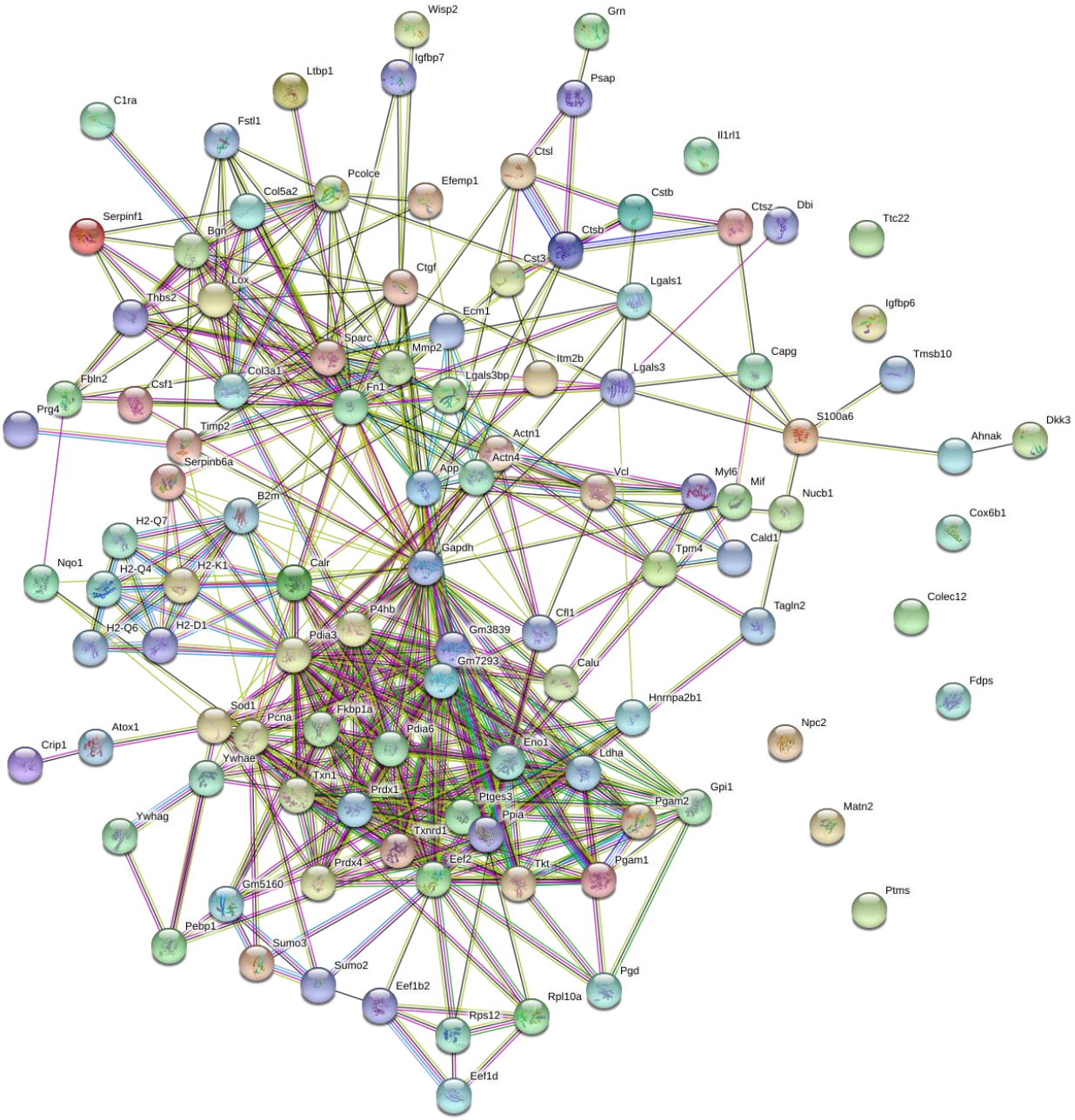

Figure S 3-1 String DB network illustrating interactions between proteins in the osteocyte secretome, with significant degree of protein-protein interaction ($p < 10^{-16}$)

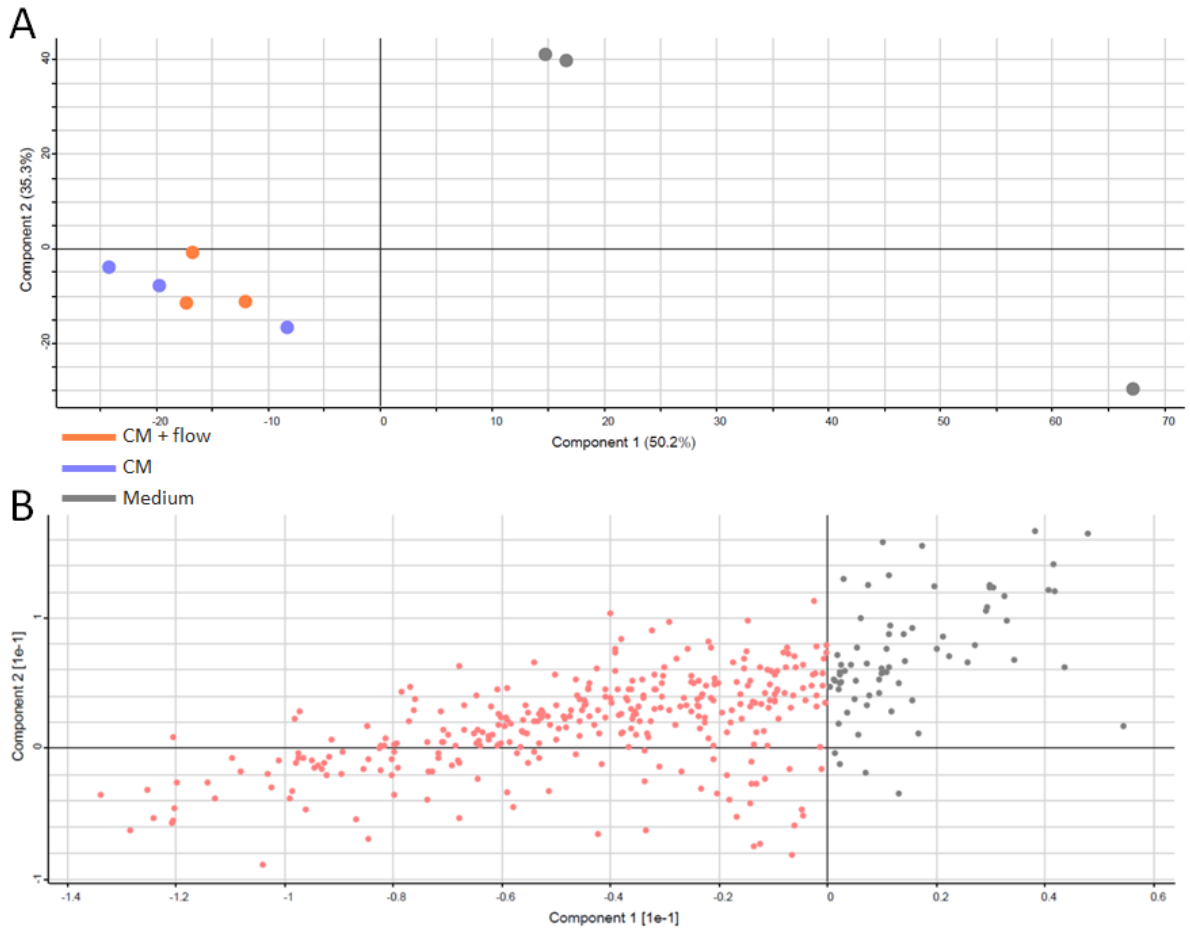

Figure S 3-2 Principal Component Analysis (PCA) revealing the variance between the three experimental groups and indicating three main clusters of data (C). The proteins primarily driving the separation between the medium groups and the control groups are highlighted in red (D).

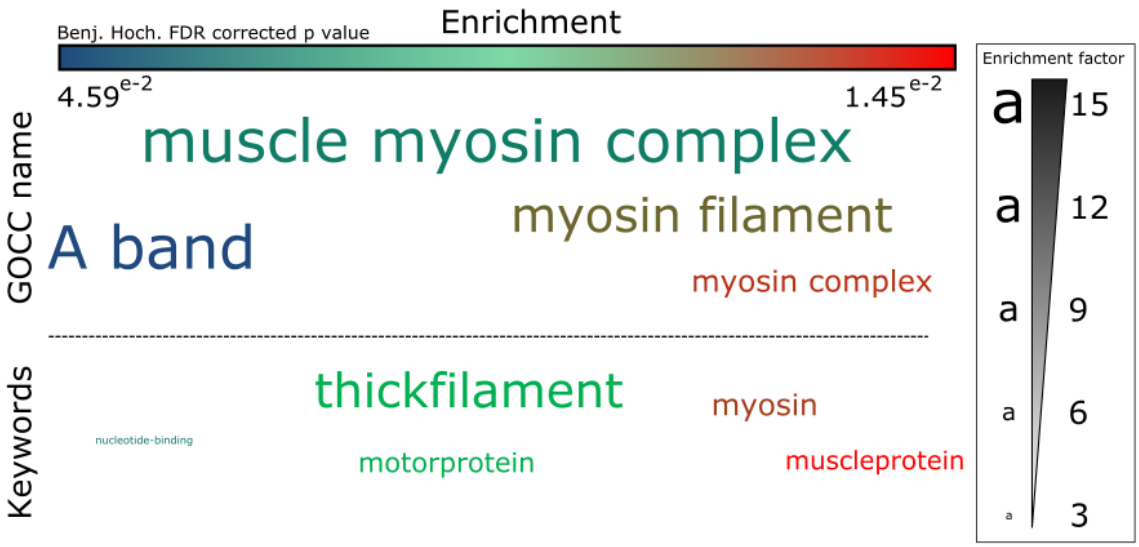

Figure S 3-3 Enrichment analysis of GOCC terms and Uniprot keywords in proteins with greater expression in control medium samples, using Fisher's exact test represented as a word cloud (D). The size of the word represents enrichment of terms, while colour represents FDR corrected p value. All terms with a minimum 0.05 FDR corrected p value were included.

Table S 3-2 Functional enrichments in Medium proteins using String DB, with observed gene count out of a total 35 proteins with an FDR cut-off of 2%.

Pathway description	Observed gene count	False discovery rate (FDR)
GOCC		
myosin filament	6	1.67E-10
myofibril	7	6.42E-06
actin cytoskeleton	8	2.41E-05
muscle myosin complex	3	2.66E-05
contractile fiber	6	1.08E-04
stress fiber	4	2.23E-04
myosin complex	4	2.23E-04
sarcomere	5	5.37E-04
filopodium	4	8.68E-04
intracellular non-membrane-bounded organelle	15	3.03E-03
GOBP		
mesenchyme migration	4	3.24E-07
muscle contraction	6	2.41E-04
muscle filament sliding	3	5.11E-04
mesenchyme morphogenesis	4	5.46E-04
tissue morphogenesis	8	4.41E-03
striated muscle contraction	4	4.56E-03
skeletal muscle contraction	3	8.26E-03
GOMF		
microfilament motor activity	4	3.47E-05
purine ribonucleoside binding	14	3.67E-05
purine ribonucleotide binding	14	3.67E-05
purine ribonucleoside triphosphate binding	14	3.67E-05
small molecule binding	15	2.09E-04
anion binding	15	2.31E-04
motor activity	5	2.42E-04
organic cyclic compound binding	20	3.93E-04
ATP binding	11	8.46E-04
heterocyclic compound binding	19	1.34E-03
Pfam		
Actin	4	1.78E-05
Myosin N-terminal SH3-like domain	3	9.33E-05

Myosin tail	3	3.72E-04
Myosin head (motor domain)	3	1.07E-03
Ribosomal protein L6e	2	1.07E-03
Ribosomal protein L6, N-terminal domain	2	1.07E-03

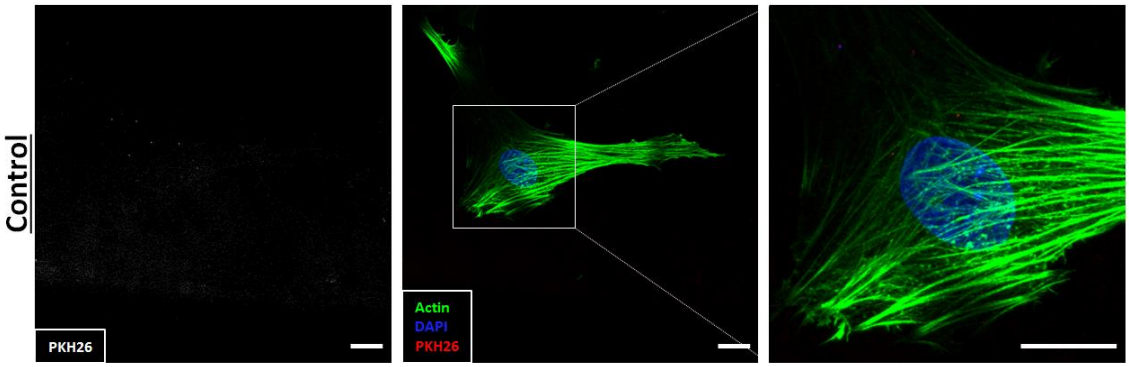

Figure S 3-4 Control samples with no EVs and PKH26 staining demonstrating minimal unspecific fluorescence (Scale = 10µm).

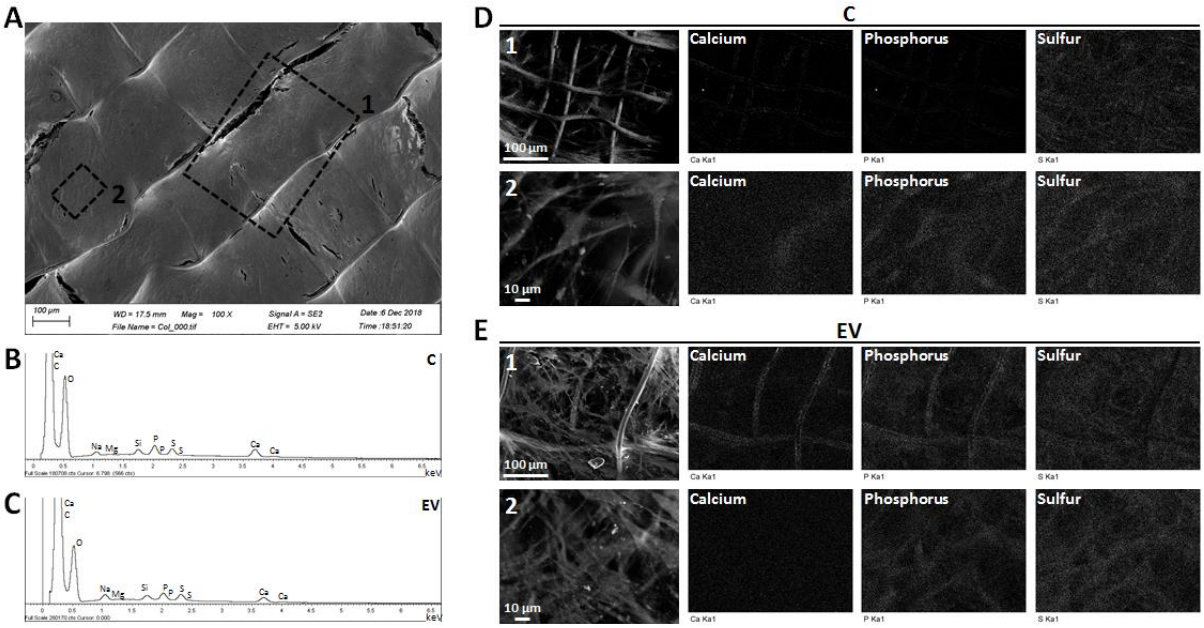

Figure S 7-1 EDX analysis of constructs at D21. Element mapping was conducted in regions 1 and 2 for C and EV scaffolds, as these groups have the lowest and highest osteogenic capacity respectively at D21 (A). Spectra were similar for both C (B) and EV (C) groups, revealing the presence of sodium and magnesium in addition to the minerals calcium, phosphorus and sulfur. Element maps show a consistent spread of calcium and phosphorus, in addition to the presence of sulfur in C (D) and EV (F).